Manganese Speciation in Soil
Studied by
Mn K-edge X-ray Absorption Spectroscopy

Von der Naturwissenschaftlichen Fakultät der

Gottfried Wilhelm Leibniz Universität Hannover

zur Erlangung des Grades

Doktorin der Naturwissenschaften

(Dr. rer. nat.)

genehmigte Dissertation

von

Teresa Elisabeth Zahoransky, M.Sc.

2022

Referent:	Prof. Dr. rer. nat. Christian Mikutta
Korreferenten:	PD Dr. rer. nat. Stefan Dultz
	Prof. Dr. rer. nat. Thilo Rennert
Tag der Promotion:	11.07.2022

Indes sie forschten, röntgten, filmten, funkten, entstand von selbst die köstlichste Erfindung: Der Umweg als die kürzeste Verbindung zwischen zwei Punkten.

Erich Kästner

Dedicated to my family and Uwe

for their countless support, faith, and love.

In memory of my father.

ACKNOWLEDGEMENTS

Throughout my time as a PhD student, I experienced the support and friendship of numerous people, to whom I am most grateful. In the first place, I want to express my gratitude to Christian Mikutta for the immense support, long discussions and telephone calls ($N = \infty$) around the clock – and for making the world of soils for me more colorful than I could have expected. I am particularly grateful for the opportunity to dive into the world of synchrotron analysis and I will miss the endorphins of these trips. Morning tea discussions became part of the daily routine, which I will certainly miss in the future, too. Finally, thank you for your patience with me as a newbie in the world of soils. Funding of the project was provided by the German Research foundation (DFG), to whom I am indebted.

Part of the analytics was carried out at the institute of soil science under laboratory guidance of Leopold Sauheitl. I thank him for letting me use his labs and for sharing his expertise on soil-related questions. My deepest thanks belong to Ulrike Pieper, who took me under her wings as a technician and supported me in every way during the on-site soil analyses. I will miss your warm-heartedness. I also thank Anne, Heike, Kladdi, Silke, Sanne, and Viola for sharing their analytical knowledge with me.

Rebekka Stünkel was a great technician. Thank you for your hard work and your motivated and cheerful nature during long sample preparation sessions. It was a pleasure to hear the Sherlock Holmes audios with you, Watson.

Klaus Kaiser from the working group of Soil Science and Soil Protection (Martin-Luther-Universität Halle-Wittenberg) is thanked for his great support during field sampling, for sharing his expertise on soil nomenclature, and for many fruitful comments and discussions.

Titration experiments at the Federal Institute for Geosciences and Natural Resources (BGR) were enabled by Rainer Dohrmann, to whom I am indebted. Anna Bachmann is gratefully acknowledged for her work and discussions and for sharing some excellent mineral specimen with me. I also thank Winnie Huong for her effective work and the documentation of titration experiments.

Collaborations in terms of XPS analysis with Robert Mikutta, head of the Soil Science and Soil Protection working group (Martin-Luther-Universität Halle-Wittenberg), enriched my work. I would also like to thank Thimo Klotzbücher, who spend a lot of time keeping the machine and my samples running.

I would like to thank Mister Buhl from the former Crystallography working group of the Institute of Mineralogy for his patient explanations on crystal systems. Crystallographic knowledge and support of Irma Peschke were most valuable to me, thank you very much.

I also thank all technicians and lab managers from the institute who supported me in many ways, especially Alexandra and Maria. And not to forget Andreas and Uli for repetitive practical help in the workshop. Julian is thanked for perfect EPMA sample preparation and chats about new mineral

and mushroom discoveries. I also thank Sabine and Kristin for help with all paperwork – I would have been totally lost without you.

Life at university would only be half as nice without my colleagues from the institute. I would like to thank all people from the 'lunch group', for welcoming me to the institute and understanding my Schwarzwälderisch, and for all serious and not so serious conversations, especially Andreas, Dominik, Flo, Insa, Lili, Marie, Philipp, Sarah, Sebastian, and Sven.

Furthermore, I would like to express my gratitude to all members of the group of Soil Mineralogy. Particularly to Svenja and Max for our good teamwork when our working group was still under construction. Thank you, Ricarda and Lena, for the great time together in the office, the valuable chats, and laughs we had and for repetitive proofreading of this thesis. Lena and Yvonne – thank you very much for being great friends and for always having a bed for me when I was stranded in Hannover again. Your friendship is most valuable to me and I cannot express how grateful I am for all the time we have spent – and will spend – together.

I would also like to give special thanks to some friends from outside the university: Beate, Carmen, Dr. Barnasch, Denise, Hagen, and Raik, my friends and colleagues from home, Tübingen, and the Werra for their constant interest, sympathy, and encouragement during this turbulent time. Your friendship is worth so much to me. I thank Gregor for his sincere friendship and honest advices, and Henrik, Toril, and Ann-Helén from Oslo for still holding contact with me.

The most valuable support is the unlimited love, care, and encouragement I have always received from my family. I thank you for your endless support and I look forward to spending more time with you again. I also want to thank Uwe`s family, who always welcomes me so warmly as part of their family. Most of all, I am indebted to my husband Uwe. Thank you for the cheese-sandwich on the stairs when I just came home half-starved once again. I cannot express how much you enrich my life.

ABSTRACT

Manganese (Mn) is one of the most redox-sensitive elements on Earth, participating in a plethora of environmental processes. Its reactivity and mobility largely rely on its specific chemical form, i.e., Mn^{2+}, Mn^{3+}, or Mn^{4+}. In soils, Mn is recognized as a major player controlling oxidative transformation of organic and inorganic constituents. Various Mn minerals are found in soils, but among all, Mn oxides and hydroxides are commonly referred to as key species, whose precipitation and dissolution primarily control the sequestration of (heavy) metal pollutants and nutrients. Despite their ecological relevance, their typically low concentration and poor crystallinity in soils render their analytical accessibility challenging. Thus, studies identifying and quantifying effectively occurring chemical forms of Mn in soils are remarkably rare. To overcome this lack of knowledge, this work provides the first Mn K-edge (6,539 eV) X-ray absorption spectroscopy (XAS) library of soil Mn species and presents the first quantitative species inventory of bulk soils.

The first study compiles a database of 32 well characterized (in)organic Mn compounds potentially occurring in soils. Their Mn average oxidation state (AOS) was inferred from Mn K-edge X-ray absorption near edge structure (XANES) and their local (<5 Å) Mn coordination environment form extended X-ray absorption fine structure (EXAFS) spectroscopy. Principal component and cluster analyses of k^2-weighted EXAFS spectra of Mn compounds implied that at least five primary Mn species groups can be identified and quantified by EXAFS linear combination fit analysis of environmental samples. The results highlight the potential of Mn K-edge EXAFS spectroscopy to assess bulk Mn speciation in soils and establish the first extensive framework for the analysis and interpretation of Mn XAS spectra of natural samples.

The second study explores Mn speciation of 47 soil samples (45.1-2,280 mg/kg Mn) of nine Central European soils by XAS and relates the obtained information to major soil properties. In litter horizons, Mn was mainly present in the form of organically complexed and 'physisorbed' Mn, but also minor amounts of manganates, Mn(III) oxyhydroxides, and silicate-bound Mn occurred. In all mineral soil horizons, manganates clearly dominated, but we also highlight the occurrence of feitknechtite (β-MnOOH), groutite (α-MnOOH), and hausmannite (Mn_3O_4) in acidic soils. The low occurrence of primary silicate-bound and exchangeable Mn phases confirms the early release of Mn from primary silicate minerals and the rapid conversion into manganates, respectively. These results have far-reaching implications for the functioning of soil and biogeochemical element cycles, as manganates play a fundamental role in metal binding, plant nutrition, and redox-related processes in the critical zone.

KEYWORDS

Manganese, X-ray absorption near edge spectroscopy (XANES), extended X-ray absorption fine spectroscopy (EXAFS), Mn average oxidation state (Mn AOS), linear combination fitting (LCF), spectral fingerprinting, soils

ZUSAMMENFASSUNG

Mangan (Mn) ist eines der redoxempfindlichsten Elemente der Erde, das an einer Vielzahl von Umweltprozessen beteiligt ist. Seine Reaktivität und Mobilität hängen weitgehend von seiner spezifischen chemischen Form ab, d. h. von Mn^{2+}, Mn^{3+} oder Mn^{4+}. In Böden gilt Mn als wichtiger Akteur, der die oxidative Umwandlung von organischen und anorganischen Bestandteilen kontrolliert. Verschiedene Mn-Minerale kommen in Böden vor, doch werden Mn-Oxide und -Hydroxide gemeinhin als Schlüsselspezies bezeichnet, deren Ausfällung und Auflösung in erster Linie die Rückhaltung von (Schwer-) Metall-Schadstoffen und Nährstoffen steuern. Trotz ihrer ökologischen Bedeutung ist ihre analytische Erfassung durch ihre typischerweise niedrige Konzentration und geringe Kristallinität in Böden eine Herausforderung. Daher sind Studien zur Identifizierung und Quantifizierung der tatsächlich vorkommenden chemischen Formen von Mn in Böden erstaunlich selten. Zur Behebung dieses Wissensmangels liefert diese Studie die erste Mn K-Kanten (6.539 eV) Röntgenabsorptionsspektroskopie (XAS) Bibliothek von Mn-Spezies in Böden und stellt das erste quantitative Speziesinventar von Böden vor.

Die erste Studie umfasst eine Datenbank mit 32 gut charakterisierten (an)organischen Mn-Verbindungen, die potentiell in Böden vorkommen. Ihr durchschnittlicher Mn Oxidationszustand (AOS) wurde aus der Röntgen-Nahkanten-Absorptionsspektroskopie (XANES) an der Mn K-Kante und ihre lokale (<5 Å) Mn-Koordinationsumgebung aus der erweiterten Röntgenabsorptions-Feinstrukturspektroskopie (EXAFS) abgeleitet. Hauptkomponenten- und Clusteranalysen von k^2-gewichteten EXAFS-Spektren der Mn-Verbindungen ergaben, dass mindestens fünf primäre Mn-Speziesgruppen durch EXAFS Linearkombination-Fit-Analysen von Umweltproben identifiziert und quantifiziert werden können. Die Ergebnisse unterstreichen das Potential der Mn K-Kanten EXAFS Spektroskopie zur Erfassung der Mn Speziierung in Böden und bieten den ersten umfassenden Rahmen für die Analyse und Interpretation von Mn XAS-Spektren natürlicher Proben.

Die zweite Studie untersucht die Mn-Speziierung von 47 Bodenproben (45,1-2.280 mg/kg Mn) aus neun mitteleuropäischen Böden mittels XAS und setzt die gewonnenen Informationen mit wichtigen Bodeneigenschaften in Beziehung. In den Streuhorizonten war hauptsächlich organisch komplexiertes und ‘physisorbiertes’ Mn vorhanden, aber auch geringe Mengen an Manganaten, Mn(III)-Oxyhydroxiden und silikatgebundenem Mn kamen vor. In allen mineralischen Bodenhorizonten dominierten eindeutig die Manganate, aber wir betonen auch das Vorkommen von Feitknechtite (β-MnOOH), Groutite (α-MnOOH) und Hausmannite (Mn_3O_4). Das geringe Vorkommen von primären silikatgebundenen und austauschbaren Mn-Phasen bestätigt die frühe Freisetzung von Mn aus primären Mineralen bzw. die schnelle Umwandlung in Manganate. Diese Ergebnisse haben weitreichende Auswirkungen auf die Funktionsweise des Bodens und auf biogeochemischen Elementkreisläufe, da Manganate eine grundlegende Rolle bei der Metallbindung, der Pflanzenernährung und den Redoxprozessen in der kritischen Zone spielen.

SCHLÜSSELWÖRTER

Mangan, Röntgen-Nahkanten-Absorptionsspektroskopie (XANES), erweiterte Röntgenabsorptions-Feinstruktur-spektroskopie (EXAFS), mittlerer Mn Oxidationszustand (Mn AOS), Linearkombination-Fit-Analyse (LCF), spektraler Fingerabdruck, Böden

ABBREVIATIONS

Å	Ångström (10^{-10} m)
AOS	Average oxidation state
apfu	Atoms per formula unit
CN	Coordination number
DOM	Dissolved organic matter
EPMA	Electron probe micro analysis
EXAFS	Extended X-ray absorption fine structure
FT	Fourier transform
ICP-OES	Inductively coupled plasma optical emission spectroscopy
LCF	Linear combination fitting
n.d.	Not determined
LMWO	Low molecular weight organic (acid/compound)
Mn (oxyhydr)oxides	Manganese oxides and hydroxides
MS	Multiple scattering
PCA	Principal component analysis
SE	Sequential extraction
SEM	Scanning electron microscopy
s.s.	Sensu stricto (indicating endmember composition of a mineral group)
TEM	Transmission electron microscopy
v.u.	Valence units
v/v	'Volume per volume'; volume concentration of a solution
wt.%	Weight percent
(P)XRD	(Powder) X-ray diffraction
XAS	X-ray absorption spectroscopy
XANES	X-ray absorption near edge spectroscopy
(μ-)XRF	(Micro-) X-ray fluorescence

Table of contents

CITATION **3**
DEDICATION **5**
ACKNOWLEDGEMENTS **7**
ABSTRACT **9**
KEYWORDS **10**
ZUSAMMENFASSUNG **11**
SCHLÜSSELWÖRTER **12**
ABBREVIATIONS **13**
TABLE OF CONTENTS **15**

1. INTRODUCTION **19**
1.1. Ecological relevance of Mn 21
1.2. Mn mineralogy in soils 23
1.3. Analytical approaches to Mn speciation 28
1.4. Research motivation and outline of this thesis 33
1.5. References 35

2. X-RAY ABSORPTION SPECTROSCOPY STUDY OF MN REFERENCE COMPOUNDS FOR MN SPECIATION IN TERRESTRIAL SURFACE ENVIRONMENTS **43**
Abstract 43
2.1. Introduction 44
2.2. Materials and methods 47
2.2.1. Manganese reference compounds 47
2.2.2. Characterization of Mn reference compounds 50
2.2.2.1. X-ray diffraction 50
2.2.2.2. Chemical composition 50
2.2.2.3. Redox titration 51
2.2.2.4. Manganese K-edge XAS 51
2.2.2.5. Manganese XAS data analysis 52
2.2.2.6. Statistics 53
2.3. Results and discussion 53
2.3.1. XANES spectra of Mn references compounds 53
2.3.2. Average oxidation state of Mn reference compounds 59
2.3.3. EXAFS spectra of Mn references compounds 61
2.3.3.1. Phyllo- and tectomanganates 66
2.3.3.2. Oxide minerals without layer or tunnel structure 68
2.3.3.3. Manganese(III) oxyhydroxides 68

2.3.3.4. Carbonate, phosphate, and silicate minerals 69
2.3.3.5. Organic Mn(II/III) compounds 70
2.3.3.6. Adsorbed Mn(II) species 71
2.3.3.7. Comparison of interatomic distances 71
2.3.3.8. Statistical XAS spectrum comparisons 73
2.4. Implications 77
2.5. Acknowledgements 79
2.6. References 80

A. SUPPORTING INFORMATION TO CHAPTER 2 85
A.1. Synthesis of Mn(II) adsorption samples 85
A.2. X-ray diffraction patterns of Mn reference compounds 85
A2.1. Phyllo- and tectomanganates 85
A2.2. Oxide minerals without layer or tunnel structure 86
A2.3. Mn(III) oxyhydroxides 86
A2.4. Carbonate, phosphate, and silicate minerals 86
A2.5. Compounds used for Mn(II) adsorption 87
A.3. Chemical characterization of Mn reference compounds 91
A3.1. Notes on empirical formula calculations 91
A.4. Manganese K-edge XAS of Mn reference compounds 96
A4.1. Sample preparation 96
A4.2. Manganese K-edge EXAFS fits 97
A.5. Statistical XANES comparisons 100
A.6. PCA output parameters for Mn K-edge EXAFS spectra 102
A.7. References 103

3. HIGH MANGANESE REDOX VARIABILITY AND MANGANATE PREDOMINANCE IN TEMPERATE SOIL PROFILES AS DETERMINED BY X-RAY ABSORPTION SPECTROSCOPY 105
Abstract 105
3.1. Introduction 107
3.2. Materials and methods 109
3.2.1. Soil sampling and classification 109
3.2.2. Basic soil characterization 109
3.2.3. Manganese K-edge XAS 110
3.2.4. XAS data analysis 111
3.2.4.1. XANES analysis 111
3.2.4.2. EXAFS analysis 112
3.2.5. Statistics 112
3.3. Results 113
3.3.1. Physicochemical soil properties 113

3.3.2. XANES analysis 116
3.3.3. EXAFS analyses 120
3.3.3.1. Linear combination fitting 120
3.3.3.2. Shell fitting 126
3.4. Discussion 131
3.4.1. Soil parameter correlations with Mn 131
3.4.2. Manganese oxidation states 132
3.4.3. EXAFS-based Mn speciation 133
3.4.3.1. Data interpretation 133
3.4.3.2. EXAFS speciation of soil samples 134
3.5. Summary and Conclusion 136
3.6. Acknowledgements 137
3.7. References 138

B. SUPPORTING INFORMATION TO CHAPTER 3 144
B.1. Sampling site description 144
B.2. Additional soil properties 146
B.3. Selective Mn extraction 147
B.4. Manganese K-edge X-ray absorption spectroscopy 148
B4.1. EXAFS-Linear combination fit interpretation scheme 149
B4.2. Initial PCA-TT-based EXAFS linear combination fits 150
B.5. References 154

4. CONCLUSIONS, IMPLICATIONS, AND PERSPECTIVES 155
4.1. References 160

CURRICULUM VITAE 161
LIST OF PUBLICATIONS 163

1. INTRODUCTION

Manganese (Mn) is a ubiquitous element, whose relatively low crustal abundance of about 0.1 wt.% (Yaroshevsky, 2006) is vastly disproportionate to its importance to life on Earth. Naturally, it occurs in the three oxidation states +2, +3, and +4, which account for its large number of existing organic and inorganic compounds. In that, the highly redox-sensitive transition metal is not only used by modern humans in the steel industry, as catalyst, and battery material, it is also one of the most effective natural oxidizing agents participating in a large variety of (in)organic redox-reactions (Bartlett, 1988; Remucal and Ginder-Vogel, 2014). Understanding the biogeochemical cycling of Mn, and thus its role in the environment affecting the fate of nutrients and environmental pollutants, involves detailed knowledge of its speciation – a topic that increasingly attracts scientific interest. In this context, advances in analytical technology and, in particular, the use of highly brilliant X-rays, known as synchrotron radiation, provide the opportunity to pursue questions related to Mn speciation in detail that had long been impossible.

The following section summarizes the current state of knowledge on Mn speciation and Mn-related processes at the interface of (biogeo-) chemistry and mineralogy, with particular emphasis on the soil system. This is of special interest considering that the soil system is influenced by processes of the atmosphere, biosphere, geosphere, and hydrosphere. Some of the most important Mn-based processes and sites of species transformation of Mn in the environment, which are addressed in the subsequent subchapters, are illustrated schematically in Figure 1.1. Also, analytical approaches to assess Mn speciation in in soils and sediments are addressed.

The final part of this chapter details the research motivation and outline of this thesis, which involves two consecutive studies. The first study focuses on the compilation of an extensive reference library of Mn XAS spectra potentially occurring in soils. The second study employs this XAS library to quantitatively explore Mn species (-groups) in different bulk soils for the first time. Here, largely undisturbed soils were investigated, which are unrelated to mining or other obvious human influences, that may have affected Mn speciation. These studies follow the superordinate aim to enhance our knowledge of quantitative Mn species distribution in soils with different pedogenic backgrounds, and thus on the species-dependent dynamics of Mn in terrestrial surface environments.

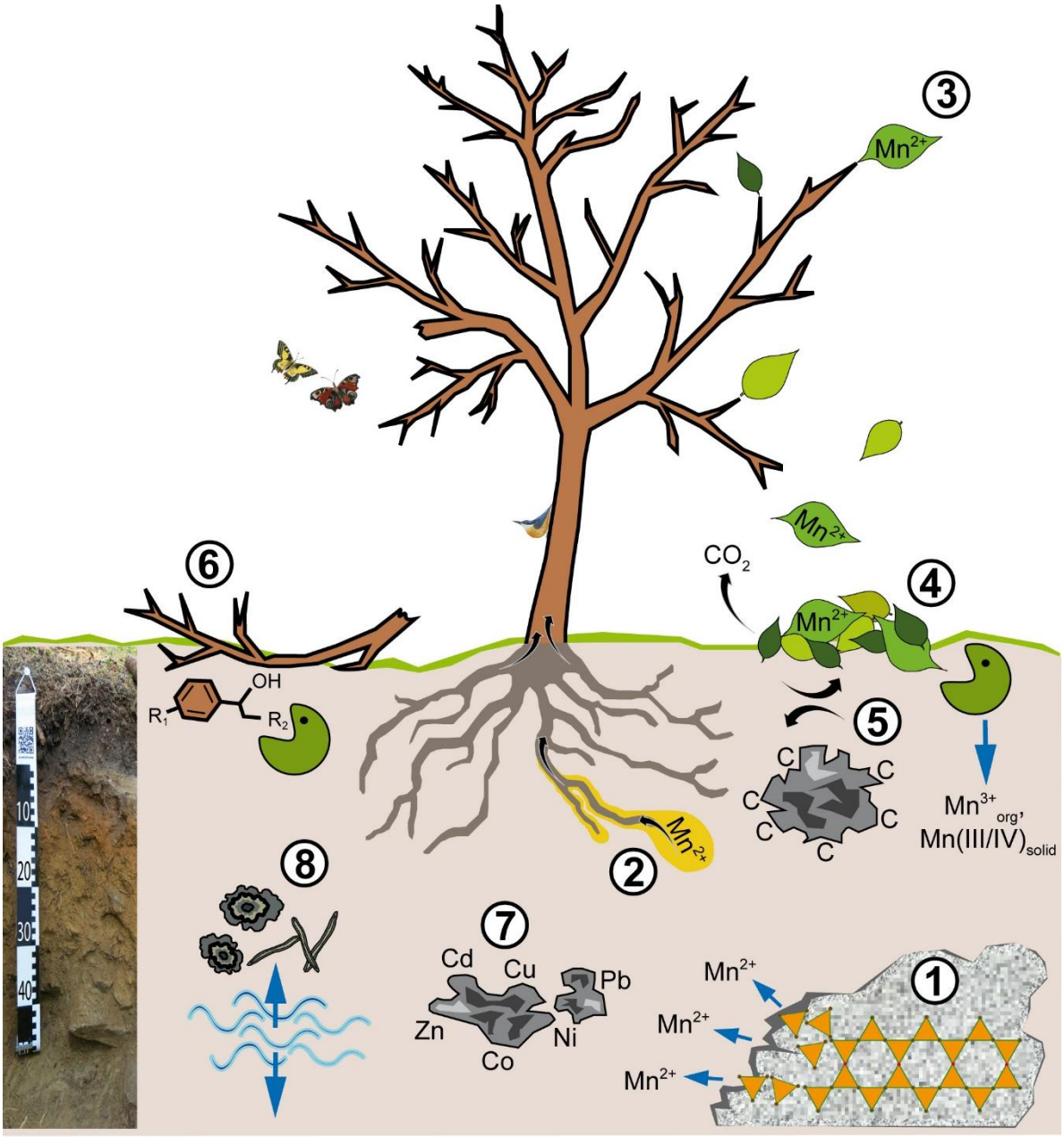

Figure 1.1. Schematic illustration of important processes of the Mn cycle in the critical zone, involving atmosphere, biosphere, geosphere, and hydrosphere. (1) Release of Mn^{2+} upon weathering of primary rock forming minerals, (2) Mn^{2+} uptake in the rhizosphere, where a more acid microenvironment can be created, (3) Mn^{2+} storage in foliar tissue, (4) Microbial (i.e., fungal) processing of litterborne Mn^{2+} and subsequent formation of higher valent Mn species, (5) Mn (oxyhydr)oxides, which are partially reductively dissolved upon oxidative decomposition of organic litter, showing a high maximum sorption capacity for organic carbon (C), (6) Microbially accessible low molecular-weight organic (LMWO) compounds after the Mn mediated oxidative degradation of former complex organic structures, (7) Mn (oxyhydr)oxides as effective scavengers of heavy- and trace metals, (8) Formation of soil nodules and concretions under recurring wetting and drying cycles, that constantly change soil Eh and pH conditions.

1.1. ECOLOGICAL RELEVANCE OF MN

Manganese is an essential element for all forms of life on Earth (Blume et al., 2016). It is, for example, involved in biochemical reactions of numerous enzymes, such as in manganese-dependent superoxide dismutase and oxalate oxidase (Finley and Davis, 1999; Broadley et al., 2012) as well as in oxidative lignin degradation (Keiluweit et al., 2015) through lignin-modifying manganese peroxidase (Hofrichter, 2002). Moreover, Mn is crucial for physiological processes like brain function of mammals (Takeda, 2003), DNA-repair (Sava et al., 2004), and reproduction (Studer et al., 2022). Manganese toxicity in humans, a phenomenon observed in Mn mining or steel-production sites with high Mn exposure, can cause severe neurological diseases similar to Parkinson and dystonia (Pal et al., 1999; Flynn and Susi, 2009; Michalke, 2016; Dlamini et al., 2020).

In soil, rocks are the primary source of Mn, which is released during weathering of rock-forming minerals such as ferromagnesian silicates (i.e., olivine, pyroxene, amphibole, biotite) or spinels (magnetite, ilmenite, chromite) (Gilkes and McKenzie, 1988) (Fig. 1.1 (1)). For plants, Mn is an essential micronutrient and its role in plant nutrition and soil fertility took shape in the early 20th century for the first time (Brenchley, 1914; McHargue, 1922). Since in aerobic soils, insoluble, plant unavailable Mn(III) and Mn(IV) species prevail at typical soil pH values (see section 1.2), the rhizosphere of plants can create an acid microenvironment upon the release of H^+ or low molecular weight organic (LMWO) acids, that move the thermodynamic equilibria in favor of mobile and bioavailable Mn^{2+}, enabling its uptake by plant roots (Millaleo et al., 2010) (Fig. 1.1 (2)). Likewise, a more oxic root microenvironment in, for example, reduced anoxic estuarine sediments, can lead to the formation of Mn-rich rhizo-concretions or plaque on the root, limiting phytotoxic metal uptake (Weis and Weis, 2004). Nowadays it is known that plants taking up water soluble Mn^{2+} later store it in foliar tissue, likely predominantly as free or carboxylate-bound Mn^{2+} (Fernando et al., 2010) and potentially organic Mn^{3+} complexes (Herndon et al., 2014) (Fig. 1.1 (2-3)). Within the plant, Mn is crucially involved in the oxygen evolving complex of photosystem II, which contains a catalytic Mn_4Ca site that participates in water oxidation (Wydrzynski et al., 2005) and in chlorophyll biosynthesis (Bottrill et al., 1970; Macfie and Taylor, 1992). In plant shoots, Mn concentrations are typically around 50-800 µg/g dry weight (Fernando et al., 2009). At foliar concentrations <10 µg/g, symptoms of Mn deficiency may occur (Fernando et al., 2009). The first scientific description of such symptoms in plants, dating back to the mid-19th century, was reported from oat leaves (Salm-Horstmar 1849). They typically appear as interveinal chlorosis of young leaves (Blume et al., 2016) and arise in soils with a naturally low plant-available Mn content or with alkaline pH containing free carbonates, e.g., after liming (Page, 1962), and in intensely weathered soils (Zech and Drechsel, 1991; Naidu and Rengasamy, 1993). Toxicity thresholds, that decreased dry matter production by 10%, are reported from 200 µg/g (maize) to 5,300 µg/g (sunflower) dry weight (Edwards

and Asher, 1982). Phytotoxic levels of Mn can occur when soil pH is low and/or in reducing environments, such as during flooding or poor drainage (Porter et al., 2004), providing high levels of plant available Mn^{2+} in the soil solution.

Manganese toxicity in plants may lead to photo-oxidative stress, disruption of electron flow in chloroplasts, and cellulose formation and can be visible as small dark spots, chlorosis, or necrosis (Fernando and Lynch, 2015; Blamey et al., 2018). Since Mn speciation – and thus its (bio)availability – is largely controlled by redox potential (Eh) and pH (see section 1.2), Mn toxicity and deficiency symptoms may generally occur independently of the bulk Mn concentration of the soil (Schlichting and Sparrow, 1988). Also, the thresholds for Mn toxicity and deficiency are strongly dependent on the Mn tolerance of the specific species and on the availability of other elements such as Si, that can mediate alleviation of metal-derived stresses in plants through different mechanisms (Liang et al., 2007; Blamey et al., 2018). As a result of both, Mn deficiency and toxicity, impaired plant growth, reduced photosynthetic activity, chlorophyll content and evolution of molecular oxygen (O_2) are observed (Terry and Ulrich, 1974; Ohki et al., 1979; Macfie and Taylor, 1992; Shenker et al., 2004; Schmidt et al., 2016; Blamey et al., 2018), drastically reducing crop yields and quality. Upon litterfall, Mn stored in leaves is liberated as bioavailable Mn^{2+} and subsequently (microbially) oxidized to reactive Mn^{3+} and later to insoluble Mn(III/IV) species during ongoing litter decomposition (Herndon et al., 2014; Keiluweit et al., 2015) (Fig. 1.1 (4)).

Increasing attention is being paid to Mn species on the retention and lability of organic carbon (C) in soils, an essential topic, as they affect the ecological C cycle and thus ultimately climate change (Estes et al., 2016; Li et al., 2021). In that, the role of poorly crystalline soil Mn oxides and hydroxides, collectively termed Mn (oxyhydr)oxides, is characterized by a complex redox chemistry with dissolved organic matter (DOM) (Stuckey et al., 2018). Organo-mineral complexes with iron (Fe) and aluminum (Al) oxides and hydroxides were shown to be stable against biological degradation (Miltner and Zech, 1998b; Kaiser et al., 2002; Mikutta et al., 2006; Eusterhues et al., 2014) and thus contribute to prolonged C retention in soils. Conversely, Mn (oxyhydr)oxides such as birnessite (see section 1.2) were found to be involved in the oxidative decomposition of organic litter (i.e., lignin) (Sunda and Kieber, 1994; Miltner and Zech, 1998a, 1998b), a process that liberates C, some of which evolves as CO_2 (Miltner and Zech, 1998a) (Fig. 1.1 (5)). At the same time, Mn (oxyhydr)oxides are partially reductively dissolved (Stuckey et al., 2018). However, the remaining Mn (oxyhydr)oxides eventually showed a higher maximum sorption capacity for dissolved organic matter (DOM) (Stuckey et al., 2018), such that they may also act as important scavengers of organic carbon (Estes et al., 2016) (Fig. 1.1 (5)). These two distinct roles of Mn in the release and storage of C highlight the complex behavior of Mn in the ecological C cycle. Additionally, through the oxidative degradation of former complex DOM (i.e., humic and fulvic acids), LMWO compounds, such as pyruvate, acetone, formaldehyde, and acetaldehyde (in

order of decreasing importance) are formed (Sunda and Kieber, 1994), which are then easily accessible energy sources for microbes (Fig. 1.1 (6)).

Overall, the demand for Mn in human, animal, and plant enzymatic processes, as well as its involvement in the global cycling of other environmentally relevant elements and in the conversion of recalcitrant organic matter into microbially available substrates, illustrates the multifaceted relevance of Mn in terrestrial ecosystems. The expression 'Mn, key to life' (Bartlett, 1988) is thus supported in every respect by scientific evidence.

1.2. MN MINERALOGY IN SOILS

Typical Mn concentrations in soils range from 40-1,000 mg/kg, however, they can be <20 mg/kg in quartz-rich sands and up to >3,000 mg/kg in soils with pedogenic Mn accumulation (Blume et al., 2016). The fact that neither total nor exchangeable Mn concentration in soil is correlated with bedrock composition is the result of its high mobility in the Earth´s crust (Mortvedt, 2000), that depends largely on biological processes controlling its redox state, (Tebo et al., 2005), and thus Eh and pH conditions of the soil (Blume et al., 2016) (Fig. 1.2). The three natural oxidation states of Mn, i.e., +2, +3, and +4, account for the panoply of single- and mixed valent Mn minerals in soils. These include carbonates, phosphates, silicates, Mn (oxyhydr)oxides, organic Mn complexes, and Mn being adsorbed to various soil compounds.

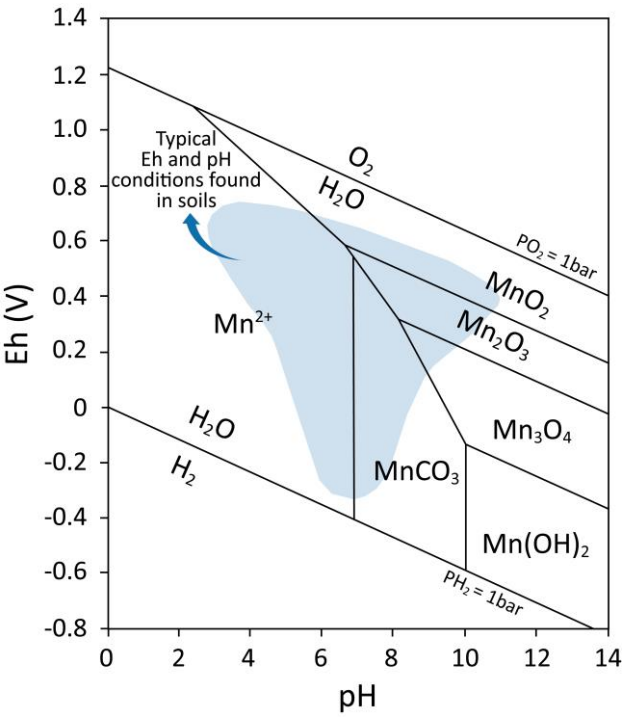

Figure 1.2. Pourbaix diagram, illustrating Mn speciation as a function of redox potential (Eh) and pH. Typical soil conditions are indicated in blue. The stability field of rhodochrosite ($MnCO_3$) varies – influencing the fields of pyrolusite (MnO_2), bixbyite (Mn_2O_3), and hausmannite (Mn_3O_4) – depending on the CO_2 content of the soil (Blume et al., 2011). Modified after Husson (2013).

At typical soil pH >5.5, Mn(III/IV) (oxyhydr)oxides precipitate under aerobic conditions (Blume et al., 2016) (Fig. 1.2), a fact that accounts for their ubiquity in many soils. Mn(III) hydroxides in particular are, however, rather rare in soils (Vodyanitskii, 2009) since they are typically unstable and disproportionate at pH <7 to MnO_2 and Mn^{2+} (Blume et al., 2016). Mn (oxyhydr)oxides are characterized by a large surface area (5-360 m^2/g), a low point of zero charge between two and five (McKenzie, 1989; Kämpf et al., 2000), and they offer structural vacancies which render them effective scavengers for trace and heavy metals like Cd, Cu, Co, Ni, Pb, and Zn (Burns, 1976) (Fig. 1.1 (7)). Their dissolution and precipitation thus influences the release of these metals as well as of bioavailable Mn^{2+} back into solution (Junta and Hochella, 1994; Tebo et al., 2004), which affects the retention of these elements in soil systems. Mn (oxyhydr)oxides belong to the strongest oxidants in our environment (Remucal and Ginder-Vogel, 2014), which assigns them a decisive role in the redox-chemistry of organic and inorganic soil compounds. The latter includes the oxidation of As(III) to As(V) (Lafferty et al., 2010; Han et al., 2011; Ehlert et al., 2014), Cr(III) to Cr(VI) (Kim et al., 2002; Feng et al., 2007), Fe(II) to Fe(III) (Villinski et al., 2001; Ehlert et al., 2014), Se(IV) to Se(VI) (Scott and Morgan, 1996), nitrite to nitrate (Bartlett, 1981), and the oxidation of iodide (Fox et al., 2009).

The fundamental building unit of Mn (oxyhydr)oxides, the MnO_6 octahedron, is linked by sharing edges and/or corners to form either layer or tunnel structures. Layered Mn (oxyhydr)oxides ('phyllomanganates') consist of stacked sheets of edge-sharing MnO_6 octahedra (McKenzie, 1989; Post, 1999) (Fig. 1.3).

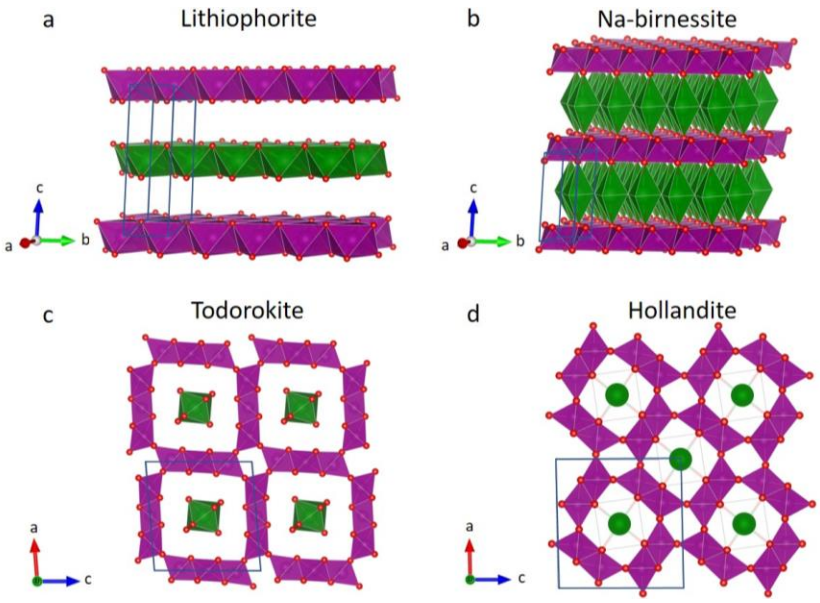

Figure 1.3. Polyhedral illustration of selected phyllomanganates (a, b) and tectomanganates (c, d) occurring in soils. MnO_6 octahedra are shown in magenta. Green colored octahedra in lithiophorite are structural $(Al,Li)(OH)_6$ octahedra alternating with octahedral Mn layers. Na-birnessite shows disordered Na sites (green) between the octahedral Mn layers. In todorokite and hollandite, green sites represent Mg and Ba interlayer cations. Unit cells are indicated in blue.

The most common member of this group in soils are hexagonal and triclinic birnessite and lithiophorite (Table 1.1). In Mn (oxyhydr)oxides with tunnel structure ('tectomanganates'), edge-sharing MnO_6 octahedra form single, double or triple chains, in which MnO_6 octahedra share corners to produce tunnels of varying size (Fig. 1.3). Prominent representatives of this mineral group occurring in soils are cryptomelane and hollandite (2×2 tunnel), romanèchite (2×3 tunnel), and todorokite (3×3 tunnel) (Table 1.1). Both, large tunnels and interlayer regions between octahedral sheets may host various exchangeable cations (e.g., H^+, Na^+, K^+, Ca^{2+}, Cu^{2+}, Mg^{2+}, Ni^{2+}) as well as water molecules, which compensate positive charge deficits from Mn^{4+}-site vacancies or from substitution by lower valent cations (Tebo et al., 2004). Generally, more than 30 Mn (oxyhydr)oxides are known, however, the number of those identified in soils is lower (Table 1.1).

Table 1.1. Important Mn (oxyhydr)oxides found in soils (McKenzie, 1989)

Mineral	Mineral formula[a]	Crystal system[a]	Structure
Phyllomanganates			
Birnessite (vernadite, δ-MnO_2)	$(Mn^{4+},Fe^{3+},Ca,Na)_{\Sigma 1.00}(O,OH)_2 \cdot nH_2O$	Hexagonal	Layer
Lithiophorite	$(Al,Li)Mn^{4+}{}_2O_2(OH)_2$	Hexagonal	Layer
Tectomanganates			
Cryptomelane	$K(Mn^{4+},Mn^{3+})_8O_{16}$	Monoclinic, Pseudotetragonal	2×2[b]
Hollandite	$Ba(Mn^{4+},Mn^{3+})_8O_{16}$	Monoclinic	2×2 [b]
Romanèchite	$(Ba,H_2O)_2(Mn^{4+},Mn^{3+})_5O_{10}$	Monoclinic	2×3 [b]
Todorokite	$(Mn^{2+},Ca,Na,K)(Mn^{4+},Mn^{2+},Mg)_6O_{12} \cdot 3H_2O$	Monoclinic	3×3 [b]
Mn(III) oxyhydroxides			
Manganite[c]	γ-$Mn^{3+}O(OH)$	Monoclinic, Pseudo-orthorhombic	
Other			
Hausmannite[d]	$(Mn^{2+},Mn^{3+})_3O_4$	Tetragonal	Spinel

[a]After Anthony et al. (2003).
[b]Size of tunnels formed by MnO_6 octahedra.
[c]Reported by Post (1999) to be the most stable Mn(III) oxyhydroxide mineral in the environment. The other two MnOOH polymorphs are feitknechtite (β-$Mn^{3+}O(OH)$), whose unequivocal evidence as a pedogenic soil formation product is so far not given, and groutite (α-$Mn^{3+}O(OH)$) (Shobayo et al., 2019).
[d]First described by Chukhrov and Gorshkov (1981) in a Chernozem subsoil (pH 8.3; Priazov district, former USSR) and in a subsoil of a 'meadow soil' (pH 8.1; Prisalair district, former USSR).

Mn (oxyhydr)oxides in soils may be formed by different pathways. Typically, they are the result of oxidation of dissolved Mn^{2+} (Mayanna et al., 2015), which may occur by three different pathways in soils:

(1) Heterogeneous metal-oxide surface catalyzed oxidation, where Mn^{2+} is oxidized at the surfaces of e.g., albite, goethite, hematite, lepidocrocite, or MnO_2 (Wilson, 1980; Davies and Morgan, 1989; Junta and Hochella, 1994; Tu et al., 1994). Reaction products from aqueous Mn^{2+} at pH ≥6 at room temperature were reported to consist of Mn(III) oxyhydroxides, predominantly feitknechtite (β-$Mn^{3+}O(OH)$) (Junta and Hochella, 1994; Tu et al., 1994).
(2) Oxidation of Mn^{2+} by O_2 in homogeneous solution at pH ≥8 in the absence of surface catalysts or bacteria (Morgan, 2005). Abiotic oxidation of Mn^{2+} at approximately neutral pH typically produces layer-type phases of the birnessite mineral group, with either triclinic or hexagonal symmetry, and with varying degrees of crystallinity, from poorly crystalline δ-MnO_2 to crystalline birnessite (e.g., Villalobos et al., 2003).
(3) Enzymatic oxidation of Mn^{2+} by bacteria such as *Pseudomonas putida* strain MnB1 (Villalobos et al., 2003), or fungi like *Acremonium* KR21-2 (Saratovsky et al., 2009). Under neutral to slightly alkaline pH and under (hyp)oxic conditions, the microbially mediated oxidation of Mn^{2+} in environmental systems is well established (Francis and Tebo, 2001; Tebo et al., 2004; Nealson, 2006; Santelli et al., 2011; Remucal and Ginder-Vogel, 2014). Also, this process is being considered magnitudes faster than abiotic Mn^{2+} oxidation (Nealson et al., 1988; Morgan, 2000). Recently, Mn^{2+}-oxidizing bacteria were even isolated from a former uranium mining site with a pH as low as 5.5 (Akob et al., 2014). However, the mechanism of biological Mn^{2+} oxidation at acidic pH remains to be solved (Bohu et al., 2015). Microbial Mn^{2+} oxidation may generally yield poorly crystalline and highly reactive phases with hexagonal symmetry, which are mineralogically and morphologically similar to δ-MnO_2 (Bargar et al., 2005; Webb et al., 2005; Villalobos et al., 2006).

In acidic environments, the abiotic oxidation of Mn^{2+} is thermodynamically unfavorable and slow and it is smaller than rates at circumneutral-alkaline pH reported for microbial Mn^{2+} oxidation (Nealson et al., 1988; Tebo et al., 2004; Morgan, 2005). For example, at pH = 8, half-lives for bacterial oxidation of Mn^{2+} are suggested to be 20 hours, oxide catalyzed oxidation may require 30 days, and the oxidation in homogeneous solution 400 days (Morgan, 2005). Thus, Mn (oxyhydr)oxides generally formed in natural systems are assumed to be largely of biogenic origin. These may then in turn oxidize Mn^{2+} at their highly reactive surfaces or are further transformed abiotically to serve as precursors for more crystalline Mn phases, e.g., todorokite and various birnessites (i.e., triclinic birnessite, 10 Å hydrated phyllomanganate), or feitknechtite and manganite (γ-$Mn^{3+}O(OH)$) (Bargar et al., 2005; Elzinga, 2011; Santelli et al., 2011).

In mineral soil horizons, Mn minerals are typically finely dispersed and poorly crystalline. Soils characterized by recurrent wetting-drying cycles and thus changing redox potential (Eh) and pH may, however, form micrometer to centimeter sized mottles, nodules, or concretions with strong Fe and Mn enrichments (Schwertmann and Fanning, 1976; Glasby et al., 1979; Tebo and He, 1998; D'Amore

et al., 2004; Reddy and DeLaune, 2008) (Figs. 1.1 (8) and 1.3). During wet seasons and under anaerobic conditions, solid Fe(III) and Mn(III/IV) species are reduced, mobilized and dissolved in pore waters, while during dry seasons and aerobic conditions, they reprecipitate, become concentrated and cement soil particles (Tebo and He, 1998; Manceau et al., 2003; Habibah et al., 2014). The result of such alternating wetting-drying intervals is the typical concentric layering of these *in-situ* formed soil Fe-Mn nodules (Manceau et al., 2003; Ettler et al., 2017). An increased occurrence of Mn nodules at the bottom of the soil profiles was described by Sipos et al. (2011) and Ettler et al. (2017), likely due to enhanced hydromorphism effects at depth and downward leaching of Fe and Mn.

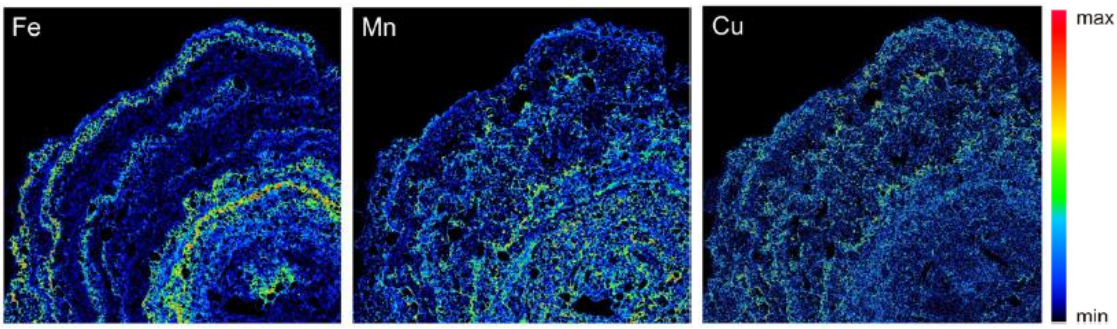

Figure 1.4. X-ray mapping from field emission gun-electron probe microanalysis (FEG-EPMA) on a section of a soil Fe-Mn nodule. The elemental distribution of Fe, Mn and Cu is visible in discrete, concentric layers (modified after Ettler et al., 2017).

Mineralogically, Fe-Mn nodules typically contain primary minerals like quartz, feldspars, and micas, which are cemented by a matrix of phyllosilicates and Fe and Mn (oxyhydr)oxides (Manceau et al., 2003). In nodules from Carpathian Albeluvisols, Szymański et al. (2014) found todorokite in illuvial horizons and manganite. Liao et al. (2019) examined deep sea sediments from the Central North Pacific and detected vernadite, birnessite, and todorokite therein. The latter increased in abundance with depth, affirming the transformation of birnessite to increasingly crystalline todorokite with time. Other Mn (oxyhydr)oxides reported from Mn nodules and concretions typically include poorly crystalline, turbostatic birnessite (δ-MnO_2) and ferric vernadite (δ-$(Mn,Fe)O_2$), cryptomelane, Mn-ferroxyhyte (δ-(Fe,Mn)OOH), hausmannite, hollandite, lithiophorite, manganite, pyrolusite ($Mn^{4+}O_2$), and romanèchite (Taylor et al., 1964; Chukhrov and Gorshkov, 1981; Vodyanitskii et al., 2002; De Bakker et al., 2003; Manceau et al., 2003; Manceau et al., 2005; Neaman et al., 2008) (see Table 1.1 for additional mineral formulas). Compared to the surrounding soil matrix, soil Fe-Mn nodules and concretions show strong enrichment factors for many trace and heavy metals like, e.g., Ba, Ca, Co, Cd, Fe, Mn, Pb, Ni, Nu, V and the rare earth elements La and Ce (Burns, 1976; Latrille et al., 2001; Palumbo et al., 2001; Liu et al., 2002; Manceau et al., 2003) underlining the role of Mn (oxyhydr)oxides in the sequestration of (heavy) metal pollutants, rare earth elements (REE), and nutrients.

1.3. ANALYTICAL APPROACHES TO MN SPECIATION

Since bulk Mn concentration is typically low in soils (often <0.1 wt.%) and Mn (oxyhydr)oxides in particular are additionally characterized by poor crystallinity, their identification and quantification by conventional mineralogical and crystallographic methods (e.g., scanning electron microscopy (SEM) or electron probe microanalysis (EPMA), (powder-) X-ray diffraction ((P)XRD), Infrared (IR) and Raman spectroscopy) is challenging, if not impossible. Wet-chemical methods such as redox-based titration, which are a classical method to infer the average oxidation state (AOS) of Mn in, e.g., mineral specimen (Grangeon et al., 2012), are not suitable for soils due to low their Mn concentrations and interference with other redox-active elements such as Fe. Studies targeting Mn speciation in soils and sediments thus typically apply the following analytical approaches: (1) Sequential extractions (SE), (2) X-ray or electron diffraction, and (3) Mn K-edge X-ray absorption spectroscopy (XAS).

(1) Sequential extractions

Sequential extraction methods are amongst the most commonly used procedures to assess the speciation of (trace) metals in soils (Peltier et al., 2005) since they are easy to apply, cost- and time effective. Sequential extractions selectively separate Mn species upon leaching by using a sequence of appropriate chemical extractants with increasing extraction strength (Qiang et al., 1994; Narwall and Singh, 2001; Kalembkiewicz et al., 2008; Frommer et al., 2011; Habibah et al., 2014). As a result, operationally defined Mn fractions can be determined. Depending on the extractants used, these may include fractions like 'ready soluble and exchangeable Mn' (1 M NH_4NO_3), 'specifically sorbed, carbonate-bound, or other weakly bound Mn' (1 M NH_4OAc, pH 6), 'Mn oxides' (0.1 M $NH_2OH{\cdot}Cl$ + 1 M NH_4OAc, pH 6), 'amorphous and poorly crystalline Fe oxide-bound Mn' (0.2 M NH_4 oxalate, pH 3.25), 'crystalline Fe oxide-bound Mn' (0.1 M ascorbic acid in 0.2 M NH_4 oxalate, pH 3.25), and 'residual Mn', as conducted by Frommer et al. (2011) following the extraction protocol of Zeien and Brümmer (1989). Quite different particulate metal pools are obtained when applying, e.g., the extraction procedure of Tessier et al. (1979). Here, the operationally defined Mn pools 'exchangeable' (1 M $MgCl_2$, pH 7 or 1 M NaOAc, pH 8.2), 'carbonate-bound' (1 M NaOAc, pH 5), 'iron- and manganese- bound' (0.3 M Na2S2O4 + 0.175 M Na-citrate + 0.025 M H-citrate), 'organic matter-bound' (5.3% NaOCl, pH 8.5 or (0.02 M HNO3, 30% H_2O_2, pH 2, 3.2 M NH_4OAc in 20% v/v HNO_3), and 'residual' (HF-$HClO_4$) can be explored. This protocol was applied slightly modified by e.g., Qiang et al. (1994) and Kalembkiewicz et al. (2008), who both studied topsoil materials. Apperently, such speciation results are hardly comparable, owing to the different protocols used and the resulting different operationally defined metal fractions. Thus, although sequential extractions offer the possibility to infer information on metal mobility, transportation, and partitioning in particulate materials (Qiang et al., 1994), they must be discussed controversially: The poor selectivity of extractants, Mn redistribution during extractions, incomplete

dissolution of the target material, and above all, the outlined use of a large variety of non-standardized extraction protocols differing in experimental specifications and chemical extractants, severely limit the accuracy, explanatory power, and comparability of this speciation approach (Qiang et al., 1994; Sutherland and Tack, 2003; Hlavay et al., 2004; Hass and Fine, 2010).

(2) X-ray or electron diffraction

To identify and characterize crystalline Mn minerals, X-ray or electron diffraction is frequently used (Chukhrov and Gorshkov, 1981; Hem and Lind, 1983; Manceau et al., 1992; Drits et al., 1997; Liao et al., 2019) (Fig. 1.5). However, the application of these diffraction techniques is largely restricted by the low degree of crystallinity of Mn (oxyhydr)oxides, leading to broad and less diagnostic X-ray diffraction (XRD) reflections and particularly in inhomogeneous matrices such as soils these are also often overlapped by more intense peaks from other minerals (Zhang and Karathanasis, 1997; Liu et al., 2002). In addition, the concentrations of well-ordered crystals, which are necessary to obtain suitable reflections of Mn minerals with laboratory diffractometers, are rarely reached in soils. For these reasons, diffraction-based studies in soils almost exclusively focused on more crystalline Mn minerals in ferromanganese nodules and concretions in soils and sediments (e.g., Taylor et al., 1964; Uzochukwu and Dixon, 1986; Liu et al., 2002; Manceau et al., 2003; Szymański et al., 2014; Liao et al., 2019).

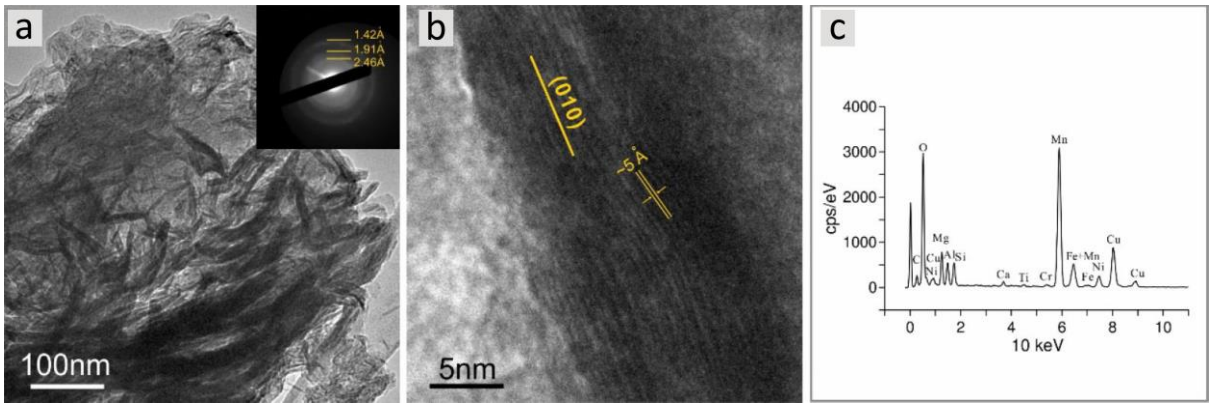

Figure 1.5. Transmission electron microscope (TEM) image of fibrous todorokite nanocrystals from a Fe-Mn micronodule obtained from a sedimentary core sample of the Central North Pacific Ocean. (a) Fiber-like todorokite nanocrystals with (b) lattice fringes, (c) corresponding energy-dispersive X-ray spectrum showing the elemental composition of the sample (modified after Liao et al., 2019).

Various Mn (oxyhydr)oxides were detected in ferromanganese nodules and concretions. However, it is highly questionable whether Mn speciation results from these studies can be transferred to (terrestrial) bulk soils omitting pedogenic Mn accumulation.

(3) Manganese K-edge X-ray absorption spectroscopy

The rapid development in the field of high brilliance, 3rd generation synchrotron radiation allows

spectroscopic investigations down to the grain size range of poorly crystalline pedogenic Mn minerals. On that account, synchrotron-based Mn K-edge X-ray absorption spectroscopy (XAS) is an attractive method for the speciation of soil Mn (Manceau et al., 2005; Frommer et al., 2011; Hernandez-Soriano et al., 2012; Herndon et al., 2014; Keiluweit et al., 2015; Mayanna et al., 2015). As opposed to diffraction-based approaches, XAS is sensitive to the atomic short range order (Manceau and Combes, 1988), enabling analysis of crystalline and non-crystalline multicomponent samples such as soils, even when Mn concentrations are only several hundred milligrams per kilogram. In particular, bulk XAS analyses can be used to determine the average oxidation state and average local (<5 Å) coordination environment of Mn within a sample, supporting the characterization and identification of specific Mn species therein. Many speciation studies make use of micro-focused µ-XAS, with which information on the spatial distribution of Mn at the micrometer scale and thus processes in e.g., chemical species transformation can be inferred (Manceau et al., 2002; Manceau et al., 2005). However, despite all advantages of highly spatially resolved species information, under which e.g., a synergistic use with synchrotron µ-XRF, that can yield a lateral resolution of a few μm^2, and µ-XRD falls (Manceau et al., 2002), the local speciation results provided may not reflect 'the big picture' within a bulk sample (Pickering and George, 2007).

The XAS spectrum consists of two sub-regions, the Mn K-edge X-ray absorption near edge structure (XANES) and the extended X-ray absorption fine structure (EXAFS), both of which are used to gain supplementary information. The XANES region offers information on the coordination geometry and AOS (Kelly et al., 2008) of a metal, based on the shift of the absorption edge towards higher energies with increasing AOS (e.g., McKeown and Post, 2001; Manceau et al., 2012) (Fig. 1.6).

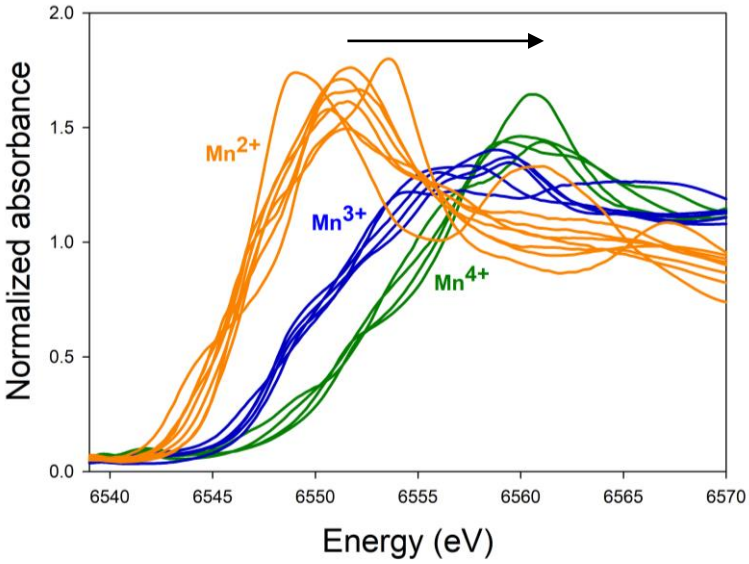

Figure 1.6. XANES absorption spectra of single-valent Mn species. The shift of the absorbance edge towards higher energies with increasing Mn valence (i.e., +2, +3, +4) is indicated by the arrow. XANES spectra are obtained from the publicly available database of Manceau et al. (2012).

By applying linear combination fitting (LCF) of the unknown XANES spectrum with well-characterized multivalent Mn references, it is possible to obtain information on the fractional amounts of Mn^{2+}, Mn^{3+}, and Mn^{4+} present in the sample (Manceau et al., 2012) with an accuracy of the resulting Mn AOS of environmental samples down to ~0.1 valence units (v.u.) over the entire AOS range (see chapter 2). The EXAFS region starts from approximately the absorption edge of the target element, i.e., 6,539 eV in the case of Mn, and covers the subsequent high energy region of a spectrum. Observed spectral oscillations arise from interference effects between the photoelectron wave emitted from the absorbing atom and the fraction of the photoelectron wave that is backscattered by atoms surrounding the absorbing atom (Manceau et al., 2002).

Various techniques exist for untangling the EXAFS region for the purpose of species determination. The simplest one is spectral 'fingerprinting' (Friedl et al., 1997; McKeown and Post, 2001; Mayanna et al., 2015), where qualitative identification of Mn species is possible, if the species in question exhibits unique spectral EXAFS features. For example, the peak near 8.0 $Å^{-1}$ was previously used as a diagnostic fingerprint to differentiate between phyllo- and tectomanganates (McKeown and Post, 2001). Moreover, in tectomanganates, the left-side shoulder of the ~6.7-$Å^{-1}$ oscillation becomes more intense with increasing content of corner-sharing octahedra (i.e., smaller tunnel size) and eventually results in a split oscillation at 6.4 and 6.7 $Å^{-1}$ (Manceau and Combes, 1988).

Another qualitative technique uses a Fourier transformed, background subtracted EXAFS spectrum. Here, the obtained radial structure function in real space features peaks, that are diagnostic for the local environment of the target atom (Manceau et al., 2002) (Fig. 1.7).

The sensitivity of the EXAFS to the local molecular structure (Manceau et al., 2002; Kelly et al., 2008) enables so-called 'EXAFS shell fitting', where nearest-neighbor distances (interatomic distances) and coordination numbers around the X-ray absorbing atom can be determined. In manganates, the central Mn atom is typically surrounded by six O atoms and interatomic first shell Mn-Mn distances of ~2.85-2.95 and ~3.40-3.80 Å are diagnostic for edge- and corner-sharing $Mn^{4+}O_6$-octahedra respectively (Fig. 1.7) (Duff et al., 2002; Webb et al., 2005). Typically, interatomic distances can be resolved by EXAFS shell fitting down to 0.02 Å and the coordination number may show an error of 25% at best (Manceau and Combes, 1988).

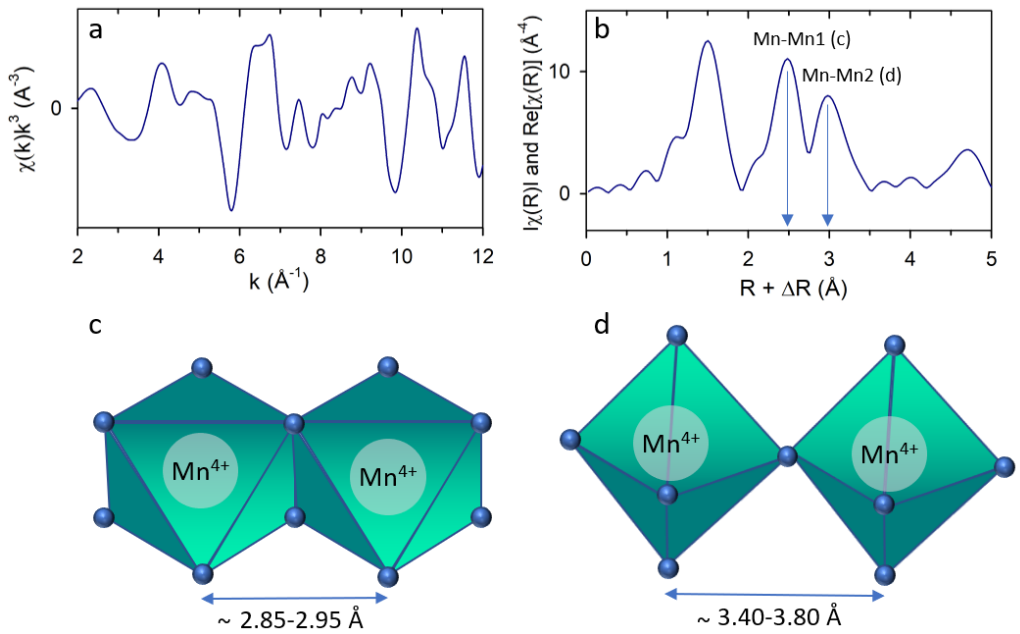

Figure 1.7. Relationship between EXAFS spectrum and atomic coordination. (a) EXAFS spectrum of the tectomanganate cryptomelane and (b) its Fourier transform. Interatomic distances of (c) edge- and (d) corner-sharing $Mn^{4+}O_6$ octahedra can be directly inferred from the Fourier transform by adding a shift of ~0.5 A to the values indicated by the blue arrows in (b).

When it comes to quantification of metal species in environmental samples, EXAFS LCF is commonly applied, frequently in combination with preceding principal component analysis (PCA) and target transformation (TT) testing (Manceau et al., 2002; Scheinost et al., 2002; Langner et al., 2012; Mikutta and Rothwell, 2016). The statistical PCA approach is basically used to reduce the dimensionality in a set of sample spectra, thus it provides the number of unique species within all samples and clarifies spectral membership. The TT is used to relate the PC's to physical standards and derive the probability that a standard spectrum reflects a species within the sample (Kelly et al., 2008). In the subsequent LCF analysis, the spectrum from a sample with unknown speciation is modelled by additive linear combination of the selected reference spectra of known speciation, likely to occur within the sample (Kelly et al., 2008). When applying LCF, knowledge on spectral (non-)uniqueness of

reference spectra is a main issue. Similar to XANES LCF, a comprehensive EXAFS reference spectrum library, containing all species possibly occurring in the unknown material, is decisive for successful species quantification with EXAFS LCF.

1.4. RESEARCH MOTIVATION AND OUTLINE OF THIS THESIS

Despite decades of research on soil Mn speciation, available XAS studies are limited to the locally resolved Mn speciation, which do not allow unrestricted conclusions with respect to the bulk sample, to selected soil components (e.g., ferromanganese nodules and concretions), individual soil horizons, or single soil profiles. Moreover, relationships between Mn speciation and physicochemical soil properties are largely missing – such that also causal relationships remain poorly understood. Even though XAS overcomes the limitations of conventional bulk XRD and SE analyses and can yield information on major Mn species or species groups present in natural samples, a comprehensive overview of bulk Mn speciation in soils is lacking. Moreover, the identification of single Mn species in soils of different pedogenesis is entirely missing and Mn K-edge EXAFS spectroscopy has, to my knowledge, never been used to quantitatively examine Mn speciation in bulk soils or sediments. Although the general predominance of manganates in soils is typically assumed, possibly due to their ubiquity, quantitative evidence is rare (Manceau et al., 2002; Vodyanitskii et al., 2002) and is totally absent for a comprehensive suite of soil types.

As pointed out previously, XANES and EXAFS LCF is bound to the existence of an extensive spectrum library. However, different to other redox-active elements like Fe, and even though several Mn EXAFS studies of solid and aqueous Mn compounds provide fundamental information on the local Mn coordination (Manceau and Combes, 1988; Silvester et al., 1997; McKeown and Post, 2001; Manceau et al., 2005; Webb et al., 2005; Bhattacharya and Elzinga, 2018; Ahmad et al., 2019), a publicly available, comprehensive spectroscopic database of Mn in fundamentally different coordinations does not exist. The number of those available is either not sufficient for validation of EXAFS parameters previously determined for specific Mn species, or they are not suited for Mn speciation analysis in soils. Moreover, molecular-level information on Mn coordination of various potentially relevant soil Mn species, such as organic Mn species or Mn being adsorbed to soil components, is totally absent. Furthermore, systematic studies on spectral uniqueness of Mn compounds, a recurrently discussed topic in LCF analyses (Scheinost et al., 2002; Gustafsson et al., 2020), are largely missing.

Therefore, this work comprises two consecutive studies that serve the overall goal to deepen our understanding of the dynamics of Mn in soils, which is directly connected to its speciation. In doing so, the studies link the pure observation of quantitatively determined species present in soils to the

prevailing physicochemical soil parameter. Various analytical techniques are used in the work, with the focus of both studies being on Mn-K edge XAS.

The first study (chapter 2) was designed to provide the first comprehensive framework for the analysis and interpretation of Mn XAS spectra of environmental samples and thus for the evaluation of the role of Mn in environmental processes. The study presents a suite of 32 Mn reference compounds, including Mn (oxyhydr)oxides, carbonate, phosphate, and silicate minerals, as well as organic and adsorbed Mn species, which were investigated by classic analytical methods (XRD, EPMA, LA-ICP-OES) as well as Mn K-edge XANES and EXAFS spectroscopy. Their local (<5 Å) Mn coordination environment was studied by EXAFS shell-fit analysis. To clarify how well and to what extent individual Mn species or species groups can be distinguished by XAS based on spectral uniqueness, descriptive and multivariate statistics were applied. In addition, the accuracy of XAS to determine the Mn AOS in natural soil samples was inferred by comparing XANES-derived AOS with the AOS obtained from redox titrations.

The second study (chapter 3) focuses on the quantification of Mn species in five undisturbed major Central European soil types (Cambisols, Chernozems, Luvisols, Podzol, and Stagnosol). For this, basic soil properties of 47 soil samples (45.1-2,280 mg/kg Mn) were determined and a suite of 46 soil samples was investigated by Mn K-edge XANES and EXAFS spectroscopy. The obtained information was correlated with major soil properties to relate variations and trends in Mn speciation to pedogenic properties. For quantification of major Mn species groups in organic and mineral soil horizons, an improved EXAFS LCF approach was developed and applied after PCA-TT on 20 soil samples, based on the previously compiled Mn reference spectrum library from chapter 2. The study highlights the suitability of Mn K-edge EXAFS spectroscopy and specifically EXAFS LCF for the quantification of the bulk Mn species inventory of soils. Moreover, this is the first comprehensive study to quantify Mn species in bulk soils by EXAFS spectroscopy. Since Mn speciation is directly connected with Mn mobility and reactivity in soil and adjacent ecological systems, this study contributes to a deeper understanding of the dynamics of Mn and the fate of pollutants and micronutrients in surface environments.

1.5. References

Ahmad, A., van der Wal, A., Bhattacharya, P. and van Genuchten, C.M. (2019) Characteristics of Fe and Mn bearing precipitates generated by Fe(II) and Mn(II) co-oxidation with O_2, MnO_4 and HOCl in the presence of groundwater ions. *Water Res.* **161**, 505-516.

Anthony, J.W., Bideaux, R.A., Bladh, K.W. and Nichols, M.C. (2003) *Handbook of Mineralogy*. Mineralogical Society of America, Chantilly, VA 20151-1110, USA.

Bargar, J.R., Tebo, B.M., Bergmann, U., Webb, S.M., Glatzel, P., Chiu, V.Q. and Villalobos, M. (2005) Biotic and abiotic products of Mn(II) oxidation by spores of the marine *Bacillus sp*. strain SG-1. *Am. Mineral.* **90**, 143-154.

Bartlett, R.J. (1981) Nonmicrobial nitrite-to-nitrate transformation in soils. *Soil. Sci. Soc. Am. J.* **45**, 1054-1058.

Bartlett, R.J. (1988) Manganese redox reactions and organic interactions in soils. In: *Manganese in Soils and Plants*. Springer, pp. 59-73.

Bhattacharya, L. and Elzinga, E.J. (2018) A comparison of the solubility products of layered Me(II)-Al(III) hydroxides based on sorption studies with Ni(II), Zn(II), Co(II), Fe(II), and Mn(II). *Soil Syst.* **2**, 20.

Blamey, F.P.C., McKenna, B.A., Li, C., Cheng, M., Tang, C., Jiang, H., Howard, D.L., Paterson, D.J., Kappen, P. and Wang, P. (2018) Manganese distribution and speciation help to explain the effects of silicate and phosphate on manganese toxicity in four crop species. *New Phytol.* **217**, 1146-1160.

Blume, H.-P., Stahr, K. and Leinweber, P. (2011) *Bodenkundliches Praktikum: Eine Einführung in pedologisches Arbeiten für Ökologen, Land- und Forstwirte, Geo- und Umweltwissenschaftler*. Springer-Verlag.

Blume, H., Brümmer, G., Fleige, H., Horn, R., Kandeler, E., Kögel-Knabner, I., Kretzschmar, R., Stahr, K. and Wilke, B. (2016) *Scheffer/Schachtschabel Soil Science*. Springer: Berlin Heidelberg, Germany.

Bottrill, D., Possingham, J. and Kriedemann, P. (1970) The effect of nutrient deficiencies on phosynthesis and respiration in spinach. *Plant and Soil* **32**, 424-438.

Brenchley, W.E. (1914) *Inorganic Plant Poisons and Stimulants*. Cambridge University Press, London.

Broadley, M., Brown, P., Cakmak, I., Rengel, Z. and Zhao, F. (2012) Function of Nutrients: Micronutrients. In: *Marschner's Mineral Nutrition of Higher Plants* (ed. P. Marschner), 3rd ed. Academic Press, pp. 191-248.

Burns, R.G. (1976) The uptake of cobalt into ferromanganese nodules, soils, and synthetic manganese(IV) oxides. *Geochim. Cosmochim. Acta* **40**, 95-102.

Chukhrov, F. and Gorshkov, A. (1981) Iron and manganese oxide minerals in soils. *Trans. Royal Soc. Edinb. Earth Sci.* **72**, 195-200.

D'Amore, D.V., Stewart, S.R. and Huddleston, J.H. (2004) Saturation, reduction, and the formation of iron-manganese concretions in the Jackson-Frazier wetland, Oregon. 1012-1022.

Davies, S.H. and Morgan, J.J. (1989) Manganese(II) oxidation kinetics on metal oxide surfaces. *J. Colloid Interface Sci.* **129**, 63-77.

De Bakker, A.P., Tokashiki, Y. and Arachchi, L.P.V. (2003) Mineralogy of Okinawan terrestrial Fe/Mn nodules and their surrounding soils. *Clay Sci.* **12**, 121-130.

Dlamini, W.W., Nelson, G., Nielsen, S.S. and Racette, B.A. (2020) Manganese exposure, parkinsonian signs, and quality of life in South African mine workers. *Am. J. Ind. Med.* **63**, 36-43.

Drits, V.A., Silvester, E., Gorshkov, A.I. and Manceau, A. (1997) Structure of synthetic monoclinic Na-rich birnessite and hexagonal birnessite: I. Results from X-ray diffraction and selected-area electron diffraction. *Am. Mineral.* **82**, 946-961.

Duff, M., Hunter, D., Hobbs, D., Jurgensen, A. and Fink, S. (2002) *Characterization of Plutonium, Neptunium, Strontium on Manganese Solids from Permanganate Reduction*. Aiken, SC.

Edwards, D. and Asher, C. (1982) *Tolerance of crop and pasture species to manganese toxicity*, in: S. A. (Ed.), Proc. 9th Plant Nutrition Colloqu. Commonwealth Agricultural Bureaux, Warwick University, England, pp. 145-150.

Ehlert, K., Mikutta, C. and Kretzschmar, R. (2014) Impact of birnessite on arsenic and iron speciation during microbial reduction of arsenic-bearing ferrihydrite. *Environ. Sci. Technol.* **48**, 11320-11329.

Elzinga, E.J. (2011) Reductive transformation of birnessite by aqueous Mn(II). *Environ. Sci. Technol.* **45**, 6366-6372.

Estes, E., Andeer, P., Nordlund, D., Wankel, S. and Hansel, C. (2016) Biogenic manganese oxides as reservoirs of organic carbon and proteins in terrestrial and marine environments. *Geobiology* **15**, 158-172.

Ettler, V., Chren, M., Mihaljevič, M., Drahota, P., Kříbek, B., Veselovský, F., Sracek, O., Vaněk, A., Penížek, V. and Komárek, M. (2017) Characterization of Fe-Mn concentric nodules from Luvisol irrigated by mine water in a semi-arid agricultural area. *Geoderma* **299**, 32-42.

Eusterhues, K., Neidhardt, J., Hädrich, A., Küsel, K. and Totsche, K.U. (2014) Biodegradation of ferrihydrite-associated organic matter. *Biogeochemistry* **119**, 45-50.

Feng, X.H., Zhai, L.M., Tan, W.F., Liu, F. and He, J.Z. (2007) Adsorption and redox reactions of heavy metals on synthesized Mn oxide minerals. *Environ. Pollut.* **147**, 366-373.

Fernando, D.R., Guymer, G., Reeves, R.D., Woodrow, I.E., Baker, A.J. and Batianoff, G.N. (2009) Foliar Mn accumulation in eastern Australian herbarium specimens: Prospecting for 'new' Mn hyperaccumulators and potential applications in taxonomy. *Ann. Bot.* **103**, 931-939.

Fernando, D.R. and Lynch, J.P. (2015) Manganese phytotoxicity: New light on an old problem. *Ann. Bot.* **116**, 313-319.

Fernando, D.R., Mizuno, T., Woodrow, I.E., Baker, A.J.M. and Collins, R.N. (2010) Characterization of foliar manganese (Mn) in Mn (hyper)accumulators using X-ray absorption spectroscopy. *New Phytol.* **188**, 1014-1027.

Finley, J.W. and Davis, C.D. (1999) Manganese deficiency and toxicity: Are high or low dietary amounts of manganese cause for concern? *Biofactors* **10**, 15-24.

Flynn, M.R. and Susi, P. (2009) Neurological risks associated with manganese exposure from welding operations–a literature review. *Int. J. Hyg. Environ. Health* **212**, 459-469.

Fox, P.M., Davis, J.A. and Luther III, G.W. (2009) The kinetics of iodide oxidation by the manganese oxide mineral birnessite. *Geochim. Cosmochim. Acta* **73**, 2850-2861.

Francis, C.A. and Tebo, B.M. (2001) *cumA* multicopper oxidase genes from diverse Mn(II)-oxidizing and non-Mn(II)-oxidizing *Pseudomonas* strains. *Appl. Environ. Microbiol.* **67**, 4272-4278.

Friedl, G., Wehrli, B. and Manceau, A. (1997) Solid phases in the cycling of manganese in eutrophic lakes: New insights from EXAFS spectroscopy. *Geochim. Cosmochim. Acta* **61**, 275-290.

Frommer, J., Voegelin, A., Dittmar, J., Marcus, M.A. and Kretzschmar, R. (2011) Biogeochemical processes and arsenic enrichment around rice roots in paddy soil: Results from micro-focused X-ray spectroscopy. *Eur. J. Soil. Sci.* **62**, 305-317.

Gilkes, R. and McKenzie, R. (1988) Geochemistry and mineralogy of manganese in soils. In: *Manganese in Soils and Plants*. Springer, pp. 23-35.

Glasby, G., Rankin, P. and Meylan, M. (1979) Manganiferous soil concretions from Hawaii. *Pac. Sci.* **33**, 103-115.

Grangeon, S., Manceau, A., Guilhermet, J., Gaillot, A.-C., Lanson, M. and Lanson, B. (2012) Zn sorption modifies dynamically the layer and interlayer structure of vernadite. *Geochim. Cosmochim. Acta* **85**, 302-313.

Gustafsson, J.P., Braun, S., Tuyishime, M.J.R., Adediran, G.A., Warrinnier, R. and Hesterberg, D. (2020) A probabilistic approach to phosphorus speciation of soils using P K-edge XANES spectroscopy with linear combination fitting. *Soil Syst.* **4**, 26.

Habibah, J., Khairiah, J., Ismail, B. and Kadderi, M. (2014) Manganese speciation in selected agricultural soils of peninsular Malaysia. *Am. J. Environ. Sci.* **10**, 148-156.

Han, X., Li, Y.-L. and Gu, J.-D. (2011) Oxidation of As(III) by MnO_2 in the absence and presence of Fe(II) under acidic conditions. *Geochim. Cosmochim. Acta* **75**, 368-379.

Hass, A. and Fine, P. (2010) Sequential selective extraction procedures for the study of heavy metals in soils, sediments, and waste materials - a critical review. *Crit. Rev. Environ. Sci. Technol.* **40**, 365-399.

Hem, J.D. and Lind, C.J. (1983) Nonequilibrium models for predicting forms of precipitated manganese oxides. *Geochim. Cosmochim. Acta* **47**, 2037-2046.

Hernandez-Soriano, M.C., Degryse, F., Lombi, E. and Smolders, E. (2012) Manganese toxicity in barley is controlled by solution manganese and soil manganese speciation. *Soil. Sci. Soc. Am. J.* **76**, 399-407.

Herndon, E.M., Martínez, C.E. and Brantley, S.L. (2014) Spectroscopic (XANES/XRF) characterization of contaminant manganese cycling in a temperate watershed. *Biogeochemistry* **121**, 505-517.

Hlavay, J., Prohaska, T., Weisz, M., Wenzel, W.W. and Stingeder, G.J. (2004) Determination of trace elements bound to soils and sediment fractions (IUPAC Technical Report). *Pure Appl. Chem.* **76**, 415-442.

Hofrichter, M. (2002) Review: Lignin conversion by manganese peroxidase (MnP). *Enzyme Microb. Technol.* **30**, 454-466.

Husson, O. (2013) Redox potential (Eh) and pH as drivers of soil/plant/microorganism systems: A transdisciplinary overview pointing to integrative opportunities for agronomy. *Plant and Soil* **362**, 389-417.

Junta, J.L. and Hochella, M.F., Jr. (1994) Manganese(II) oxidation at mineral surfaces: A microscopic and spectroscopic study. *Geochim. Cosmochim. Acta* **58**, 4985-4999.

Kaiser, K., Eusterhues, K., Rumpel, C., Guggenberger, G. and Kögel-Knabner, I. (2002) Stabilization of organic matter by soil minerals – investigations of density and particle-size fractions from two acid forest soils. *J. Plant. Nutr. Soil. Sci.* **165**, 451-459.

Kalembkiewicz, J., Sitarz-Palczak, E. and Zapała, L. (2008) A study of the chemical forms or species of manganese found in coal fly ash and soil. *Microchem. J.* **90**, 37-43.

Kämpf, N., Scheinost, A. and Schulze, D. (2000) Oxide minerals. In: *Handbook of Soil Science* (ed. M.E. Sumner). CRC Press, Boca Raton, Forida, pp. F-125-F-168.

Keiluweit, M., Nico, P., Harmon, M.E., Mao, J., Pett-Ridge, J. and Kleber, M. (2015) Long-term litter decomposition controlled by manganese redox cycling. *Proc. Natl. Acad. Sci.* **112**, E5253-E5260.

Kelly, S., Hesterberg, D. and Ravel, B. (2008) Analysis of soils and minerals using X-ray absorption spectroscopy. In: *Methods of Soil Analysis. Part 5. Mineralogical Methods*. SSSA Book Series, no. 5, pp. 387-463.

Kim, J.G., Dixon, J.B., Chusuei, C.C. and Deng, Y. (2002) Oxidation of chromium(III) to (VI) by manganese oxides. *Soil. Sci. Soc. Am. J.* **66**, 306-315.

Lafferty, B.J., Ginder-Vogel, M. and Sparks, D.L. (2010) Arsenite oxidation by a poorly crystalline manganese-oxide 1. Stirred-flow experiments. *Environ. Sci. Technol.* **44**, 8460-8466.

Langner, P., Mikutta, C. and Kretzschmar, R. (2012) Arsenic sequestration by organic sulphur in peat. *Nature Geosci.* **5**, 66-73.

Latrille, C., Elsass, F., van Oort, F. and Denaix, L. (2001) Physical speciation of trace metals in Fe-Mn concretions from a rendzic lithosol developed on Sinemurian limestones (France). *Geoderma* **100**, 127-146.

Li, H., Santos, F., Butler, K. and Herndon, E. (2021) A critical review on the multiple roles of manganese in stabilizing and destabilizing soil organic matter. *Environ. Sci. Technol.* **55**, 12136-12152.

Liang, Y., Sun, W., Zhu, Y.-G. and Christie, P. (2007) Mechanisms of silicon-mediated alleviation of abiotic stresses in higher plants: A review. *Environ. Pollut.* **147**, 422-428.

Liao, J., Sun, X., Wu, Z., Sa, R., Guan, Y., Lu, Y., Li, D., Liu, Y., Deng, Y. and Pan, Y. (2019) Fe-Mn (oxyhydr)oxides as an indicator of REY enrichment in deep-sea sediments from the central North Pacific. *Ore Geol. Rev.* **112**, 103044.

Liu, F., Colombo, C., Adamo, P., He, J.Z. and Violante, A. (2002) Trace elements in manganese-iron nodules from a Chinese Alfisol. *Soil. Sci. Soc. Am. J.* **66**, 661-670.

Macfie, S.M. and Taylor, G.J. (1992) The effects of excess manganese on photosynthetic rate and concentration of chlorophyll in Triticum aestivum grown in solution culture. *Physiol. Plant.* **85**, 467-475.

Manceau, A. and Combes, J.M. (1988) Structure of Mn and Fe oxides and oxyhydroxides: A topological approach by EXAFS. *Phys. Chem. Miner.* **15**, 283-295.

Manceau, A., Gorshkov, A.I. and Drits, V.A. (1992) Structural chemistry of Mn, Fe, Co, and Ni in manganese hydrous oxides; Part I, information from XANES spectroscopy. *Am. Mineral.* **77**, 1133-1143.

Manceau, A., Marcus, M.A. and Grangeon, S. (2012) Determination of Mn valence states in mixed-valent manganates by XANES spectroscopy. *Am. Mineral.* **97**, 816-827.

Manceau, A., Marcus, M.A. and Tamura, N. (2002) Quantitative speciation of heavy metals in soils and sediments by synchrotron X-ray techniques. *Rev. Mineral. Geochem.* **49**, 341-428.

Manceau, A., Tamura, N., Celestre, R.S., MacDowell, A.A., Geoffroy, N., Sposito, G. and Padmore, H.A. (2003) Molecular-scale speciation of Zn and Ni in soil ferromanganese nodules from loess soils of the Mississippi Basin. *Environ. Sci. Technol.* **37**, 75-80.

Manceau, A., Tommaseo, C., Rihs, S., Geoffroy, N., Chateigner, D., Schlegel, M., Tisserand, D., Marcus, M.A., Tamura, N. and Chen, Z.-S. (2005) Natural speciation of Mn, Ni, and Zn at the micrometer scale in a clayey paddy soil using X-ray fluorescence, absorption, and diffraction. *Geochim. Cosmochim. Acta* **69**, 4007-4034.

Mayanna, S., Peacock, C.L., Schäffner, F., Grawunder, A., Merten, D., Kothe, E. and Büchel, G. (2015) Biogenic precipitation of manganese oxides and enrichment of heavy metals at acidic soil pH. *Chem. Geol.* **402**, 6-17.

McHargue, J. (1922) The role of manganese in plants *J. Am. Chem. Soc.* **44**, 1592-1598.

McKenzie, R.M. (1989) Manganese Oxides and Hydroxides. In: *Minerals in Soil Environments* eds. J.B. Dixon, S.B. Weed), 2nd ed. Soil Science Society of America, Madison, Wisconsin, pp. 439-465.

McKeown, D.A. and Post, J.E. (2001) Characterization of manganese oxide mineralogy in rock varnish and dendrites using X-ray absorption spectroscopy. *Am. Mineral.* **86**, 701-713.

Michalke, B. (2016) Review about the manganese speciation project related to neurodegeneration: An analytical chemistry approach to increase the knowledge about manganese related parkinsonian symptoms. *J. Trace Elem. Med. Biol.* **37**, 50-61.

Mikutta, C. and Rothwell, J.J. (2016) Peat bogs as hotspots for organoarsenical formation and persistence. *Environ. Sci. Technol.* **50**, 4314-4323.

Mikutta, R., Kleber, M., Torn, M.S. and Jahn, R. (2006) Stabilization of soil organic matter: Association with minerals or chemical recalcitrance? *Biogeochemistry* **77**, 25-56.

Millaleo, R., Reyes-Díaz, M., Ivanov, A., Mora, M. and Alberdi, M. (2010) Manganese as essential and toxic element for plants: Transport, accumulation and resistance mechanisms. *J. Soil Sci. Plant Nutr.* **10**, 470-481.

Miltner, A. and Zech, W. (1998a) Beech leaf litter lignin degradation and transformation as influenced by mineral phases. *Org. Geochem.* **28**, 457-463.

Miltner, A. and Zech, W. (1998b) Carbohydrate decomposition in beech litter as influenced by aluminium, iron and manganese oxides. *Soil Biol. Biochem.* **30**, 1-7.

Morgan, J.J. (2000) Manganese in natural waters and earth's crust: Its availability to organisms. *Met. Ions Biol. Syst.* **37**, 1-34.

Morgan, J.J. (2005) Kinetics of reaction between O_2 and Mn(II) species in aqueous solutions. *Geochim. Cosmochim. Acta* **69**, 35-48.

Mortvedt, J.J. (2000) Bioavailability of micronutrients. In: *Handbook of Soil Science* (ed. M.E. Sumner). CRC Press, Boca Raton, Forida, pp. D71-D88.

Naidu, R. and Rengasamy, P. (1993) Ion interactions and constraints to plant nutrition in Australian sodic soils. *Soil Res.* **31**, 801-819.

Narwall, R. and Singh, B. (2001) Solid phase speciation of iron and manganese in alum shale soils studied by parallel and sequential extraction. *Commun. Soil. Sci. Plant. Anal.* **32**, 331-349.

Nealson, K.H. (2006) The manganese-oxidizing bacteria. In: *Prokaryotes*, pp. 222-231.

Nealson, K.H., Tebo, B.M. and Rosson, R.A. (1988) Occurrence and mechanisms of microbial oxidation of manganese. In: *Advances in Applied Microbiology*. Elsevier, pp. 279-318.

Neaman, A., Martínez, C.E., Trolard, F. and Bourrié, G. (2008) Trace element associations with Fe-and Mn-oxides in soil nodules: Comparison of selective dissolution with electron probe microanalysis. *Appl. Geochem.* **23**, 778-782.

Ohki, K., Boswell, F., Parker, M., Shuman, L. and Wilson, D. (1979) Critical manganese deficiency level of soybean related to leaf position. *Agron. J.* **71**, 233-234.

Page, E.R. (1962) Studies in soil and plant manganese, II. The relationship of soil pH to manganese availbility. *Plant and Soil* **16**, 247-257.

Pal, P.K., Samii, A. and Calne, D. (1999) Manganese neurotoxicity: A review of clinical features, imaging and pathology. *Neurotoxicology* **20**, 227-238.

Palumbo, B., Bellanca, A., Neri, R. and Roe, M.J. (2001) Trace metal partitioning in Fe-Mn nodules from Sicilian soils, Italy. *Chem. Geol.* **173**, 257-269.

Peltier, E., Dahl, A.L. and Gaillard, J.-F. (2005) Metal speciation in anoxic sediments: When sulfides can be construed as oxides. *Environ. Sci. Technol.* **39**, 311-316.

Pickering, I.J. and George, G.N. (2007) *X-Ray Absorption Spectroscopy Imaging of Biological Tissues*, AIP Conference Proceedings. American Institute of Physics, pp. 311-315.

Porter, G., Bajita-Locke, J., Hue, N. and Strand, D. (2004) Manganese solubility and phytotoxicity affected by soil moisture, oxygen levels, and green manure additions. *Commun. Soil. Sci. Plant. Anal.* **35**, 99-116.

Post, J.E. (1999) Manganese oxide minerals: Crystal structures and economic and environmental significance. *Proc. Natl. Acad. Sci.* **96**, 3447-3454.

Qiang, T., Xiao-quan, S. and Zhe-ming, N. (1994) Evaluation of a sequential extraction procedure for the fractionation of amorphous iron and manganese oxides and organic matter in soils. *Sci. Total. Environ.* **151**, 159-165.

Reddy, K.R. and DeLaune, R.D. (2008) *Biogeochemistry of Wetlands: Science and Applications*. CRC Press, Boca Raton.

Remucal, C.K. and Ginder-Vogel, M. (2014) A critical review of the reactivity of manganese oxides with organic contaminants. *Environ. Sci.: Process. Impacts* **16**, 1247-1266.

Salm-Horstmar , L.P.d. (1849) Versuche ueber die nothwendigen Aschenbestandtheile einer Pflanzen-Species. *J. Prakt. Chem.* **46**, 193-211.

Santelli, C.M., Webb, S.M., Dohnalkova, A.C. and Hansel, C.M. (2011) Diversity of Mn oxides produced by Mn(II)-oxidizing fungi. *Geochim. Cosmochim. Acta* **75**, 2762-2776.

Saratovsky, I., Gurr, S.J. and Hayward, M.A. (2009) The structure of manganese oxide formed by the fungus *Acremonium* sp. strain KR21-2. *Geochim. Cosmochim. Acta* **73**, 3291-3300.

Sava, V., Mosquera, D., Song, S., Cardozo-Pelaez, F. and Sánchez-Ramos, J.R. (2004) Effects of melanin and manganese on DNA damage and repair in PC12-derived neurons. *Free Radic. Biol. Med.* **36**, 1144-1154.

Scheinost, A.C., Kretzschmar, R., Pfister, S. and Roberts, D.R. (2002) Combining selective sequential extractions, X-ray absorption spectroscopy, and principal component analysis for quantitative zinc speciation in soil. *Environ. Sci. Technol.* **36**, 5021-5028.

Schlichting, E. and Sparrow, L. (1988) Distribution and amelioration of manganese toxic soils. In: *Manganese in Soils and Plants* eds. R.D. Graham, R.J. Hannam, N.C. Uren). Kluwer Academic Publishers, Dordrecht, Netherlands, pp. 277-292.

Schmidt, S.B., Powikrowska, M., Krogholm, K.S., Naumann-Busch, B., Schjoerring, J.K., Husted, S., Jensen, P.E. and Pedas, P.R. (2016) Photosystem II functionality in barley responds dynamically to changes in leaf manganese status. *Front. Plant Sci.* **7**, 1772.

Schwertmann, U. and Fanning, D. (1976) Iron-manganese concretions in hydrosequences of soils in loess in Bavaria. *Soil. Sci. Soc. Am. J.* **40**, 731-738.

Scott, M.J. and Morgan, J.J. (1996) Reactions at oxide surfaces. 2. Oxidation of Se(IV) by synthetic birnessite. *Environ. Sci. Technol.* **30**, 1990-1996.

Shenker, M., Plessner, O.E. and Tel-Or, E. (2004) Manganese nutrition effects on tomato growth, chlorophyll concentration, and superoxide dismutase activity. *J. Plant Physiol.* **161**, 197-202.

Shobayo, A., Ya'u, S. and Odunze, A. (2019) Soil mineralogical characterization of selected carmine alfisols and plinthic inceptisols of Funtua, Nigeria. *Niger. J. Soil Sci.* **29**, 87-95.

Silvester, E., Manceau, A. and Drits, V.A. (1997) Structure of synthetic monoclinic Na-rich birnessite and hexagonal birnessite: II. Results from chemical studies and EXAFS spectroscopy. *Am. Mineral.* **82**, 962-978.

Sipos, P., Nemeth, T., May, Z. and Szalai, Z. (2011) Accumulation of trace elements in Fe-rich nodules in a neutral-slightly alkaline floodplain soil. *Carpathian Journal of Eearth and Environmental sciences* **6**, 13-22.

Stuckey, J.W., Goodwin, C., Wang, J., Kaplan, L.A., Vidal-Esquivel, P., Beebe, T.P. and Sparks, D.L. (2018) Impacts of hydrous manganese oxide on the retention and lability of dissolved organic matter. *Geochem. Trans.* **19**, 1-19.

Studer, J.M., Schweer, W.P., Gabler, N.K. and Ross, J.W. (2022) Functions of manganese in reproduction. *Animal Reproduction Science*, 106924.

Sunda, W.G. and Kieber, D.J. (1994) Oxidation of humic substances by manganese oxides yields low-molecular-weight organic substrates. *Nature* **367**, 62-64.

Sutherland, R.A. and Tack, F.M.G. (2003) Fractionation of Cu, Pb and Zn in certified reference soils SRM 2710 and SRM 2711 using the optimized BCR sequential extraction procedure. *Adv. Environ. Res.* **8**, 37-50.

Szymański, W., Skiba, M. and Błachowski, A. (2014) Mineralogy of Fe-Mn nodules in Albeluvisols in the Carpathian Foothills, Poland. *Geoderma* **217**, 102-110.

Takeda, A. (2003) Manganese action in brain function. *Brain Research Reviews* **41**, 79-87.

Taylor, R., McKenzie, R. and Norrish, K. (1964) The mineralogy and chemistry of manganese in some Australian soils. *Soil Res.* **2**, 235-248.

Tebo, B. and He, L. (1998) Microbially mediated oxidative precipitation reactions. In: *Mineral-Water Interface Reactions: Kinetics and Mechanisms* eds. D.L. Sparks, T.J. Grundl). American Chemical Society, Washington DC, pp. 393-414.

Tebo, B.M., Bargar, J.R., Clement, B.G., Dick, G.J., Murray, K.J., Parker, D., Verity, R. and Webb, S.M. (2004) Biogenic manganese oxides: Properties and mechanisms of formation. *Annu. Rev. Earth Planet. Sci.* **32**, 287-328.

Tebo, B.M., Johnson, H.A., McCarthy, J.K. and Templeton, A.S. (2005) Geomicrobiology of manganese(II) oxidation. *Trends Microbiol.* **13**, 421-428.

Terry, N. and Ulrich, A. (1974) Photosynthetic and respiratory CO_2 exchange of sugar beet leaves as influenced by manganese deficiency. *Crop Sci.* **14**, 502-504.

Tessier, A., Campbell, P.G. and Bisson, M. (1979) Sequential extraction procedure for the speciation of particulate trace metals. *Anal. Chem.* **51**, 844-851.

Tu, S., Racz, G.J. and Goh, T.B. (1994) Transformations of synthetic birnessite as affected by pH and manganese concentration. *Clays Clay Miner.* **42**, 321-330.

Uzochukwu, G. and Dixon, J. (1986) Managanese oxide minerals in nodules of two soils of Texas and Alabama. *Soil. Sci. Soc. Am. J.* **50**, 1358-1363.

Villalobos, M., Lanson, B., Manceau, A., Toner, B. and Sposito, G. (2006) Structural model for the biogenic Mn oxide produced by *Pseudomonas putida*. *Am. Mineral.* **91**, 489-502.

Villalobos, M., Toner, B., Bargar, J. and Sposito, G. (2003) Characterization of the manganese oxide produced by *Pseudomonas putida* strain MnB1. *Geochim. Cosmochim. Acta* **67**, 2649-2662.

Villinski, J.E., O'Day, P.A., Corley, T.L. and Conklin, M.H. (2001) In situ spectroscopic and solution analyses of the reductive dissolution of MnO_2 by Fe(II). *Environ. Sci. Technol.* **35**, 1157-1163.

Vodyanitskii, Y.N. (2009) Mineralogy and geochemistry of manganese: A review of publications. *Eurasian Soil Sci.* **42**, 1170-1178.

Vodyanitskii, Y.N., Gorshkov, A. and Sivtsov, A. (2002) Peculiarities of manganese oxides in soils of the Russian Plain. *Eurasian Soil Sci. C/C of Pochvovedenie* **35**, 1037-1045.

Webb, S.M., Tebo, B.M. and Bargar, J.R. (2005) Structural characterization of biogenic Mn oxides produced in seawater by the marine *Bacillus sp.* strain SG-1. *Am. Mineral.* **90**, 1342-1357.

Weis, J.S. and Weis, P. (2004) Metal uptake, transport and release by wetland plants: Implications for phytoremediation and restoration. *Environ. Int.* **30**, 685-700.

Wilson, D.E. (1980) Surface and complexation effects on the rate of Mn(II) oxidation in natural waters. *Geochim. Cosmochim. Acta* **44**, 1311-1317.

Wydrzynski, T.J., Satoh, K. and Freeman, J.A. (2005) *Photosystem II: The Light-driven Water: Plastoquinone Oxidoreductase*. Springer.

Yaroshevsky, A. (2006) Abundances of chemical elements in the Earth's crust. *Geochem. Int.* **44**, 48-55.

Zech, W. and Drechsel, P. (1991) Relationships between growth, mineral nutrition and site factors of teak (*Tectona grandis*) plantations in the rainforest zone of Liberia. *For. Ecol. Manag.* **41**, 221-235.

Zeien, H. and Brümmer, G. (1989) Chemical extractions to identify heavy metal binding forms in soils. *Mitt. Dtsch. Bodenkdl. Ges.* **59**, 505-510.

Zhang, M. and Karathanasis, A. (1997) Characterization of iron-manganese concretions in Kentucky Alfisols with perched water tables. *Clays Clay Miner.* **45**, 428-439.

2. X-RAY ABSORPTION SPECTROSCOPY STUDY OF MN REFERENCE COMPOUNDS FOR MN SPECIATION IN TERRESTRIAL SURFACE ENVIRONMENTS

TERESA ZAHORANSKY[a], ANNA V. WEGORZEWSKI[b], WINNIE HUONG[a], CHRISTIAN MIKUTTA[a]

[a]Soil Mineralogy, Institute of Mineralogy, Gottfried Wilhelm Leibniz University Hannover, Callinstr. 3, D-30167 Hannover, Germany

[b]Federal Institute for Geosciences and Natural Resources (BGR), Stilleweg 2, D-30655 Hannover, Germany

Corresponding author: Christian Mikutta

This chapter is accepted for publication in 'American Mineralogist' (DOI: 10.2138/am-2022-8236). The current version shows minor modifications in terms of consistent presentation and formatting in this thesis.

ABSTRACT

X-ray absorption spectroscopy (XAS) offers great potential to identify and quantify Mn species in surface environments by means of linear combination fit (LCF), fingerprint, and shell-fit analyses of bulk Mn XAS spectra. However, these approaches are complicated by the lack of a comprehensive and accessible spectrum library. Additionally, molecular-level information on Mn coordination in some potentially important Mn species occurring in soils and sediments is missing. Therefore, we investigated a suite of 32 natural and synthetic Mn reference compounds, including Mn oxide, oxyhydroxide, carbonate, phosphate, and silicate minerals, as well as organic and adsorbed Mn species, by Mn K-edge X-ray absorption near edge structure (XANES) and extended X-ray absorption fine structure (EXAFS) spectroscopy. The ability of XAS to infer the average oxidation state (AOS) of Mn was assessed by comparing XANES-derived AOS with the AOS obtained from redox titrations. All reference compounds were studied for their local (<5 Å) Mn coordination environment using EXAFS shell-fit analysis. Statistical analyses were employed to clarify how well and to what extent individual Mn species (groups) can be distinguished by XAS based on spectral uniqueness. Our results show that LCF analysis of normalized XANES spectra can reliably quantify the Mn AOS within ~0.1 v.u. in the range +2 to +4. These spectra are diagnostic for most Mn species investigated, but unsuitable to identify and quantify members of the manganate and Mn(III)-oxyhydroxide groups. First-derivative XANES fingerprinting allows the unique identification of pyrolusite, ramsdellite, and potentially lithiophorite

within the manganate group. However, XANES spectra of individual Mn compounds can vary significantly depending on chemical composition and/or crystallinity, which limits the accuracy of XANES-based speciation analyses. In contrast, EXAFS spectra provide a much better discriminatory power to identify and quantify Mn species. Principal component and cluster analyses of k^2-weighted EXAFS spectra of Mn reference compounds implied that EXAFS LCF analysis of environmental samples can identify and quantify at least the following primary Mn species groups: (1) Phyllo- and tectomanganates with large tunnel sizes (2×2 and larger; hollandite, romanèchite, todorokite), (2) tectomanganates with small tunnel sizes (2×2 and smaller; cryptomelane, pyrolusite, ramsdellite), (3) Mn(III)-dominated species (nesosilicates, oxyhydroxides, organic compounds, spinels), (4) Mn(II) species (carbonate, phosphate, and phyllosilicate minerals, adsorbed and organic species), and (5) manganosite. All Mn compounds, except for members of the manganate group (excluding pyrolusite) and adsorbed Mn(II) species, exhibit unique EXAFS spectra that would allow their identification and quantification in mixtures. Therefore, our results highlight the potential of Mn K-edge EXAFS spectroscopy to assess bulk Mn speciation in soils and sediments. A complete XAS-based speciation analysis of bulk Mn in environmental samples should preferably include the determination of Mn valences following the 'Combo' method of Manceau et al. (2012) (American Mineralogist 97, 816-827), EXAFS LCF analyses based on principal component and target transformation results, as well as EXAFS shell-fit analyses for the validation of LCF results. For this purpose, all 32 XAS reference spectra are provided in the *Supplementary material* for further use by the scientific community.

2.1. INTRODUCTION

Manganese (Mn) is a redox-sensitive element with a crustal abundance of about 0.1 wt.% (Yaroshevsky, 2006). It participates in numerous globally important environmental processes such as photosynthetic oxygen production and oxidative lignin degradation, and serves as an activator of more than 35 enzymes (Burnell, 1988; Jensen et al., 1996; Broadley et al., 2012; Keiluweit et al., 2015). The three naturally occurring Mn oxidation states +2, +3, and +4 account for the large variety of single- and mixed-valent Mn species in environmental samples, including oxides and oxyhydroxides (collectively termed (oxyhydr)oxides), carbonates, phosphates, silicates, organic compounds or Mn species being adsorbed to (in)organic surfaces. Manganese concentrations in sediments and bedrocks may be as low as 20 mg/kg in quartz sands and >1,000 mg/kg in basic rocks like basalt and gabbro (Chatzistathis et al., 2012; Blume et al., 2016). Natural background levels of soil Mn range between 40 and 1,000 mg/kg (Blume et al., 2016), but neither total nor exchangeable Mn in soil is correlated with bedrock composition, indicative of a high Mn mobility in the Earth's crust (Mortvedt, 2000).

The mobility of Mn in soils and sediments depends largely on biological processes controlling its redox state (Tebo et al., 2005). Since Mn^{2+} is more soluble than Mn^{4+}, Mn bioavailability tends to increase with decreasing pH and redox potential (Blume et al., 2016). A particularly important role in the cycling of Mn in surface environments is attributed to Mn(III/IV) (oxyhydr)oxides, since their precipitation and dissolution primarily control the amount of soluble and thus bioavailable Mn^{2+} (Tebo et al., 2004; Martin, 2005). These minerals exist either as layer or tunnel structures. Layer-type Mn(III/IV) (oxyhydr)oxides ('phyllomanganates') consist of stacked sheets of edge-sharing MnO_6 octahedra, whereas in Mn(III/IV) (oxyhydr)oxides with tunnel structure ('tectomanganates') MnO_6 octahedra form single, double or triple chains by sharing edges, which are linked together via MnO_6 corners to produce tunnels of varying size (McKenzie, 1989). Positive charge deficits created by Mn^{4+} site vacancies or the substitution of structural $Mn^{3+/4+}$ by cations of lower valence are compensated by exchangeable cations (e.g., H^+, Na^+, K^+, Ca^{2+}, Mg^{2+}, etc.) occupying the tunnel or interlayer spaces (McKenzie, 1989).

Manganate minerals are thought to be primarily formed via fast enzymatic Mn^{2+} oxidation by bacteria and fungi (Tebo et al., 2004). Resulting Mn(III/IV) (oxyhydr)oxides are poorly crystalline phyllomanganates structurally akin to H^+-birnessite ('acid birnessite') or δ-MnO_2, and may serve as precursors for more crystalline Mn oxides (e.g., todorokite) and Mn(III) oxyhydroxides (e.g., feitknechtite, manganite) through ageing and/or redox reactions involving dissolved Mn^{2+} (Miyata et al., 2007; Feng et al., 2010; Elzinga, 2011).

The role of Mn(III/IV) (oxyhydr)oxides as strong oxidants for inorganic and organic soil and sediment constituents is well documented (Bartlett, 1981; Villinski et al., 2001; Feng et al., 2007; Remucal and Ginder-Vogel, 2014; Ehlert et al., 2016). Owing to their low point of zero charge and high specific surface area, biogenic Mn(III/IV) (oxyhydr)oxides show a high affinity towards heavy metals like Co, Cu, Ni, and Zn, which frequently exceeds that of Fe(III) (oxyhydr)oxides (O'Reilly and Hochella Jr, 2003; Tebo et al., 2004). As a consequence, soil Mn contained in ferromanganese nodules and concretions is often associated with these trace metals (Latrille et al., 2001; Liu et al., 2002; Manceau et al., 2003).

Despite the ecological importance and omnipresence of Mn in terrestrial surface environments, studies targeting the identification and quantification of chemical forms (species) of Mn are surprisingly rare. Available Mn speciation studies can be grouped into three categories. Category 1 studies used sequential extraction methods (Qiang et al., 1994; Narwall and Singh, 2001; Kalembkiewicz et al., 2008; Habibah et al., 2014), which provide valuable information on operationally defined Mn fractions. However, poor selectivity of extractants, Mn redistribution during extractions, and the use of a large variety of non-standardized extraction procedures severely limit the explanatory power of this speciation approach (Sutherland and Tack, 2003; Hlavay et al., 2004; Hass and Fine,

2010). Category 2 studies employed X-ray or electron diffraction to identify and/or characterize Mn minerals in geomaterials. The use of these techniques is hampered by the fact that Mn minerals in soils and sediments are frequently nanocrystalline and amorphous to X-rays (Ross et al., 1976; Chukhrov and Gorshkov, 1981; Rhoton et al., 1993; Zhang and Karathanasis, 1997; Latrille et al., 2001; Cornu et al., 2005). Therefore, these studies almost exclusively focused on ferromanganese nodules and concretions in soils (Taylor et al., 1964; Tokashiki et al., 1986; Uzochukwu and Dixon, 1986; Liu et al., 2002; Manceau et al., 2003; Szymański et al., 2014) or sediments (Taira et al., 1981; Lee and Xu, 2016). Category 3 studies utilized synchrotron-based Mn K-edge X-ray absorption spectroscopy (XAS) to speciate soil (Manceau et al., 2005; Frommer et al., 2011; Hernandez-Soriano et al., 2012; Herndon et al., 2014; Keiluweit et al., 2015) and sediment Mn (Friedl et al., 1997; O'Day et al., 2000; Carroll et al., 2002). Regardless of the type of Mn species present, high-brilliance synchrotron facilities provide the capability for non-destructive analysis of oxidation state and average local (<5 Å) coordination of Mn in environmental samples with Mn concentrations of several hundred milligrams per kilogram. Previous XAS studies mostly employed either Mn K-edge X-ray absorption near edge structure (XANES) or microfocused extended X-ray absorption fine structure (EXAFS) spectroscopy. The XANES technique is useful to infer the average oxidation state (AOS) of Mn in soils and sediments based on the shift of the absorption edge towards higher energies with increasing Mn AOS (McKeown and Post, 2001; Manceau et al., 2012). Quantitative information on the fractional amounts of Mn^{2+}, Mn^{3+}, and Mn^{4+} and the resulting Mn AOS in a sample can be obtained by the 'Combo' linear combination fit (LCF) analysis method of (Manceau et al., 2012) using a XANES spectra database of well-characterized monovalent Mn references. The accuracy of this method was estimated to be 0.04 valence units (v.u.) in the Mn AOS range +3 to +4, which decreased when the proportion of divalent Mn was greater than 15% (Manceau et al., 2012). Although this state-of-the-art LCF approach has already been used to analyze the AOS of soil Mn (Herndon et al., 2014; Keiluweit et al., 2015), its generic applicability has not been validated by other methods available for Mn AOS quantification.

In addition to the determination of Mn oxidation states, Mn K-edge XANES spectra may in principle be useful for the identification and quantification of distinct Mn species in unknown samples using LCF analysis (Frommer et al., 2011; Leven et al., 2018; Morales-Pérez et al., 2021). However, limited numbers of fit references, spectral similarity of different species, and non-unique LCF solutions can severely limit this approach (Scheinost et al., 2002; Gustafsson et al., 2020).

In contrast to XANES analyses, EXAFS spectroscopy has hitherto only rarely been used for the identification and quantification of Mn species in soils and sediments (Manceau et al., 2005; Mayanna et al., 2015). EXAFS evaluations of environmental samples typically include shell-fit and LCF analyses (Scheckel and Ryan, 2004; Ahmad et al., 2019), the latter often combined with principal component analysis (PCA) and target transformation (TT) testing (Manceau et al., 2002; Scheinost et al., 2002;

Langner et al., 2012; Mikutta and Rothwell, 2016). Decisive for the success of Mn EXAFS LCF analysis is the existence of a comprehensive spectrum library including relevant Mn species potentially occurring in terrestrial environments. Several EXAFS studies provide fundamental information on the local Mn coordination in a range of Mn compounds (Manceau and Combes, 1988; Silvester et al., 1997; McKeown and Post, 2001; Manceau et al., 2005; Webb et al., 2005; Bhattacharya and Elzinga, 2018; Ahmad et al., 2019). However, the number of publicly available Mn EXAFS spectra is neither sufficient for validation of EXAFS parameters previously determined for specific Mn species, nor for Mn speciation analysis of soils and sediments. Additionally, systematic studies on spectral uniqueness of Mn compounds are largely missing. Complicating matters further, EXAFS data are lacking for various potentially important Mn species such as Mn-containing silicate and phosphate minerals, organic Mn(II/III) compounds, and adsorbed Mn(II) species.

The main objective of this study was to evaluate how well and to what extent different Mn species potentially occurring in terrestrial surface environments such as soils and sediments can be distinguished by Mn K-edge XANES and EXAFS spectroscopy. To this end, we collected XAS spectra of 32 well-characterized mineral and organic Mn compounds and analyzed these spectra for features and structural information that allow the discrimination of distinct Mn species (groups). This information is indispensable for the correct analysis and interpretation of Mn XAS spectra of environmental samples. In addition, we used redox titrations to verify the accuracy of the 'Combo' XANES LCF method of Manceau et al. (2012) for determining the AOS of Mn in geomaterials

2.2. MATERIALS AND METHODS

2.2.1. MANGANESE REFERENCE COMPOUNDS

The 32 natural and synthetic Mn reference samples analyzed in this study, 15 natural and 17 synthetic, belong to seven main groups: (1) Phyllomanganates, (2) tectomanganates, (3) oxide minerals without tunnel or layer structure, (4) Mn(III) oxyhydroxides, (5) carbonate, phosphate, and silicate minerals, (6) organic Mn(II/III) compounds, and (7) Mn(II) adsorbed to (in)organic materials. Table 2.1 lists all reference compounds along with information on, for example, ideal and empirical formulas, structure type where appropriate, Mn content, and XAS spectrum source.

Table 2.1. Manganese reference compounds studied by XAS

No.	Reference	Mineral formula (nominal / empirical)[a]	Remarks	Mn (wt.%)[b]	Spectrum source
Phyllomanganates					
1	Acid Na-birnessite (hex, syn)	$H_{0.06}K_{0.18}(H_2O)_{0.54}Mn^{3+}_{0.08}(H_2O)_{0.24}(Mn^{4+}_{0.88},vac_{0.12})_{\Sigma 1.00}O_2$		54	This study
2	δ-MnO_2 (syn)	$(Mn^{4+},Fe^{3+},Ca,Na)_{\Sigma 1.00}(O,OH)_2 \cdot nH_2O$		49	This study
3	Lithiophorite	$(Al,Li)Mn^{4+}{}_2O_2(OH)_2$ / $Al_2LiMn^{4+}{}_2Mn^{3+}O_6(OH)_6$		39[c]	McKeown and Post (2001)
4	Na-birnessite (tricl, syn)	$Na_{0.26}(Mn^{4+}_{0.74}Mn^{3+}_{0.26})_{\Sigma 1.00}O_2$		55	This study
Tectomanganates					
5	Cryptomelane	$K(Mn^{4+},Mn^{3+})_8O_{16}$ / $(K_{0.78}Na_{0.06}Si_{0.05}Ca_{0.04}Zn_{0.03}Sr_{0.02})_{\Sigma 0.98}(Mn^{4+}_{6.73}Mn^{3+}_{1.22}Al_{0.06})_{\Sigma 8.01}O_{16}$	2×2 tunnel	57	This study
6	Cryptomelane (syn)	$K(Mn^{4+},Mn^{3+})_8O_{16}$ / $(K_{0.89}Pb_{0.01})_{0.90}(Mn^{4+}_{6.79}Mn^{3+}_{1.31})_{\Sigma 8.10}O_{16}$	2×2 tunnel	62	This study
7	Hollandite s.s.	$Ba(Mn^{4+},Mn^{3+})_8O_{16}$ / $(Ba_{0.75}Pb_{0.16})_{0.91}(Mn^{4+}Mn^{3+}Fe)_{\Sigma 8.00}O_{16}$	2×2 tunnel	n.d.	McKeown and Post (2001)
8	Pyrolusite	β-$Mn^{4+}O_2$ / $(Mn^{4+}_{0.99}Al_{0.01})_{\Sigma 1.00}O_2$	1×1 tunnel	61	This study
9	Pyrolusite (syn)	β-$Mn^{4+}O_2$	1×1 tunnel	61[c]	This study
10	Ramsdellite	R-$Mn^{4+}O_2$ / $(Mn^{4+}_{0.99}Al_{0.01})_{\Sigma 1.00}O_2$	1×2 tunnel	62	This study
11	Romanèchite	$(Ba,H_2O)_2(Mn^{4+},Mn^{3+})_5O_{10}$ / $Ba_{0.66}(Mn^{4+}_{3.68}Mn^{3+}_{1.32})_{\Sigma 5.00}O_{10} \cdot 1.34H_2O$	2×3 tunnel	50[c]	McKeown and Post (2001)
12	Romanèchite (Ba-free, syn)	$(Na,H_2O)_2(Mn)_{10}O_{20}$ / $Na_{1.08}(Mn^{4+}_{4.17}Mn^{3+}_{0.74})_{\Sigma 4.91}O_{10} \cdot H_2O$	2×3 tunnel	60	This study
13	Todorokite	$(Mn^{2+},Ca,Na,K)(Mn^{4+},Mn^{2+},Mg)_6O_{12} \cdot 3H_2O$ / $(Mn^{2+}_{0.18}Ca_{0.22}Na_{0.22}Sr_{0.14}K_{0.11}Zn_{0.08}Ba_{0.03}Si_{0.02})_{\Sigma 0.99}(Mn^{4+}_{5.15}Mn^{2+}_{0.62}Mg_{0.23})_{\Sigma 6.00}O_{12} \cdot 3H_2O$	3×3 tunnel	52	This study
14	Todorokite (syn)	$(Mn^{2+},Ca,Na,K)(Mn^{4+},Mn^{2+},Mg)_6O_{12} \cdot 3H_2O$ / $Mn_{6.1}Mg_{0.7}O_{12} \cdot 3H_2O$	3×3 tunnel	56[c]	Peacock and Moon (2012)
Oxide minerals without layer or tunnel structure					
15	Bixbyite	$(Mn^{3+},Fe^{3+})_2O_3$ / $(Mn^{3+}_{1.74}Fe^{3+}_{0.21}Al_{0.05})_{\Sigma 2.00}O_3$		60	This study
16	Bixbyite (syn)	$Mn^{3+}{}_2O_3$		70[c]	This study
17	Hausmannite	$(Mn^{2+},Mn^{3+})_3O_4$ / $(Mn^{3+}_{1.97}Mn^{2+}_{1.00}Fe^{3+}_{0.02})_{\Sigma 3.00}O_{4.00}$	Spinel	70	This study
18	Manganosite (syn)	$Mn^{2+}O$		77[c]	This study
Mn(III) oxyhydroxides					
19	Feitknechtite (syn)	β-$Mn^{3+}O(OH)$		62[c]	Lefkowitz et al. (2013)
20	Groutite	α-$Mn^{3+}O(OH)$ / α-$(Mn^{3+}_{0.98}Mg_{0.1})_{\Sigma 0.99}O(OH)$		60	This study
21	Manganite (syn)	γ-$Mn^{3+}O(OH)$ / γ-$Mn^{3+}_{1.00}O(OH)$		66	This study

Table 2.1 *(continued)*

No.	Reference	Mineral formula (nominal / empirical)[a]	Remarks	Mn (wt.%)[b]	Spectrum source
Carbonate, phosphate, and silicate minerals					
22	Braunite	$Mn^{3+}Mn^{2+}_6O_8SiO_4$ / $(Mn^{3+}_{6.08}Mn^{2+}_{0.80}Ca_{0.15}Al_{0.01})_{\Sigma 7.04}O_8Si_{0.95}O_4$	Nesosilicate	61	This study
23	Hendricksite	$K(Zn,Mg,Mn^{2+})_3Si_3AlO_{10}(OH)_2$ / $(K_{0.93}Na_{0.07})_{\Sigma 1.00}(Zn_{1.28}Mg_{0.76}Mn^{2+}_{0.76}Fe^{2+}_{0.28}Ba_{0.01}Ti_{0.01})_{\Sigma 3.10}(Si_{2.83}Al_{1.17})_{\Sigma 4.00}O_{10}(F_{0.03}(OH)1_{.97})_{\Sigma 2.00}$	Trioctahedral mica	8	This study
24	Masutomilite	$K(Li,Al,Mn^{2+})_3(Si,Al)_4O_{10}(F,OH)_2$ / $(K_{0.85}Na_{0.04})_{\Sigma 0.89}(Li_{1.53}Al_{1.23}Mn^{2+}_{0.18})_{\Sigma 2.94}(Si_{3.43}Al_{0.57})_{\Sigma 4.00}O_{9.93}(F_{2.06}Cl_{0.01})_{\Sigma 2.07}$	Trioctahedral mica	2	This study
25	Rhodochrosite	$Mn^{2+}CO_3$ / $(Mn^{2+}_{0.94}Zn_{0.03}Ca_{0.02}Mg_{0.01})_{\Sigma 1.00}CO_3$	Carbonate	43	This study
26	Triplite	$(Mn^{2+},Fe^{2+},Ca,Mg)_2(PO_4)(F,OH)$ / $(Mn^{2+}_{1.10}Fe^{2+}_{0.74}Ca_{0.10}Mg_{0.05})_{\Sigma 2.00}(P_{0.99}O_{3.96})(F_{0.79}(OH)_{0.21})_{\Sigma 1.00}$	Phosphate	27	This study
Organic Mn(II/III) compounds					
27	Mn(II) acetate tetrahydrate (syn)	$Mn^{2+}(CH_3COO)_2{\cdot}4H_2O$		22[c]	Ehlert et al. (2014)
28	Mn(II) oxalate dihydrate (syn)	$Mn^{2+}C_2O_4{\cdot}2H_2O$		31[c]	This study
29	Mn(III) acetate dihydrate (syn)	$Mn^{3+}(CH_3COO)_3{\cdot}2H_2O$		20[c]	This study
Adsorbed Mn(II) species					
30	Mn(II) ads. illite pH7	$K_{0.65}Al_{2.0}(Al_{0.65}Si_{3.35}O_{10})(OH)_2{\cdots}Mn^{2+}_x$	Phyllosilicate	0.7	This study
31	Mn(II) ads. peat pH7		Organic sediment	0.9	This study
32	Mn(II) ads. peat pH5		Organic sediment	1.2	This study

[a]Nominal mineral formulas after Anthony et al. (2003). Empirical formulas of birnessites and δ-MnO_2 are taken from Villalobos et al. (2003, 2006), those of hollandite, lithiophorite, and romanèchite from McKeown and Post (2001), and the formula of todorokite (syn) from Feng et al. (1995). All other empirical mineral formulas are based on chemical analysis of this study.
[b]Determined by chemical analysis of this study unless stated otherwise. n.d. = not determined.
[c]Calculated from mineral formula (empirical if two formulas are stated). No chemical analysis performed in this study.

Natural mineral samples were carefully handpicked using a binocular microscope. The cleanest looking crystals or parts with least alteration were chosen for further analysis. Synthetic bixbyite, manganosite, and pyrolusite were purchased as mineral powders. Cryptomelane was synthesized according to McKenzie (1971), δ-MnO_2, hexagonal acid and triclinic Na-birnessites following Villalobos et al. (2003), manganite was synthesized using a slightly modified protocol from Chiu and Hering (2000), and Ba-free romanèchite following Shen et al. (2005).

Manganese(II) adsorption samples were prepared by batch experiments using a natural 85:15-90:10 illite-smectite mineral with R3 ordering from Füzérradvány, Hungary (<2-µm fraction; Dohrmann et al., 2009) and peat from a raised peat bog (Federseemoor) near Bad Buchau, Germany (40-250-µm fraction; Hoffmann et al., 2012) as adsorbents. Experimental conditions are detailed in the *Supplementary material.*

2.2.2. Characterization of Mn reference compounds

2.2.2.1. X-ray diffraction

All available solids were analyzed by powder X-ray diffraction (PXRD) in Bragg-Brentano geometry using a Bruker AXS D4 Endeavor diffractometer equipped with a secondary graphite monochromator (CuK$\alpha_{1,2}$ radiation) and a scintillation counter. X-ray diffraction patterns were collected at room temperature within a 2theta range of 5-110° using a measuring time of 4-10 s per 0.02° step (tube settings: 40 kV/40 mA). The identity of all minerals was confirmed (Figs. A.1 and A.2). Minor impurities in ramsdellite result from its transition to pyrolusite. Natural pyrolusite and groutite showed minor manganite impurities. An unknown reflection was found in the diffractograms of triclinic Na-birnessite and synthetic cryptomelane. Remaining additional diffraction peaks in different Mn compounds could be assigned to non-Mn phases such as calcite in groutite, annite in hendricksite, and quartz in braunite and in the peat sample. Literature references or powder diffraction file (pdf) numbers used for XRD evaluation are compiled in Table A.1.

2.2.2.2. Chemical composition

Twelve natural minerals were prepared as polished and carbon-coated thin sections. Their chemical composition was determined by electron probe microanalysis (EPMA) using a CAMECA SX100 instrument equipped with five wavelength-dispersive spectrometers. A focused beam was used with an acceleration voltage of 15 kV and a beam current of 15 nA for major elements (Al, Cr, K, Mg, Mn, P, Si, Ti) and 100 nA for minor or trace elements (Ba, Ca, Cl, F, Fe, Na, Sr, Zn). Counting time on element peaks was 10 s for Al, Ba, Cr, K, Mn, Na, Si, 20 s for Ca, Cl, Fe, Mg, P, Sr, Ti, 30 s for Zn, and 50 s for F. Background counting times were half on-peak counting times. The following standards were used for calibrations (element, analyzer crystal): Fe_2O_3 (Fe, large lithium fluoride (LLIF)), jadeite (Na, thallium

acid phthalate (TAP)), kyanite (Al, TAP), Mn_3O_4 (Mn, LLIF), orthoclase (K, pentaerythritol (PET)), wollastonite (Si, Ca, TAP and PET, respectively), olivine (Mg, TAP), TiO_2 (Ti, large pentaerythritol (LPET)), Cr_2O_3 (Cr, LPET), apatite (P, PET), NaCl (Cl, LPET), ZnS (Zn, LLIF), SrF_2 (F, Sr, TAP and LPET, respectively), $BaSO_4$ (Ba, LPET). Results of these analyses are summarized in Table S2. Detection limits for each element measured are listed in Table A.3. The elemental composition of remaining reference compounds is given as provided by the supplier (synthetic bixbyite, manganosite, pyrolusite, organic Mn(II/III) Mn compounds) or as stated in the respective publications (synthetic feitknechtite and todorokite) (Table 2.1). For references with adsorbed Mn(II), the Mn content was determined as described in the *Supplementary material*.

The chemical composition of six synthetic mineral compounds (acid Na-birnessite, cryptomelane, δ-MnO_2, manganite, Na-birnessite (tricl), romanèchite) was determined by inductively coupled plasma–optical emission spectrometry (ICP-OES, Agilent 5900 SVDV) after acid digestion of the samples at 120-140 °C (Table A.2.). Acid reagents included 69% HNO_3 (Suprapur®, Roth), 37% HCl (p.a., Roth), and, if necessary, 40% HF (p.a., Merck) and 30% H_2O_2 (Suprapur®, Merck). Peat samples were previously combusted at 550 °C overnight in a ceramic crucible. Digestions are described in the *Supplementary material*, and detection limits for each element measured can be found in Table A.3.

Based on chemical composition, empirical mineral formulas (Table 2.1) were calculated after normalization to oxygen. Fractional amounts of Mn valences per formula unit were determined by charge-balance calculations. Mineral formulas of synthetic Na-birnessites and δ-MnO_2 are those stated in their respective synthesis protocols. Details on empirical formula calculations are presented in the *Supplementary material.*

2.2.2.3. REDOX TITRATION

Redox titrations for the determination of bulk Mn AOS were performed after Grangeon et al. (2012) using an automated titration system (TitroLine 7800, SI Analytics). Briefly, $(NH_4)_2Fe(SO_4)_2{\cdot}6H_2O$ ('Mohr´s salt') was used to reduce $Mn^{3+/4+}$ in Mn reference compounds to dissolved Mn^{2+}. The excess reductant (Fe^{2+}) was back-titrated with $KMnO_4$ solution and total Mn determined by the re-oxidation of Mn^{2+} to Mn^{3+}, stabilized by pyrophosphate ($P_2O_7^{4-}$). All measurements were carried out in duplicates or triplicates.

2.2.2.4. MANGANESE K-EDGE XAS

Bulk Mn K-edge XAS spectra of 26 Mn reference compounds were collected at beamline 7-3 of the Stanford Synchrotron Radiation Lightsource (SSRL, Menlo Park, USA), beamline 5-BM-D of the Advanced Photon Source (APS, Argonne, USA), and beamlines P64 and P65 of PETRA III at the Deutsches Elektronen-Synchrotron (DESY, Hamburg, Germany). The beamlines were equipped with

Si(220) (7-3) and Si(111) double-crystal monochromators (5-BM-D, P64, P65), which were calibrated by setting the first-derivative maximum of the K-edge absorption spectrum of elemental Mn to 6,539 eV. Higher harmonics in the beam were reduced by detuning monochromators by 15-50% and by harmonic rejection mirrors (P65). In addition, 3-µm Cr filters were used to reduce undesired fluorescence radiation at beamlines 7-3 and P65. Measurements were performed in both fluorescence and transmission mode utilizing solid-state fluorescence detectors (7- or 30-element Ge detectors, Vortex SDDs) and ionic chambers, respectively. To avoid beam damage, all samples were measured at 5-20 K employing He-cryostats or at 77 K (5-BM-D) using a Lincam cell. Details of the sample preparation can be found in the *Supplementary material*.

Spectra were recorded with a maximum energy increment of 5 eV before the edge and 0.2-0.3 eV along the edge. The EXAFS was recorded with a *k*-space resolution of 0.05 $Å^{-1}$. Five to 20 scans were collected per sample. Spectra of a Mn metal foil were used to correct for slight energy shifts during sample measurements.

Spectral pre-processing, including merging of individual scans, rebinning, and energy calibration, was conducted in SIXPack (Webb, 2005) or Athena (Ravel and Newville, 2005). The spectra were further processed in Athena following standard routines. The pre-edge region was fit with a linear function and the post-edge region with a quadratic polynomial. The edge-step energy, E_0, was defined as the first maximum of the first XANES derivative. For background removal the Autobk algorithm was applied. The frequency cut-off parameter, R_{bkg}, was set to 0.9-1.1, and the *k*-weight for background removal to two or three. A Hanning window function with a sill width of 2 $Å^{-1}$ was used to Fourier transform the data.

In addition to the measured spectra, six XAS spectra were obtained from external sources (Table 1.2). Details on their origin and measurement can be found in the respective publications.

2.2.2.5. MANGANESE XAS DATA ANALYSIS

For the determination of Mn AOS and the fractional amount of each Mn oxidation state present in the reference compounds, we applied the 'Combo' LCF method of Manceau et al. (2012). For this, normalized XANES spectra were fit using 17 Mn K-edge XANES spectra of monovalent Mn references available as open source in Manceau et al. (2012) (deposit item AM-12-037), which were processed as described above. The fits were performed in Athena over an energy range of -20 to 30 eV (E–E_0) by applying a non-negativity constraint. A single E_0 shift was used for all standards. During the fits, negatively loaded references were progressively eliminated until only references with positive (or zero) loadings remained. Each previously deleted reference was then again randomly added and the fit run again to assure that the global minimum was found using the normalized sum of squared residuals (*R*-factor) as best-fit criterion (Manceau et al., 2012). Eventually, no negative loadings

remained and the total fraction of each Mn oxidation state in the sample analyzed was calculated as the sum of the individual component fractions (Manceau et al., 2012).

Least-squares fits of k^3-weighted EXAFS spectra of Mn reference compounds were performed in Artemis (Ravel and Newville, 2005) on a shell-by-shell basis in *R*-space ($R+\Delta R$ ~1-4 Å). *R*-space resolution as given by the Rayleigh criterion ($0.5\pi/(k_{max}-k_{min})$) was 0.14-0.20 Å, such that atomic shells separated by lower values could not be resolved. Theoretical phase-shift and amplitude functions were calculated with FEFF6 (Ankudinov et al., 1998) based on crystal-structure information. Partial occupancies due to chemical substitution as revealed by chemical analyses were accounted for by adding additional atoms into the respective feff.inp file. For structures containing two or more inequivalent Mn sites (e.g., bixbyite, hausmannite), aggregated FEFF calculations were used, that is, path lists of individual sites were automatically merged together and weighted by the fractional population of the site in the unit cell (Ravel, 2014). The passive amplitude reduction factor, S_0^2, was fixed to 0.8 during optimization. If individually fitted Debye-Waller parameters, σ^2, converged towards similar values, they were equated in the final fit to reduce the number of fit variables.

2.2.2.6. STATISTICS

The Pearson correlation coefficient was used as a similarity metric for normalized and first-derivative XANES (E = 6,530-6,600 eV) as well as k^2-weighted EXAFS spectra (k = 2.0-11.5 Å^{-1}, E_0 = 6,563 eV). Principal component analysis (PCA) was performed on the k^2-weighted Mn EXAFS spectra. Suitability of this data for PCA was confirmed by the Kaiser-Meyer-Olkin (KMO) test in SPSS Statistics (IBM Corp.). In addition, an unsupervised hierarchical cluster analysis of the EXAFS spectra was conducted using Ward's clustering algorithm (Ward, 1963) with squared Euclidean distances as distance measure. Correlation, PC, and cluster analyses were conducted in Statistica (TIBCO Software Inc.). For linear regression between XANES- and titration-based Mn AOS, normal distribution of data points, constant variance of the dependent variable, and independence of residuals were assured by Shapiro-Wilk and Spearman rank correlation tests as well as Durbin-Watson statistic, respectively, using SigmaPlot v.14 (Systat Software Inc.).

2.3. RESULTS AND DISCUSSION

2.3.1. XANES SPECTRA OF MN REFERENCES COMPOUNDS

Figure 2.1 illustrates absorbance shifts to higher energies with increasing Mn AOS of Mn reference compounds. Here, a zero-energy value was defined by setting the first maximum of the first XANES derivative in the pre-edge region (~6,539 eV) to 0 eV. The ordinate represents the relative energy at which the normalized absorbance XANES signal first reaches 50% of the edge absorption maximum.

Manganese compounds belonging to different Mn AOS groups are clearly separated, confirming that XANES data allow a general classification of Mn species with respect to Mn oxidation state.

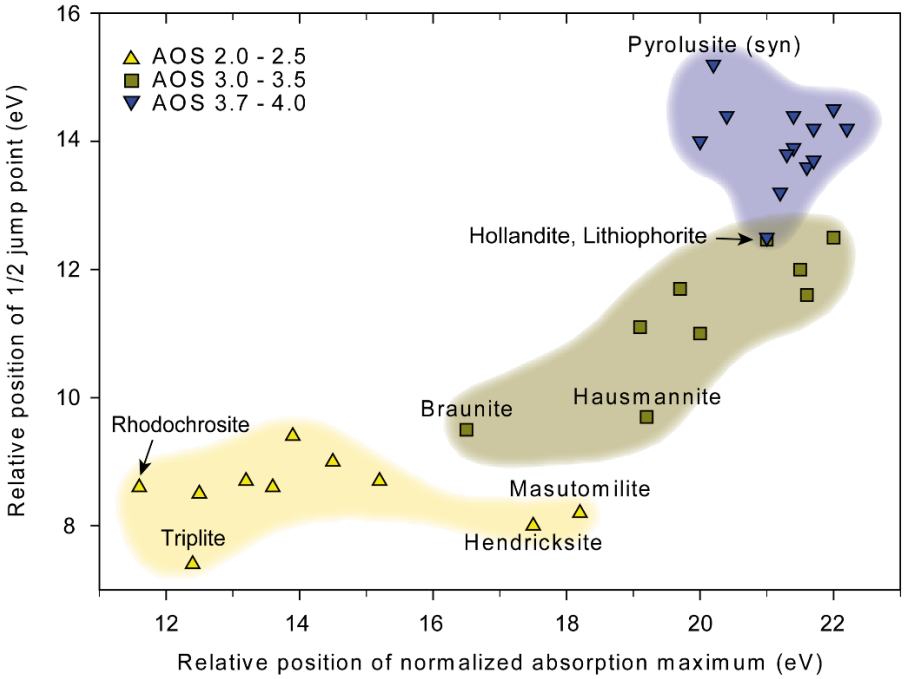

Figure 2.1. Classification plot of Mn reference compounds. Different XANES-derived Mn AOS based on absorption-edge position are shown relative to the first maximum in the first XANES derivative at ~6,540 eV (after Marcus et al., 2008). Note that masutomilite and hendricksite as well as hausmannite and braunite are separated from other members of the low- and medium-AOS range. Synthetic pyrolusite shows the highest Mn AOS of 4.0 of all reference compounds.

Figures 2.2 and 2.3 show normalized XANES and corresponding first-derivative spectra of Mn reference compounds, and Table 2.2 summarizes primary absorption peaks identified up to 6,570 eV. Phyllo- and tectomanganates with varying amounts of Mn^{3+} and Mn^{4+} generally show XANES spectra with broad pre-peaks at 6,541.5-6,543.4 eV, smoothly rising absorption edges, and maximal absorbances between 6,560.3 and 6,562.5 eV (Fig. 2.2, Table 2.2). The similarity of their XANES features suggests that a unique identification of single members in mixtures would not generally be possible. However, lithiophorite exhibits a unique edge feature, leading to two distinct peaks in the first-derivative XANES spectrum at 6,551.5 and 6,557.5 eV. This feature may aid the identification of lithiophorite in mixtures with other phyllomanganates. Among tectomanganates, cryptomelane (2×2 tunnels), hollandite *sensu stricto* (*s.s.*) (2×2 tunnels), romanèchite (2×3 tunnels), and todorokite (3×3 tunnels) possess similar XANES spectra. In contrast, the first-derivative XANES of pyrolusite (1×1 tunnels) and ramsdellite (1×2 tunnels) feature characteristic double peaks at ~6,552 and ~6,558 eV (Fig. 2.2, Table 2.2), potentially allowing the identification of tectomanganates with the smallest tunnel sizes in environmental samples. Differences in XANES spectra observed for natural and synthetic tectomanganates

(cryptomelanes, pyrolusites, todorokites) reflect the sensitivity of XANES spectroscopy to variations in mineral composition and/or crystallinity (Fig. 2.2).

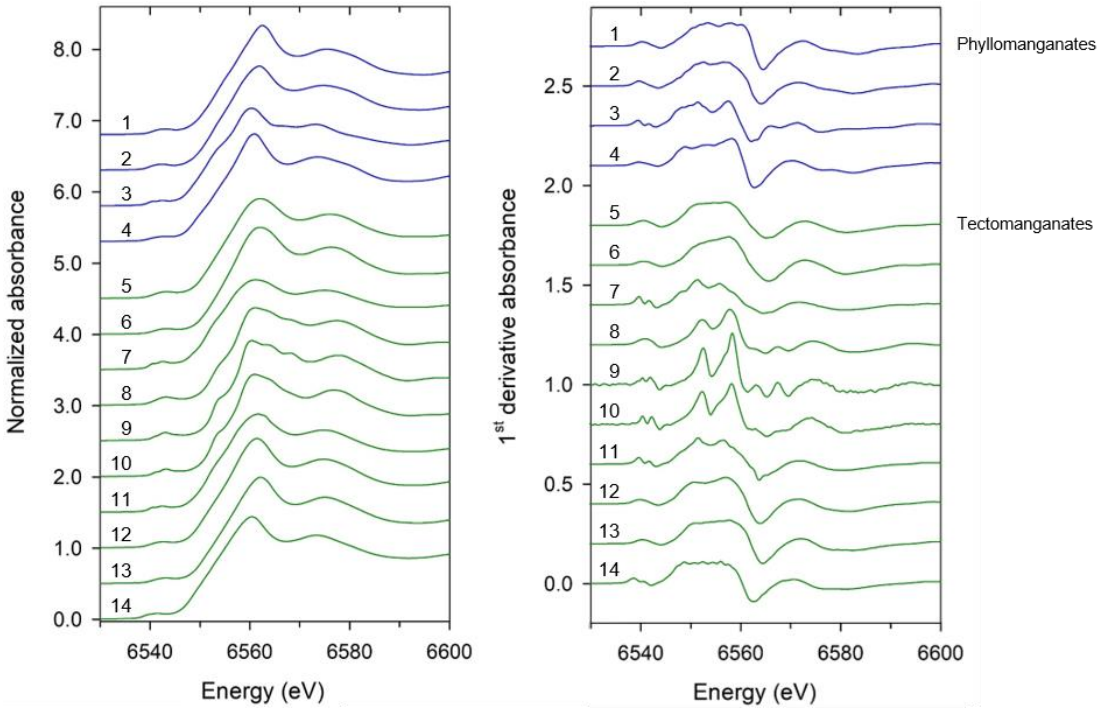

Figure 2.2. Stacked normalized Mn K-edge XANES (left) and corresponding first-derivative spectra (right) of phyllo- and tectomanganates. The spectrum numbers match the numbers in Table 2.1: 1 - acid Na-birnessite (hex, syn), 2 - δ-MnO_2 (syn), 3 - lithiophorite, 4 - Na-birnessite (tricl, syn), 5 - cryptomelane, 6 - cryptomelane (syn), 7 - hollandite s.s., 8 - pyrolusite, 9 - pyrolusite (syn), 10 - ramsdellite, 11 - romanèchite, 12 - romanèchite (Ba-free, syn), 13 - todorokite, 14 - todorokite (syn).

Manganese oxides without layer or tunnel structure such as bixbyite (ferric Mn(III) oxide), hausmannite (Mn(II/III) spinel), and manganosite (Mn(II) oxide) show a greater variability in their XANES spectra, reflecting different Mn oxidation states and Mn coordination environments (Fig. 2.3). While natural and synthetic bixbyites show featureless absorption edges similar to phyllo- and tectomanganates (but distinct differences in their first-derivative spectra), hausmannite exhibits a prominent shoulder in the absorption edge at ~6,553 eV and a well-defined absorption maximum at 6,559.1 eV (Fig. 2.3, Table 2.2). Similarly, the XANES of manganosite possesses a modulated absorption edge, a well-defined absorption maximum at 6,555.0 eV, and a distinct post-edge oscillation at 6,568.6 eV (Fig. 2.3, Table 2.2). These results suggest that hausmannite and manganosite can be readily identified in soils and sediments based on XANES analysis.

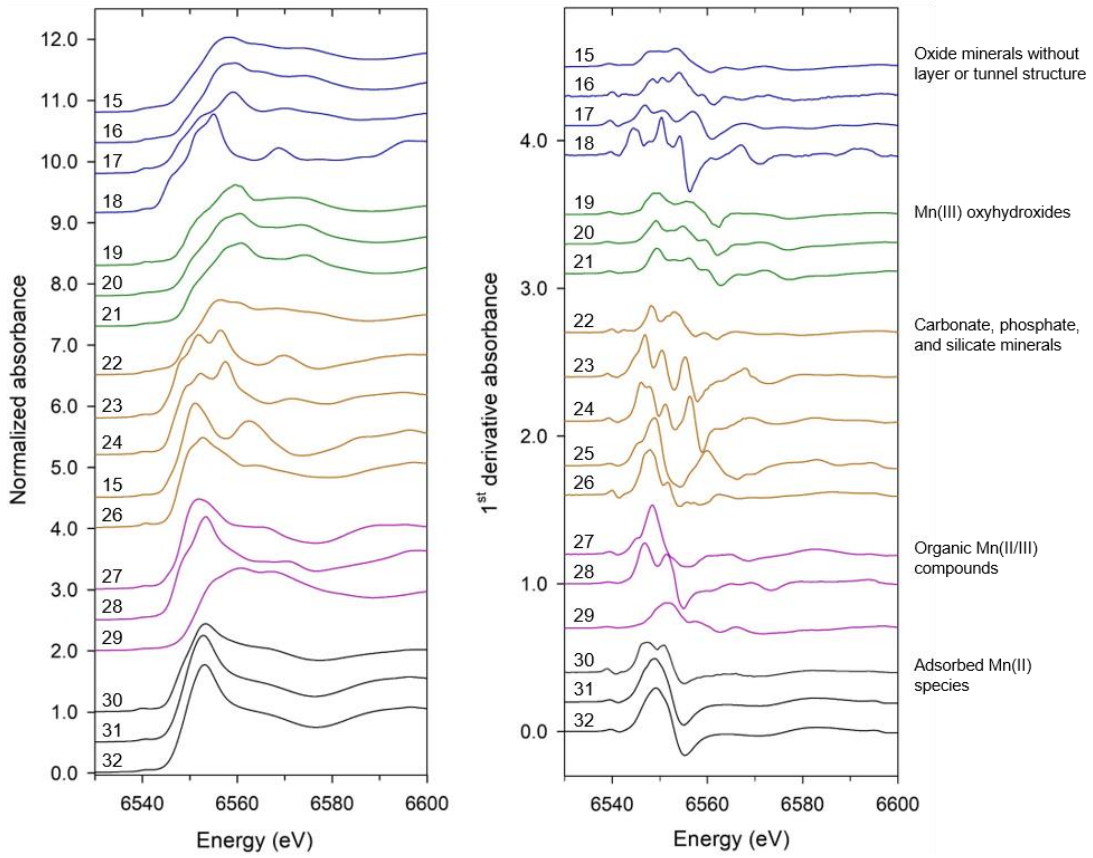

Figure 2.3. Stacked normalized Mn K-edge XANES (left) and corresponding first-derivative spectra (right) of Mn oxide minerals without layer or tunnel structure as well as Mn(III) oxyhydroxides, carbonate, phosphate, and silicate minerals, organic Mn(II/III) compounds, and adsorbed Mn(II) species. The spectrum numbers match the numbers in Table 2.1: 15 - bixbyite, 16 - bixbyite (syn), 17 - hausmannite, 18 - manganosite, 19 - feitknechtite (syn), 20 - groutite, 21 - manganite (syn), 22 - braunite, 23 - hendricksite, 24 - masutomilite, 25 - rhodochrosite, 26 - triplite, 27 - Mn(II) acetate tetrahydrate (syn), 28 - Mn(II) oxalate dihydrate (syn), 29 - Mn(III) acetate dihydrate (syn), 30 - Mn(II) ads. illite pH7, 31 - Mn(II) ads. peat pH5, 32 - Mn(II) ads. peat pH7.

The $Mn^{3+}O(OH)$ polymorphs feitknechtite, groutite, and manganite exhibit similar XANES features, consisting of smoothly rising absorption edges with two inflection points at ~6,549 and ~6,556 eV, and absorption maxima located at ~6,560 eV (Fig. 2.3, Table 2.2). Variations among these minerals are subtle, and suggest that groutite and manganite are virtually indistinguishable by XANES spectroscopy.

Carbonate, phosphate, and silicate minerals have unique XANES spectra which also differ from those of Mn (oxyhydr)oxide minerals. Unsurprisingly, this group displays the greatest diversity of XANES characteristics. Triplite, a Mn^{2+}-containing phosphate, shows a steep rise in the absorption edge with a non-unique absorption maximum of 6,552.7 eV. In contrast, rhodochrosite has a pronounced absorption-edge maximum at 6,551.1 eV and a distinct post-edge absorption maximum at 6,562.4 eV, leading to diagnostic first-derivative XANES maxima at 6,548.9 and 6,559.9 eV (Fig. 2.3, Table 2.2). The two Mn^{2+}-bearing trioctahedral micas hendricksite and masutomilite show similar spectral features

with double absorbance peaks at ~6,552 and ~6,557 eV, which are distinct from all other Mn compounds. The identification of 2:1 phyllosilicates with structural Mn(II) may thus be possible in unknown sample materials. Braunite, a Mn(II/III) nesosilicate, shows a marked step in the absorption edge and two pronounced peaks in the first-derivative XANES at 6,548.1 and 6,552.9 eV (Fig. 2.3, Table 2.2), comparable to feitknechtite.

The XANES of organic Mn compounds differ from each other: While Mn(II) acetate tetrahydrate has a smoothly rising absorption edge and a broad absorbance maximum similar to triplite, Mn(II) oxalate dihydrate shows a marked shoulder in the rising part of the edge, a sharp absorption maximum at 6,553.3 eV, and a characteristic double peak in the first-derivative XANES at 6,547.0 and 6,551.5 eV (Fig. 2.3, Table 2.2). In contrast, Mn(III) acetate dihydrate exhibits a broad, undulating absorption maximum, which is distinct from all other Mn references (Fig. 2.3).

Samples with adsorbed Mn(II) (illite, peat) are characterized by smoothly rising absorption edges, well-defined absorption maxima at ~6,553 eV, and a comparatively featureless post-edge absorption (Fig. 2.3, Table 2.2). In comparison to the peat samples, Mn(II) adsorbed to illite has a less prominent white-line and two discernible main peaks in the first-derivative XANES (Fig. 2.3). The XANES spectra of the peat samples are different from all other references, and resemble those of Mn(II) citrate, Mn(II) malate, and Mn(II) succinate (Fernando et al., 2010). This result suggests that Mn^{2+} complexed by natural organic matter should be uniquely identifiable in environmental samples. Noteworthy, peat samples prepared at pH 5 and 7 possess identical XANES spectra, implying that pH had no effect on the coordination environment of organically bound Mn(II) (Fig. 2.3).

Our results illustrate that Mn compounds differ in absorption-edge energies as related to Mn AOS, and that several Mn compounds and mineral classes show characteristic inflection points in their XANES spectra. Manganese K-edge XANES features are more pronounced in the respective first-derivative spectra. Since small post-edge normalization errors do not affect the shape of the derivatives (Manceau et al., 2012), they might be better suited for fingerprinting and LCF analysis than the respective absorbance spectrum. However, XANES LCF analyses of natural samples may become biased because XANES spectra of individual Mn compounds can differ substantially due to variations in chemical composition and/or crystallinity, as evidenced for bixbyites, cryptomelanes, pyrolusites and todorokites (Figs. 2.2 and 2.3).

Table 2.2. Primary XANES absorption and first-derivative peaks of Mn reference compounds

No.	Reference	Absorption		First derivative				
		1	2	1	2	3	4	5
Phyllomanganates								
1	Acid Na-birnessite (hex, syn)	6562.5		6540.5		6553.5	6558.0	6560.0
2	δ-MnO_2 (syn)	6561.8		6539.8		6552.5	6556.5	
3	Lithiophorite	6560.4		6539.5	6541.7	6551.5	6557.5	
4	Na-birnessite (tricl, syn)	6560.9		6539.7		6549.2	6553.6	6558.2
Tectomanganates								
5	Cryptomelane	6562.0		6540.8		6556.8		
6	Cryptomelane (syn)	6562.0		6540.6		6557.6		
7	Hollandite *s.s*	6561.2		6540.0	6542.0	6551.5	6556.0	
8	Pyrolusite	6561.0		6541.0		6552.3	6558.2	
9	Pyrolusite (syn)	6560.3		6540.6	6542.2	6552.7	6558.5	
10	Ramsdellite	6560.9		6540.6	6542.4	6552.2	6558.3	
11	Romanèchite	6561.7		6539.8	6541.7	6551.5	6556.5	
12	Romanèchite (Ba-free, syn)	6561.4		6539.8		6550.7	6557.3	
13	Todorokite	6562.1		6540.6		6551.1	6557.8	
14	Todorokite (syn)	6560.4		6538.9		6549.0	6556.2	
Oxide minerals without layer or tunnel structure								
15	Bixbyite	6558.2		6539.4		6547.9	6549.9	6553.4
16	Bixbyite (syn)	6559.5		6539.8		6548.4	6550.7	6553.8
17	Hausmannite	6559.1		6539.8		6546.8	6550.8	6556.8
18	Manganosite (syn)	6555.0	6568.6	6539.8		6544.5	6550.2	6554.0
Mn(III) oxyhydroxides								
19	Feitknechtite (syn)	6559.7		6539.5		6549.2	6555.5	
20	Groutite	6560.4		6539.0		6549.1	6555.1	
21	Manganite (syn)	6560.7		6539.4		6549.3	6556.1	
Carbonate, phosphate, and silicate minerals								
22	Braunite	6556.4		6540.0		6548.1	6553.0	
23	Hendricksite	6551.9	6556.4	6539.0		6546.9	6550.3	6555.3
24	Masutomilite	6552.3	6557.5	6539.3		6546.1	6551.1	6556.3
25	Triplite	6552.7		6540.1		6547.4	6548.1	
26	Rhodochrosite	6551.1	6562.4	6539.4		6548.9	6559.9	
Organic Mn(II/III) compounds								
27	Mn(II) acetate tetrahydrate (syn)	6551.9		6539.4		6548.4	6564.7	
28	Mn(II) oxalate dihydrate (syn)	6553.3		6539.0		6547.0	6551.5	
29	Mn(III) acetate dihydrate (syn)	6560.8		6539.0		6552.0	6557.5	
Adsorbed Mn(II) species								
30	Mn(II) ads. illite pH7	6552.2		6539.1		6547.4	6551.0	
31	Mn(II) ads. peat pH7	6552.8		6539.8		6549.3		
32	Mn(II) ads. peat pH5	6553.1		6539.5		6549.0		

2.3.2. Average oxidation state of Mn reference compounds

To obtain information on the Mn AOS and relative fractions of Mn^{2+}, Mn^{3+}, and Mn^{4+} in the reference compounds, we used the XANES LCF 'Combo' method (Manceau et al., 2012). The results are tabulated in Table 2.3. Note, different from other LCF procedures, the 'Combo' method does not claim the samples to be mixtures of the standards (Manceau et al., 2012; Manceau and Nagy, 2012). Therefore, no uncertainties are assigned to individual fractions or the derived AOS. Manceau et al. (2012) estimated the accuracy of AOS determination by the 'Combo' method to be ~0.04 v.u. in phyllo- and tectomanganates (AOS range 3.0-4.0) with a negligible amount of Mn^{3+} in layer structures and less than about 15% Mn^{2+}. Based on our fit results for the synthetic monovalent Mn references manganosite (AOS 2.0), bixbyite (AOS 3.0), and pyrolusite (AOS 4.0), the absolute accuracy of Mn AOS determination using the 'Combo' method was not better than 0.12 v.u. Regression of nominal vs. LCF-derived AOS for these references resulted in a standard error of the AOS estimate of 0.07 v.u. (R^2 = 0.995, p <0.001). This result is consistent with Manceau et al. (2012) showing that increasing proportions of Mn^{2+} lead to a decreased accuracy of the LCF 'Combo' method.

Manganese reference compounds with a nominal Mn AOS of two (N = 10) yielded XANES-derived AOS of 2.0-2.49 ($\bar{x}$ = 2.13). In this group, higher AOS determined for hendricksite (2.21), masutomilite (2.49), and Mn(II) adsorbed to illite (2.35) suggest the presence of up to 50% Mn^{3+}. For the mica minerals, this result can be explained by partial oxidation of Mn(II) in their octahedral layers. For the illite sample, the result may indicate the formation of a Mn(III/IV) phase upon partial re-oxidation of adsorbed Mn^{2+}, but this could not be confirmed by EXAFS shell-fit results (see below). LCF results of reference compounds with a nominal AOS of three (N = 6) and four (N = 4), were largely in agreement with their nominal AOS ($\bar{x}$ = 3.07 and 3.96, respectively; Table 2.3).

In order to validate XANES-based Mn AOS, we performed redox titrations for selected reference compounds with Mn concentrations >1.5 wt.% (N = 25). These experiments showed that the AOS of hausmannite was significantly overestimated by the 'Combo' method, most likely because its pronounced Jahn-Teller distortion of $Mn^{3+}O_6$ octahedra (Jarosch, 1987) was not adequately reflected by the standard spectra used (Manceau et al., 2012). An unreasonable titration-based Mn AOS was also observed for triplite (Table 2.3), which can be attributed to incomplete reductive dissolution of the sample during the experiment.

Table 2.3. Nominal, titration-, and XANES-derived bulk Mn AOS of Mn reference compounds, as well as fractional amounts of Mn^{2+}, Mn^{3+}, and Mn^{4+} (normalized to unity) determined from XANES analysis

No.	Reference	AOS[a] (nominal)	AOS[b] (titration)	AOS (XANES)	Mn^{2+}	Mn^{3+}	Mn^{4+}	Fit sum	*R*-factor[c] ($\times 10^5$)
Phyllomanganates									
1	Acid Na-birnessite (hex, syn)	3.92	3.94(0)	3.86	0.04	0.05	0.91	0.99	5
2	δ-MnO_2 (syn)	4.00	3.98(2)	3.90	0.01	0.08	0.91	0.99	11
3	Lithiophorite	3.70	n.d.	3.49	0.02	0.47	0.51	0.97	36
4	Na-birnessite (tricl, syn)	3.57	3.69(1)	3.84	0.03	0.10	0.87	0.97	22
Tectomanganates									
5	Cryptomelane	3.88	3.85(1)	3.84	0.04	0.08	0.88	0.99	9
6	Cryptomelane (syn)	3.88	3.88(2)	3.95	0.00	0.05	0.95	1.02	18
7	Hollandite *s.s.*	3.75	n.d.	3.75	0.08	0.09	0.83	0.96	42
8	Pyrolusite	4.00	4.03(2)	3.98	0.01	0.00	0.99	0.98	31
9	Pyrolusite (syn)	4.00	4.03(0)	4.00	0.00	0.00	1.00	1.00	21
10	Ramsdellite	4.00	4.02(1)	3.98	0.01	0.00	0.99	1.00	9
11	Romanèchite	3.50	n.d.	3.82	0.02	0.14	0.84	0.98	10
12	Romanèchite (Ba-free, syn)	3.84	3.76(1)	3.91	0.03	0.03	0.94	1.04	8
13	Todorokite	3.67	3.77(2)	3.77	0.01	0.21	0.78	1.02	6
14	Todorokite (syn)	3.67	3.70(2)	3.74	0.04	0.17	0.79	0.99	9
Oxide minerals without layer or tunnel structure									
15	Bixbyite	3.00	3.11(3)	3.08	0.16	0.61	0.24	1.00	17
16	Bixbyite (syn)	3.00	3.05	3.07	0.08	0.78	0.15	1.02	10
17	Hausmannite	2.67	2.72(1)	3.35	0.19	0.27	0.54	0.93	32
18	Manganosite (syn)	2.00	2.04(0)	2.12	0.94	0.00	0.06	1.00	118
Mn(III) oxyhydroxides									
19	Feitknechtite (syn)	3.00	n.d.	3.02	0.02	0.93	0.04	0.97	58
20	Groutite	3.00	3.05(1)	3.17	0.03	0.78	0.20	0.99	14
21	Manganite (syn)	3.00	3.07(3)	3.01	0.02	0.96	0.03	1.02	16
Carbonate, phosphate, and silicate minerals									
22	Braunite	2.86	2.98(4)	2.99	0.10	0.80	0.10	0.98	57
23	Hendricksite	2.00	2.32(11)	2.21	0.79	0.21	0.00	0.96	655
24	Masutomilite	2.00	2.41(13)	2.49	0.51	0.49	0.00	0.98	1130
25	Rhodochrosite	2.00	2.06(1)	2.08	0.96	0.00	0.04	0.99	38
26	Triplite	2.00	1.39(5)	2.01	0.99	0.01	0.00	0.99	62
Organic Mn(II/III) compounds									
27	Mn(II) acetate tetrahydrate (syn)	2.00	n.d.	2.00	1.00	0.00	0.00	0.96	45
28	Mn(II) oxalate dihydrate (syn)	2.00	2.04(1)	2.05	0.95	0.05	0.00	1.01	133
29	Mn(III) acetate dihydrate (syn)	3.00	3.00(0)	3.06	0.00	0.94	0.06	1.02	202
Adsorbed Mn(II) species									
30	Mn(II) ads. illite pH7	2.00	2.48	2.35	0.69	0.26	0.05	1.01	11
31	Mn(II) ads. peat pH5	2.00	n.d.	2.00	1.00	0.00	0.00	1.01	218
32	Mn(II) ads. peat pH7	2.00	n.d.	2.00	1.00	0.00	0.00	1.02	280

[a]Based on nominal mineral formulas (*cf.* Table 2.1).

[b]Errors are given as standard deviation of triplicate measurements for the last significant figure. n.d. = not determined. Figures without error assignment are based on single measurements due to limited sample availability.

[c]*R*-factor = $\Sigma_i(data_i - fit_i)^2/\Sigma_i data_i$.

With the exception of these two references, the Mn AOS derived from redox titrations were in excellent agreement with the XANES-based AOS (R^2 = 0.988) (Fig. 2.4). The regression slope was 0.997±0.024 (p <0.0001) and the standard error of estimate 0.08. This result implies that the 'Combo' LCF method, when applied to environmental samples, provides accurate Mn AOS data within approximately 0.1 v.u. for the entire Mn valence range +2 to +4.

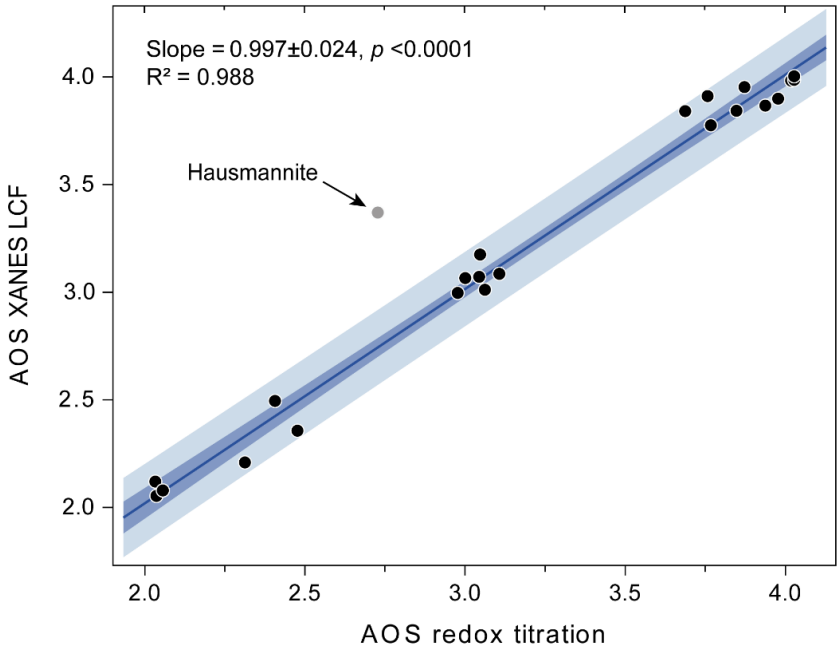

Figure 2.4. Linear regression (solid line) between average oxidation state (AOS) of Mn obtained from redox titrations against Mn AOS determined by XANES LCF. Confidence and prediction bands (95%) are indicated by dark and light blue color, respectively. Data for hausmannite and triplite (out of range) were excluded from analysis.

2.3.3. EXAFS SPECTRA OF MN REFERENCES COMPOUNDS

Figure 2.5 shows k^3-weighted Mn K-edge EXAFS spectra and Fourier-transform (FT) magnitudes and real parts of one representative of each Mn species group along with the corresponding model fit. The figure exemplifies the diversity of local Mn bonding environments, which can be expected in natural samples. Corresponding data of the remaining references are shown in Figures A.3 and A.4. EXAFS shell-fit parameters of all compounds are summarized in Table 2.4. In the following, we detail EXAFS results for each species group, and clarify (dis)similarities of EXAFS parameters among species (groups).

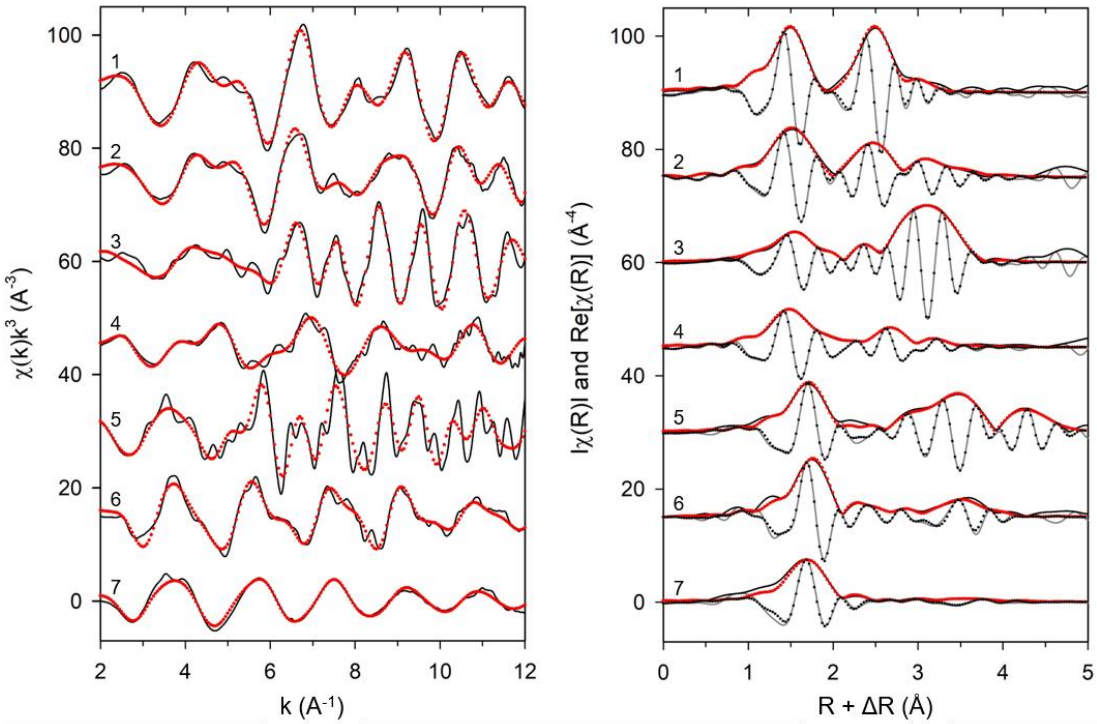

Figure 2.5. Stacked k^3-weighted Mn K-edge EXAFS spectra (left) as well as corresponding Fourier-transform magnitudes and real parts (right) of selected Mn reference compounds: 1 - δ-MnO_2 (syn), 2 - hollandite *s.s.*, 3 - hausmannite, 4 - feitknechtite, 5 - rhodochrosite, 6 - Mn(II) oxalate dihydrate, 7 - Mn(II) ads. peat pH5. Solid lines represent experimental data and dotted lines model fits. EXAFS parameters are summarized in Table 2.4. The fits of other Mn compounds are displayed in Figures A.3 and A.4.

Table 2.4. EXAFS parameter determined by shell-fitting of k^3-weighted Mn K-edge EXAFS spectra of Mn reference compounds[a]

No.	Reference	*R*-factor[b]	χ_v^{2b}	N_{idp}[c] k-range	N_{var}[c] R-range	ΔE_0 (eV)[d]	*CN*[e] σ^2 (Å²)[f]	*R* (Å)[g]	*CN* σ^2 (Å²)	*R* (Å)	*CN* σ^2 (Å²)	*R* (Å)	*CN* σ^2 (Å²)	*R* (Å)	*CN* σ^2 (Å²)	*R* (Å)
Phyllomanganates																
1	Acid Na-birnessite (hex, syn)	0.005	856	14.4 2.8-13.2	6 1.0-3.2	2.2(6)	O: 6.2(6) 0.0049(3)	1.90(0)	Mn: 5.3(4) 0.0046(1)	2.89(0)	Mn: 1.2(4) 0.0046	3.49(1)				
2	δ-MnO_2 (syn)	0.007	793	16.1 2.9-13.1	6 1.0-3.5	3.0(7)	O: 5.6(6) 0.0042(3)	1.90(0)	Mn: 4.7(3) 0.0044(2)	2.87(0)	Mn: 1.0 0.0044	3.44(2)				
3	Lithiophorite	0.009	74	14.7 3.5-11.3	8 1.0-4.0	-0.8(11)	O: 4.1(5) 0.0022(3)	1.92(1)	Mn: 6.0 0.0067(3)	2.92(1)	O: 4.0 0.0082(38)	3.56(3)	Mn: 4.0 0.0082	4.14(12)		
4	Na-birnessite (tricl, syn)	0.006	781	12.7 2.6-11.8	5 1.0-3.2	6.1(8)	O: 5.3(5) 0.0030(3)	1.92(0)	Mn: 6.8(8) 0.0066(3)	2.89(0)						
Tectomanganates																
5	Cryptomelane	0.008	769	16.2 2.7-13.0	6 1.0-3.5	0.8(7)	O: 5.0(4) 0.0025(3)	1.90(0)	Mn: 3.7(3) 0.0032(2)	2.88(0)	Mn: 4.0(4) 0.0032	3.44(0)				
6	Cryptomelane (syn)	0.016	351	17.8 2.7-13.0	6 1.0-3.5	1.4(10)	O: 5.8(7) 0.0024(7)	1.91(0)	Mn: 3.7(4) 0.0026(4)	2.89(1)	Mn: 4.2(6) 0.0026	3.45(1)				
7	Hollandite	0.006	142	13.6 3.5-11.3	7 1.0-3.8	-0.7(9)	O: 4.3(5) 0.0032(3)	1.91(0)	Mn: 3.6(4) 0.0062(4)	2.91(1)	Mn: 3.5(5) 0.0062	3.48(1)	Mn: 1.9(5) 0.0062	3.75(1)		
8	Pyrolusite	0.013	290	18.28 2.6-12.3	9 1.0-4.0	-5.5(9)	O: 5.6(8) 0.0028(4)	1.88(1)	Mn: 2.1(4) 0.0018(2)	2.87(1)	Mn: 5.6(6) 0.0018	3.43(1)	O: 8.0 0.0102(35)	4.01(5)	Mn: 4.0 0.0102	4.42(4)
9	Pyrolusite (syn)	0.013	53	23.0 2.7- 4.2	9 1.0-4.2	-5.3(7)	O: 5.6(6) 0.0023(3)	1.88(0)	Mn: 1.9(2) 0.0020(2)	2.88(1)	Mn: 7.1(6) 0.0020	3.43(0)	O: 8.0 0.0030(8)	3.93(2)	Mn: 4.0 0.0030	4.41(1)
10	Ramsdellite	0.006	70	69.3 2.7-13.8	7 1.0-3.6	-6.2(6)	O: 5.6(4) 0.0026(2)	1.89(0)	Mn: 3.2(4) 0.0026(2)	2.88(0)	Mn: 3.8(5) 0.0010(2)	3.43(0)				
11	Romanèchite	0.005	309	10.2 2.8-10.2	6 1.0-3.2	-2.9(10)	O: 4.7(9) 0.0025(4)	1.90(1)	Mn: 4.6(18) 0.0077(6)	2.90(1)	Mn: 2.8(13) 0.0077	3.47(2)				
12	Romanèchite (Ba-free, syn)	0.013	1548	14.5 2.9-11.8	6 1.0-3.6	-2.5(10)	O: 5.7(8) 0.0035(4)	1.90(1)	Mn: 4.4(8) 0.0044(4)	2.88(1)	Mn: 2.4(7) 0.0044	3.44(1)				
13	Todorokite	0.011	1593	18.5 2.6-13.9	9 1.0-3.6	0.4(8)	O: 5.3(5) 0.0032(3)	1.92(0)	Mn: 4.2(7) 0.0049(3)	2.87(0)	Mn: 2.7 0.0027(10)	3.43(1)	O: 6.0 0.0024(21)	3.71(3)		
14	Todorokite (syn)	0.011	834	18.3 2.7-13.9	9 1.0-3.6	-2.1(9)	O: 4.7(4) 0.0033(3)	1.92(0)	Mn: 3.8(8) 0.0055(4)	2.88(1)	Mn: 2.7 0.0069(19)	3.44(2)	O: 6.0 0.0072(43)	3.72(7)		
Oxide minerals without layer or tunnel structure																
15	Bixbyite[h]	0.011	667	14.2 2.6-11.0	5 1.0 - 3.7	-4.3(12)	O1: 4.0(5) 0.0070(6) O2: 1.7(4) 0.0070	1.92(1) 2.24(1)	Mn: 5.2(10) 0.0053(3)	3.11(1)	Mn: 6.0 0.0118(13)	3.57(1)				
16	Bixbyite (syn)[h]	0.020	204	15.9 2.7-12.1	5 1.0-3.7	-6.8(13)	O1: 4.0(6) 0.0059(7) O2: 1.3(6) 0.0076	1.90(1) 2.23(1)	Mn: 5.1(12) 0.0057(4)	3.09(1)	Mn: 6.0 0.0086(9)	3.54(1)				

Table 2.4. ***(continued)***

No.	Reference	*R* -factor[b]	χ_v^{2b}	N_{idp}[c] k-range	N_{var}[c] R-range	ΔE_0 (eV)[d]	*CN* [e] σ^2 (Å²)[f]	*R* (Å)[g]	*CN* σ^2 (Å²)	*R* (Å)	*CN* σ^2 (Å²)	*R* (Å)	*CN* σ^2 (Å²)	*R* (Å)	*CN* σ^2 (Å²)	*R* (Å)
Oxide minerals without layer or tunnel structure																
17	Hausmannite	0.002	66	16.8 2.9-11.8	10 1.0-4.0	0.4(11)	O1: 4.1(3) 0.0071(3) O2: 1.9(3) 0.0071	1.95(1) 2.27(1)	Mn1: 1.3(1) 0.0028(5) Mn2: 2.7(2) 0.0028	2.88(1) 3.10(0)	Mn: 8.1(8) 0.0082	3.44(1)	Mn: 7.7(7) 0.0082(3)	3.73(1)		
Oxide minerals without layer or tunnel structure																
18	Manganosite (syn)[h]	0.010	29	21.8 2.3-13.6	5 1.0-3.6	-2.8(6)	O: 5.8(10) 0.0063(9)	2.22(0)	Mn: 12.0 0.0048(2)	3.13(0)	O: 8.0 0.0164(92)	3.84(0)				
Mn(III) oxyhydroxides																
19	Feitknechtite (syn)	0.002	8	14.2 2.7-11.1	10 1.0-3.7	0.3(7)	O1: 4.0(2) 0.0052(1) O2: 2.0(2) 0.0052	1.91(0) 2.22(1)	Mn1: 1.9(3) 0.0074(4) Mn2: 3.8(11) 0.0074	2.83(1) 2.99(0)	Mn: 4.0 0.0141(1)	3.33(1)	O: 8.0 0.0141	3.60(2)		
20	Groutite	0.008	113	19.1 2.8-13.7	12 1.0-3.8	3.6(11)	O1: 4.2(4) 0.0040(4) O2: 0.9(4) 0.0040 O3: 1.4(3) 0.0040	1.93(1) 2.15(4) 2.34(2)	Mn: 2.1(4) 0.0028(3)	2.88(1)	Mn: 2.0 0.0115(36)	3.38(3)	Mn: 4.0 0.0035(7) O: 8.0 0.0035	3.61(1) 3.77(2)		
21	Manganite (syn)	0.005	214	16.2 2.8-12.4	11 1.1-3.8	1.7(9)	O1: 4.7(4) 0.0062(3) O2: 2.0(3) 0.0062	1.93(0) 2.28(1)	Mn1: 1.0(1) 0.0021(6) Mn2: 1.0(1) 0.0021	2.77(1) 2.98(2)	O: 8.4(18) 0.0062 Mn: 4.0 0.0075(18)	3.61(2) 3.69(1)	Mn: 4.0 0.0075(14)	3.83(2)		
Carbonate, phosphate, and silicate minerals																
22	Braunite	0.011	26	14.9 2.9-11.4	8 1.0-3.8	5.4(10)	O1: 2.6(2) 0.0045(5) O2: 2.1(3) 0.0045 O3: 0.9(3) 0.0045	1.94(1) 2.25(1) 2.55(3)	Mn: 1.9(5) 0.0038(5)	3.17(1)	O2: 5.3(18) 0.0063	3.77(2)				
23	Hendricksite	0.017	22	12.1 2.6-11.4	5 1.1-3.3	3.9(13)	4.9(9) 0.0042(8)	2.16(1)	Mn/Fe: 2.0 0.0037(4) Zn: 2.5 0.0037	3.14(1) 3.14						
24	Masutomilite	0.022	52	12.1 2.1-10.5	6 1.0-3.3	4.2(15)	O/F: 4.9(7) 0.0027(1)	2.15(1)	Al: 2.5 0.0100 Mn: 0.4 0.0100	3.02(5) 3.02	Al/Si: 4.0 0.0100	3.24(3)	O: 4.0 0.0100	3.47(3)		

Table 2.4. ***(continued)***

No.	Reference	*R*-factor[b]	χ_v^{2b}	N_{idp}[c] k-range	N_{var}[c] R-range	ΔE_0 (eV)[d]	*CN*[e] σ^2 (Å^2)[f]	*R* (Å)[g]	*CN* σ^2 (Å^2)	*R* (Å)	*CN* σ^2 (Å^2)	*R* (Å)	*CN* σ^2 (Å^2)	*R* (Å)	*CN* σ^2 (Å^2)	*R* (Å)
Carbonate, phosphate, and silicate minerals																
25	Rhodochrosite	0.012	42	21.7 2.2-11.5	12 1.1-4.8	2.7(9)	O: 6.3(8) 0.0050(5)	2.19(1)	C: 6.0 0.0034	3.08(2)	O: 6.0 0.0033(14)	3.28(1)	Mn: 6.0 0.0048	3.79(1)	O1: 6.0 0.0048(4) O2: 4.0 0.0048 Mn: 6.0 0.0032(1)	4.10(3) 4.58(1) 4.75(1)
26	Triplite	0.008	91	12.4 2.3-10.6	7 1.0-3.4	3.6(8)	F: 1.6 0.0067 O: 4.4 0.0067(1)	2.05(3) 2.15(1)	Mn/Fe: 1.0(4) 0.0073(13)	2.93(2)	P: 2.8(7) 0.0073	3.55(1)				
Organic Mn(II/III) compounds																
27	Mn(II) acetate tetrahydrate (syn)	0.015	175	13.2 2.3-11.1	6.0 1.0-3.4	2.1(10)	O:5.9(7) 0.0045(0)	2.18(1)	C: 5.2 0.0112(62)	3.19(4)	Mn: 1.6 0.0060(20)	3.40(2)				
28	Mn(II) oxalate dihydrate (syn)	0.029	476	19.0 2.8-12.3	8.0 1.0-4.2	6.9(9)	O: 6.5(6) 0.0041(4)	2.18(1)	C: 4.0 0.0041	2.95(2)	O-C[i]: 8.0 0.0062	3.11(12)	O: 6.0 0.0040	3.93(2)	C-O-C[i]: 4.0 0.0083 C-O[i]: 8.0 0.0062	4.08(4) 4.23(2)
29	Mn(III) acetate dihydrate (syn)	0.013	703	24.2 2.7-13.7	9 0.9-4.4	5.7(8)	O1: 5.2(5) 0.0041(0) O2: 1.5(5) 0.0041	1.93(0) 2.20(1)	C: 4.0 0.0077(24)	2.98(2)	Mn: 2.0 0.0014(3)	3.40(0)	O: 2.0 0.0068(40)	4.37(5)		
Adsorbed Mn(II) species																
30	Mn(II) ads. illite pH7	0.005	5	9.9 2.5-10.5	5 1.0-3.0	-2.4(9)	O1: 2.0 0.0123(18) O2: 4.0 0.0123	1.92(1) 2.16(1)								
31	Mn(II) ads. peat pH5	0.016	540	14.4 2.0-10.5	5 1.3-4.0	3.3(9)	O: 6.0 0.0057(0)	2.18(1)	C: 1.0 0.0057	3.20(7)	C-O[i]: 8.0 0.0086	4.48(5)				
32	Mn(II) ads. peat pH7	0.017	266	14.4 2.0-10.5	5 1.3-4.0	3.4(10)	O: 6.0 0.0051(5)	2.18(1)	C: 1.0 0.0051	3.21(8)	C-O[i]: 8.0 0.0077	4.49(5)				

[a]The amplitude reduction factor, S_0, was set to 0.8 for all fits. Parameter uncertainties are given in parenthesis for the last significant figure.

[b]*R*-factor = $\Sigma_i(\text{data}_i-\text{fit}_i)^2/\Sigma_i\text{data}_i$ and reduced $\chi^2 = (N_{idp}/N_{pts})\Sigma_i((\text{data}_i-\text{fit}_i)/\varepsilon_i)^2/(N_{idp}-N_{var})$, where N_{idp} is the number of independent data points in the model fit, N_{pts} the total number of data points, N_{var} the number of fit variables (with all *CN*s set in the final fit), and ε_i is the uncertainty of the ith data point.

[c]Number of independent points and fit variables in final fit, respectively.

[d]Energy-shift parameter.

[e]Coordination number (path degeneracy). Coordination numbers with assigned errors were fit individually and subsequently set in the final fit.

[f]Debye-Waller parameter. If no uncertainties are indicated, parameters were constrained.

[g]Mean half path length.

[h]A volumetric lattice expansion parameter was used to calculate atomic distances in bixbyites and manganosite (cubic crystal system).

[i]Multiple-scattering (MS) path. For Mn(II) oxalate dihydrate, the Debye-Waller parameter of the Mn-O-C obtuse triangle MS path was defined as σ^2(Mn-O1)+0.5σ^2(Mn-C); MS2 (Mn-C-O-C) and MS3 (Mn-C-O) are forward triangle MS paths. Their Debye-Waller parameters were defined as
σ^2(Mn-C)+σ^2(Mn-O1) and σ^2(Mn-C)+0.5σ^2(Mn-O1), respectively. For Mn(II) adsorbed to peat, the Debye-Waller parameter of the obtuse triangle MS path was defined as 1.5σ^2(Mn-O).

2.3.3.1. PHYLLO- AND TECTOMANGANATES

Figure 2.6 illustrates k^3-weighted Mn K-edge EXAFS spectra of phyllo- and tectomanganates. Phyllomanganates with hexagonal layer symmetry (acid Na-birnessite, δ-MnO_2, lithiophorite) show very similar EXAFS spectra featuring comparatively symmetrical oscillations centered at approximately 4.2, 6.7, 9.2, and 10.4 $Å^{-1}$. In contrast, the spectrum of triclinic birnessite exhibits a split of the small oscillation between 7.9 and 8.2 $Å^{-1}$. This antinode splitting is attributed to the ordering of structural Mn^{3+} in triclinic birnessite (Webb et al., 2005; Ling et al., 2018) and allows the distinction of phyllomanganates with hexagonal and triclinic layer symmetry. The peak near 8.0 $Å^{-1}$ was previously used as a diagnostic fingerprint to differentiate between phyllo- and tectomanganates (McKeown and Post, 2001). In this study, however, also 2×3 and 3×3 tectomanganates exhibit a similar spectral feature in this region (Fig. 2.6).

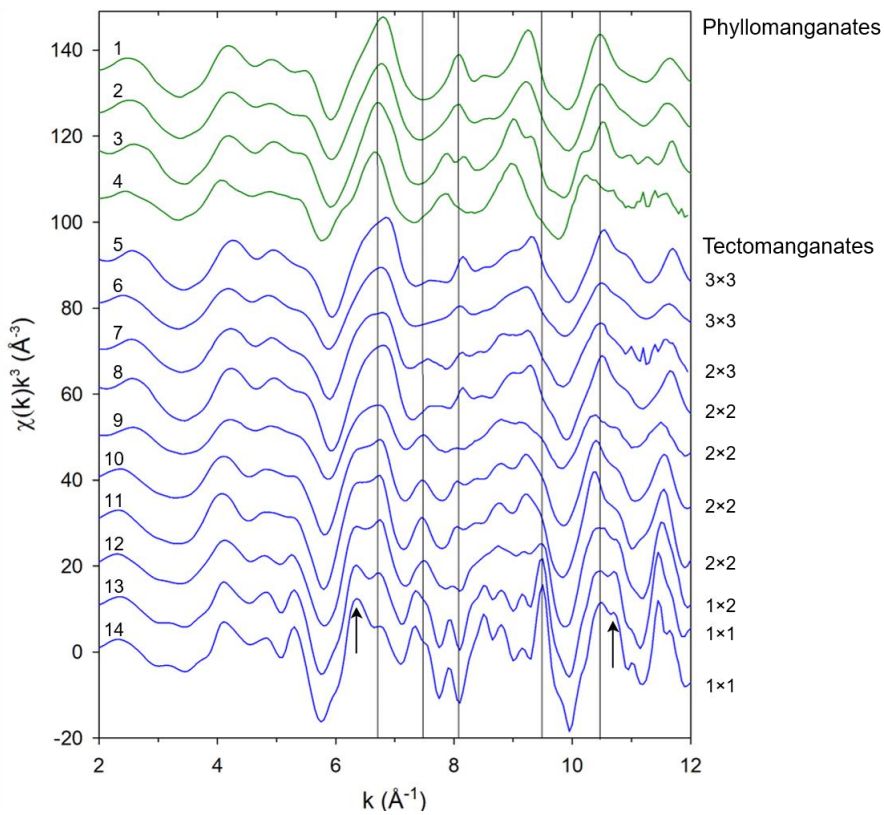

Figure 2.6. Stacked k^3-weighted Mn K-edge EXAFS spectra of phyllo- and tectomanganates. 1 - acid Na-birnessite (hex, syn), 2 - δ-MnO_2 (syn), 3 - Na-birnessite (tricl, syn), 4 - lithiophorite, 5 - todorokite, 6 - todorokite (syn), 7 - romanèchite (nat), 8 - romanèchite (Ba-free, syn), 9 - hollandite *s.s.*, 10 - cryptomelane (nat), 11 - cryptomelane (syn), 12 - ramsdellite, 13 - pyrolusite (nat), 14 - pyrolusite (syn). Vertical lines and black arrows indicate important spectral features (see text for details).

Tectomanganates can be generally discerned from phyllomanganates by a gradually emerging left-side shoulder of the 6.7-$Å^{-1}$ oscillation. This shoulder becomes more intense with increasing

content of corner-sharing octahedra (i.e., smaller tunnel size) and eventually results in a split oscillation at 6.4 and 6.7 $Å^{-1}$. The relative intensities of this double-feature are reversed for pyrolusite (1×1 tunnel) as compared to other tectomanganates (Manceau and Combes, 1988) (Fig. 2.6). Tectomanganates with 2×2 (hollandite *s.s.*, cryptomelane), 1×2 (ramsdellite), and 1×1 (pyrolusite) tunnel structure also possess a pronounced and diagnostic oscillation at ~7.4 $Å^{-1}$, which increases and shifts to lower wavenumbers with decreasing tunnel size (Fig. 2.6). Pyrolusites show two distinct troughs at 7.8 and 8.1 $Å^{-1}$, which are also visible in attenuated form for ramsdellite, and thus can serve as another diagnostic fingerprint for tectomanganates with small tunnel sizes. In combination with the pronounced peak near 7.4 $Å^{-1}$ and the unique oscillation at 9.5 $Å^{-1}$, these results suggest that pyrolusite should be unambiguously identifiable in mixtures of phyllo- and tectomanganates.

All manganates are additionally characterized by an oscillation at 10.2-10.5 $Å^{-1}$ (Fig. 2.6). Because this oscillation is not accompanied by a pronounced right-side shoulder in case of phyllomanganates with hexagonal layer structure (Fig. 2.6), it can aid the identification of tectomanganates, especially those with 1×1, 1×2, and 2×2 tunnel structures, in mixtures with hexagonal phyllomanganates.

First O neighbors of Mn in phyllomanganates could be modelled with a single shell at 1.90-1.92 Å (Figs. 2.5 and A.3a). Mn-Mn distances of edge-sharing octahedra (Mn-Mn1) were fit at 2.87-2.92 Å, which accord with values published for hexagonal and pseudo-orthogonal phyllomanganate structures (Webb et al., 2005). For hexagonal birnessite and δ-MnO_2, we obtained Mn-Mn2 distances of 3.44-3.49 Å (Table 2.4). These distances are typically assigned to triple corner-sharing Mn3+ octahedra at interlayer sites above or below cation vacancies (Silvester et al., 1997; Villalobos et al., 2003; Ling et al., 2018). Similar to triclinic birnessite, no Mn-Mn2 contribution was observed for lithiophorite, in agreement with the presence of exclusively edge-sharing octahedra (Silvester et al., 1997; Lanson et al., 2000; McKeown and Post, 2001; Villalobos et al., 2003). Two additional O shells were fit at 3.56(3) and 4.14(12) Å, which accord with the lithiophorite structure published by Wadsley (1952) (Table 2.4).

Tectomanganates (Figs. 2.5 and A.3b) show similar variations in their Mn-O, Mn-Mn1, and Mn-Mn2 distances as compared to phyllomanganates (Table 2.4). Within this group, first-shell O neighbors are located at 1.88-1.92 Å, and second- and third-shell Mn neighbors at 2.87-2.90 and 3.43-3.48 Å, respectively. Shell-fit models also included additional O shells at 3.7-3.8 Å (todorokites) and 3.9-4.0 Å (pyrolusites) as well as higher Mn shells at 3.7-3.8 Å (hollandite *s.s.*) and 4.4 Å (pyrolusites) (Miura, 1986; Bolzan et al., 1993; Post et al., 2003) (Table 2.4). It generally follows that Mn coordination environments in phyllo- and tectomanganates are largely similar, such that interatomic distances up to the third coordination shell preclude any meaningful discrimination of these minerals in environmental samples using EXAFS shell-fit analysis.

2.3.3.2. Oxide minerals without layer or tunnel structure

Bixbyite possesses two inequivalent Mn sites with an occupancy of 25 and 75% in its unit cell (Geshnizgani, 2014). As a result, two O subshells at ~1.91 and ~2.24 Å were needed to account for the generally low first-shell amplitudes of natural and synthetic bixbyite (Fig. A.3c). The cubic structure of bixbyite is further characterized by edge- and corner-sharing Mn^{3+} octahedra, for which we obtained Mn-Mn distances of 3.09-3.11 and 3.54-3.57 Å, respectively (Table 2.4). These distances are consistent with those published by Longo et al. (2010).

The unit cell of hausmannite also contains two inequivalent Mn sites (Jarosch, 1987). Here, tetrahedral sites are occupied by Mn^{2+} and octahedral sites by Mn^{3+} cations. For octahedrally coordinated Mn^{3+}, Mn-O distances were fit with 4.1(3) equatorial O atoms at 1.95(1) Å and 1.9(3) axial O atoms at 2.27(1) Å, which account for the octahedral Jahn-Teller distortion approximately parallel to [001] (Jarosch, 1987). A third O shell (~2.01 Å) for tetrahedrally coordinated Mn^{2+} (Longo et al., 2010) was too close to the Mn-O_{eq} distance to be included in the model and did not improve the fit (F-test; Hamilton, 1965). First-shell oxygens are followed by two Mn subshells at 2.88(1) and 3.10(0) Å, corresponding to edge-sharing Mn^{3+} octahedra (Longo et al., 2010). The third FT peak of hausmannite (Figs. 2.5 and A.3c) was reproduced with Mn shells at 3.44(1) and 3.73(1) Å (Table 2.4). These values are consistent with tetrahedra-octahedra corner linkages (Longo et al., 2010) and Mn-Mn distances of Mn^{2+} tetrahedra, respectively (Jarosch, 1987).

In contrast to the former two minerals, the first FT peak of cubic manganosite could be modeled with a single O shell at 2.22(0) Å (Fig. A.3c). Analogous to Ressler et al. (1999), higher coordination shells were fit with Mn neighbors at 3.13(0) Å, indicative of edge-sharing Mn^{2+} octahedra, and third-shell O atoms at 3.84(0) Å (Fig. A.3c, Table 2.4).

2.3.3.3. Manganese(III) oxyhydroxides

Minerals of this group are characterized by reduced first-shell amplitudes typically caused by the broad distribution of Mn-O bond lengths and associated scattering cancellation effects (Silvester et al., 1997; Webb et al., 2005) (Figs. 2.5 and A.4a). Consequently, first-shell oxygens in Mn(III) oxyhydroxides were fit with two or three O subshells. For feitknechtite, we obtained Mn-O1 distances of 1.91(0) and 2.22(1) Å, for groutite 1.93(1), 2.15(4), and 2.34(2) Å, and for manganite 1.93(0) and 2.28(1) Å (Table 2.4). Second-shell Mn in feitknechtite was fit at 2.83(1) and 2.99(0) Å, respectively, and third-shell Mn at 3.33(1) Å (Table 2.4). The latter distance is considerably shorter than the 3.43 Å reported by Mackle et al. (1993), but more consistent with the presumed sole presence of edge-sharing Mn^{3+} octahedra in feitknechtite. The coordination numbers (*CN*s) of the two Mn1 subshells in feitknechtite were previously either set to four and two, respectively (Ressler et al., 1999), or to unity (Mackle et al.,

1993). We obtained *CN*s of 1.9(3) and 3.8(11) (Table 2.4), which are in good agreement with the values used by Ressler et al. (1999).

In contrast to the other two polymorphs, first Mn neighbors in groutite could be fit with a single shell at 2.88(1) Å (Table 2.4). Higher Mn coordination shells corresponding to edge- and corner-sharing Mn^3+ octahedra occur at 3.38(3) and 3.61(1) Å, respectively (Table 2.4). These distances are within the error range of values published by Scheinost et al. (2001). For manganite, we obtained Mn-Mn1 distances of 2.77(1) and 2.98(2) Å, a Mn-Mn2 distance of 3.69(1), and a Mn-Mn3 distance of 3.83(2) Å (Table 2.4). The former can be assigned to Mn atoms in chains of edge-sharing Mn^{3+} octahedra and the latter two to corner-sharing octahedra (Mackle et al., 1993). Even though our Mn-Mn1/2 distances are up to ~0.07 Å longer than those reported for manganite by Mackle et al. (1993), they fit well with crystallographic data (Dachs, 1963). Contrary to Mackle et al. (1993), who postulated a similar local Mn coordination environment in manganite and feitknechtite, our data imply a substantially different Mn coordination within these minerals.

2.3.3.4. CARBONATE, PHOSPHATE, AND SILICATE MINERALS

In minerals of this group, atoms other than O and Mn/Fe contribute to their EXAFS: Al/Si in masutomilite, C in rhodochrosite, P in triplite, and Zn in hendricksite. To the best of our knowledge, most of these minerals have not previously been studied by Mn EXAFS spectroscopy. Their spectra and model fits are depicted in Figures 2.5 and A.4b. Generally, first-shell O/F neighbors within this mineral group are found at distances of 1.94-2.55 Å, and were accounted for by one (hendricksite, masutomilite, rhodochrosite), two (triplite) or three subshells (braunite) (Table 2.4). Braunite shows a very broad first FT peak with low amplitude (Fig. A.4b), which was fit with 2.6(2), 2.1(3), and 0.9(3) O neighbors at 1.94(1), 2.25(1), and 2.55(3) Å, respectively. Higher shells included 1.9(5) Mn atoms at 3.17(1) Å, typical of edge-sharing Mn octahedra, and 5.3(18) O atoms at 3.77(2) Å (Table 2.4). All parameters agree well with crystallographic data (Ohmann et al., 1998).

The first coordination shell of hendricksite was fit with 4.9(9) O atoms at 2.16(1) Å, implying fairly distorted Mn2+ octahedra in this mica mineral. Second-shell signals arise from Mn/Fe and Zn neighbors at 3.14(1) Å, sharing the same atomic position in the unit cell (Robert, 1985). The *CN*s of second-shell Mn/Fe and Zn atoms were set to 2.0 and 2.5, respectively, based on chemical analysis (1.04 apfu Mn+Fe and 1.28 apfu Zn in octahedral coordination). Magnesium was neglected due to its low scattering amplitude, and Ba and Ti atoms due to their low concentrations (Table 2.1).

Similar to hendricksite, the first coordination shell in masutomilite was reproduced by 4.9(9) O/F atoms at a distance of 2.15(1) Å. The *CN*s of second-shell Al and Mn, both located at 3.02(5) Å, were set to 2.5 and 0.4, respectively, based on chemical analysis (1.23 apfu Al and 0.18 apfu Mn in octahedral coordination). Octahedral-layer Li was not included in the model due to its low scattering

amplitude. Higher shells of masutomilite include four Al/Si atoms at 3.24(3) and four O atoms at 3.47(3) Å (Table 2.4).

For rhodochrosite, the only important Mn carbonate occurring in soils and sediments (Ying et al., 2011; Barreto et al., 2016), first O neighbors belonging to the CO_3^{2-} group were fit at 2.19(1) Å. These were followed by a C shell at 3.08(2) Å, Mn shells at 3.79(1) and 4.75(1) Å, and O shells at 3.28(1), 4.10(3), and 4.58(1) Å (Table 2.4). All distances are in agreement with Friedl et al. (1997), except for the longest Mn-O distance, which is ~0.03 Å shorter than previously reported.

The FT of triplite is dominated by first-shell F/O atoms, followed by two smaller peaks hosting Fe/Mn and P neighbors (Fig. A.4b). First-shell F and O atoms were fit at 2.05(3) and 2.15(1) Å, respectively, atoms of edge-sharing Fe/Mn octahedra at 2.93(2) Å, and P atoms at 3.55(1) Å (Table 2.4). Chemical analysis suggested 1.6 F and 4.4 O neighbors (0.79 apfu F and 2.21 apfu O) in the first coordination shell, which is close to theoretical F and O *CN*s of two and four, respectively (Waldrop, 1969).

2.3.3.5. Organic Mn(II/III) compounds

The local Mn coordination in Mn(II) acetate tetrahydrate, Mn(II) oxalate dihydrate, and Mn(III) acetate dihydrate has, to our knowledge, not previously been studied by EXAFS spectroscopy. Their spectra are displayed in Figures 2.5 and A.4c. The first coordination shell of both Mn(II) compounds was fit with approximately six O atoms at 2.18(1) Å. In contrast, two O subshells housing 5.2(5) and 1.5(5) O atoms at 1.93(0) and 2.20(1) Å, respectively, were needed to model the first FT peak of Mn(III) acetate dihydrate (Table 2.4). For Mn(II) acetate tetrahydrate, distances of C and Mn shells were fit at 3.19(4) and 3.40(2) Å, respectively (Table 2.4). Remarkably, the best fit was obtained with C and Mn *CN*s fixed to nominal values of monoclinic Mn(II) acetate dihydrate ($P2_1/c$) (Cheng and Wang, 1991). The determined Mn-Mn distance is 0.2 Å shorter than expected for single corner-sharing Mn octahedra present in monoclinic Mn(II) acetate tetrahydrate (P21/c) (Bertaut et al., 1974; Tranqui et al., 1977), but is consistent with long edge-sharing octahedral linkages as in Mn(II) acetate dihydrate (Cheng and Wang, 1991).

In Mn(II) oxalate dihydrate, four proximal C atoms are located at 2.95(2) Å, followed by distant O atoms at 3.93(2) Å. In addition, three multiple-scattering (MS) paths were included in the model (Table 2.4), which significantly improved the fit (F-test). Our fit results comply with XRD data for monoclinic Mn(II) oxalate dihydrate (C2/c), and demonstrate the absence of octahedral linkages in Mn(II) oxalate dihydrate (Puzan et al., 2018).

In Mn(III) acetate dihydrate, the first coordination shell is followed by four proximal C atoms at 2.98(2) Å, a substantially shorter distance compared to Mn(II) acetate tetrahydrate (Table 2.4). Best fits of higher coordination shells were obtained with two Mn atoms at 3.40(0) Å and two O atoms at

4.37(5) Å (Table 2.4). Both, distances and *CN*s comply with XRD data for monoclinic Mn(III) triacetate dihydrate (P21/m), in which Mn(III) octahedra are linked to chains via single corners (Le Bail, 2016; personal communication to the crystallography open database (COD), COD ID 3500063).

2.3.3.6. ADSORBED MN(II) SPECIES

To the best of our knowledge, molecular-scale information on Mn(II) adsorbed to clay minerals (illite) and particulate natural organic matter (peat) is currently not available. Spectra of Mn(II) adsorbed to illite and peat are illustrated in Figures 2.5 and A.4d. The EXAFS of Mn(II) adsorbed to illite is dominated by first-shell signals, housing two O atoms at 1.92(1) Å and four O atoms at 2.16(1) Å (Table 2.4). Implementation of Al or Si backscatterers into the model proved unsuccessful, suggesting that hydrated Mn^{2+} ions are primarily adsorbed as outersphere complexes on siloxane surfaces. We found no evidence of a Mn(III/IV) phase, which could explain the XANES- and titration-derived AOS values >2 obtained for the illite sample (Table 3). This may suggest a similar adsorption mechanism for Mn^{3+} ions or a systematic error in both AOS determination methods, which we consider less likely.

Nearly identical shell-fit results were obtained for Mn(II) adsorbed to peat at pH 5 and 7, showing that pH had a negligible effect on the coordination of organically bound Mn(II). Both EXAFS were well reproduced with one proximal C atom at 3.20(7) (pH 5) and 3.21(8) Å (pH 7), implying monodentate Mn^{2+} complexation by carboxyl groups. Owing to their low scattering amplitudes, distal C atoms were not included in the model; instead, an obtuse triangle Mn-C-O MS path was used to reproduce the low FT peaks at ~4.5 Å (Fig. 2.5, Table 2.4). Interestingly, Mn^{2+} complexation by particulate organic matter did not lead to Mn^{2+} oxidation under oxic conditions (Table 2.3).

2.3.3.7. COMPARISON OF INTERATOMIC DISTANCES

When XAS is applied to soils or sediments, overabsorption can frequently affect the EXAFS amplitude, leading to a bias of fitted *CN*s. Additionally, *CN*s can be influenced by poor crystallinity (i.e., high static disorder) and/or small particle size relative to crystalline reference compounds (O'Day et al., 2004). As these issues do not affect the EXAFS frequency, atomic distances are more robust parameters when comparing average Mn coordination environments of natural samples.

Figure 2.7 compiles all absorber-single scatter distances determined in this study. The figure also includes data from various literature sources for comparison (Table A.4). Note that the designation of individual coordination shells is somewhat arbitrary, and for simplicity, atoms in subshells were considered part of a 'shell'. As evidenced by Friedl et al. (1997), Mn-O bond distances depend on the oxidation state of Mn. In agreement with this, the shortest Mn-O distances were observed for tectomanganates, and the longest Mn-O distances for (in)organic Mn(II) species (Fig. 2.7).

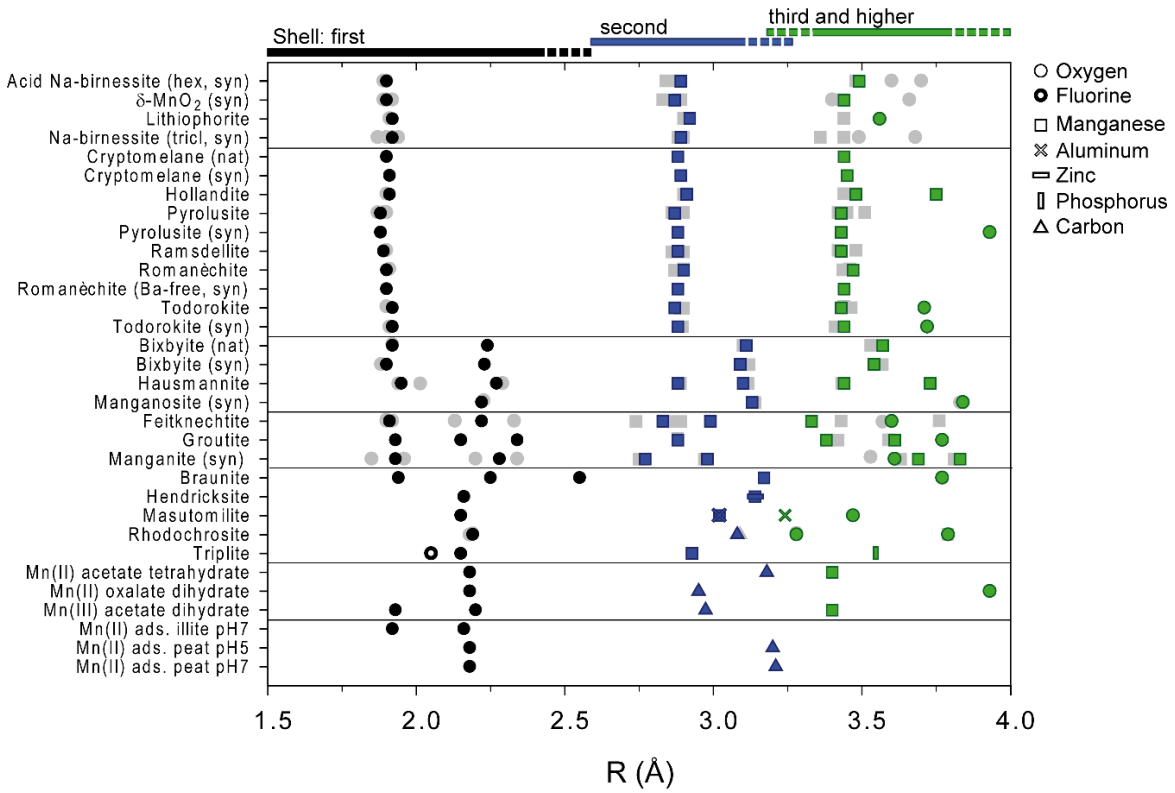

Figure 2.7. Interatomic distances between Mn and near-neighbor atoms in Mn reference compounds obtained from this study (colored symbols) and the literature (gray symbols). Literature references are listed in Table A.4. In masutomilite, first-shell O could also be F and third-shell Al could be Si. In triplite and hendricksite, second-shell Mn may also be Fe. Horizontal lines separate the seven different Mn species groups (see text for further details).

In general, average first-shell distances of all reference compounds can be classified according to their XANES-derived Mn AOS: 2.14±0.04 Å ($\bar{x}\pm\sigma$) for AOS 2.0-2.5 members (N = 10), 2.02±0.06 Å for AOS 3.0-3.5 members (N = 9), and 1.90±0.01 Å for AOS 3.7-4.0 members (N = 13). Differences in average Mn-O/F bond lengths of AOS groups are significant at the p <0.05 level (Kruskal-Wallis rank-based ANOVA, Dunn´s method), except for those of the AOS 3.0-3.5 and 3.7-4.0 groups. Figure 2.7 also illustrates that split shells of first O neigbors are absent in the phyllo- and tectomanganate groups. In contrast, Mn-O1 subshells or longer Mn-O distances are typical features of all other Mn species groups. Likewise, Mn-Mn1 distances of edge-sharing Mn octahedra in phyllo- and tectomanganates (2.87-2.92 Å) are substantially shorter than corresponding (average) Mn-Mn distances in (1) oxides without layer or tunnel structure (3.03-3.13 Å; bixbyite, hausmannite, manganosite), (2) members of the phosphate and silicate group (2.93-3.17 Å; braunite, hendricksite, masutomilite, triplite), and (3) organic Mn(II) compounds (3.40 Å; Mn(II) acetate tetrahydrate). Although Mn-Mn1 distances of phyllo- and tectomanganates are similar to (average) Mn-Mn1 distances in Mn(III) oxyhydroxides, the need to fit two Mn-Mn1 subshells to an EXAFS spectrum of an environmental sample, may indicate the presence of feitknechtite and manganite (or hausmannite) (Fig. 2.7).

Organic Mn(II/III) compounds may possess edge- or corner-sharing MnO_6 linkages, whose Mn-Mn distances can overlap with those of manganate and oxyhydroxide minerals, notably groutite (Fig. 2.7). In contrast, organically complexed Mn(II) species lack Mn or other heavy atoms in higher coordination shells. Their Mn-C distances are either significantly shorter or longer than the Mn-C distance of rhodochrosite (3.08(2) Å), thus facilitating the distinction between rhodochrosite and organic Mn(II) species in environmental samples (Fig. 2.7).

2.3.3.8. STATISTICAL XAS SPECTRUM COMPARISONS

Key to species detection and quantification by means of Mn XAS LCF is spectral dissimilarity. Therefore, Pearson correlations were used to compare the (dis)similarity of XAS spectra of all reference compounds. Normalized XANES spectra (6,530-6,600 eV) were highly positively correlated due to similar overall shape (Fig. A.5), complicating a meaningful species identification and quantification based on LCF analysis of this data without auxiliary information. Significantly lower spectral correlations for first-derivative XANES spectra (Fig. A.6) indicate much better discriminative power of these data. Here, low and moderate correlations (r ≤0.7) exist between adsorbed Mn(II) species and most other species-group members. The same holds for carbonate, silicate, and phosphate minerals as well organic Mn(II) compounds (Fig. A.6). This suggests that members of these groups can likely be identified based on their first-derivative XANES, provided data quality is sufficient. However, high correlations (r >0.8) were still observed between manganates, oxide minerals without layer or tunnel structure, and Mn(III) oxyhydroxides, making it difficult to identify and quantify individual members of these species groups in mixtures using first-derivative XANES spectra (Fig. A.6). A much better discriminative power can be achieved on the basis of Mn EXAFS spectra. Figure 2.8 shows the Pearson correlation matrix of k^2-weighted EXAFS spectra (k = 2.0-11.5 Å^{-1}, E_0 = 6,563 eV) of all reference compounds. A k^2-weighting was chosen because environmental studies usually deal with low-Mn concentration samples that would not allow a higher k-weighting in LCF analyses without risking excessive spectral noise amplification. However, caution must be exercised in interpreting these correlation coefficients because strong correlations were observed for species whose EXAFS spectra differ substantially, for example, pyrolusite and Ba-free romanèchite (r = 0.82) (*cf*. Fig. 2.6). It follows that correlation coefficients of less than approximately 0.8 can be taken as indication of spectral dissimilarity. Using this criterion, Figure 2.8 shows that EXAFS spectra of most reference compounds are unique, only exceptions being spectra of several members of the manganates, organic Mn(II/III) compounds, adsorbed Mn(II) species, and triplite. This result confirms the supreme potential of EXAFS LCF analysis to identify and quantify individual Mn species in environmental samples.

Next, we performed a PCA to reduce the dimensionality of the k^2-weighted Mn K-edge EXAFS dataset and clarify spectral group membership. Output parameters for the first ten principal components (PCs) are summarized in Table A.5. The number of statistical meaningful PCs based on eigenvalues >1 (Kaiser-Guttman criterion; Guttman, 1954) was five (Table A.5). These PCs explained 88.6% of the total variance of all Mn EXAFS spectra, suggesting five superordinate variables defining spectral group membership. A loading plot of PC1 *vs*. PC2, explaining 56.08% and 13.33% of spectral variance, respectively, is illustrated in Figure 2.9. Here, PC1 mainly reflects the oxidation state of Mn reference compounds, as members of manganates load highly negatively, Mn(II) species positively, and species with predominantly Mn(III) intermediately and negatively on PC1. Combined, PCA implies that at least five Mn species (groups) can be distinguished in the entire EXAFS data set, and Figure 2.9 suggests that the Mn oxidation state plays a major role.

	Acid Na-birnessite (hex, syn)	δ-MnO_2 (syn)	Lithiophorite	Na-birnessite (tricl, syn)	Cryptomelane	Cryptomelane (syn)	Hollandite	Pyrolusite	Pyrolusite (syn)	Ramsdellite	Romanèchite (Ba-free, syn)	Romanèchite	Todorokite	Todorokite (syn)	Bixbyite	Bixbyite (syn)	Hausmannite	Manganosite (syn)	Feitknechtite (syn)	Groutite	Manganite (syn)	Braunite	Hendricksite	Masutomilite	Rhodochrosite	Triplite	Mn(II) acetate tetrahydrate	Mn(II) oxalate dihydrate	Mn(III) acetate dihydrate	Mn(II) ads. illite	Mn(II) ads. peat pH5	Mn(II) ads. peat pH7
Acid Na-birnessite (hex, syn)			PM*							Tectomanganates																						
δ-MnO_2 (syn)	0.99																															
Lithiophorite	0.73	0.80																														
Na-birnessite (tricl, syn)	0.86	0.90	0.88																													
Cryptomelane	0.92	0.94	0.78	0.88																												
Cryptomelane (syn)	0.91	0.93	0.77	0.87	1.00																											
Hollandite	0.84	0.88	0.90	0.87	0.94	0.94																										
Pyrolusite	0.76	0.78	0.58	0.70	0.90	0.90	0.81																									
Pyrolusite (syn)	0.69	0.72	0.53	0.65	0.84	0.85	0.76	0.98																								
Ramsdellite	0.86	0.88	0.69	0.80	0.96	0.96	0.87	0.96	0.92																							
Romanèchite (Ba-free, syn)	0.92	0.94	0.78	0.96	0.95	0.94	0.89	0.82	0.76	0.90																						
Romanèchite	0.90	0.93	0.89	0.89	0.95	0.95	0.98	0.79	0.73	0.88	0.91																					
Todorokite	0.95	0.95	0.73	0.92	0.95	0.94	0.86	0.82	0.77	0.90	0.99	0.90																				
Todorokite (syn)	0.94	0.97	0.82	0.96	0.95	0.94	0.91	0.80	0.74	0.89	0.98	0.94	0.98																			
Bixbyite							0.20					0.20				Oxide minerals without layer or tunnel structure																
Bixbyite (syn)							0.22					0.21			0.99																	
Hausmannite	0.34	0.38	0.37	0.30	0.52	0.52	0.55	0.57	0.57	0.50	0.39	0.50	0.37	0.40	0.37	0.36																
Manganosite (syn)	-0.24	-0.30	-0.47	-0.42	-0.26	-0.27	-0.33	-0.19	-0.23	-0.26	-0.31	-0.30	-0.26	-0.32	0.38	0.31				Mn(III) oxyhydroxides												
Feitknechtite (syn)	0.54	0.56	0.49	0.43	0.48	0.44	0.56	0.41	0.39	0.45	0.43	0.59	0.49	0.54	0.64	0.62	0.43															
Groutite	0.80	0.82	0.77	0.73	0.68	0.65	0.71	0.48	0.41	0.60	0.69	0.78	0.69	0.77	0.16	0.15	0.26	-0.22	0.66													
Manganite (syn)	0.52	0.56	0.55	0.50	0.42	0.39	0.49	0.34	0.31	0.42	0.43	0.55	0.47	0.54	0.34	0.34	0.27	-0.17	0.84	0.72												
Braunite	0.35	0.38	0.32	0.26	0.37	0.35	0.42	0.29	0.26	0.33	0.29	0.43	0.34	0.37	0.75	0.73	0.48	0.29	0.75	0.39	0.49			Carbonate, phosphate, and silicate minerals								
Hendricksite	-0.42	-0.47	-0.55	-0.58	-0.47	-0.48	-0.51	-0.40	-0.42	-0.47	-0.52	-0.48	-0.50	-0.53	0.33	0.28	0.03	0.63		-0.39	-0.27	0.12										
Masutomilite	-0.37	-0.41	-0.30	-0.42	-0.38	-0.37	-0.38	-0.39	-0.40	-0.40	-0.43	-0.37	-0.45	-0.45					-0.46	-0.39	-0.38	-0.35	0.57									
Rhodochrosite	-0.34	-0.37	-0.35	-0.36	-0.29	-0.27	-0.34	-0.16	-0.14	-0.21	-0.35	-0.37	-0.37	-0.40	-0.33	-0.34			-0.37	-0.44	-0.26	-0.24	0.31	0.46								
Triplite	-0.62	-0.63	-0.48	-0.64	-0.58	-0.56	-0.57	-0.47	-0.43	-0.53	-0.67	-0.58	-0.70	-0.69	-0.29	-0.29	-0.16	0.16	-0.50	-0.45	-0.46	-0.37	0.50	0.72	0.56							
Mn(II) acetate tetrahydrate	-0.44	-0.49	-0.46	-0.50	-0.44	-0.43	-0.49	-0.32	-0.30	-0.37	-0.49	-0.50	-0.49	-0.53	-0.31	-0.34	-0.22	0.22	-0.48	-0.50	-0.47	-0.42	0.54	0.76	0.70	0.77						
Mn(II) oxalate dihydrate	-0.43	-0.45	-0.35	-0.43	-0.40	-0.39	-0.42	-0.31	-0.29	-0.36	-0.47	-0.43	-0.51	-0.51	-0.27	-0.29	-0.25	0.20	-0.42	-0.33	-0.45	-0.33	0.44	0.60	0.48	0.84	0.80		Organic Mn(II/III) compounds			
Mn(III) acetate dihydrate	0.64	0.70	0.71	0.63	0.75	0.74	0.80	0.71	0.72	0.76	0.64	0.80	0.66	0.71	0.29	0.30	0.56	-0.28	0.71	0.63	0.64	0.54	-0.49	-0.46	-0.25	-0.41	-0.49	-0.38				
Mn(II) ads. illite	-0.37	-0.40	-0.30	-0.45	-0.40	-0.40	-0.41	-0.36	-0.36	-0.38	-0.49	-0.38	-0.50	-0.48	-0.18	-0.19		0.25	-0.29	-0.25	-0.23	-0.22	0.63	0.81	0.60	0.86	0.85	0.81	-0.35			
Mn(II) ads. peat pH5	-0.55	-0.59	-0.50	-0.57	-0.56	-0.55	-0.59	-0.48	-0.47	-0.53	-0.61	-0.58	-0.63	-0.64	-0.29	-0.30	-0.27	0.26	-0.49	-0.47	-0.45	-0.41	0.61	0.80	0.65	0.87	0.94	0.87	-0.57	0.92		Adsorbed Mn(II) species
Mn(II) ads. peat pH7	-0.53	-0.57	-0.48	-0.56	-0.54	-0.54	-0.57	-0.46	-0.46	-0.51	-0.59	-0.56	-0.62	-0.63	-0.29	-0.30	-0.25	0.27	-0.49	-0.45	-0.45	-0.40	0.61	0.80	0.65	0.88	0.94	0.87	-0.55	0.93	1.00	

1	>0.9	>0.8	>0.7	>0.6	≤0.6

*PM = Phyllomanganates

Figure 2.8. Pearson correlation matrix for k^2-weighted Mn K-edge EXAFS spectra (k = 2.0-11.5 Å^{-1}, E_0 = 6,563 eV) of Mn reference compounds. Only significant correlations (p <0.05) are reported.

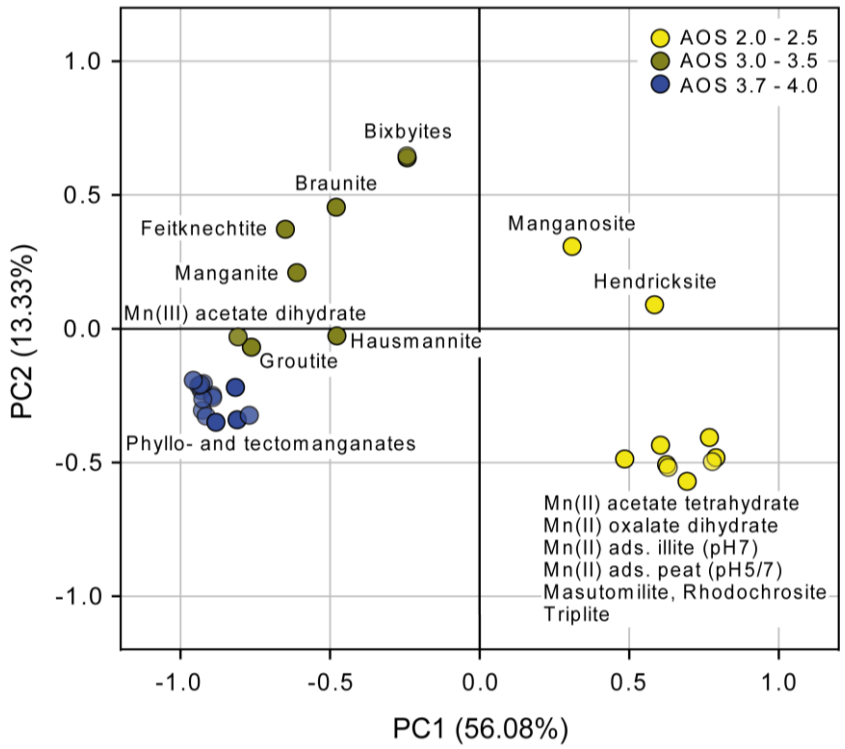

Figure 2.9. Loading plot of the first two PCs obtained from PCA of k^2-weighted Mn K-edge EXAFS spectra (k = 2.0-11.5 Å^{-1}, E_0 = 6,563 eV) of Mn reference compounds. Species are colored according to their XANES-derived Mn AOS.

To validate the PCA results, an unsupervised tree-clustering analysis was performed using Ward´s method (Ward, 1963). Figure 2.10 shows the output of the cluster analysis. The length of the horizontal lines (linkage distances) is proportional to spectral dissimilarity. Like PCA, hierarchical cluster analysis generally separated Mn(III/IV) phases from Mn(III)- and Mn(II)-containing compounds at a linkage distance of 25-40 (Fig. 2.10). A division into five meaningful clusters, as suggested by PCA, is given at a linkage distance of about 18. Here, cluster one consists of all phyllo- and tectomanganates with large tunnel sizes (2×2 and larger) including hollandite *s.s.* (2×2 tectomanganate). Cluster two comprises tectomanganates with small tunnel sizes (2×2 and smaller). Minerals dominated by Mn(III) are grouped into cluster three. Cluster four unites all Mn(II) species, and cluster five is exclusively formed by manganosite. A closer inspection of inner-cluster variability revealed that bixbyite, hausmannite, hendricksite, masutomilite, pyrolusite, and rhodochrosite are clearly distinct within their respective clusters. While EXAFS spectra with a linkage distance >6 show discriminable spectral features, they become virtually indistinguishable at a linkage distance <5 based on direct comparisons. This implies that six of the 32 Mn reference compounds (hausmannite, hendricksite, manganosite, masutomilite, Mn(III) acetate dihydrate, rhodochrosite) are clearly recognizable and quantifiable as individual species when present in mixtures. All other Mn compounds can at least be reliably assigned to a particular species group.

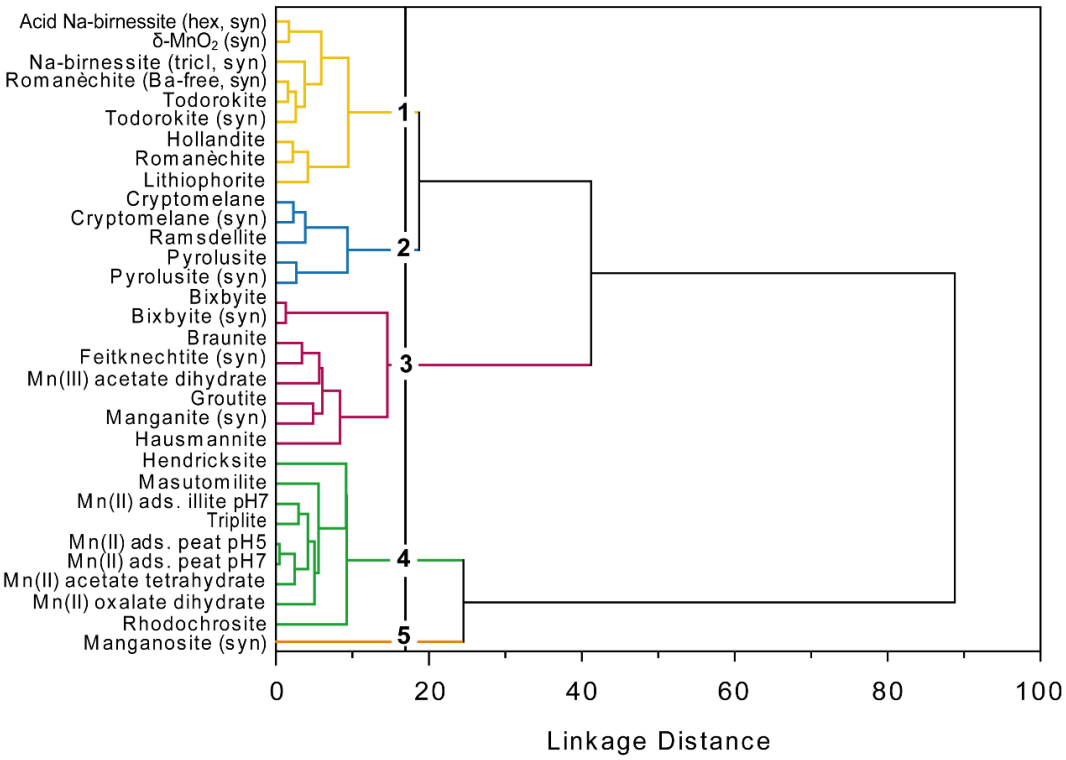

Figure 2.10. Unsupervised tree clustering of k^2-weighted Mn K-edge EXAFS spectra (k = 2.0-11.5 Å^{-1}, E_0 = 6,563 eV) of Mn reference compounds using Ward´s method. Five clusters are indicated at a linkage distance of 18.

2.4. IMPLICATIONS

Research on Mn oxidation states in soils and sediments is prerequisite to better understand redox cycling of Mn and its participation in environmental processes. Since accurate Mn AOS determination in soils and sediments by wet-chemical methods is impossible due to the excess of other electron donors/acceptors, especially Fe and organic matter, XANES spectroscopy is currently the only available tool for process-oriented research relying on this key parameter. By comparing XANES LCF- and redox titration-based AOS results for mono- and multivalent Mn compounds, we found that the XANES LCF 'Combo' method of Manceau et al. (2012) provides accurate Mn AOS data within approximately 0.1 v.u. over the entire natural Mn valence range.

Linear combination fitting of XAS spectra is a widely used method for the identification and quantification of element species in environmental samples (Hutchison et al., 2001; Scheckel and Ryan, 2004; Langner et al., 2012; Mikutta and Rothwell, 2016; Leven et al., 2018). This approach requires comprehensive databases with suitable reference spectra (Scheinost et al., 2002; Gustafsson et al., 2020). While these exist for several key elements such as Fe (Wilke et al., 2001; O'Day et al., 2004), they are not available for Mn. Therefore, we provide (energy-calibrated) XAS spectra of 32 Mn compounds, potentially occurring in soils and sediments, in the *Supplementary material*. This spectrum

library can be used by the scientific community for Mn species identification and quantification in terrestrial surface environments.

Prerequisite to the application of XAS LCF for species recognition and quantification is spectral uniqueness (Scheinost et al., 2002; Gustafsson et al., 2020). Our results show that, compared to EXAFS spectra, normalized and first-derivative Mn K-edge XANES spectra provide far less discriminative power to distinguish and thus identify individual Mn species in environmental samples. Owing to high spectral correlations, the use of normalized Mn XANES spectra for species identification and quantification in LCF analysis of environmental samples is not recommended without proper justification based on auxiliary species information. First-derivative XANES spectra of most analyzed Mn compounds are unique, suggesting that identification and quantification of most Mn species would be possible. However, members of the manganate and Mn(III)-oxyhydroxide groups are probably indistinguishable in mixtures using (first-derivative) XANES spectra. Prominent exceptions are pyrolusite, ramsdellite, and perhaps lithiophorite, which possess unique first-derivative XANES fingerprints. Nonetheless, the employment of XANES LCF for Mn species identification and quantification in natural samples is limited. First, because XANES features are not solely dependent on the Mn oxidation state or structural and electronic factors, but also on energy calibration and monochromator resolution (Manceau et al., 2002; Manceau et al., 2012). Second, because XANES spectra are influenced by subtle changes in chemical composition and/or crystallinity of Mn compounds. Comparisons of XANES and EXAFS spectra of natural and synthetic Mn compounds (bixbyites, cryptomelanes, pyrolusites, todorokites) document the robustness of EXAFS spectroscopy to variations in chemistry and/or crystallinity, demonstrating its superior value for bulk Mn species identification and quantification in natural samples. Based on PCA and cluster analyses, EXAFS LCF analysis of environmental samples is at least capable of discriminating the following species groups: (1) phyllomanganates and tectomanganates with large tunnel sizes (2×2 and larger; hollandite *s.s.*, romanèchite, todorokite), (2) tectomanganates with small tunnel sizes (2×2 and smaller; cryptomelane, pyrolusite, ramsdellite), (3) Mn(III)-dominated species (nesosilicates, organic compounds, oxyhydroxides, spinels), (4) Mn(II) species (carbonate, phosphate, and phyllosilicate minerals, adsorbed and organic species), and (5) manganosite. Within these conservatively established species groups, most Mn compounds exhibit unique EXAFS features, which would assist their identification and quantification in mixtures using EXAFS LCF analysis. Sole exceptions are manganate minerals (except for pyrolusite) and adsorbed Mn(II) species whose EXAFS are dominated by first-shell O signals. These results highlight the potential of Mn K-edge EXAFS spectroscopy to quantitatively assess bulk Mn speciation in soils and sediments, which so far has not been exploited. For speciation analysis of natural samples using Mn K-edge EXAFS spectroscopy, we recommend stepwise application

of PCA-TT and LCF analysis and subsequent validation of LCF results by spectral fingerprinting as well as EXAFS shell-fitting in order to justify the presence of individual Mn species.

In summary, the results of this study provide a comprehensive framework for the analysis and interpretation of Mn XAS spectra of natural samples and for the evaluation of the role of Mn in environmental processes. Our spectrum library thus lays the foundation for further process-oriented environmental Mn research.

2.5. ACKNOWLEDGEMENTS

We are especially grateful to Evert Elzinga, Flora Brocza, Caroline Peacock, and David McKeown for providing additional XAS spectra and Reiner Dohrmann for the illite reference. Special thanks go to Julian Feige for the preparation of thin sections and Philip Weigel for EPMA assistance. Tobias Fußwinkel is thanked for sharing his knowledge on mineral formula calculation. Furthermore, we are indebted to Jens Gröger-Trampe and Bodo Mieke (LBEG) for their support during redox titrations. Use of the Stanford Synchrotron Radiation Lightsource, SLAC National Accelerator Laboratory, was supported by the U.S. Department of Energy, Office of Science, Office of Basic Energy Sciences under Contract No. DE-AC02-76SF00515s. Use of the Advanced Photon Source, an Office of Science User Facility operated for the U.S. Department of Energy (DOE) Office of Science by Argonne National Laboratory, was supported by the U.S. DOE under Contract No. DE-AC02-06CH11357. We also thank PETRA III at DESY for providing us with beamtime. Assistance at synchrotron facilities by Ritimukta Sarangi (SSRL), Qing Ma (APS), and Edmund Welter, Wolfgang Caliebe, Akhil Tayal, and Vadim Murzin (all DESY) is gratefully acknowledged. This work was financially supported by the DFG (project no. 326242261).

2.6. REFERENCES

Ahmad, A., van der Wal, A., Bhattacharya, P. and van Genuchten, C.M. (2019) Characteristics of Fe and Mn bearing precipitates generated by Fe(II) and Mn(II) co-oxidation with O_2, MnO_4 and HOCl in the presence of groundwater ions. *Water Res.* **161**, 505-516.

Ankudinov, A.L., Ravel, B., Rehr, J.J. and Conradson, S.D. (1998) Real-space multiple-scattering calculation and interpretation of X-ray-absorption near-edge structure. *Phys. Rev. B* **58**, 7565.

Anthony, J.W., Bideaux, R.A., Bladh, K.W. and Nichols, M.C. (2003) *Handbook of Mineralogy*. Mineralogical Society of America, Chantilly, VA 20151-1110, USA.

Barreto, M.B., Mónaco, S.L., Díaz, R., Barreto-Pittol, E., López, L. and Peralba, M.d.C.R. (2016) Soil organic carbon of mangrove forests (*Rhizophora* and *Avicennia*) of the Venezuelan Caribbean coast. *Org. Geochem.* **100**, 51-61.

Bartlett, R.J. (1981) Nonmicrobial nitrite-to-nitrate transformation in soils. *Soil. Sci. Soc. Am. J.* **45**, 1054-1058.

Bertaut, E., Tran Qui, D., Burlet, P., Thomas, M. and Moreau, J. (1974) Crystal structure of manganese acetate tetrahydrate. *Acta Crystallogr. B* **30**, 2234-2236.

Bhattacharya, L. and Elzinga, E.J. (2018) A comparison of the solubility products of layered Me(II)-Al(III) hydroxides based on sorption studies with Ni(II), Zn(II), Co(II), Fe(II), and Mn(II). *Soil Syst.* **2**, 20.

Blume, H., Brümmer, G., Fleige, H., Horn, R., Kandeler, E., Kögel-Knabner, I., Kretzschmar, R., Stahr, K. and Wilke, B. (2016) *Scheffer/Schachtschabel Soil Science*. Springer: Berlin Heidelberg, Germany.

Bolzan, A., Fong, C., Kennedy, B. and Howard, C. (1993) Powder neutron diffraction study of pyrolusite, β-MnO_2. *Australian Journal of Chemistry* **46**, 939-944.

Broadley, M., Brown, P., Cakmak, I., Rengel, Z. and Zhao, F. (2012) Function of Nutrients: Micronutrients. In: *Marschner's Mineral Nutrition of Higher Plants* (ed. P. Marschner), 3rd ed. Academic Press, pp. 191-248.

Burnell, J.N. (1988) The biochemistry of manganese in plants. In: *Manganese in Soils and Plants* (ed. R.J.H. Robin D. Graham, Nicholas C. Uren), Dordrecht, pp. 125-137.

Carroll, S., O'Day, P.A., Esser, B. and Randall, S. (2002) Speciation and fate of trace metals in estuarine sediments under reduced and oxidized conditions, Seaplane Lagoon, Alameda Naval Air Station (USA). *Geochem. Trans.* **3**, 81-101.

Chatzistathis, T., Therios, I. and Alifragis, D. (2012) Manganese deficiency and toxicity in soils and mechanisms adopted by plants in order to face these nutritional disorders: A review In: *Soil Nutrients* (ed. M. Mohammad). Nova Science Publishers Inc., Isfahan, Iran, pp. 177-197.

Cheng, C.-Y. and Wang, S.-L. (1991) Structure of manganese acetate dihydrate. *Acta Crystallogr. C* **47**, 1734-1736.

Chiu, V.Q. and Hering, J.G. (2000) Arsenic adsorption and oxidation at manganite surfaces. 1. Method for simultaneous determination of adsorbed and dissolved arsenic species. *Environ. Sci. Technol.* **34**, 2029-2034.

Chukhrov, F.V. and Gorshkov, A.I. (1981) Iron and manganese oxide minerals in soils. *Trans. Royal Soc. Edinb. Earth Sci.* **72**, 195-200.

Cornu, S., Deschatrettes, V., Salvador-Blanes, S., Clozel, B., Hardy, M., Branchut, S. and Le Forestier, L. (2005) Trace element accumulation in Mn-Fe-oxide nodules of a planosolic horizon. *Geoderma* **125**, 11-24.

Dachs, H. (1963) Neutronen-und Röntgenuntersuchungen am Manganit, MnOOH. *Z. Kristallogr. Cryst. Mater.* **118**, 303-326.

Dohrmann, R., Rüping, K.B., Kleber, M., Ufer, K. and Jahn, R. (2009) Variation of preferred orientation in oriented clay mounts as a result of sample preparation and composition. *Clays Clay Miner.* **57**, 686-694.

Ehlert, K., Mikutta, C. and Kretzschmar, R. (2014) Impact of birnessite on arsenic and iron speciation during microbial reduction of arsenic-bearing ferrihydrite. *Environ. Sci. Technol.* **48**, 11320-11329.

Ehlert, K., Mikutta, C. and Kretzschmar, R. (2016) Effects of manganese oxide on arsenic reduction and leaching from contaminated floodplain soil. *Environ. Sci. Technol.* **50**, 9251-9261.

Elzinga, E.J. (2011) Reductive transformation of birnessite by aqueous Mn(II). *Environ. Sci. Technol.* **45**, 6366-6372.

Feng, Q., Kanoh, H., Miyai, Y. and Ooi, K. (1995) Metal ion extraction/insertion reactions with todorokite-type manganese oxide in the aqueous phase. *Chem. Mater.* **7**, 1722-1727.

Feng, X.H., Zhai, L.M., Tan, W.F., Liu, F. and He, J.Z. (2007) Adsorption and redox reactions of heavy metals on synthesized Mn oxide minerals. *Environ. Pollut.* **147**, 366-373.

Feng, X.H., Zhu, M., Ginder-Vogel, M., Ni, C., Parikh, S.J. and Sparks, D.L. (2010) Formation of nano-crystalline todorokite from biogenic Mn oxides. *Geochim. Cosmochim. Acta* **74**, 3232-3245.

Fernando, D.R., Mizuno, T., Woodrow, I.E., Baker, A.J.M. and Collins, R.N. (2010) Characterization of foliar manganese (Mn) in Mn (hyper)accumulators using X-ray absorption spectroscopy. *New Phytol.* **188**, 1014-1027.

Friedl, G., Wehrli, B. and Manceau, A. (1997) Solid phases in the cycling of manganese in eutrophic lakes: New insights from EXAFS spectroscopy. *Geochim. Cosmochim. Acta* **61**, 275-290.

Frommer, J., Voegelin, A., Dittmar, J., Marcus, M.A. and Kretzschmar, R. (2011) Biogeochemical processes and arsenic enrichment around rice roots in paddy soil: Results from micro-focused X-ray spectroscopy. *Eur. J. Soil. Sci.* **62**, 305-317.

Geshnizgani, E.R. (2014) *Low temperature oxidation of VOCs in air by catalytic ozonation*. University of Saskatchewan.

Grangeon, S., Manceau, A., Guilhermet, J., Gaillot, A.-C., Lanson, M. and Lanson, B. (2012) Zn sorption modifies dynamically the layer and interlayer structure of vernadite. *Geochim. Cosmochim. Acta* **85**, 302-313.

Gustafsson, J.P., Braun, S., Tuyishime, M.J.R., Adediran, G.A., Warrinnier, R. and Hesterberg, D. (2020) A probabilistic approach to phosphorus speciation of soils using P K-edge XANES spectroscopy with linear combination fitting. *Soil Syst.* **4**, 26.

Guttman, L. (1954) Some necessary conditions for common-factor analysis. *Psychometrika* **19**, 149-161.

Habibah, J., Khairiah, J., Ismail, B. and Kadderi, M. (2014) Manganese speciation in selected agricultural soils of peninsular Malaysia. *Am. J. Environ. Sci.* **10**, 148-156.

Hamilton, W.C. (1965) Significance tests on the crystallographic R factor. *Acta Crystallogr.* **18**, 502-510.

Hass, A. and Fine, P. (2010) Sequential selective extraction procedures for the study of heavy metals in soils, sediments, and waste materials – a critical review. *Crit. Rev. Environ. Sci. Technol.* **40**, 365-399.

Hernandez-Soriano, M.C., Degryse, F., Lombi, E. and Smolders, E. (2012) Manganese toxicity in barley is controlled by solution manganese and soil manganese speciation. *Soil. Sci. Soc. Am. J.* **76**, 399-407.

Herndon, E.M., Martínez, C.E. and Brantley, S.L. (2014) Spectroscopic (XANES/XRF) characterization of contaminant manganese cycling in a temperate watershed. *Biogeochemistry* **121**, 505-517.

Hlavay, J., Prohaska, T., Weisz, M., Wenzel, W.W. and Stingeder, G.J. (2004) Determination of trace elements bound to soil and sediment fractions (IUPAC Technical Report). *Pure Appl. Chem.* **76**, 415-442.

Hoffmann, M., Mikutta, C. and Kretzschmar, R. (2012) Bisulfide reaction with natural organic matter enhances arsenite sorption: Insights from X-ray absorption spectroscopy. *Environ. Sci. Technol.* **46**, 11788-11797.

Hutchison, K.J., Hesterberg, D. and Chou, J.W. (2001) Stability of reduced organic sulfur in humic acid as affected by aeration and pH. *Soil. Sci. Soc. Am. J.* **65**, 704-709.

Jarosch, D. (1987) Crystal structure refinement and reflectance measurements of hausmannite, Mn_3O_4. *Mineral. Petrol.* **37**, 15-23.

Jensen, K.A., Bao, W., Kawai, S., Srebotnik, E. and Hammel, K.E. (1996) Manganese-dependent cleavage of nonphenolic lignin structures by *Ceriporiopsis subvermispora* in the absence of lignin peroxidase. *Appl. Environ. Microbiol.* **62**, 3679-3686.

Kalembkiewicz, J., Sitarz-Palczak, E. and Zapała, L. (2008) A study of the chemical forms or species of manganese found in coal fly ash and soil. *Microchem. J.* **90**, 37-43.

Keiluweit, M., Nico, P., Harmon, M.E., Mao, J., Pett-Ridge, J. and Kleber, M. (2015) Long-term litter decomposition controlled by manganese redox cycling. *Proc. Natl. Acad. Sci.* **112**, E5253-E5260.

Langner, P., Mikutta, C. and Kretzschmar, R. (2012) Arsenic sequestration by organic sulphur in peat. *Nature Geosci.* **5**, 66-73.

Lanson, B., Drits, V.A., Silvester, E. and Manceau, A. (2000) Structure of H-exchanged hexagonal birnessite and its mechanism of formation from Na-rich monoclinic buserite at low pH. *Am. Mineral.* **85**, 826-838.

Latrille, C., Elsass, F., Van Oort, F. and Denaix, L. (2001) Physical speciation of trace metals in Fe-Mn concretions from a rendzic lithosol developed on Sinemurian limestones (France). *Geoderma* **100**, 127-146.

Lee, S. and Xu, H. (2016) XRD and TEM studies on nanophase manganese oxides in freshwater ferromanganese nodules from Green Bay, Lake Michigan. *Clays Clay Miner.* **64**, 523-536.

Lefkowitz, J.P., Rouff, A.A. and Elzinga, E.J. (2013) Influence of pH on the reductive transformation of birnessite by aqueous Mn(II). *Environ. Sci. Technol.* **47**, 10364-10371.

Leven, A., Vlassopoulos, D., Kanematsu, M., Goin, J. and O'Day, P.A. (2018) Characterization of manganese oxide amendments for in situ remediation of mercury-contaminated sediments. *Environ. Sci.: Process. Impacts* **20**, 1761-1773.

Ling, F.T., Post, J.E., Heaney, P.J. and Ilton, E.S. (2018) The relationship between Mn oxidation state and structure in triclinic and hexagonal birnessites. *Chem. Geol.* **479**, 216-227.

Liu, F., Colombo, C., Adamo, P., He, J.Z. and Violante, A. (2002) Trace elements in manganese-iron nodules from a Chinese Alfisol. *Soil. Sci. Soc. Am. J.* **66**, 661-670.

Longo, A., Liotta, L.F., Carlo, G.D., Giannici, F., Venezia, A.M. and Martorana, A. (2010) Structure and the metal support interaction of the Au/Mn oxide catalysts. *Chem. Mater.* **22**, 3952-3960.

Mackle, P., Charnock, J.M., Garner, C.D., Meldrum, F.C. and Mann, S. (1993) Characterization of the manganese core of reconstituted ferritin by X-ray absorption spectroscopy. *J. Am. Chem. Soc.* **115**, 8471-8472.

Manceau, A. and Combes, J.M. (1988) Structure of Mn and Fe oxides and oxyhydroxides: A topological approach by EXAFS. *Phys. Chem. Miner.* **15**, 283-295.

Manceau, A., Marcus, M.A. and Grangeon, S. (2012) Determination of Mn valence states in mixed-valent manganates by XANES spectroscopy. *Am. Mineral.* **97**, 816-827.

Manceau, A., Marcus, M.A. and Tamura, N. (2002) Quantitative speciation of heavy metals in soils and sediments by synchrotron X-ray techniques. *Rev. Mineral. Geochem.* **49**, 341-428.

Manceau, A. and Nagy, K.L. (2012) Quantitative analysis of sulfur functional groups in natural organic matter by XANES spectroscopy. *Geochim. Cosmochim. Acta* **99**, 206-223.

Manceau, A., Tamura, N., Celestre, R.S., MacDowell, A.A., Geoffroy, N., Sposito, G. and Padmore, H.A. (2003) Molecular-scale speciation of Zn and Ni in soil ferromanganese nodules from loess soils of the Mississippi Basin. *Environ. Sci. Technol.* **37**, 75-80.

Manceau, A., Tommaseo, C., Rihs, S., Geoffroy, N., Chateigner, D., Schlegel, M., Tisserand, D., Marcus, M.A., Tamura, N. and Chen, Z.-S. (2005) Natural speciation of Mn, Ni, and Zn at the micrometer scale in a clayey paddy soil using X-ray fluorescence, absorption, and diffraction. *Geochim. Cosmochim. Acta* **69**, 4007-4034.

Marcus, M.A., Westphal, A.J. and Fakra, S.C. (2008) Classification of Fe-bearing species from K-edge XANES data using two-parameter correlation plots. *J. Synchrotron Rad.* **15**, 463-468.

Martin, S.T. (2005) Precipitation and dissolution of iron and manganese oxides. In: *Environmental Catalysis* (ed. V.H. Grassian). CRC Press, Boca Raton, Florida, pp. 61-82.

Mayanna, S., Peacock, C.L., Schäffner, F., Grawunder, A., Merten, D., Kothe, E. and Büchel, G. (2015) Biogenic precipitation of manganese oxides and enrichment of heavy metals at acidic soil pH. *Chem. Geol.* **402**, 6-17.

McKenzie, R. (1971) The synthesis of birnessite, cryptomelane, and some other oxides and hydroxides of manganese. *Mineral. Mag.* **38**, 493-502.

McKenzie, R.M. (1989) Manganese Oxides and Hydroxides. In: *Minerals in Soil Environments* eds. J.B. Dixon, S.B. Weed), 2nd ed. Soil Science Society of America, Madison, Wisconsin, pp. 439-465.

McKeown, D.A. and Post, J.E. (2001) Characterization of manganese oxide mineralogy in rock varnish and dendrites using X-ray absorption spectroscopy. *Am. Mineral.* **86**, 701-713.

Mikutta, C. and Rothwell, J.J. (2016) Peat bogs as hotspots for organoarsenical formation and persistence. *Environ. Sci. Technol.* **50**, 4314-4323.

Miura, H. (1986) The crystal structure of hollandite. *Mineral. Journal* **13**, 119-129.

Miyata, N., Tani, Y., Sakata, M. and Iwahori, K. (2007) Microbial manganese oxide formation and interaction with toxic metal ions. *J. Biosci. Bioeng.* **104**, 1-8.

Morales-Pérez, A., Moreno-Rodríguez, V., Del Rio-Salas, R., Imam, N.G., González-Méndez, B., Pi-Puig, T., Molina-Freaner, F. and Loredo-Portales, R. (2021) Geochemical changes of Mn in contaminated agricultural soils nearby historical mine tailings: Insights from XAS, XRD and SEP. *Chem. Geol.*

Mortvedt, J.J. (2000) Bioavailability of micronutients. In: *Handbook of Soil Science* (ed. M.E. Sumner). CRC Press, Boca Raton, FL, pp. D-71-88.

Narwall, R. and Singh, B. (2001) Solid phase speciation of iron and manganese in alum shale soils studied by parallel and sequential extraction. *Commun. Soil. Sci. Plant. Anal.* **32**, 331-349.

O'Day, P.A., Carroll, S.A., Randall, S., Martinelli, R.E., Anderson, S.L., Jelinski, J. and Knezovich, J.P. (2000) Metal speciation and bioavailability in contaminated estuary sediments, Alameda Naval Air Station, California. *Environ. Sci. Technol.* **34**, 3665-3673.

O'Day, P.A., Rivera, N., Jr., Root, R. and Carroll, S.A. (2004) X-ray absorption spectroscopic study of Fe reference compounds for the analysis of natural sediments. *Am. Mineral.* **89**, 572-585.

O'Reilly, S.E. and Hochella Jr, M.F. (2003) Lead sorption efficiencies of natural and synthetic Mn and Fe-oxides. *Geochim. Cosmochim. Acta* **67**, 4471-4487.

Ohmann, S., Abs-Wurmbach, I., Stüßer, N., Sabine, T. and Westerholt, K. (1998) The magnetic structure of braunite $Mn^{2+}Mn^{3+6}O_8/SiO_4$. *Z. Kristallogr. Cryst. Mater.* **213**, 19-27.

Peacock, C.L. and Moon, E.M. (2012) Oxidative scavenging of thallium by birnessite: Explanation for thallium enrichment and stable isotope fractionation in marine ferromanganese precipitates. *Geochim. Cosmochim. Acta* **84**, 297-313.

Post, J.E., Heaney, P.J. and Hanson, J. (2003) Synchrotron X-ray diffraction study of the structure and dehydration behavior of todorokite. *Am. Mineral.* **88**, 142-150.

Puzan, A.N., Baumer, V.N., Lisovytskiy, D.V. and Mateychenko, P.V. (2018) Structure disordering and thermal decomposition of manganese oxalate dihydrate, $MnC_2O_4{\cdot}2H_2O$. *J. Solid State Chem.* **260**, 87-94.

Qiang, T., Xiao-quan, S. and Zhe-ming, N. (1994) Evaluation of a sequential extraction procedure for the fractionation of amorphous iron and manganese oxides and organic matter in soils. *Sci. Total. Environ.* **151**, 159-165.

Ravel, B. (2014) Path degeneracy and EXAFS analysis of disordered materials. *J. Synchrotron Rad.* **21**, 1269-1274.

Ravel, B. and Newville, M. (2005) *ATHENA, ARTEMIS, HEPHAESTUS*: Data analysis for X-ray absorption spectroscopy using *IFEFFIT*. *J. Synchrotron Rad.* **12**, 537-541.

Remucal, C.K. and Ginder-Vogel, M. (2014) A critical review of the reactivity of manganese oxides with organic contaminants. *Environ. Sci.: Process. Impacts* **16**, 1247-1266.

Ressler, T., Brock, S.L., Wong, J. and Suib, S.L. (1999) Multiple-scattering EXAFS analysis of tetraalkylammonium manganese oxide colloids. *J. Phys. Chem. B* **103**, 6407-6420.

Rhoton, F., Bigham, J. and Schulze, D. (1993) Properties of iron-manganese nodules from a sequence of eroded Fragipan soils. *Soil. Sci. Soc. Am. J.* **57**, 1386-1392.

Ross, S.J., Franzmeier, D.P. and Roth, C.B. (1976) Mineralogy and chemistry of manganese oxides in some Indiana doils. *Soil. Sci. Soc. Am. J.* **40**, 137-143.

Scheckel, K.G. and Ryan, J.A. (2004) Spectroscopic speciation and quantification of lead in phosphate-amended soils. *J. Environ. Qual.* **33**, 1288-1295.

Scheinost, A.C., Kretzschmar, R., Pfister, S. and Roberts, D.R. (2002) Combining selective sequential extractions, X-ray absorption spectroscopy, and principal component analysis for quantitative zinc speciation in soil. *Environ. Sci. Technol.* **36**, 5021-5028.

Scheinost, A.C., Stanjek, H., Schulze, D.G., Gasser, U. and Sparks, D.L. (2001) Structural environment and oxidation state of Mn in goethite-groutite solid-solutions. *Am. Mineral.* **86**, 139-146.

Shen, X.F., Ding, Y.S., Liu, J., Cai, J., Laubernds, K., Zerger, R.P., Vasiliev, A., Aindow, M. and Suib, S.L. (2005) Control of Nanometer-Scale Tunnel Sizes of Porous Manganese Oxide Octahedral Molecular Sieve Nanomaterials. *Adv. Mater.* **17**, 805-809.

Silvester, E., Manceau, A. and Drits, V.A. (1997) Structure of synthetic monoclinic Na-rich birnessite and hexagonal birnessite: II. Results from chemical studies and EXAFS spectroscopy. *Am. Mineral.* **82**, 962-978.

Sutherland, R.A. and Tack, F.M. (2003) Fractionation of Cu, Pb and Zn in certified reference soils SRM 2710 and SRM 2711 using the optimized BCR sequential extraction procedure. *Adv. Environ. Res.* **8**, 37-50.

Szymański, W., Skiba, M. and Błachowski, A. (2014) Mineralogy of Fe-Mn nodules in Albeluvisols in the Carpathian Foothills, Poland. *Geoderma* **217**, 102-110.

Taira, H., Kitano, Y. and Kaneshima, K. (1981) Terrestrial ferro-manganese nodules formed in limestone areas of the Ryukyu Islands Part I Major and minor constituents of terrestrial ferro-manganese nodules. *Geochem. J.* **15**, 69-80.

Taylor, R., McKenzie, R. and Norrish, K. (1964) The mineralogy and chemistry of manganese in some Australian soils. *Soil Res.* **2**, 235-248.

Tebo, B.M., Bargar, J.R., Clement, B.G., Dick, G.J., Murray, K.J., Parker, D., Verity, R. and Webb, S.M. (2004) Biogenic manganese oxides: Properties and mechanisms of formation. *Annu. Rev. Earth Planet. Sci.* **32**, 287-328.

Tebo, B.M., Johnson, H.A., McCarthy, J.K. and Templeton, A.S. (2005) Geomicrobiology of manganese(II) oxidation. *Trends Microbiol.* **13**, 421-428.

Tokashiki, Y., Dixon, J. and Golden, D. (1986) Manganese oxide analysis in soils by combined X-ray diffraction and selective dissolution methods. *Soil. Sci. Soc. Am. J.* **50**, 1079-1084.

Tranqui, D., Burlet, P., Filhol, A. and Thomas, M. (1977) Redetermination by neutron diffraction of the structure of manganese acetate tetrahydrate (MAT). *Acta Crystallogr. B* **33**, 1357-1361.

Uzochukwu, G. and Dixon, J. (1986) Managanese oxide minerals in nodules of two soils of Texas and Alabama. *Soil. Sci. Soc. Am. J.* **50**, 1358-1363.

Villalobos, M., Lanson, B., Manceau, A., Toner, B. and Sposito, G. (2006) Structural model for the biogenic Mn oxide produced by *Pseudomonas putida*. *Am. Mineral.* **91**, 489-502.

Villalobos, M., Toner, B., Bargar, J. and Sposito, G. (2003) Characterization of the manganese oxide produced by *Pseudomonas putida* strain MnB1. *Geochim. Cosmochim. Acta* **67**, 2649-2662.

Villinski, J.E., O'Day, P.A., Corley, T.L. and Conklin, M.H. (2001) In situ spectroscopic and solution analyses of the reductive dissolution of MnO_2 by Fe(II). *Environ. Sci. Technol.* **35**, 1157-1163.

Wadsley, A. (1952) The structure of lithiophorite, $(Al,Li)MnO_2(OH)_2$. *Acta Crystallogr.* **5**, 676-680.

Waldrop, L. (1969) The crystal structure of triplite, $(Mn,Fe)_2FPO_4$. *Z. Kristallogr. Cryst. Mater.* **130**, 1-14.

Ward, J.H. (1963) Hierarchical grouping to optimize an objective function. *J. Am. Stat. Assoc.* **58**, 236-244.

Webb, S.M. (2005) SIXpack: A graphical user interface for XAS analysis using IFEFFIT. *Phys. Scr.* **2005**, 1011.

Webb, S.M., Tebo, B.M. and Bargar, J.R. (2005) Structural characterization of biogenic Mn oxides produced in seawater by the marine *Bacillus sp.* strain SG-1. *Am. Mineral.* **90**, 1342-1357.

Wilke, M., Farges, F., Petit, P.-E., Brown, G.E., Jr. and Martin, F. (2001) Oxidation state and coordination of Fe in minerals: An Fe *K*-XANES spectroscopic study. *Am. Mineral.* **86**, 714-730.

Yaroshevsky, A. (2006) Abundances of chemical elements in the Earth's crust. *Geochem. Int.* **44**, 48-55.

Ying, S.C., Kocar, B.D., Griffis, S.D. and Fendorf, S. (2011) Competitive microbially and Mn oxide mediated redox processes controlling arsenic speciation and partitioning. *Environ. Sci. Technol.* **45**, 5572-5579.

Zhang, M. and Karathanasis, A. (1997) Characterization of iron-manganese concretions in Kentucky Alfisols with perched water tables. *Clays Clay Miner.* **45**, 428-439.

A. Supporting information to chapter 2

A.1. Synthesis of Mn(II) adsorption samples

Batch Mn(II) adsorption experiments were performed with a natural 85:15-90:10 illite-smectite mineral from Füzérradvány, Hungary (<2-µm fraction; Dohrmann et al., 2009) and peat from a raised peat bog (Federseemoor) near Bad Buchau, Germany (40-250-µm fraction; Hoffmann et al., 2012). Both adsorbents were previously homogenized with agate mortar and pestle. Stock solutions of Mn^{2+} (10 mM) were prepared from $MnCl_2$ (98%, Merck) or $MnCl_2{\cdot}4H_2O$ (p.a., Roth) and ultrapure water (>18.2 MΩ·cm), which was purged with N_2 for a minimum of two hours to remove CO_2 and O_2. After Mn^{2+} addition, the suspension pH was adjusted to 5 or 7 with HNO_3 or NaOH. The suspensions (2 g/L solid concentration) were horizontally shaken (100 rpm) in the dark at room temperature for 24 hours, centrifuged, and vacuum-filtered through 12-25-µm cellulose filter papers (Whatman). The filter residues were rinsed with ultrapure water, shock-frozen in liquid N_2, freeze-dried, and stored in the dark at room temperature. Adsorbed Mn was calculated as the difference between initial Mn concentrations and Mn concentrations determined in the filtrates using inductively coupled plasma–mass spectrometry (Agilent 8900). Results are reported in Table 2.1

A.2. X-ray diffraction patterns of Mn reference compounds

Diffractograms of Mn reference compounds are shown in Figures A.1 and A.2. Mineral identities were confirmed in all cases using literature data and reference patterns (Table A.1). Here, we only detail important features (e.g., impurities) of the diffractograms where appropriate.

A2.1. Phyllo- and tectomanganates

Acid Na-birnessite shows four broad diffraction peaks. The peaks located at 11.7 and 24.0° 2theta are also visible for triclinic Na-birnessite and arise from (001) and (002) reflections of stacked octahedral sheets (Villalobos et al., 2003). Compared to triclinic Na-birnessite, both peaks are slightly shifted by about -0.4°. The broad peaks at 36.8 and 66.0° 2theta correspond to d-values of 2.4 and 1.4 Å respectively. The resulting d-value quotient of 1.71 is close to the expected ratio of unit-cell parameters, *b/a,* for hexagonal symmetry (Villalobos et al., 2003). δ-MnO_2 is characterized by broad *hkl* diffraction bands caused by its X-ray amorphous character. The poorly resolved basal (001) peak and the absence of a (002) reflection are typical features of δ-MnO_2 (Chukhrov and Gorshkov, 1980; Chukhrov et al., 1987; Post, 1999) indicating a small number of randomly stacked sheets per diffracting particle (Chukhrov et al., 1987; Grangeon et al., 2008). As with acid Na-birnessite, a hexagonal layer

symmetry is evident from the broad peaks at ~37.4 and ~65.8° 2theta, corresponding to a d-value quotient of 1.71.

Triclinic Na-birnessite shows a set of sharp and well-defined reflections, indicating a high crystallinity. The peak at 19.3° 2theta could not be assigned to any phase. In any case, hausmannite, a typical interstitial phase that can form during synthesis, could be excluded.

The XRD patterns of natural and synthetic cryptomelanes show a perfect match of all reflections. Compared to the natural mineral, the reflections of synthetic cryptomelane have smaller widths, suggesting a slightly higher crystallinity. Synthetic cryptomelane shows one additional sharp peak at 8.7° 2theta, which could not be explained. Remains of the acid birnessite precursor phase were not detectable.

Natural and synthetic pyrolusites exhibit similar XRD patterns with the main (110) reflection at 28.6° 2theta. Natural pyrolusite shows two small additional peaks at 26.2° and 34.0° 2theta caused by a manganite impurity. The sharper reflections of synthetic compared to natural pyrolusite indicate a higher crystallinity of the synthetic mineral.

Ramsdellite shows its main (110) and (130) reflections at 21.8 and 35.1° 2theta. The XRD pattern is characterized by sharp diffraction peaks indicating a high degree of crystallinity. Pyrolusite was identified as an impurity phase.

The diffractogram of synthetic Ba-free romanèchite is similar to that presented in Shen et al. (2005) with characteristic (200) and (400) reflections at 12.5 and 25.1° 2theta. However, the typical small (001) reflection at ~9.2° 2theta (d ~9.7 Å) was not observed, potentially caused by preferred orientation of the needle-shaped crystals along [001]. The peak labelled as (-311) in Shen et al. (2004) actually lies at ~38.0° 2theta (Turner and Post, 1988).

A2.2. Oxide minerals without layer or tunnel structure

Natural and synthetic bixbyites show nearly identical XRD patterns, which are in agreement with the standard pattern of bixbyite. Synthetic bixbyite shows an additional peak at 28.8° 2theta, which likely arises from a pyrolusite impurity.

A2.3. Mn(III) oxyhydroxides

The peaks at 29.5 and 43.2° 2theta in the diffraction pattern of groutite originate from calcite. Additional reflections of a manganite impurity appear at 26.4, 33.7, 37.1, 54.4, and 55.6° 2theta. All other peaks are consistent with groutite.

A2.4. Carbonate, phosphate, and silicate minerals

The XRD pattern of braunite is fully consistent with the corresponding reference pattern. Additional reflections originate from quartz.

The XRD pattern of hendricksite shows additional small peaks of another mica, likely annite, the Fe-endmember of trioctahedral micas. Diffraction patterns of hendricksite and masutomilite are influenced by preferred orientation, resulting in enhanced 00*l* reflections. However, peak displacements due to preferred orientation (da Silva and de Oliveira, 2011) were not observed.

The XRD pattern of triplite is consistent with a solid-solution of triplite and zwiselite, the Fe-endmember of this mineral group. As evidenced by EPMA, the sample contains a considerable amount of Fe^{2+} (0.74 apfu; Tables 2.1 and A.2). The diffraction peaks are intermediate between triplite and zwiselite and occasionally show double peaks due to slight shifts of each endmember pattern.

A2.5. Compounds used for Mn(II) adsorption

The 'illite' sample is a natural 85:15-90:10 R3-ordered illite-smectite mixed layer mineral (Dohrmann et al., 2009). Its diffraction pattern shows prominent 00*l* reflections at 8.6, 17.8, 26.6 and 45.3° 2theta, which are common to illite and smectite minerals. Contributions of other crystalline mineral phases were not detected. The peat material is characterized by broad diffuse scattering and a single quartz reflection at 26.6° 2theta.

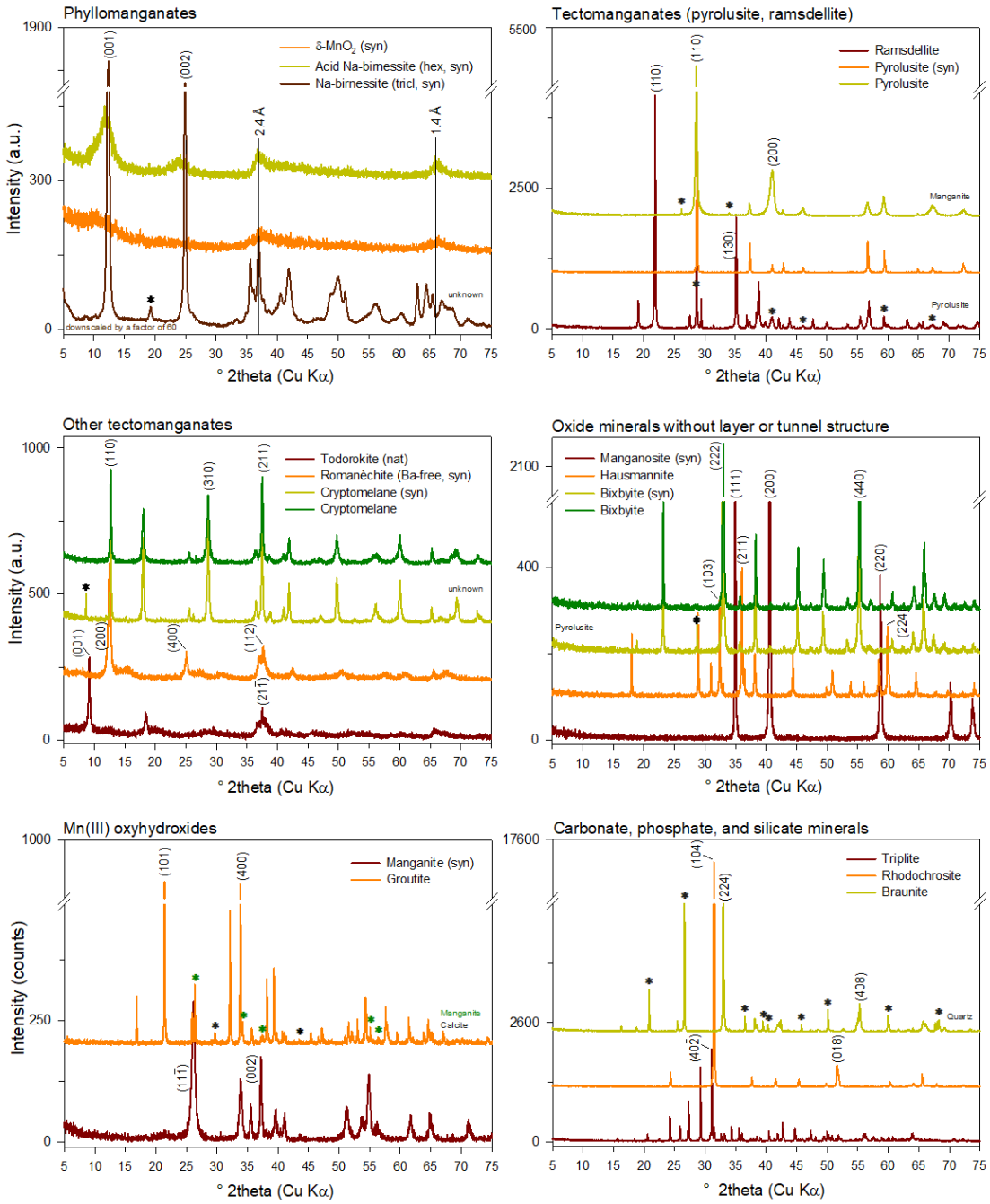

Figure A.1. Diffractograms of phyllo- and tectomanganates, oxide minerals without layer or tunnel structure, Mn(III) oxyhydroxides as well as carbonate, phosphate, and silicate minerals. Main reflections are indexed and asterisks indicate impurities (see text for further details).

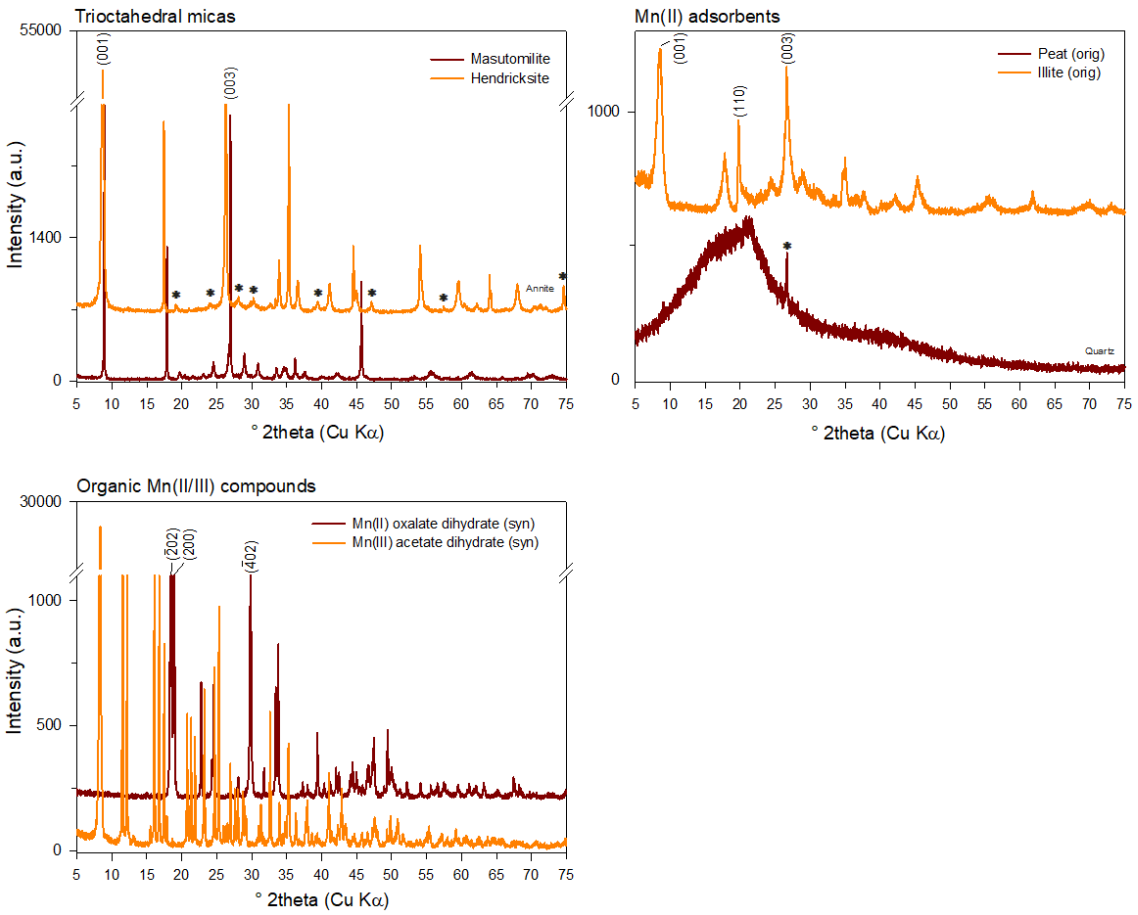

Figure A.2. Diffractograms of trioctahedral micas, the Mn(II) adsorbents illite and peat, and organic Mn(II)/(III) compounds. Main reflections are indexed and asterisks indicate impurities (see text for further details).

Table A.1. Crystallographic properties and literature references or powder diffraction file (pdf) numbers used for the evaluation of XRD patterns of Mn reference compounds

Mineral	Crystal system	Space group	Literature reference or reference pattern (pdf no.)
Pyllomanganates			
Acid Na-birnessite (hex, syn)	Hexagonal	-	Villalobos et al. (2003)
δ-MnO_2	Hexagonal	-	Villalobos et al. (2003)
Na-birnessite (tricl, syn)	Triclinic	-	Villalobos et al. (2003)
Tectomanganates			
Cryptomelane	Monoclinic	***I*2/*m***	Cryptomelane (00-044-1386)
Cryptomelane (syn)	Monoclinic	***I*2/*m***	Cryptomelane (00-044-1386)
Pyrolusite	Tetragonal	$P4_2/mnm$	Pyrolusite syn (01-081-2261) Manganite (01-088-0649)
Pyrolusite (syn)	Tetragonal	$P4_2/mnm$	Pyrolusite syn (01-081-2261)
Ramsdellite	Orthorhombic	*Pbnm*	Ramsdellite (00-043-1455)
Romanèchite (Ba-free)	Monoclinic	C2/m	Romanèchite (00-014-0627)
Todorokite (nat)	Monoclinic	*P*2/*m*	Todorokite (00-038-0475)
Oxide minerals without layer or tunnel structure			
Bixbyite (nat)	Cubic	*Ia*3	Bixbyite C (01-075-0894)
Bixbyite (syn)	Cubic	*Ia*3	Bixbyite C (01-075-0894)
Hausmannite	Tetragonal	$I4_1/amd$	Hausmannite calc. (01-080-0382)
Manganosite (syn)	Cubic	*Fm*3*m*	Manganosite (01-075-1090)
Mn(III) oxyhydroxides			
Manganite (syn)	Monoclinic	$P2_1/c$	Manganite (00-088-0649)
Groutite	Orthorhombic	*Pnma*	Groutite (01-088-0648), Calcite (00-005-0586), Manganite (01-088-0649)
Carbonate, phosphate, and silicate minerals			
Braunite	Tetragonal	$I4_1/acd$	Braunite-1Q (v00-033-0904) Quartz (01-079-1910)
Hendricksite	Monoclinic	*B2/m*	Hendricksite-1M (00-019-0544) Annite-1 (00-045-1444)
Masutomilite	Monoclinic	*C2*	Masutomilite (00-029-0822)
Rhodochrosite	Trigonal	$R\bar{3}c$	Rhodochrosite, syn (00-044-1472)
Triplite	Monoclinic	$I2/a$	Triplite (00-005-0621), Zwiselite (00-021-0811)
Organic Mn(II/III) compounds			
Mn(II) oxalate dihydrate (syn)	Monoclinic	*C*2/*c*	Mn oxalate dihydrate (00-025-0544)
Mn(III) acetate dihydrate (syn)	-	-	-
Adsorbed Mn(II) species			
Illite	Monoclinic	*C*2/*m*	Illite-1 (00-029-1496), Montmorillonite (00-029-1499), Illite-Montmorillonite (00-035-0652)
Peat	-	-	Quartz (01-083-0539)

A.3. CHEMICAL CHARACTERIZATION OF MN REFERENCE COMPOUNDS

Based on chemical compositions determined by EPMA and acid digestions followed by ICP-OES measurements, empirical mineral formulas were calculated after normalization to oxygen (Table 1). Fractional amounts of Mn^{2+}, Mn^{3+}, and Mn^{4+} per formula unit were determined by charge-balance calculations (Deer, 1992). All chemical analysis results are summarized in Table S2. Detection limits for each element measured are provided in Table A.3.

For acid digestions, ~100 mg of powdered sample material was placed in Teflon beakers with screw caps. Acid reagents used were 69% HNO_3 (suprapur, Roth), 37% HCl (p.a., Roth), and, if necessary, 40% HF (p.a., Merck) and 30% H_2O_2 (suprapur, Merck). The peat material was previously combusted at 550 °C over night in a ceramic crucible and quantitatively transferred to a Teflon beaker. The illite sample was previously digested in 3 mL HNO_3 and 5 mL HF over night at 120 °C. Afterwards, the peat and illite samples were treated identically to all other samples. Sample powders of all compounds were digested at 120-140 °C in aqua regia (3:1 v/v HCl:HNO_3) for 12-24 hours. After complete dissolution and vaporization of reagents, the samples were finally taken up in 3% (w/w) HNO_3 and elemental concentrations in solutions determined by ICP-OES (Agilent 5900 SVDV). All samples were digested at least in duplicate. Data quality was monitored by including procedural and measurements blanks. The accuracy of digestions was determined by comparing measured element concentrations of USGS BHVO-1 (basalt) and NIST SRM 2710a (Montana I Soil) reference materials with their certified values. Percent recoveries were always >96%.

A3.1. NOTES ON EMPIRICAL FORMULA CALCULATIONS

The determination of correct empirical mineral formulas for birnessite modifications is complex. Especially the calculation of vacancies is closely related to the valence of structural Mn cations (Drits et al., 1997; Villalobos et al., 2003). For example, Drits et al. (1997) showed that different empirical mineral formulas ($Na_{0.6}Mn^{4+}_{1.4}Mn^{3+}_{0.6}O_4$ and $Na_{0.6}Mn^{4+}_{1.85}vac_{0.15}O_4$; vac = lattice vacancy) can be calculated from the same chemical birnessite analysis. Variable proportions of each Mn valence might be present in members of the birnessite family, and there is also the possibility of O atom replacements by OH groups and the formation of layer vacancies (Drits et al., 1997). Villalobos et al. (2006) stated the mineral formula of hexagonal acid Na-birnessite with $H_{0.06}K_{0.18}(H_2O)_{0.54}Mn^{3+}_{0.08}(H_2O)_{0.24}[Mn^{4+}_{0.88},vac_{0.12}]O_2$, and we adopted this formula since the mineral synthesis was exactly carried out as described in this study. The same is true for triclinic Na-birnessite and δ-MnO_2, whose formulas were given by Villalobos et al. (2003) as $Na_{0.26}(Mn^{4+}_{0.74}Mn^{3+}_{0.26})O_2$ and $Na_{0.24}(H_2O)_{0.72}(Mn^{4+}_{0.94},vac_{0.06})O_2$, respectively. Formula calculation of natural and synthetic cryptomelane was based on 16 O atoms and 9 cations. As for hollandite, Mn in cryptomelane is mainly

reported as Mn^{4+} and Mn^{3+} (Post et al., 1982; Biagioni et al., 2013). Similar to these studies, we also used the assumption of Mn^{4+} and Mn^{3+} prevalence in cryptomelanes. For Ba-free romanèchite, the mineral formula calculation based on 24 O atoms (Shen et al., 2004) did not provide results consistent with elemental analysis. Therefore, the formula calculation was based on oxygen and cation numbers typical for Ba-romanèchite, that is, 6 cations, 10 O atoms, and one H_2O molecule as given in Anthony et al. (2003).

Table A.2. Average composition of Mn reference compounds determined by EPMA and acid digestions (ICP-OES). Chemical data were recalculated into atoms per formula unit (apfu) based on the number of oxygens given below. Numbers in parentheses represent standard deviations of the last significant figure

	Acid Na-birnessite (hex, syn)	**Bixbyite**	**Braunite**	**Cryptomelane (nat)**	**Cryptomelane (syn)**	**δ-MnO_2**
wt. %	**ICP-OES**	**EPMA**	**EPMA**	**EPMA**	**ICP-OES**	**ICP-OES**
	***N* = 3**[a]	***N* = 4**	***N* = 6**	***N* = 3**	***N* = 1**	***N* = 2**
P_2O_5	n.d.[b]	b.d.l.[c]	b.d.l.	b.d.l.	n.d.	n.d.
SiO_2	0.00(0)	b.d.l.	9.26(80)	0.37(0)	0.01	0.00(0)
TiO_2	n.d.	0.15(2)	b.d.l.	b.d.l.	n.d.	n.d.
Al_2O_3	b.d.l.	1.44(7)	0.07(10)	0.42(4)	0.01	b.d.l.
Cr_2O_3	0.01(0)	b.d.l.	b.d.l.	b.d.l.	0.01	0.00(0)
Fe_2O_3	b.d.l.	10.41(27)	b.d.l.	b.d.l.	0.00	b.d.l.
MnO	70.27(47)	77.37(46)	79.02(120)	73.91(37)	79.87	62.78(15)
BaO	0.00	b.d.l.	b.d.l.	0.09(0)	b.d.l.	b.d.l.
CaO	b.d.l.	b.d.l.	1.38(26)	0.30(1)	0.03	b.d.l.
FeO	n.a.[d]	n.a.	n.a.	n.a.	n.a.	n.a.
MgO	0.00	b.d.l.	b.d.l.	b.d.l.	0.00	0.00(0)
PbO[e]	0.37(4)	n.d.	n.d.	n.d.	0.36	0.14(14)
SrO	n.d.	b.d.l.	b.d.l.	0.21(2)	n.d.	n.d.
ZnO	0.00(0)	b.d.l.	b.d.l.	0.30(1)	0.00	0.00(0)
K_2O	5.49(29)	b.d.l.	b.d.l.	4.84(10)	5.81	b.d.l.
Li_2O[e]	0.30(42)	n.d.	n.d.	n.d.	b.d.l.	b.d.l.
Na_2O	b.d.l.	b.d.l.	b.d.l.	0.25(2)	b.d.l.	6.09(125)
Cl	n.d.	b.d.l.	b.d.l.	b.d.l.	n.d.	n.d.
F	n.d.	b.d.l.	b.d.l.	b.d.l.	n.d.	n.d.
Total	**76.44**	**89.37(23)**	**89.73(71)**	**80.68(51)**	**86.10**	**69.01(129)**
O = Cl, F						
H_2O calculated[f]						
CO_2 calculated[f]						
Total corrected	**n.d.**	**98.10(27)**	**97.74(77)**	**96.07(63)**	**102.66**	**n.d.**
apfu based on:						
Moles O[g]		3.00	12.00	16.00	16.00	
Moles cations		2.00	8.00	9.00	9.00	
Moles H_2O						
Moles OH						
apfu						
P^{5+}		b.d.l.	b.d.l.	b.d.l.	0.00	
Mn^{4+}		0.00(0)	0.00(0)	6.73(3)	6.79	
Si^{4+}		b.d.l.	0.95(8)	0.05	0.00	
Ti^{4+}		0.00(0)	b.d.l.	b.d.l.	0.00	
Al^{3+}		0.05(0)	0.01(1)	0.06(1)	0.00	
Cr^{3+}		b.d.l.	b.d.l.	b.d.l.	0.00	
Fe^{3+}		0.21(1)	b.d.l.	b.d.l.	0.00	
Mn^{3+}		1.74(1)	6.08(16)	1.22(5)	1.31	
Ba^{2+}		b.d.l.	b.d.l.	0.00(0)	b.d.l.	
Ca^{2+}		b.d.l.	0.15(3)	0.04(0)	0.00	
Fe^{2+}		0.00(0)	b.d.l.	b.d.l.	0.00	
Mg^{2+}		b.d.l.	b.d.l.	b.d.l.	0.00	
Mn^{2+}		0.00(0)	0.80(8)	0.00(0)	0.00	
Pb^{2+}		n.d.	n.d.	n.d.	0.01	
Sr^{2+}		b.d.l.	b.d.l.	0.02(0)	0.00	
Zn^{2+}		b.d.l.	b.d.l.	0.03(0)	0.00	
K^{+}		b.d.l.	b.d.l.	0.78(1)	0.89	
Li^{+}		n.d.	n.d.	n.d.	b.d.l.	
Na^{+}		b.d.l.	b.d.l.	0.06(0)	b.d.l.	
H^{+}		-	-	-	-	
Cl		b.d.l.	b.d.l.	b.d.l.	-	
F		b.d.l.	b.d.l.	b.d.l.	-	

[a]*N* = number of analysis points/samples analyzed. [b]n.d. = not determined. [c]b.d.l. = below detection limit (Table A.3).
[d]n.a.= not applicable. [e]PbO and Li_2O determined from ICP-OES measurements. [f]Calculated from stoichiometry. H_2O for hendricksite and masutomilite calculated 'by difference' such as to yield Σ(OH, F) = 2.0 and for triplite Σ(O, OH, F) = 1.0. [g]Moles (O, OH, F) for hendricksite, masutomilite, and triplite.

Table A.2. *(continued)*

	Groutite	**Hausmannite**	**Hendricksite**	**Manganite (syn)**	**Masutomilite**	**Na-birnessite (tricl, syn)**
wt. %	**EPMA**	**EPMA**	**EPMA**	**ICP-OES**	**EPMA**	**ICP-OES**
	***N* = 4**	***N* = 3**	***N* = 3**	***N* = 1**	***N* = 4**	***N* = 2**
P_2O_5	b.d.l.	b.d.l.	b.d.l.	n.d.	b.d.l.	n.d.
SiO_2	0.22(10)	b.d.l.	33.94(3)	0.01	51.09(47)	0.00(0)
TiO_2	b.d.l.	b.d.l.	0.21(1)	n.d.	b.d.l.	n.d.
Al_2O_3	0.25(7)	b.d.l.	11.86(4)	0.01	22.74(43)	0.02(2)
Cr_2O_3	b.d.l.	b.d.l.	b.d.l.	0.01	b.d.l.	0.00(0)
Fe_2O_3	b.d.l.	0.77(56)	-	0.01	-	0.00(0)
MnO	77.77(70)	90.92(79)	10.69(14)	84.80	3.15(24)	71.14(25)
BaO	0.57(82)	b.d.l.	0.23(2)	b.d.l.	b.d.l.	0.00(0)
CaO	b.d.l.	0.00(0)	b.d.l.	0.01	b.d.l.	0.01(0)
FeO	-	-	3.99(6)	-	b.d.l.	
MgO	0.35(5)	0.04(2)	6.09(2)	b.d.l.	b.d.l.	0.00(0)
PbO[e]	n.d.	n.d.	n.d.	0.38	b.d.l.	0.40(5)
SrO	b.d.l.	b.d.l.	b.d.l.	n.d.	b.d.l.	n.d.
ZnO	b.d.l.	b.d.l.	20.72(9)	0.00	0.08(2)	b.d.l.
K_2O	b.d.l.	b.d.l.	8.73(17)	b.d.l.	9.96(22)	0.01(1)
Li_2O[e]	n.d.	n.d.	n.d.	b.d.l.	5.68(0)	b.d.l.
Na_2O	b.d.l.	b.d.l.	0.41(0)	b.d.l.	0.32(8)	8.42(47)
Cl	b.d.l.	b.d.l.	b.d.l.	n.d.	0.08(2)	n.d.
F	b.d.l.	b.d.l.	b.d.l.	n.d.	9.70(48)	n.d.
Total	79.16(36)	91.73(32)	96.85(26)	85.22	102.80(111)	80.01(28)
O = Cl, F			0.00(0)		4.10(20)	
H_2O calculated[f]	10.25(6)		3.55(0)	10.22		
CO_2 calculated[f]						
Total corrected	**98.17(32)**	**98.55(37)**	**100.41(27)**	**105.00**	**98.70(96)**	**n.d.**
apfu based on:						
Moles O[g]	1.50	4.00	12.00	1.50	12.00	
Moles cations	1.00	3.00	8.00	1.00	8.00	
Moles H_2O			1.00			
Moles OH	1.00			1.00		
apfu						
P^{5+}	b.d.l.	b.d.l.	b.d.l.	0.00	b.d.l.	
Mn^{4+}	0.00(0)	0.00(0)	0.00(0)	0.00	0.00(0)	
Si^{4+}	0.00(0)	b.d.l.	2.83(0)	0.00	3.43(3)	
Ti^{4+}	b.d.l.	b.d.l.	0.01(0)	0.00	b.d.l.	
Al^{3+}	0.00(0)	b.d.l.	1.17(0)	0.00	1.80(1)	
Cr^{3+}	b.d.l.	b.d.l.	b.d.l.	0.00	b.d.l.	
Fe^{3+}	b.d.l.	0.02(2)	0.00(0)	0.00	b.d.l.	
Mn^{3+}	0.98(1)	1.98(2)	0.00(0)	1.00	0.00(0)	
Ba^{2+}	0.00(0)	b.d.l.	0.01(0)	b.d.l.	b.d.l.	
Ca^{2+}	b.d.l.	0.00(0)	b.d.l.	0.00	b.d.l.	
Fe^{2+}	b.d.l.	0.00(0)	0.28(0)	0.00	b.d.l.	
Mg^{2+}	0.01(0)	0.00(0)	0.76(0)	b.d.l.	b.d.l.	
Mn^{2+}	0.00(0)	1.00(0)	0.76(1)	0.00	0.18(1)	
Pb^{2+}	n.d.	n.d.	n.d.	0.00	n.d.	
Sr^{2+}	b.d.l.	b.d.l.	b.d.l.	0.00	b.d.l.	
Zn^{2+}	b.d.l.	b.d.l.	1.28(1)	0.00	0.00(0)	
K^+	b.d.l.	b.d.l.	0.93(2)	b.d.l.	0.85(1)	
Li^+	n.d.	n.d.	0.00(0)	b.d.l.	1.53(2)	
Na^+	b.d.l.	b.d.l.	0.07(0)	b.d.l.	0.04(1)	
H^+	1.00(0)	-	1.98(0)	1.00	0.00(0)	
Cl^-	b.d.l.	b.d.l.	b.d.l.	n.d.	0.01(0)	
F^-	b.d.l.	b.d.l.	b.d.l.	n.d.	2.06(9)	

[a]*N* = number of analysis points/samples analyzed. [b]n.d. = not determined. [c]b.d.l. = below detection limit (Table A.3). [d]n.a.= not applicable. [e]PbO and Li_2O determined from ICP-OES measurements. [f]Calculated from stoichiometry. H_2O for hendricksite and masutomilite calculated 'by difference' such as to yield Σ(OH, F) = 2.0 and for triplite Σ(O, OH, F) = 1.0. [g]Moles (O, OH, F) for hendricksite, masutomilite, and triplite.

Table A.2. ***(continued)***

	Pyrolusite	**Ramsdellite**	**Rhodochrosite**	**Romanèchite (Ba-free, syn)**	**Todorokite**	**Triplite**
wt. %	**EPMA**	**EPMA**	**EPMA**	**ICP-OES**	**EPMA**	**EPMA**
	***N* = 5**	***N* = 4**	***N* = 3**	***N* = 2**	***N* = 4**	***N* = 3**
P_2O_5	b.d.l.	b.d.l.	b.d.l.	b.d.l.	b.d.l.	31.45(2)
SiO_2	0.13(7)	0.17(10)	b.d.l.	b.d.l.	0.17(4)	b.d.l.
TiO_2	b.d.l.	b.d.l.	b.d.l.	0.00(0)	b.d.l.	0.16(0)
Al_2O_3	0.84(18)	0.37(34)	b.d.l.	b.d.l.	b.d.l.	b.d.l.
Cr_2O_3	b.d.l.	b.d.l.	b.d.l.	b.d.l.	b.d.l.	b.d.l.
Fe_2O_3	b.d.l.	b.d.l.	0.44(62)	b.d.l.	b.d.l.	-
MnO	79.33(26)	79.55(45)	55.39(148)	77.16(91)	67.00(42)	34.94(14)
BaO	0.20(4)	0.07(4)	b.d.l.	b.d.l.	0.67(18)	b.d.l.
CaO	0.06(1)	0.21(6)	0.79(21)	b.d.l.	1.94(11)	2.46(1)
FeO	-	-	-	-	-	23.86(16)
MgO	b.d.l.	0.07(4)	0.21(2)	b.d.l.	1.48(26)	0.93(4)
PbO[e]	n.d.	n.d.	n.d.	0.38(3)	n.d.	n.d.
SrO	b.d.l.	b.d.l.	b.d.l.	b.d.l.	2.36(55)	b.d.l.
ZnO	b.d.l.	b.d.l.	1.88(21)	0.00(0)	1.09(5)	0.11(1)
K_2O	b.d.l.	b.d.l.	b.d.l.	b.d.l.	0.82(9)	b.d.l.
Li_2O[e]	n.d.	n.d.	n.d.	b.d.l.	n.d.	n.d.
Na_2O	b.d.l.	0.05(1)	0.08(1)	7.42(3)	1.08(12)	b.d.l.
Cl^-	b.d.l.	b.d.l.	b.d.l.	b.d.l.	b.d.l.	b.d.l.
F^-	b.d.l.	b.d.l.	b.d.l.	b.d.l.	b.d.l.	6.68(9)
Total	**80.57(28)**	**80.48(23)**	**58.79(98)**	**85.07(94)**	**76.62(83)**	**100.60(0)**
O = Cl, F						2.81(4)
H_2O calculated[f]				3.81	8.73(5)	0.85(0)
CO_2 calculated[f]			38.34(7)			
Total corrected	**98.46(33)**	**98.42(24)**	**97.08(91)**	**104.46(109)**	**98.42(88)**	**99.99(4)**
apfu based on:						
Moles O[g]	2.00	2.00	1.00	10.00	12.00	5.00
Moles cations	1.00	1.00	1.00	6.00	7.00	3.00
Moles H_2O				1.00	3.00	
Moles OH						
apfu						
P^{5+}	b.d.l.	b.d.l.	b.d.l.	b.d.l.	b.d.l.	0.99(0)
Mn^{4+}	0.99(0)	0.99(1)	0.00(0)	4.16(2)	5.15(1)	0.00(0)
Si^{4+}	0.00(0)	0.00(0)	b.d.l.	b.d.l.	0.02(0)	b.d.l.
Ti^{4+}	b.d.l.	b.d.l.	b.d.l.	0.00(0)	b.d.l.	0.00(0)
Al^{3+}	0.01	0.01(1)	b.d.l.	b.d.l.	b.d.l.	b.d.l.
Cr^{3+}	b.d.l.	b.d.l.	b.d.l.	b.d.l.	b.d.l.	b.d.l.
Fe^{3+}	b.d.l.	b.d.l.	0.00(1)	b.d.l.	b.d.l.	0.00(0)
Mn^{3+}	0.00(0)	0.00(0)	0.00(0)	0.75(2)	0.00(0)	0.00(0)
Ba^{2+}	0.00(0)	0.00(0)	b.d.l.	b.d.l.	0.03(1)	b.d.l.
Ca^{2+}	b.d.l.	0.00(0)	0.02(0)	b.d.l.	0.22(1)	0.10(0)
Fe^{2+}	b.d.l.	b.d.l.	0.00(0)	0.00(0)	b.d.l.	0.75(1)
Mg^{2+}	b.d.l.	0.00(0)	0.01(0)	b.d.l.	0.23(4)	0.05(0)
Mn^{2+}	0.00(0)	0.00(0)	0.94(1)	0.00(0)	0.80(3)	1.11(0)
Pb^{2+}	n.d.	n.d.	n.d.	0.01(0)	n.d.	n.d.
Sr^{2+}	b.d.l.	b.d.l.	b.d.l.	b.d.l.	0.14(3)	b.d.l.
Zn^{2+}	b.d.l.	b.d.l.	0.03(0)	0.00(0)	0.08(0)	0.00(0)
K^+	b.d.l.	b.d.l.	b.d.l.	b.d.l.	0.11(1)	b.d.l.
Li^+	n.d.	n.d.	n.d.	b.d.l.	n.d.	n.d.
Na^+	b.d.l.	0.00(0)	0.00(0)	1.08(1)	0.22(2)	b.d.l.
H^+	-	-	-	2.00(0)	-	0.21(0)
Cl^-	b.d.l.	b.d.l.	b.d.l.	b.d.l.	b.d.l.	b.d.l.
F^-	b.d.l.	b.d.l.	b.d.l.	b.d.l.	b.d.l.	0.79(1)

[a]*N* = number of analysis points/samples analyzed. [b]n.d. = not determined. [c]b.d.l. = below detection limit (Table A.3). [d]n.a.= not applicable. [e]PbO and Li_2O determined from ICP-OES measurements. [f]Calculated from stoichiometry. H_2O for hendricksite and masutomilite calculated 'by difference' such as to yield Σ(OH, F) = 2.0 and for triplite Σ(O, OH, F) = 1.0. [g]Moles (O, OH, F) for hendricksite, masutomilite, and triplite.

Table A.3. Detection limits (µg/g) of EPMA and ICP-OES analysis

Element	EPMA	ICP-OES
Al	318	0.061
Ba	308	0.004
Ca	259	0.145
Cl	69	n.d.
Cr	334	0.182
F	1,318	n.d.
Fe	338	0.018
K	572	1.583
Li	n.d.	0.018
Mg	234	0.184
Mn	825	0.026
Na	210	0.324
P	564	n.d.
Pb	n.d.	0.047
Si	392	0.211
Sr	555	n.d.
Ti	273	n.d.
Zn	439	0.055

n.d. = not determined.

A.4. Manganese K-edge XAS of Mn reference compounds

A4.1. Sample preparation

Samples were hand-ground to a very fine powder in an agate mortar. For transmission measurements (absorber concentration: >20 g/kg), powders were diluted with boron nitride and CEREOX® wax (Fluxana) such as to yield an edge-step absorption, µx, of ~1 and prepared as pressed pellets (Ø: 1.3 cm) sealed with Kapton® tape. Samples for fluorescence measurements were directly filled into sample holders and sealed with Kapton® tape (BL 7-3 (SSRL), P64 and 65 (DESY)). At beamline 5-BM-D (APS), pellets for transmission-mode measurements were mounted into a Lincam cell.

A4.2. Manganese K-edge EXAFS fits

Figures A.3 and A.4 show k^3-weighted Mn K-edge EXAFS spectra, their Fourier-transform magnitudes and real parts as well as corresponding model fits (dotted lines) of all Mn reference compounds. Table A.4 lists literature sources used to compare interatomic distances extracted from shell-fit analyses and summarized in Figure 2.7.

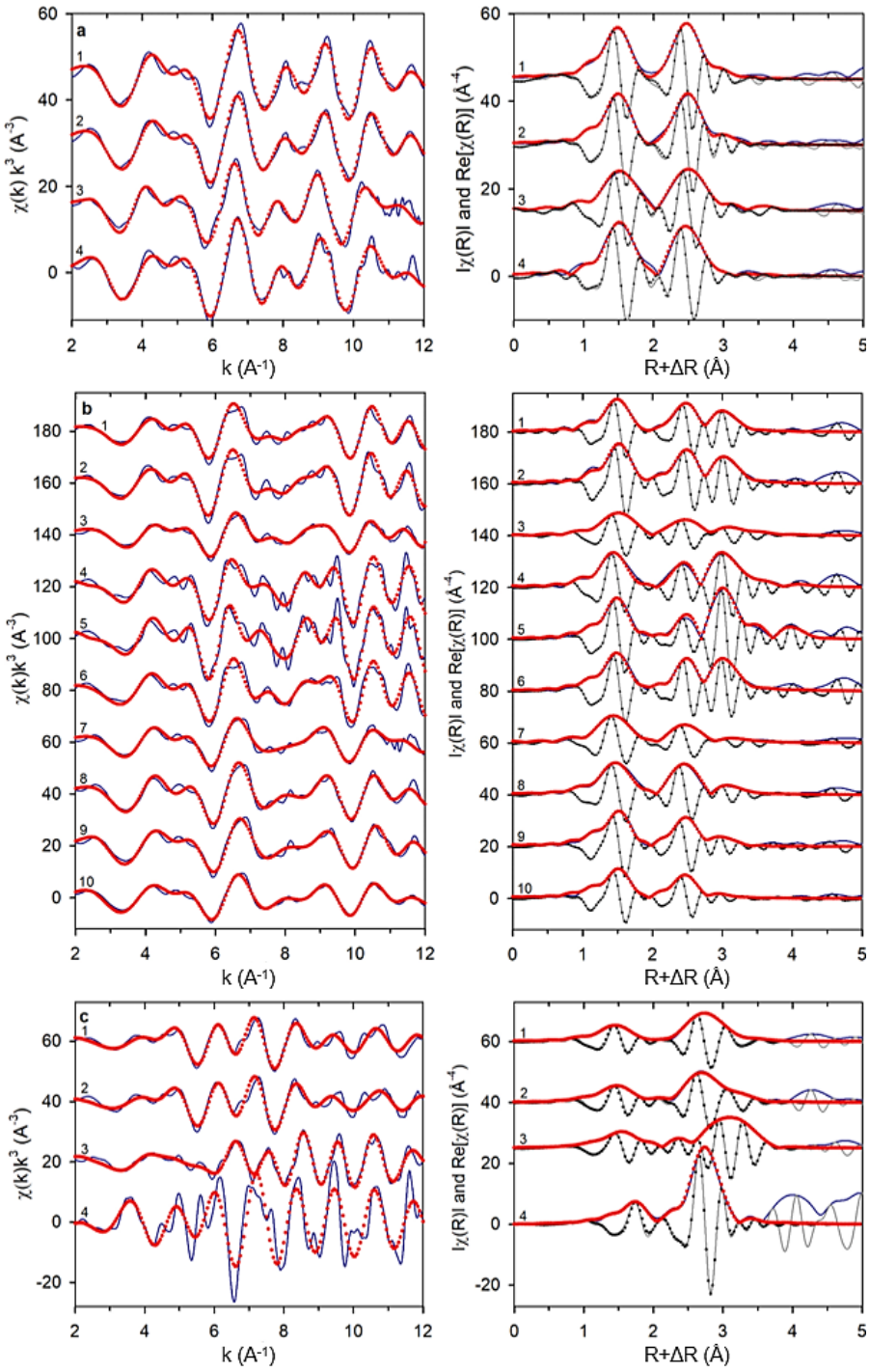

Figure A.3.
Phyllomanganates (a):
1 - acid Na-birnessite (hex, syn),
2 - δ-MnO_2 (syn),
3 - lithiophorite,
4 - Na-birnessite (tricl, syn);

Tectomanganates (b):
1 - cryptomelane (nat),
2 - cryptomelane (syn),
3 - hollandite,
4 - pyrolusite,
5 - pyrolusite (syn),
6 - ramsdellite,
7 - romanèchite (nat),
8 - romanèchite (Ba-free, syn),
9 - todorokite,
10 - todorokite (syn);

Oxide minerals without layer or tunnel structure (c):
1 - bixbyite (nat),
2 - bixbyite (syn),
3 - hausmannite,
4 - manganosite (syn).

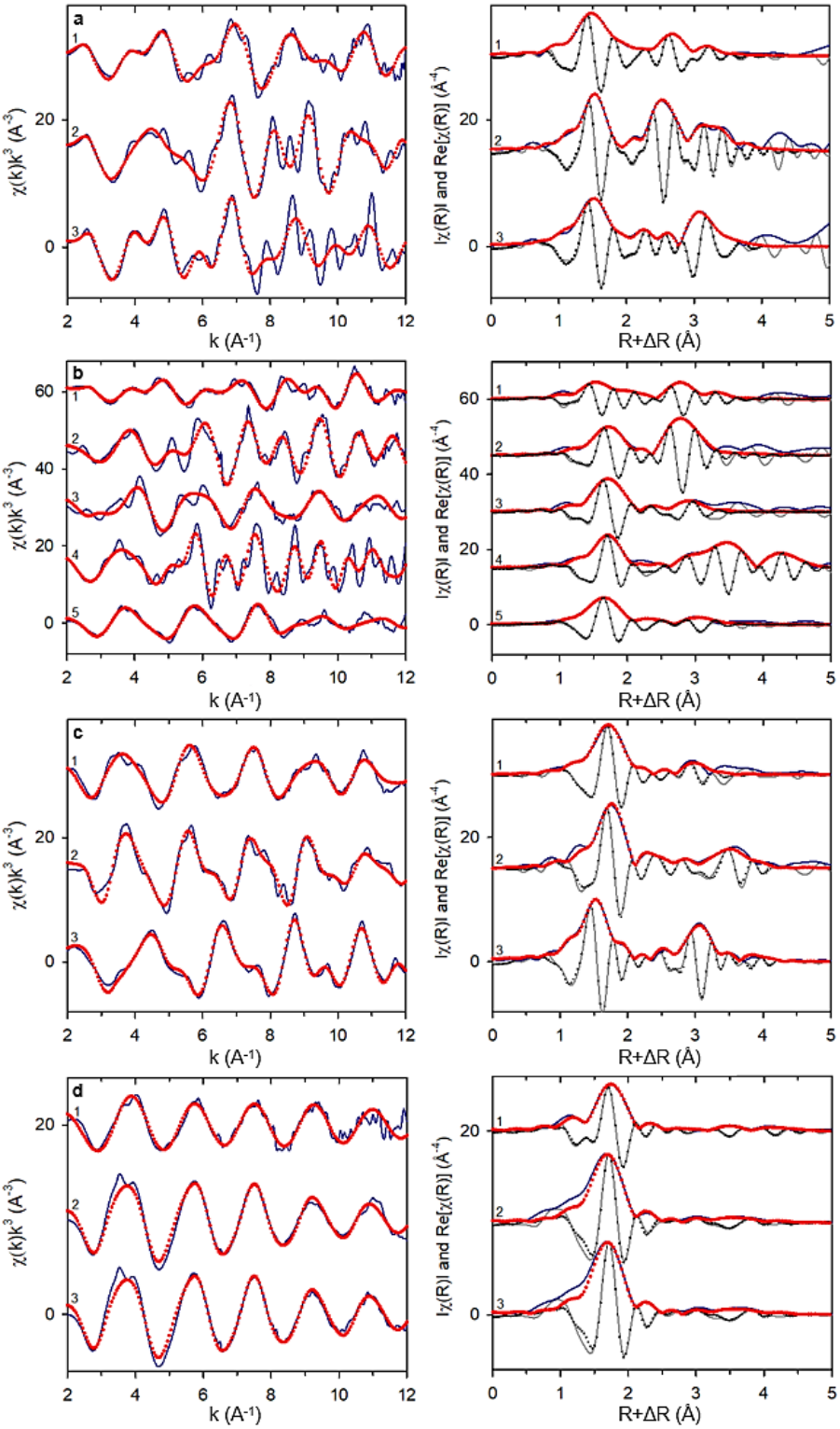

Figure A.4. Mn(III) oxyhydroxides (a):
1 - feitknechtite (syn),
2 - groutite,
3 - manganite (syn);

Carbonate, phosphate, and silicate minerals (b):
1 - braunite, 2 - hendricksite,
3 - masutomilite,
4 - rhodochrosite,
5 - triplite;

Organic Mn(II/III) compounds (c):
1 - Mn(II) acetate tetrahydrate,
2 - Mn(II) oxalate dihydrate,
3 - Mn(III) acetate dihydrate;

Adsorbed Mn(II) species (d):
1 - Mn(II) ads. illite,
2 - Mn(II) ads. peat pH5,
3 - Mn(II) ads. peat pH7.

Table A.4. Literature references used to compare interatomic distances (Fig. 2.7)

Reference	Literature reference
Phyllomanganates	
Acid Na-birnessite (hex, syn)	Webb et al. (2005)
	Bargar et al. (2009)
δ-MnO_2 (syn)	Webb et al. (2005)
	Ahmad et al. (2019)
Lithiophorite	McKeown and Post (2001)
	Manceau and Combes (1988)
Na-birnessite (tricl, syn)	Bargar et al. (2009)
	Webb et al. (2005)
	McKeown and Post (2001)
Tectomanganates	
Hollandite	McKeown and Post (2001)
	Manceau and Combes (1988)
Pyrolusite	Silvester et al. (1997)
	McKeown and Post 2001
	Manceau and Combes (1988)
	Elzinga and Kustka (2015)
Ramsdellite	Silvester et al. (1997)
	McKeown and Post (2001)
	Manceau and Combes (1988)
Romanèchite	Silvester et al. (1997)
	McKeown and Post (2001)
Todorokite (syn)	Webb et al. (2005)
Todorokite	McKeown and Post (2001)
	Manceau and Combes (1988)
Oxide minerals without layer or tunnel structure	
Bixbyite (syn)	Longo et al. (2010)
Bixbyite (nat)	Ahmad et al. (2019)
Hausmannite	Longo et al. (2010)
Manganosite (syn)	Ressler et al. (1999)
Mn(III) oxyhydroxides	
Manganite (syn)	Mackle et al. (1993)
Groutite	Scheinost et al. (2001)
Feitknechtite	Ressler et al. (1999)
	Mackle et al. (1993)
Carbonate, phosphate, and silicate minerals	
Rhodochrosite	Lee et al. (2002)
	Effenberger et al. (1981) (XRD)

A.5. STATISTICAL XANES COMPARISONS

	Acid Na-birnessite (hex, syn)	δ-MnO_2 (syn)	Lithiophorite	Na-birnessite (tricl, syn)	Cryptomelane	Cryptomelane (syn)	Hollandite	Pyrolusite	Pyrolusite (syn)	Ramsdellite	Romanèchite (Ba-free, syn)	Romanèchite	Todorokite	Todorokite (syn)	Bixbyite	Bixbyite (syn)	Hausmannite	Manganosite (syn)	Feitknechtite (syn)	Groutite	Manganite (syn)	Braunite	Hendricksite	Masutomilite	Rhodochrosite	Triplite	Mn(II) acetate tetrahydrate	Mn(II) oxalate dihydrate	Mn(III) acetate dihydrate	Mn(II) ads. illite	Mn(II) ads. peat pH5	Mn(II) ads. peat pH7
Acid Na-birnessite (hex, syn)																																
δ-MnO_2 (syn)	1.00																															
Lithiophorite	0.98	0.99																														
Na-birnessite (tricl, syn)	0.99	1.00	1.00																													
Cryptomelane	1.00	1.00	0.99	0.99																												
Cryptomelane (syn)	1.00	1.00	0.98	0.99	1.00																											
Hollandite s.s	0.99	0.99	1.00	0.99	0.99	0.99																										
Pyrolusite	0.99	0.99	0.97	0.98	1.00	1.00	0.98																									
Pyrolusite (syn)	0.99	0.99	0.97	0.98	0.99	0.99	0.98	1.00																								
Ramsdellite	1.00	1.00	0.98	0.99	1.00	1.00	0.99	1.00	1.00																							
Romanèchite (Ba-free, syn)	1.00	1.00	0.99	1.00	1.00	0.99	0.99	0.99	0.99	0.99																						
Romanèchite	0.99	1.00	0.99	1.00	1.00	0.99	1.00	0.99	0.98	0.99	1.00																					
Todorokite	1.00	1.00	0.99	0.99	1.00	1.00	0.99	0.99	0.99	1.00	1.00	1.00																				
Todorokite (syn)	0.98	0.99	1.00	1.00	0.98	0.97	0.99	0.96	0.96	0.97	0.99	0.99	0.98																			
Bixbyite	0.95	0.96	0.99	0.97	0.96	0.94	0.98	0.93	0.93	0.94	0.97	0.97	0.96	0.99																		
Bixbyite (syn)	0.96	0.97	0.99	0.98	0.97	0.96	0.99	0.95	0.94	0.95	0.98	0.98	0.97	0.99	1.00																	
Hausmannite	0.91	0.93	0.97	0.95	0.93	0.91	0.95	0.90	0.89	0.90	0.94	0.95	0.92	0.97	0.99	0.98																
Manganosite (syn)	0.66	0.69	0.77	0.72	0.68	0.64	0.75	0.64	0.63	0.64	0.70	0.72	0.68	0.77	0.85	0.82	0.89															
Feitknechtite (syn)	0.95	0.97	0.99	0.98	0.96	0.95	0.98	0.94	0.94	0.95	0.97	0.98	0.96	0.99	1.00	1.00	0.99	0.83														
Groutite	0.96	0.97	0.99	0.99	0.97	0.96	0.99	0.95	0.94	0.95	0.98	0.98	0.97	1.00	1.00	1.00	0.98	0.82	1.00													
Manganite (syn)	0.97	0.98	1.00	0.99	0.97	0.96	0.99	0.95	0.95	0.96	0.98	0.99	0.97	1.00	0.99	1.00	0.98	0.81	1.00	1.00												
Braunite	0.93	0.94	0.98	0.96	0.94	0.92	0.97	0.91	0.91	0.92	0.95	0.96	0.94	0.98	1.00	0.99	0.99	0.88	0.99	0.99	0.99											
Hendricksite	0.69	0.71	0.80	0.75	0.71	0.67	0.77	0.66	0.65	0.67	0.73	0.74	0.70	0.80	0.87	0.84	0.91	0.98	0.86	0.84	0.83	0.89										
Masutomilite	0.70	0.73	0.81	0.77	0.72	0.68	0.78	0.67	0.66	0.68	0.74	0.76	0.72	0.82	0.87	0.85	0.92	0.95	0.86	0.85	0.84	0.89	0.99									
Rhodochrosite	0.67	0.68	0.75	0.71	0.68	0.64	0.72	0.63	0.62	0.64	0.69	0.71	0.68	0.75	0.81	0.78	0.86	0.92	0.80	0.78	0.78	0.83	0.94	0.93								
Triplite	0.69	0.71	0.79	0.75	0.71	0.67	0.77	0.66	0.65	0.67	0.73	0.74	0.71	0.80	0.87	0.83	0.91	0.97	0.85	0.84	0.83	0.89	0.98	0.98	0.97							
Mn(II) acetate tetrahydrate	0.67	0.69	0.77	0.73	0.69	0.65	0.74	0.64	0.63	0.65	0.70	0.72	0.68	0.78	0.84	0.81	0.89	0.96	0.83	0.81	0.81	0.87	0.98	0.97	0.98	0.99						
Mn(II) oxalate dihydrate	0.65	0.68	0.76	0.72	0.67	0.63	0.73	0.62	0.61	0.63	0.69	0.71	0.67	0.77	0.84	0.81	0.89	0.98	0.83	0.81	0.80	0.87	0.98	0.97	0.95	0.99	0.99					
Mn(III) acetate dihydrate	0.96	0.97	0.99	0.98	0.97	0.96	0.98	0.95	0.94	0.95	0.97	0.98	0.97	0.99	0.99	0.99	0.97	0.80	0.99	0.99	0.99	0.98	0.82	0.82	0.77	0.82	0.80	0.79				
Mn(II) ads. illite	0.76	0.78	0.85	0.82	0.78	0.75	0.83	0.73	0.73	0.74	0.80	0.81	0.78	0.86	0.91	0.89	0.94	0.97	0.90	0.89	0.89	0.93	0.98	0.98	0.96	0.99	0.98	0.98	0.88			
Mn(II) ads. peat pH5	0.62	0.64	0.73	0.69	0.64	0.60	0.70	0.58	0.57	0.60	0.66	0.68	0.64	0.74	0.81	0.78	0.86	0.96	0.80	0.78	0.78	0.84	0.97	0.96	0.96	0.99	0.99	0.99	0.77	0.98		
Mn(II) ads. peat pH7	0.63	0.65	0.74	0.70	0.65	0.61	0.71	0.59	0.58	0.61	0.67	0.69	0.65	0.75	0.82	0.79	0.86	0.96	0.81	0.79	0.79	0.85	0.96	0.96	0.96	0.99	0.99	0.99	0.78	0.98	1.00	

PM*

Tectomanganates

Oxide minerals without layer or tunnel structure

Mn(III) oxyhydroxides

Carbonate, phosphate, and silicate minerals

Organic Mn(II/III) compounds

Adsorbed Mn(II) species

1	>0.9	>0.8	>0.7	>0.6	≤0.6

*PM = Phyllomanganates

Figure A.5. Pearson correlation matrix for normalized XANES spectra (6,530-6,600 eV) of Mn reference compounds. Only significant correlations (p <0.05) are listed.

	Acid Na-birnessite (hex, syn)	δ-MnO_2 (syn)	Lithiophorite	Na-birnessite (tricl, syn)	Cryptomelane	Cryptomelane (syn)	Hollandite	Pyrolusite	Pyrolusite (syn)	Ramsdellite	Romanèchite (Ba-free, syn)	Romanèchite	Todorokite	Todorokite (syn)	Bixbyite	Bixbyite (syn)	Hausmannite	Manganosite (syn)	Feitknechtite (syn)	Groutite	Manganite (syn)	Braunite	Hendricksite	Masutomilite	Rhodochrosite	Triplite	Mn(II) acetate tetrahydrate	Mn(II) oxalate dihydrate	Mn(III) acetate dihydrate	Mn(II) ads. illite	Mn(II) ads. peat pH5	Mn(II) ads. peat pH7
Acid Na-birnessite (hex, syn)																																
δ-MnO_2 (syn)	0.97																															
Lithiophorite	0.75	0.88																														
Na-birnessite (tricl, syn)	0.86	0.94	0.94																													
Cryptomelane	0.96	0.98	0.84	0.90																												
Cryptomelane (syn)	0.96	0.97	0.80	0.88	0.99																											
Hollandite *s.s*	0.88	0.95	0.92	0.90	0.95	0.91																										
Pyrolusite	0.87	0.91	0.82	0.86	0.93	0.94	0.86																									
Pyrolusite (syn)	0.77	0.81	0.75	0.78	0.84	0.85	0.77	0.96																								
Ramsdellite	0.87	0.90	0.82	0.86	0.93	0.94	0.86	0.98	0.97																							
Romanèchite (Ba-free, syn)	0.94	0.99	0.91	0.97	0.97	0.95	0.95	0.89	0.80	0.89																						
Romanèchite	0.93	0.98	0.91	0.93	0.97	0.95	0.98	0.88	0.79	0.89	0.98																					
Todorokite	0.99	0.99	0.83	0.92	0.98	0.97	0.93	0.89	0.79	0.89	0.98	0.97																				
Todorokite (syn)	0.78	0.90	0.97	0.96	0.85	0.81	0.92	0.78	0.70	0.77	0.93	0.92	0.85																			
Bixbyite	0.58	0.68	0.80	0.69	0.69	0.60	0.83	0.53	0.46	0.54	0.69	0.76	0.64	0.83																		
Bixbyite (syn)	0.62	0.73	0.81	0.74	0.74	0.67	0.86	0.60	0.52	0.59	0.74	0.80	0.69	0.85	0.97																	
Hausmannite	0.39	0.55	0.82	0.69	0.51	0.45	0.68	0.48	0.45	0.48	0.61	0.63	0.49	0.81	0.78	0.73																
Manganosite (syn)						-0.18		-0.2	-0.2	-0.2					0.43	0.35	0.30															
Feitknechtite (syn)	0.56	0.71	0.92	0.81	0.68	0.61	0.83	0.59	0.52	0.59	0.76	0.78	0.66	0.92	0.89	0.89	0.88	0.30														
Groutite	0.66	0.78	0.90	0.85	0.75	0.68	0.87	0.61	0.51	0.61	0.82	0.84	0.75	0.94	0.92	0.93	0.79	0.30	0.96													
Manganite (syn)	0.71	0.82	0.91	0.87	0.79	0.72	0.88	0.64	0.54	0.65	0.86	0.87	0.79	0.94	0.88	0.88	0.77	0.25	0.95	0.98												
Braunite	0.45	0.55	0.70	0.60	0.54	0.45	0.69	0.40	0.3	0.40	0.56	0.62	0.51	0.75	0.93	0.90	0.70	0.53	0.84	0.86	0.81											
Hendricksite			0.17					-0.2	-0.3	-0.2				0.24	0.45	0.35	0.60	0.60	0.43	0.39	0.32	0.45										
Masutomilite			0.33	0.18			0.25					0.19		0.37	0.50	0.38	0.71	0.31	0.51	0.45	0.42	0.48	0.82									
Rhodochrosite			0.20											0.18	0.21		0.36	0.38	0.32	0.27	0.31	0.31	0.46	0.46								
Triplite			0.28				0.18							0.28	0.51	0.35	0.59	0.53	0.50	0.43	0.40	0.61	0.70	0.75	0.80							
Mn(II) acetate tetrahydrate			0.24											0.23	0.43	0.30	0.48	0.59	0.46	0.40	0.40	0.56	0.63	0.61	0.90	0.95						
Mn(II) oxalate dihydrate			0.27											0.25	0.46	0.29	0.57	0.64	0.42	0.33	0.31	0.55	0.65	0.65	0.63	0.87	0.79					
Mn(III) acetate dihydrate	0.64	0.74	0.83	0.72	0.73	0.65	0.84	0.65	0.60	0.65	0.73	0.80	0.69	0.81	0.89	0.88	0.68	0.43	0.85	0.86	0.85	0.85	0.28	0.28	0.19	0.37	0.34	0.43				
Mn(II) ads. illite			0.40	0.22			0.31				0.18	0.25		0.38	0.59	0.44	0.65	0.67	0.57	0.49	0.49	0.66	0.70	0.68	0.74	0.92	0.88	0.95	0.56			
Mn(II) ads. peat pH5			0.27				0.17							0.25	0.45	0.31	0.51	0.66	0.48	0.39	0.41	0.56	0.63	0.60	0.82	0.92	0.94	0.91	0.44	0.96		
Mn(II) ads. peat pH7			0.29				0.20							0.27	0.49	0.35	0.50	0.69	0.49	0.41	0.43	0.59	0.60	0.55	0.77	0.89	0.91	0.91	0.49	0.96	0.99	

Tectomanganates; PM*; Oxide minerals without layer or tunnel structure; Mn(III) oxyhydroxides; Carbonate, phosphate, and silicate minerals; Organic Mn(II/III) compounds; Adsorbed Mn(II) species

1	>0.9	>0.8	>0.7	>0.6	≤0.6

*PM = Phyllomanganates

Figure A.6. Pearson correlation matrix for first-derivative XANES spectra (6,530-6,600 eV) of Mn reference compounds. Only significant correlations (p <0.05) are listed.

A.6. PCA OUTPUT PARAMETERS FOR MN K-EDGE EXAFS SPECTRA

Table A.5. Output parameters for the first ten PCs obtained from PCA analysis of k^2-weighted EXAFS spectra (k = 2.0-11.5 Å^{-1}, E_0 = 6,563 eV) of Mn reference compounds

Component	Eigenvalue	Total variance	Cumulative eigenvalue	Cumulative variance
1	17.94	56.08	17.94	56.08
2	4.26	13.33	22.21	69.40
3	3.45	10.80	25.66	80.20
4	1.56	4.87	27.22	85.06
5	1.14	3.56	28.36	88.62
6	0.86	2.70	29.22	91.32
7	0.62	1.95	29.84	93.26
8	0.47	1.47	30.32	94.74
9	0.41	1.28	30.73	96.02
10	0.27	0.83	30.99	96.85

A.7. REFERENCES

Ahmad, A., van der Wal, A., Bhattacharya, P. and van Genuchten, C.M. (2019) Characteristics of Fe and Mn bearing precipitates generated by Fe(II) and Mn(II) co-oxidation with O_2, MnO_4 and HOCl in the presence of groundwater ions. *Water Res.* **161**, 505-516.

Anthony, J.W., Bideaux, R.A., Bladh, K.W. and Nichols, M.C. (2003) *Handbook of Mineralogy*. Mineralogical Society of America, Chantilly, VA 20151-1110, USA.

Bargar, J.R., Fuller, C.C., Marcus, M.A., Brearley, A.J., De la Rosa, M.P., Webb, S.M. and Caldwell, W.A. (2009) Structural characterization of terrestrial microbial Mn oxides from Pinal Creek, AZ. *Geochim. Cosmochim. Acta* **73**, 889-910.

Biagioni, C., Capalbo, C. and Pasero, M. (2013) Nomenclature tunings in the hollandite supergroup. *Eur. J. Mineral.* **25**, 85-90.

Chukhrov, F.V., Drits, V.A., Gorshkov, A.I., Sakharov, B.A. and Dikov, Y.P. (1987) Structural models of vernadite. *Int. Geol. Rev.* **29**, 1337-1347.

Chukhrov, F.V. and Gorshkov, A.I. (1980) Reply to R. Giovanoli's comment. *Miner. Deposita* **15**, 255-257.

da Silva, A.L. and de Oliveira, A.H.F., Maria Lourdes Souza (2011) Influence of preferred orientation of minerals in the mineralogical identification process by X-ray diffraction.

Deer, W.A., Robert Andrew Howie, and Jack Zussman (1992) *An Introduction to the Rock-Forming Minerals*, 2nd ed. Longman, London.

Dohrmann, R., Rüping, K.B., Kleber, M., Ufer, K. and Jahn, R. (2009) Variation of preferred orientation in oriented clay mounts as a result of sample preparation and composition. *Clays Clay Miner.* **57**, 686-694.

Drits, V.A., Silvester, E., Gorshkov, A.I. and Manceau, A. (1997) Structure of synthetic monoclinic Na-rich birnessite and hexagonal birnessite: I. Results from X-ray diffraction and selected-area electron diffraction. *Am. Mineral.* **82**, 946-961.

Effenberger, H., Mereiter, K. and Zemann, J. (1981) Crystal structure refinements of magnesite, calcite, rhodochrosite, siderite, smithonite, and dolomite, with discussion of some aspects of the stereochemistry of calcite type carbonates. *Z. Kristallogr. Cryst. Mater.* **156**, 233-243.

Elzinga, E.J. and Kustka, A.B. (2015) A Mn-54 radiotracer study of Mn isotope solid–liquid exchange during reductive transformation of vernadite (δ-MnO_2) by aqueous Mn(II). *Environ. Sci. Technol.* **49**, 4310-4316.

Grangeon, S., Lanson, B., Lanson, M. and Manceau, A. (2008) Crystal structure of Ni-sorbed synthetic vernadite: A powder X-ray diffraction study. *Mineral. Mag.* **72**, 1279-1291.

Hoffmann, M., Mikutta, C. and Kretzschmar, R. (2012) Bisulfide reaction with natural organic matter enhances arsenite sorption: Insights from X-ray absorption spectroscopy. *Environ. Sci. Technol.* **46**, 11788-11797.

Lee, Y.J., Reeder, R.J., Wenskus, R.W. and Elzinga, E.J. (2002) Structural relaxation in the $MnCO_3$-$CaCO_3$ solid solution: A Mn K-edge EXAFS study. *Phys. Chem. Miner.* **29**, 585-594.

Longo, A., Liotta, L.F., Carlo, G.D., Giannici, F., Venezia, A.M. and Martorana, A. (2010) Structure and the metal support interaction of the Au/Mn oxide catalysts. *Chem. Mater.* **22**, 3952-3960.

Mackle, P., Charnock, J.M., Garner, C.D., Meldrum, F.C. and Mann, S. (1993) Characterization of the manganese core of reconstituted ferritin by X-ray absorption spectroscopy. *J. Am. Chem. Soc.* **115**, 8471-8472.

Manceau, A. and Combes, J.M. (1988) Structure of Mn and Fe oxides and oxyhydroxides: A topological approach by EXAFS. *Phys. Chem. Miner.* **15**, 283-295.

McKeown, D.A. and Post, J.E. (2001) Characterization of manganese oxide mineralogy in rock varnish and dendrites using X-ray absorption spectroscopy. *Am. Mineral.* **86**, 701-713.

Post, J.E. (1999) Manganese oxide minerals: Crystal structures and economic and environmental significance. *Proc. Natl. Acad. Sci.* **96**, 3447-3454.

Post, J.E., Von Dreele, R.B. and Buseck, P.R. (1982) Symmetry and cation displacements in hollandites: Structure refinements of hollandite, cryptomelane and priderite. *Acta Crystallogr. B* **38**, 1056-1065.

Ressler, T., Brock, S.L., Wong, J. and Suib, S.L. (1999) Multiple-scattering EXAFS analysis of tetraalkylammonium manganese oxide colloids. *J. Phys. Chem. B* **103**, 6407-6420.

Scheinost, A.C., Stanjek, H., Schulze, D.G., Gasser, U. and Sparks, D.L. (2001) Structural environment and oxidation state of Mn in goethite-groutite solid-solutions. *Am. Mineral.* **86**, 139-146.

Shen, X., Ding, Y., Liu, J., Laubernds, K., Zerger, R.P., Polverejan, M., Son, Y.-C., Aindow, M. and Suib, S.L. (2004) Synthesis, characterization, and catalytic applications of manganese oxide octahedral molecular sieve (OMS) nanowires with a 2×3 tunnel structure. *Chem. Mater.* **16**, 5327-5335.

Shen, X.F., Ding, Y.S., Liu, J., Cai, J., Laubernds, K., Zerger, R.P., Vasiliev, A., Aindow, M. and Suib, S.L. (2005) Control of Nanometer-Scale Tunnel Sizes of Porous Manganese Oxide Octahedral Molecular Sieve Nanomaterials. *Adv. Mater.* **17**, 805-809.

Silvester, E., Manceau, A. and Drits, V.A. (1997) Structure of synthetic monoclinic Na-rich birnessite and hexagonal birnessite: II. Results from chemical studies and EXAFS spectroscopy. *Am. Mineral.* **82**, 962-978.

Turner, S. and Post, J.E. (1988) Refinement of the substructure and superstructure of romanechite. *Am. Mineral.* **73**, 1155-1161.

Villalobos, M., Lanson, B., Manceau, A., Toner, B. and Sposito, G. (2006) Structural model for the biogenic Mn oxide produced by *Pseudomonas putida*. *Am. Mineral.* **91**, 489-502.

Villalobos, M., Toner, B., Bargar, J. and Sposito, G. (2003) Characterization of the manganese oxide produced by *Pseudomonas putida* strain MnB1. *Geochim. Cosmochim. Acta* **67**, 2649-2662.

Webb, S.M., Tebo, B.M. and Bargar, J.R. (2005) Structural characterization of biogenic Mn oxides produced in seawater by the marine *Bacillus sp.* strain SG-1. *Am. Mineral.* **90**, 1342-1357.

3. High Manganese redox variability and manganate predominance in temperate soil profiles as determined by X-ray absorption spectroscopy

TERESA ZAHORANSKY[a], KLAUS KAISER[b], CHRISTIAN MIKUTTA[a]

[a]Soil Mineralogy, Institute of Mineralogy, Gottfried Wilhelm Leibniz University Hannover, Callinstr. 3, D-30167 Hannover, Germany

[b]Soil Science and Soil Protection, Martin Luther University Halle-Wittenberg, Von-Seckendorff-Platz 3, D-06120, Halle (Saale), Germany

Corresponding author: Christian Mikutta

This chapter is published in 'Geochimica et Cosmochimica Acta' (DOI: 10.1016/j.gca.2022.10.016). The current version shows minor modifications in terms of consistent presentation and formatting in this thesis.

Abstract

Manganese speciation is a key to understanding the fate of contaminants, nutrients, and organic matter in soils. To date, quantification of Mn species in bulk soils has been performed mainly by sequential extraction methods and rarely supported by spectroscopic analysis. In order to obtain quantitative information on the Mn species inventory of soils, we investigated 46 soil horizons (<2-mm fraction, 45.1-2,280 mg/kg Mn) of nine typical Central European soils (Cambisols, Chernozems, Luvisols, Podzol, Stagnosol) by chemical Mn analyses and Mn K-edge X-ray absorption spectroscopy, and related speciation results to major soil properties. Amounts of Mn^{2+}, Mn^{3+}, and Mn^{4+}, and the average oxidation state of Mn were evaluated by linear combination fitting (LCF) of X-ray absorption near edge structure (XANES) spectra. Additionally, we used extended X-ray absorption fine structure (EXAFS) spectroscopy to identify and quantify major Mn species. For this, EXAFS spectra of 20 organic and mineral soil samples from five soils (Cambisols, Chernozem, Luvisol) were analyzed by LCF and shell fitting. XANES analyses revealed a high Mn redox variability in organic surface layers, with Mn^{2+} being most abundant (≤100%, $\bar{x}$ = 54%), followed by Mn^{3+} (≤80%, $\bar{x}$ = 32%) and Mn^{4+} (≤55%, $\bar{x}$ = 14%). Mineral soil horizons contained significantly less Mn^{2+} (≤56%, $\bar{x}$ = 23%), about equal quantities of Mn^{3+} (≤68%, $\bar{x}$ = 31%), and were enriched in Mn^{4+} (≤89%, $\bar{x}$ = 46%). EXAFS analyses implied the presence of

six major Mn species groups: Manganates, organically complexed Mn, Mn(III) oxyhydroxides, silicate-bound Mn, Mn oxides without tunnel- or layer structure, and physisorbed Mn. In litter horizons (Oi), Mn was mainly present in organic complexes (58-91%, $\bar{x}$ = 78%) and as physisorbed Mn (≤15%), but individual horizons also comprised manganates, Mn(III) oxyhydroxides, and silicate-bound Mn. Manganates, likely mixtures of phyllomanganates with hexagonal layer symmetry and tectomanganates, dominated in all mineral soil horizons (37-94%, $\bar{x}$ = 67%). Correlation analysis showed that manganates dissolve completely during dithionite-citrate and acid ammonium oxalate extractions, and suggested that Mn^{4+}-rich manganates preferentially form under less acidic soil conditions, partly by oxidation of organically complexed Mn(II), and that they are enriched in the soil clay fraction. Mineral soil horizons also contained minor quantities of organically complexed Mn (≤39%, $\bar{x}$ = 11%), silicate-bound Mn (≤30%, $\bar{x}$ = 8%), Mn(III) oxyhydroxides (≤37%, $\bar{x}$ = 7%), Mn oxides without tunnel- or layer structure (≤18%, $\bar{x}$ ~5%), and physisorbed Mn (≤14%, $\bar{x}$ <1%). The detection of Mn(III) oxyhydroxides such as feitknechtite (β-MnOOH) or groutite (α-MnOOH) as well as the spinel hausmannite (Mn_3O_4) in acidic soils is remarkable, since their formation is normally linked to neutral or alkaline pH conditions. Minor contributions of silicate-bound Mn indicate the release of Mn from primary minerals already at early stages of soil formation, and low concentrations of physisorbed Mn suggest that exchangeable Mn is rapidly converted into manganates in oxic soils. The predominance of manganates in mineral soils has far-reaching implications for the functioning of soils and biogeochemical element cycles, as these minerals play an important role in metal binding, plant nutrition, and redox-related processes.

3.1. INTRODUCTION

Manganese is a redox-sensitive element that occurs naturally in the three oxidation states +2, +3, and +4 and is involved in numerous redox processes in the environment. Manganese is an essential micronutrient for plants since it plays a crucial role in photosynthesis and enzymatic reactions (Glatzel et al., 2004; Yano and Yachandra, 2008; Broadley et al., 2012). In soil, Mn is involved in oxidative lignin degradation (Jensen et al., 1996; Hofrichter, 2002; Keiluweit et al., 2015) and the oxidation of nutrients and contaminants (Shindo et al., 1996; Negra et al., 2005; Ehlert et al., 2016).

Soil Mn oxides and oxyhydroxides, collectively referred to as Mn (oxyhydr)oxides, are thought to form primarily through biologically mediated pathways (Remucal and Ginder-Vogel, 2014), although this remains to be confirmed for MnOOH polymorphs. Under sub- and anoxic conditions, these phases are reductively dissolved to water-soluble, bioavailable Mn^{2+} (Tebo et al., 2004; Martin, 2005; Frommer et al., 2011). The dissolution reaction is favored in soils with low pH and reducing conditions (Porter et al., 2004; Tebo et al., 2004; Blume et al., 2016). Manganese taken up by plants is stored as free or carboxylate bound Mn2+ in living and dead foliar tissue (plant litter) (Tam et al., 1991; Keiluweit et al., 2015). During oxidative litter decomposition it can be oxidized to Mn (oxyhydr)oxides (Herndon et al., 2014).

Understanding the biogeochemical Mn cycle in soil requires quantification of solid-phase Mn pools and their changes in space and time. Gathering this information remains a challenging task because total soil Mn concentrations are low, with a mean of 760 mg/kg (N = 8,354 soils; Ure and Berrow, 1982). Moreover, Mn (oxyhydr)oxides, are often nanocrystalline and amorphous to X-rays (Chukhrov and Gorshkov, 1981; Zhang and Karathanasis, 1997; Cornu et al., 2005). Thus, previous micromorphological, mineralogical, and chemical studies have focused mostly on soil ferromanganese nodules and concretions (Taylor et al., 1964; Tokashiki et al., 1986; Uzochukwu and Dixon, 1986; Liu et al., 2002; Manceau et al., 2003; Szymański et al., 2014), which are typical features of soils subjected to seasonal waterlogging (Reddy and DeLaune, 2008). However, the results of these studies can neither be transferred to the bulk of the same soil nor to other soils.

Studies addressing Mn speciation in soils have so far mainly relied on three analytical approaches: X-ray diffraction (XRD), sequential extractions (SE), and synchrotron-based Mn K-edge X-ray absorption spectroscopy (XAS). Although spatially resolved XRD analyses allow for identification and perhaps (semi)quantification of Mn minerals (Tokashiki et al., 1986; Golden et al., 1993; De Bakker et al., 2003; Manceau et al., 2005; Mayanna et al., 2015), XRD fails when applied to samples containing nanocrystalline or X-ray amorphous Mn minerals at low concentrations (<1 wt.%). Likewise, XRD does not provide any information on other potentially important Mn species such as organic Mn complexes (Habibah et al., 2014; Herndon et al., 2014; Redžić et al., 2014) and Mn adsorbed to or incorporated in

silicate or Fe(III) (oxyhydr)oxide minerals (Anand and Gilkes, 1984; Scheinost et al., 2001; Vodyanitskii et al., 2002).

Sequential extraction methods are based on the exposure of soil samples to a sequence of wet chemical assays of increasing extraction strength. These methods assume to selectively extract a specific solid component the metal in question is associated with (Hass and Fine, 2010). Although SE methods provide valuable information on operationally defined Mn fractions in soils (Guest et al., 2002; Kalembkiewicz et al., 2008; Frommer et al., 2011; Habibah et al., 2014; Redžić et al., 2014), poor selectivity of extractants, Mn redistribution during extractions, and the use of a large variety of non-standardized extraction procedures severely limit the explanatory power of this speciation approach.

Synchrotron-based spectroscopic techniques allow for non-destructive analysis of the oxidation state and average local (<5 Å) coordination of Mn at concentrations typical of soils and sediments. However, only few studies to date have used Mn K-edge XAS to speciate Mn in soils (Manceau et al., 2005; Frommer et al., 2011; Hernandez-Soriano et al., 2012; Herndon et al., 2014; Keiluweit et al., 2015) and sediments (Friedl et al., 1997; O'Day et al., 2000; McKeown and Post, 2001; Carroll et al., 2002). These studies usually employed Mn K-edge (micro-focused, µ-) X-ray absorption near edge structure (XANES) spectroscopy to determine the average oxidation state (AOS) of Mn. For this, the 'Combo' linear combination fit (LCF) analysis method of Manceau et al. (2012) has become increasingly popular (Herndon et al., 2014; Zhu et al., 2017; Flynn and Catalano, 2019; Becknell et al., 2021). This method utilizes XANES spectra of a set of well-characterized monovalent Mn reference compounds (Manceau et al., 2012) and can yield the Mn AOS in environmental samples with an accuracy of ~0.1 valence units (v.u.) over the entire AOS range (Zahoransky et al., 2022).

Even though specific information on the local Mn coordination environment of a given sample can be inferred from extended X-ray absorption fine structure (EXAFS) spectroscopy, (µ-)EXAFS spectroscopy has only rarely been used for identification and quantification of Mn species in soils and sediments (Manceau et al., 2005; Mayanna et al., 2015). EXAFS evaluations of environmental samples typically involve shell-fit and LCF analyses (Scheckel and Ryan, 2004; Ahmad et al., 2019), the latter often combined with prior principal component analysis (PCA) and target-transformation (TT) testing (Scheinost et al., 2002; Langner et al., 2012; Mikutta and Rothwell, 2016). Prerequisite for successful Mn K-edge EXAFS-LCF analysis of environmental samples is a comprehensive reference spectrum library of relevant Mn species potentially occurring in the studied system. To this end, we compiled XAS spectra of 32 well-characterized Mn reference compounds, including Mn oxide, oxyhydroxide, carbonate, phosphate, and silicate minerals, as well as organic and adsorbed Mn species (Zahoransky et al., 2022).

To our knowledge, Mn K-edge EXAFS spectroscopy has not been used to quantitatively examine Mn speciation in bulk soils so far. This method overcomes the limitations of bulk XRD and SE

analyses, and can yield information on major Mn species (groups) present (Zahoransky et al., 2022). Quantitative information on Mn speciation may allow disentangling its relationships with physicochemical soil properties, which are well known for other major redox-sensitive elements such as Fe (Prietzel et al., 2007; Neubauer et al., 2013; Sjöstedt et al., 2013). Despite decades of research on soil Mn speciation, available studies are limited to selected soil components (e.g., nodules), individual soil horizons, and single soil profiles, so that causal relationships between bulk Mn speciation and physicochemical soil properties remain poorly understood.

The main objectives of this study were to (1) quantify the Mn species inventory in typical Central European soils developed on different substrates and exhibiting different physicochemical properties and (2) test for possible relationships between Mn speciation and physicochemical soil parameters. For this, we determined basic physicochemical soil properties of nine soil profiles, collected bulk Mn K-edge XAS spectra of 46 soil horizons, analyzed Mn oxidation states, and evaluated Mn speciation in 20 soil samples based on EXAFS spectroscopy. The results of this study decipher major Mn species groups in bulk soils, reveal differences and similarities in Mn speciation of organic and mineral soil horizons, and clarify relationships between Mn speciation and physiochemical soil properties, thus contributing to a better understanding of soil Mn pools and their (trans)formation.

3.2. MATERIALS AND METHODS

3.2.1. SOIL SAMPLING AND CLASSIFICATION

A total of 47 soil samples were collected from nine soil profiles at different sampling locations in Germany in autumn 2018. Photographs of soil profiles, sampling location coordinates as well as information on climatic conditions, parent material, and vegetation cover are provided in the *Supplementary material* (Fig. B.1, Table B.1). With the exception of Stagnosol #9, all soils were dry and oxic at the time of sampling. All profiles were sampled on a horizon basis and classified according to the Word Reference Base for Soil Resources (IUSS Working Group WRB, 2014) as a Dystric Skeletic Cambisol (#1), an Eutric Stagnic Cambisol (#2), a Calcaric Skeletic Cambisol (#3), Haplic Chernozems (#4 and #5), Haplic Luvisols (#6 and #7), a Skeletic Albic Podzol (#8), and a Dystric Albic Folic Stagnosol (#9). Soil horizons were designated according to FAO (2006).

3.2.2. BASIC SOIL CHARACTERIZATION

For the determination of basic soil properties, samples were air-dried for two weeks, then oven-dried at 50 °C for 12 hours, and finally passed through a 2-mm sieve. Visible root fragments were removed manually. Thereafter, the samples were homogenized and stored at room temperature in the dark. The Munsell color of the soil samples was determined on field-moist samples. Soil pH was measured

in 0.01 M $CaCl_2$ (1:5 v/v for mineral horizons, 1:10 v/v for organic horizons) and water (DIN ISO 10390). Electrical conductivity was determined in the water-soil suspensions. Total C (C_{tot}) and N (N_{tot}) were analyzed by dry combustion using elemental analyzers (Vario EL III and Vario MAX cube, Elementar), and inorganic C (C_{inorg}) was quantified with Scheibler´s method using a calcimeter (DIN 18129). All analyses were carried out at least in duplicates. Particle size distribution was determined in triplicates after C_{org} removal with H_2O_2 (35%) and dispersion of soil in $Na_4P_2O_7$ (Hartge and Horn, 1992) by wet-sieving (sand fraction) and sedimentation (silt and clay fractions) using the pipette method (Gee and Bauder, 1986). The effective cation exchange capacity (ECEC) and base saturation (BS) were determined in duplicates using an unbuffered 0.1 M $BaCl_2$ solution according to DIN EN ISO 11260. In this method, $BaCl_2$-saturated soils are additionally treated with a 0.02 M $MgSO_4$ solution (compulsive exchange) to determine the ECEC by Mg occupancy on exchangeable cation sites (Gillman, 1979). Exchangeable Al, Ca, Fe, Mn, and Mg were determined by inductively coupled plasma–optical emission spectrometry (ICP-OES, Agilent 725 ES), and Na and K by atomic absorption spectrometry (AAS, Perkin Elmer AAnalyst 300). ECEC (cmolc/kg) was calculated from exchangeable cations excluding protons following Hendershot et al. (2008a). Base saturation (%) was calculated as $\sum(Na + K + Ca + Mg)/ECEC \times 100$ and exchangeable acidity (EA) was assessed by titration of the $BaCl_2$-centrifugates with 0.02 M NaOH (Hendershot et al., 2008a, 2008b). Dithionite-citrate and acid ammonium oxalate extractable Fe and Mn were determined in triplicates as described in Courchesne and Turmel (2008) and McKeague and Day (1966), respectively. Their solution concentrations were analyzed by ICP-OES. Total element contents were determined by energy-dispersive X-ray fluorescence spectrometry analysis (Spectro XEPOS HE) of pressed pellets prepared from 4 g of soil and 0.9 g of CEREOX® wax (Licowax C, Fluxana) using Compton normalization to correct for moisture effects. Prior to measurements, samples were oven-dried at 60 °C overnight and stored in a desiccator. The accuracy of measurements was assessed by reference materials (NIST SRM 2710a, USGS SDO-1) and was found to be within ±8% ($\bar{x}$ = 2%) of the certified values of main elements (Al, Ca, Fe, K, Mg, Mn, Na, Si).

3.2.3. Manganese K-edge XAS

For Mn K-edge XAS measurements, field-moist samples were shock frozen in liquid N_2, freeze-dried (Christ, Beta 1-8 LSCplus), stripped of visible root fragments, sieved to <2 mm, and homogenized in an agate mortar. Freeze-drying was used to preserve soil Mn speciation because Hjorth (2004) found no chang-es in Mn speciation after freeze-drying of lake sediments as analyzed by the sequential BCR extraction method.

Bulk Mn K-edge XAS spectra of 46 soil samples were collected at beamline 7-3 of the Stanford Synchrotron Radiation Lightsource (SSRL, Menlo Park, USA), beamline 5-BM-D of the Advanced Photon Source (APS, Argonne, USA), and beamline P64 of PETRA III at the Deutsches Elektronen-Synchrotron

(DESY, Hamburg, Germany). Beamlines were equipped with Si(220) (7-3) and Si(111) double-crystal monochromators (5-BM-D, P64), calibrated by setting the first-derivative maximum of the K-edge absorption spectrum of elemental Mn to 6,539 eV. Higher harmonics in the beam were reduced by detuning monochromators by 15-50%. In addition, 3-µm Cr filters were used to reduce undesired fluorescence radiation at beamline 7-3. Measurements were performed in fluorescence mode utilizing solid-state fluorescence detectors (7- or 30-element Ge detectors, Vortex SDD). To reduce beam damage, all samples were measured at 5-20 K employing He-cryostats or at 77 K (5-BM-D) using a Lincam cell. Spectra were recorded with a maximum energy increment of 5 eV before the edge and 0.2-0.3 eV along the edge. The EXAFS of 20 selected samples was recorded up to k = 12.2 $Å^{-1}$ with a k-space resolution of 0.05 $Å^{-1}$. Two to 11 scans were collected per sample. Spectra of a Mn metal foil were used to correct for energy shifts during sample measurements.

Spectral pre-processing, including merging of individual scans, rebinning, and energy calibration, was conducted in SIXPack (Webb, 2005) or Athena (Ravel and Newville, 2005). The pre-edge region was fit with a linear function and the post-edge region with a quadratic polynomial. The edge-step energy, E_0, was defined as first maximum of the first XANES derivative (excluding pre-peaks). For background removal, the Autobk algorithm was applied. The frequency cut-off parameter, R_{bkg}, was set to 0.9-1.1, and the k-weight for background removal to two or three. A Hanning window function with a sill width of 2 $Å^{-1}$ was used to Fourier transform the data.

3.2.4. XAS DATA ANALYSIS

Different XAS data analysis methods were applied to obtain Mn speciation information: XANES LCF was used for Mn valence determination, EXAFS LCF for Mn species identification and quantification, and EXAFS shell fitting for independent Mn species identification. These methods are detailed in the following sections.

3.2.4.1. XANES ANALYSIS

For the determination of the fractional amount of each Mn oxidation state and Mn AOS, we applied the 'Combo' LCF method of Manceau et al. (2012). For this, normalized XANES spectra were fit using 17 Mn K-edge XANES reference spectra of single-valent Mn compounds, available as open source in Manceau et al. (2012) (deposit item AM-12-037), and processed as described above. Fits were performed in Athena over an energy range of -20 to 30 eV (E–E_0) by applying a non-negativity constraint. A single E_0 shift was used for all references. During fits, negatively loaded references were progressively eliminated until only references with positive or zero loadings remained. Each previously deleted reference was then again randomly added and the fit run again to assure that the global minimum was found using the normalized sum of squared residuals (R-factor) as best-fit criterion

(Manceau et al., 2012). Eventually, no negative loadings remained and the total fraction of each Mn oxidation state in the sample analyzed was calculated as the sum of the individual component fractions (Manceau et al., 2012). Note that this LCF approach is different from other LCF procedures, since it does not consider the samples to be mixtures of the standards (Manceau and Nagy, 2012). Therefore, no uncertainties are assigned to individual valence fractions and the derived AOS (Manceau et al., 2012). To test the comparability of XANES spectra collected at different beamlines, sample Bt1 of Luvisol #7 was analyzed at beamlines 7-3 (SSRL) and 5-BM-D (APS). These measurements showed deviations in determined Mn valence fractions and calculated AOS of only ~2%.

3.2.4.2. EXAFS ANALYSIS

Twenty k^2-weighted EXAFS spectra of soil samples from all Cambisols, Chernozem #3, and Luvisol #9 were analyzed by LCF over a k-range of 2-11 $Å^{-1}$ (E_0 = 6,563 eV) in Athena after PCA-TT analysis. The number of significant PCA components as obtained by the indicator (IND) function of Malinowski (1977) was evaluated using the ITFA software package (Rossberg et al., 2003). For TT testing, we used the Mn reference database of Zahoransky et al. (2022). References were selected on the basis of their SPOIL value as obtained from SIXPack (Webb, 2005). This empirical value was categorized by Malinowski (1978) to describe the quality of the target transformation: 0-1.5 (excellent), 1.5-3 (good), 3-4.5 (fair), 4.5-6 (acceptable), and >6 for an unacceptable reference spectrum.

Shell fits of 19 suitable k^3-weighted EXAFS spectra were carried out in Artemis (Ravel and Newville, 2005) on a shell-by-shell basis in R-space ($R + \Delta R$ ~1-4 Å). R-space resolution as given by the Rayleigh criterion ($0.5\pi/(k_{max} - k_{min})$; Calvin, 2013) was 0.17-0.22 Å. Atomic shells separated by lower values could not be resolved. Theoretical phase-shift and amplitude functions were calculated with FEFF6 (Ankudinov et al., 1998) based on crystal-structure information in Zahoransky et al. (2022). The passive amplitude reduction factor, S_0^2, was fixed to 0.8 during optimization. If individually fitted Debye-Waller parameters, σ^2, converged towards similar values, they were equated in the final fit to reduce the number of fit variables (Zahoransky et al., 2022).

3.2.5. STATISTICS

Statistical analyses of Mn speciation and physicochemical soil parameters were performed in Statistica (TIBCO Software Inc.) and SigmaPlot v.14 (Systat Software GmbH). Since most data were not normally distributed (Shapiro-Wilk test), Spearman's rank correlation coefficient (r_s) was used to test for relationships between variables. Significant differences between variable groups were evaluated by parametric or nonparametric tests (paired t-tests and Wilcoxon signed rank test) and ANOVA (one-way and Kruskal-Wallis rank-based) with subsequent post-hoc tests (Dunn's and Holm-Sidak's method). Differences were considered significant at $p \leq 0.05$.

3.3. RESULTS

3.3.1. PHYSICOCHEMICAL SOIL PROPERTIES

Basic soil parameters are compiled in Tables 3.1 and B.2. Soil pH(H_2O) ranged from 3.3 to 8.0 (pH($CaCl_2$): 3.0-7.9), and most soil samples had a loamy texture. Concentrations of N_{tot} ranged from 0.0 to 1.8 wt.% ($\bar{x}$ = 0.5 wt.%) and of C_{tot} from 0.1 to 47.1 wt.% ($\bar{x}$ = 13.5 wt.%). Inorganic C was solely found in Cambisol #3 and the deeper horizons of the two Chernozems, with values up to 3.3 wt.%. ECEC varied between and within soils, and ranged from 2.1 $cmol_c$/kg in the C horizon of Luvisol #8 to 44.3 $cmol_c$/kg in the Bw horizon of Cambisol #3 ($\bar{x}$ = 16.4 $cmol_c$/kg). The EA varied between 0.0 and 16.7 $cmol_c$/kg ($\bar{x}$ = 3.2 $cmol_c$/kg). Base saturation levels ranged from 2 to 100% ($\bar{x}$ = 66%), and were particularly high in Cambisol #3, Chernozems, and Luvisols. In contrast, Cambisols #1 and #2 showed intermediate base status; BS values <38% were observed for Podzol #8 and Stagnosol #9. In most soils, $BaCl_2$-exchangeable Mn accounted for less than 1% of ECEC; higher values of up to 3.9% were found in Cambisol #2. In Cambisol, Chernozem, and Luvisol A horizons, the contribution of Mn to ECEC was higher than in directly underlying horizons, suggesting that exchangeable Mn is partly associated with organic material (Table 3.1).

Total Mn concentrations (Mn_{tot}) ranged from <50 mg/kg in the Oa horizon of Stagnosol #9 to 2,300 mg/kg in the 2Bg2 horizon of Cambisol #2 ($\bar{x}$ = 790 mg/kg). Dithionite-extractable Mn (Mn_d) varied from 20 to 1,850 mg/kg ($\bar{x}$ = 580 mg/kg), on average corresponding to 61% of Mn_{tot} (range: 20-100%) (Table 3.1). Oxalate-extractable Mn (Mn_o) showed similar concentration ranges and was highly correlated with Mn_d (r_s = 0.99, N = 33, Table 3.2), with a regression slope of 0.93±0.02 (Fig. B.2). Also, Mn_d and Mn_o were highly correlated with total Mn contents (r_s = 0.99 and 0.98, respectively, Table 3.2). The lowest Mn_d concentrations were observed in the E horizon of Podzol #8 (20% of Mn_{tot}), in all mineral horizons of Stagnosol #9 (26-34% of Mn_{tot}) as well as in the EB and Bt horizons of Luvisol #6 (28-33% of Mn_{tot}) (Table 3.1). Total Mn, Mn_d, and Mn_o were positively correlated with clay content (r_s ≥0.60) and negatively with silt content (r_s ≤-0.50). Additionally, they were positively correlated with dithionite- (Fe_d) and oxalate-extractable Fe (Fe_o) (r_s ≥0.54 and r_s ≥0.40, respectively) (Table 3.2). Statistical differences in Mn_{tot}, Mn_d or Mn_o content between O, A, B, and E horizons (excluding transition horizons) were insignificant (one-way ANOVA on ranks). However, after log_{10} data transformation, Mn_d in E horizons was significantly lower than that in A and B horizons, and Mn_o was significantly lower in A than in B and E horizons (one-way ANOVA).

Table 3.1. Selected physicochemical properties of the studied soil samples[a]

Sample	Depth (cm)	pH (H_2O)	Clay (%)	Silt (%)	Sand (%)	N_{tot} (%)	C_{tot} (%)	C_{org} (%)	C_{org}/N_{tot}	ECEC ($cmol_c/kg$)	$ECEC_{Mn}$(%)	BS (%)	EA ($cmol_c/kg$)	Mn_{tot} (mg/kg)	Mn_d (mg/kg)	Mn_d/Mn_{tot} (%)	Mn_o (mg/kg)	Mn_o/Mn_{tot} (%)	Fe_{tot} (g/kg)	Fe_d (g/kg)	Fe_o (g/kg)
Dystric Skeletic Cambisol (Hyperhumic, Loamic) #1																					
Oi	-2-0	-	-	-	-	1.0	46.6	46.6	45.0	-	-	-		960	-	-	-	-	0.29	-	-
Ah	0-5	4.3	33	60	7	1.0	15.9	15.9	15.6	17.3	0.7	31	13	973	428	44	422	43	62.9	22.2	19.2
Bw	25-55+	5.1	16	58	25	0.3	3.3	3.3	11.6	8.9	0.9	52	4.2	2240	1090	49	1060	47	92.4	19.5	18.4
Eutric Stagnic Cambisol (Loamic) #2																					
Oi	-1-0	-	-	-	-	0.8	45.0	45.0	53.7	-	-	-	-	1560	-	-	-	-	0.15	-	-
Ah	0-5	4.5	21	48	30	0.6	8.8	8.8	15.5	14.0	3.9	59	5.4	1040	791	76	685	66	37.6	23.0	8.60
Bwg	5-35	4.2	26	49	25	0.1	0.8	0.8	10.9	7.6	1.7	5.4	7.7	671	672	100	612	91	24.3	29.2	11.9
2Bg1	35-120	4.8	42	39	19	0.1	0.4	0.4	6.7	6.8	2.2	52	4.2	1150	865	75	716	62	49.2	28.8	11.2
2Bg2	120-130+	5.0	37	40	24	0.1	0.4	0.4	7.3	9.2	2.4	81	1.6	2280	1850	81	1858	82	46.7	25.8	14.9
Calcaric Skeletic Cambisol (Clayic, Humic) #3																					
Oi	-1-0	-	-	-	-	0.9	46.8	46.8	54.1	-	-	-	-	449	-	-	-	-	0.19	-	-
Ah	0-5	5.3	40	52	8	0.4	5.4	5.4	14.7	33.0	1.7	87	4.0	971	777	80	698	72	50.2	24.7	3.65
Bw	12-40	7.4	39	52	9	0.1	1.2	1.2	11.4	44.3	0.1	100	0.0	2280	1610	71	1430	63	71.6	30.4	3.47
CB	40-60	8.0	44	45	10	0.2	2.8	2.2	11.2	43.0	0.0	100	0.0	1820	1540	85	1400	77	56.6	26.3	3.16
C	60-90	8.0	63	24	13	0.2	5.4	2.1	12.4	39.1	0.0	100	0.19	1190	970	82	704	59	43.2	19.6	1.87
Haplic Chernozem (Pachic, Silitc) #4																					
Oi	-0.5-0	-	-	-	-	1.5	37.8	37.8	24.9	-	-	-	-	181	-	-	-	-	1.19	-	-
Ah1	0-20	7.3	18	78	4	0.2	2.7	2.7	10.9	24.0	0.4	97	0.84	718	517	72	496	69	24.9	6.83	1.59
Ah2	20-35	3.3	17	79	4	0.2	2.2	2.2	10.5	23.4	0.2	96	1.2	718	525	73	508	71	25.2	7.06	1.62
Ah3	35-50	8.0	16	82	2	0.2	2.1	2.0	10.8	26.0	0.0	97	1.0	691	500	72	488	71	27.1	7.26	1.57
Ck	70-145	8.2	5	93	2	0.0	1.6	0.2	9.1	7.1	0.1	97	1.0	425	211	50	152	36	18.9	4.76	0.89
Haplic Chernozem (Loamic, Pachic) #5																					
Oi	-1-0	-	-	-	-	0.9	42.4	42.4	45.5	-	-	-	-	138	-	-	-	-	1.49	-	-
Ap	0-30	6.3	10	54	35	0.1	1.4	1.4	9.6	7.1	0.6	88	0.05	518	361	70	394	76	19.6	6.35	1.84
Ah	30-50	6.8	21	52	27	0.1	0.8	0.8	7.4	12.5	0.3	99	-	556	376	68	436	79	23.8	7.51	1.63
C	60-90	8.0	4	56	44	0.0	0.3	0.3	7.8	10.3	0.0	91	1.0	370	230	62	277	75	19.3	5.85	1.01

[a]ECEC: Effective cation exchange capacity, $ECEC_{Mn}$: Mn contribution to ECEC, BS: Base saturation, EA: Exchangeable acidity, Mn_d (Fe_d) and Mn_o (Fe_o): Dithionite-citrate and ammonium-oxalate extractable Mn (Fe), respectively.

Table 3.1 ***(continued)***

Sample	Depth (cm)	pH (H_2O)	Clay (%)	Silt (%)	Sand (%)	N_{tot} (%)	C_{tot} (%)	C_{org} (%)	C_{org}/N_{tot}	ECEC ($cmol_c$/kg)	$ECEC_{Mn}$ (%)	BS (%)	EA ($cmol_c$/kg)	Mn_{tot} (mg/kg)	Mn_d (mg/kg)	Mn_d/Mn_{tot} (%)	Mn_o (mg/kg)	Mn_o/Mn_{tot} (%)	Fe_{tot} (g/kg)	Fe_d (g/kg)	Fe_o (g/kg)
Haplic Luvisol (Cutanic, Hypereutric, Siltic) #6																					
Oi	-6- -3	-	-	-	-	1.4	43.3	43.3	30.8	-	-	-	-	821	-	-	-	-	0.47	-	-
Oe	-3- -1	-	-	-	-	1.8	35.0	35.0	19.2	-	-	-	-	1590	-	-	-	-	3.25	-	-
Ah	0-6	5.5	14	85	1	0.4	6.4	6.4	16.1	23.4	1.6	97	0.40	1120	846	76	845	76	19.8	6.14	1.80
E	6-20	4.7	15	83	1	0.1	0.8	0.8	12.7	11.7	0.5	71	3.8	234	85.0	36	65.2	28	19.9	5.80	1.35
EB	20-40	5.3	18	81	1	0.1	0.7	0.7	8.9	17.3	0.1	94	1.0	204	64.0	31	37.0	18	25.5	7.44	1.20
Bt1	40-65	4.8	19	80	1	0.1	0.5	0.5	8.5	18.7	0.0	87	2.5	198	55.5	28	17.7	9	33.5	9.27	1.41
Bt2	65-95	5.2	23	76	0	0.0	0.3	0.3	6.9	18.7	0.1	97	0.62	253	83.6	33	79.9	32	32.0	9.17	0.98
Haplic Luvisol (Cutanic, Loamic, Oligeoeutric) #7																					
Ah	0-10	5.7	24	54	23	0.2	2.8	2.8	11.7	15.0	2.8	96	0.10	1190	-	-	1000	85	27.5	-	-
E	10-30	6.3	24	52	23	0.2	1.4	1.4	9.4	14.5	1.2	99	0.0	1610	1000	62	1060	66	38.9	12.1	4.44
Bt1	30-50	6.7	35	42	23	0.1	0.8	0.8	8.3	22.0	0.3	100	0.0	1410	1380	98	1170	83	29.6	16.4	4.53
Bt2	50-90+	6.8	31	54	15	0.1	0.5	0.5	7.4	27.0	0.1	100	0.0	1580	1470	93	1320	84	42.3	18.4	2.55
Skeletic Albic Podzol (Loamic) #8																					
Oi	-9- -7	-	-	-	-	1.4	47.1	47.1	34.6	-	-	-	-	503	-	-	-	-	0.20	-	-
Oe	-7- -2.5	-	-	-	-	1.7	44.6	44.6	25.8	-	-	-	-	54.7	-	-	-	-	1.95	-	-
Oa	-2.5-0	-	-	-	-	1.8	36.3	36.3	20.7	-	-	-	-	143	-	-	-	-	8.59	-	-
E	0-5	3.8	14	57	30	0.2	4.5	4.5	23.4	18.9	0.0	1.9	17	106	20.8	20	8.26	8	22.2	11.9	4.46
Bs	5-18	4.3	22	49	29	0.2	3.8	3.8	20.2	12.7	0.3	2.2	11	342	193	56	93.9	28	65.6	43.9	28.2
Bw	18-30	4.8	11	55	34	0.1	2.6	2.6	18.3	2.5	0.6	2.8	3.0	416	248	60	162	39	40.7	18.3	8.07
C	30-50+	4.9	6	47	46	0.1	1.0	1.0	14.3	2.1	0.3	16	0.41	422	326	77	207	49	36.4	8.92	1.51
Dystric Albic Folic Stagnosol (Nechic, Siltic) #9																					
Oi	-15.5- -12.5	-	-	-	-	1.3	43.7	43.7	32.9	-	-	-	-	1910	-	-	-	-	0.38	-	-
Oe	-12.5- -4.5	-	-	-	-	1.7	44.6	44.6	25.5	-	-	-	-	461	-	-	-	-	1.15	-	-
Oa	-4.5-0	-	-	-	-	1.8	35.2	35.2	19.7	-	-	-	-	45.1	-	-	-	-	7.78	-	-
EA	0-10	4.1	11	71	18	0.2	4.5	4.5	21.7	6.3	0.0	3.9	7.5	109	28.5	26	18.0	16	12.3	5.23	4.60
E	10-18	4.3	11	72	18	0.0	0.6	0.6	15.0	2.1	0.1	3.4	3.0	142	48.2	34	37.7	27	12.9	5.38	2.71
Eg	18-68	4.3	17	66	17	0.0	0.2	0.2	7.5	4.8	0.2	9.6	5.0	154	44.5	29	53.4	35	19.3	7.04	2.02
Bg	68-100+	4.7	17	53	30	0.0	0.1	0.1	5.9	5.3	0.4	38	3.9	88.3	28.5	32	19.8	22	15.2	7.12	0.91

[a]ECEC: Effective cation exchange capacity, $ECEC_{Mn}$: Mn contribution to ECEC, BS: Base saturation, EA: Exchangeable acidity, Mn_d (Fe_d) and Mn_o (Fe_o): Dithionite-citrate and ammonium-oxalate extractable Mn (Fe), respectively.

Table 3.2: Spearman rank order correlations (r_s) of different Mn and Fe pools with physicochemical soil properties.[a] Significant correlations at p <0.05 and <0.01 are marked with * and **, respectively. Correlation coefficients >0.7 are displayed in bold.

	Mn_{tot}	**Mn_d**	**Mn_o**	**Fe_d**	**Fe_o**	**Mn^{2+}**	**Mn^{3+}**	**Mn^{4+}**	**Mn AOS**
Mn_{tot}	1	**0.99****	**0.98****	0.56**	0.42*	-0.41**	-0.65**	**0.71****	0.64**
Mn_d	**0.99****	1	**0.99****	0.58**	0.41*	-0.58**	**-0.77****	**0.87****	**0.82****
Mn_o	**0.98****	**0.99****	1	0.54**	0.40*	-0.55**	**-0.77****	**0.86****	**0.81****
Fe_d	0.56**	0.58**	0.54**	1	0.67**	-0.54**	-0.39*	0.56**	0.53**
Fe_o	0.42*	0.41*	0.40*	0.67**	1	-0.46**	-0.18	0.31	0.29
Clay	0.62**	0.61**	0.60**	**0.78****	0.41*	-0.32	-0.54**	0.65**	0.57**
Silt	-0.45**	-0.50**	-0.50**	-0.68**	-0.48**	0.57**	0.56**	-0.69**	-0.65**
Sand	-0.02	0.00	0.04	0.18	0.37*	-0.37*	-0.09	0.15	0.18
N_{tot}	0.07	0.32	0.32	0.24	0.45**	0.15	-0.04	-0.16	-0.21
C_{tot}	0.04	0.20	0.18	0.19	0.42	0.29	-0.13	-0.24	-0.32*
C_{org}	0.03	0.20	0.18	0.25	0.51**	0.26	-0.07	-0.26	-0.33*
C_{org}/N_{tot}	-0.15	-0.12	-0.14	0.06	0.42*	0.33*	0.09	-0.40**	-0.45**
ECEC	0.48**	0.49**	0.45**	0.32	-0.06	-0.16	-0.36*	0.44**	0.41*
$ECEC_{Mn}$	0.38*	0.36*	0.40*	0.33	0.47**	-0.20	-0.26	0.23	0.18
BS	0.43*	0.42*	0.43*	0.02	-0.37*	-0.09	-0.52**	0.46**	0.44**
EA	-0.49**	-0.49	-0.51	0.10	0.40*	0.23	0.41**	-0.48**	-0.50**
pH(H_2O)	0.48**	0.47**	0.48**	-0.13	-0.46**	-0.18	-0.55**	0.51**	0.49**
pH($CaCl_2$)	0.41*	0.41*	0.41*	-0.19	-0.51**	-0.17	-0.48**	0.46**	0.45**
EC	0.22	0.16	0.17	-0.15	-0.28	0.18	-0.31	0.18	0.13

[a]ECEC: Effective cation exchange capacity, $ECEC_{Mn}$: Mn contribution to ECEC, BS: Base saturation, EA: Exchangeable acidity, EC: Electrical conductivity.

3.3.2. XANES ANALYSIS

Normalized XANES and corresponding first-derivative spectra of soils are illustrated in Figure 3.1. Table B.3 summarizes prominent absorption features and first-derivative peaks up to 6,580 eV. Fractions of Mn^{2+}, Mn^{3+}, and Mn^{4+} and the resulting Mn AOS are compiled in Table 3.3.

Organic soil horizons consisting of fresh, undecomposed plant debris (Oi) tended to be enriched in Mn^{2+} when compared to their underlying A and E horizons (Cambisols #1 and #2, Chernozems, Luvisol #6, Podzol #8). In organic surface layers consisting of partially decomposed, fragmented organic matter (Oe) or amorphous organic matter without mineral material (Oa), the Mn valence varied considerably. For example, in Luvisol #6 the Oi horizon was dominated by Mn^{3+} (40%) with approximately equal shares of Mn^{2+} and Mn^{4+} (ca. 30%). In contrast, its Oe horizon had a high proportion of Mn^{4+} (55%), an intermediate share of Mn^{3+} (33%), and little Mn^{2+} (12%). In Podzol #8, we observed continuously decreasing Mn^{2+} shares from 100% in the Oi horizon to 15% in the Oa horizon. This decrease was accompanied by an increase in Mn^{3+} content, reaching 80% in the Oa horizon, while the Mn^{4+} share in the Podzol's organic surface layers was negligible (≤5%) (Table 2). In Stagnosol #9, organic surface layers derived from a mixed forest stand were also dominated by Mn^{2+} and Mn^{3+}, which

together accounted for 70-100% of Mn_{tot} (Table 3.3). Remarkably, Mn^{4+} contents steadily declined from 29% in the Oi horizon to 0% in the Oa horizon (Table 3.3).

In mineral horizons of most soils, Mn^{4+} was the dominant species; only a few soils (Luvisol #6, Podzol #8, Stagnosol #9) were dominated by Mn^{3+}. Substantial fractions (>40%) of Mn^{2+} in mineral horizons were solely observed in Stagnosol #9, which is characterized by recurring reducing conditions, and in the Ck horizon of Chernozem #4, whose loess material contained 1.4 wt.% inorganic C, likely favoring Mn^{2+} incorporation into carbonate minerals (Ji and Chen, 2000) (Tables 3.1 and Table **3.3**).

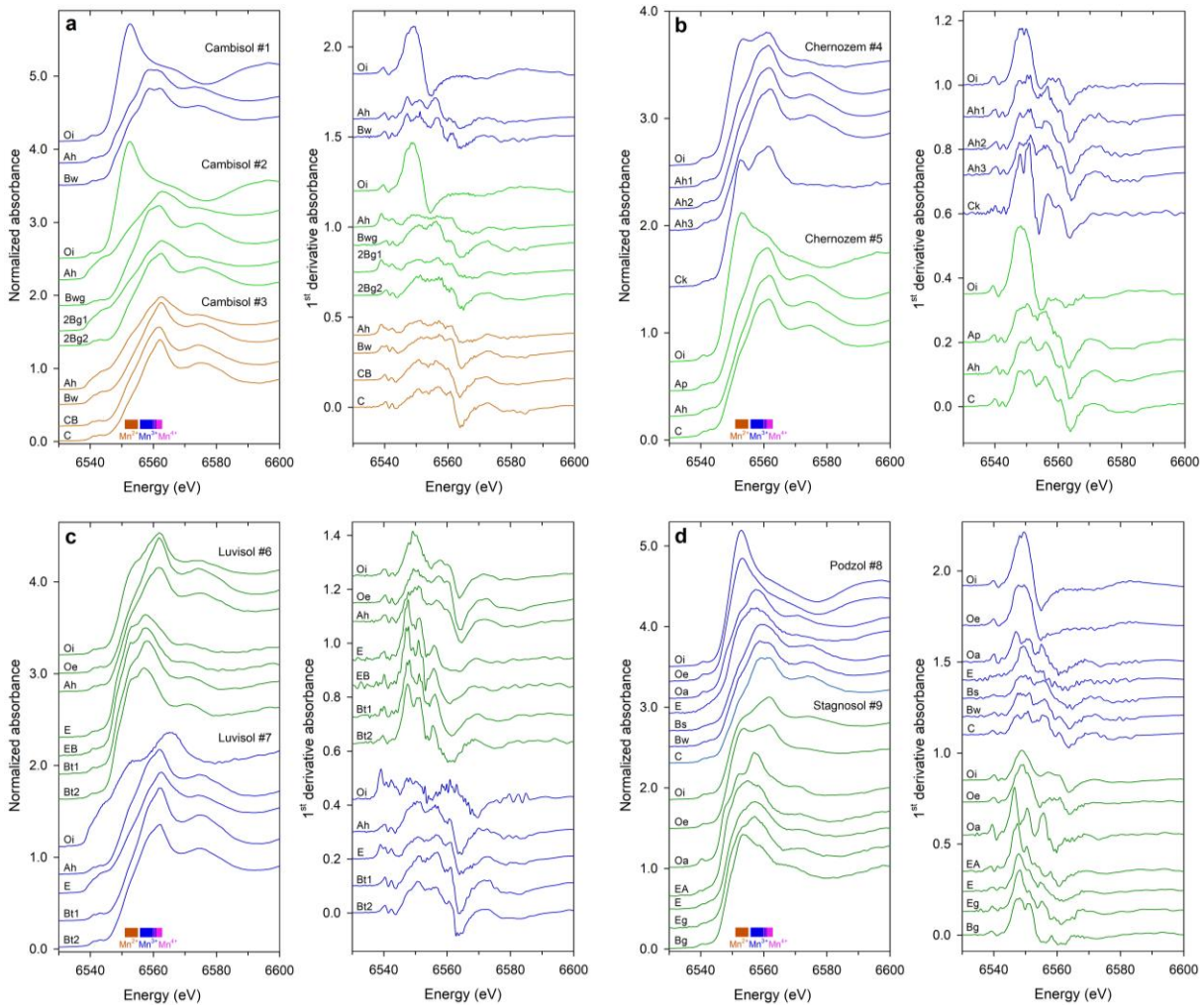

Figure 3.1. Stacked normalized Mn K-edge XANES (left) and corresponding first-derivative spectra (right) of soil horizons of (a) Cambisols, (b) Chernozems, (c) Luvisols, and (d) Podzol and Stagnosol. White-line position ranges of monovalent Mn references (Zahoransky et al., 2022) are shown at the bottom of each XANES panel. Spectra were slightly smoothed (box-car averaging, Kernel size ≤3) to increase the signal-to-noise ratio in order to better differentiate relevant absorption features.

Table 3.3. Fractional amounts of Mn^{2+}, Mn^{3+}, and Mn^{4+} and calculated average oxidation state (AOS) of Mn

Sample	Mn^{2+}	Mn^{3+}	Mn^{4+}	Mn AOS	Fit sum	*R*-factor (× 10^4)[a]
Dystric Skeletic Cambisol (Hyperhumic, Loamic) #1						
Oi	1.00	0.00	0.00	2.00	0.98	11.2
Ah	0.10	0.36	0.54	3.44	0.96	4.26
Bw	0.15	0.36	0.49	3.34	1.01	3.37
Eutric Stagnic Cambisol (Loamic) #2						
Oi	1.00	0.00	0.00	2.00	0.98	7.53
Ah	0.32	0.00	0.68	3.36	0.93	314
Bwg	0.04	0.25	0.72	3.68	0.99	4.26
2Bg1	0.29	0.00	0.71	3.42	0.94	255
2Bg2	0.11	0.19	0.70	3.59	0.93	6.17
Calcaric Skeletic Cambisol (Clayic, Humic) #3						
Ah	0.29	0.00	0.71	3.43	0.96	168
Bw	0.17	0.00	0.83	3.67	0.99	49.9
CB	0.11	0.11	0.78	3.68	0.96	3.27
C	0.11	0.00	0.89	3.78	0.93	3.80
Haplic Chernozem (Pachic, Silitc) #4						
Oi	0.48	0.29	0.23	2.75	0.99	4.58
Ah1	0.18	0.30	0.52	3.34	0.98	3.16
Ah2	0.17	0.27	0.56	3.38	0.97	3.21
Ah3	0.16	0.25	0.60	3.44	0.97	5.07
Ck	0.51	0.01	0.48	2.97	1.00	30.3
Haplic Chernozem (Loamic, Pachic) #5						
Oi	0.61	0.39	0.00	2.40	1.01	3.25
Ap	0.12	0.35	0.53	3.40	0.98	3.96
Ah	0.14	0.17	0.69	3.56	0.98	6.23
C	0.16	0.21	0.63	3.47	0.97	7.06
Haplic Luvisol (Cutanic, Hypereutric, Siltic) #6						
Oi	0.28	0.40	0.32	3.03	0.97	2.54
Oe	0.12	0.33	0.55	3.43	0.99	1.22
Ah	0.20	0.35	0.45	3.25	0.98	3.19
E	0.35	0.61	0.04	2.68	1.01	12.0
EB	0.32	0.68	0.00	2.68	1.03	22.4
Bt1	0.36	0.64	0.00	2.64	1.05	29.2
Bt2	0.37	0.63	0.00	2.63	1.07	66.0
Haplic Luvisol (Cutanic, Loamic, Oligeoeutric) #7						
Ah	0.16	0.17	0.67	3.51	0.99	586
E	0.23	0.00	0.77	3.53	0.98	6.66
Bt1	0.07	0.12	0.81	3.73	1.00	106
Bt2	0.13	0.15	0.73	3.60	0.97	7.33
Skeletic Albic Podzol (Loamic) #8						
Oi	1.00	0.00	0.00	2.00	1.00	10.7
Oe	0.77	0.23	0.00	2.23	1.02	19.5
Oa	0.15	0.80	0.05	2.90	0.98	24.1
E	0.34	0.66	0.00	2.66	1.00	57.7
Bs	0.08	0.63	0.29	3.21	0.99	6.01
Bw	0.12	0.55	0.33	3.21	0.98	8.11
C	0.08	0.35	0.57	3.48	0.97	4.12
Dystric Albic Folic Stagnosol (Nechic, Siltic) #9						
Oi	0.37	0.34	0.29	2.92	0.98	2.22
Oe	0.50	0.32	0.18	2.68	1.02	2.84
Oa	0.20	0.80	0.00	2.80	1.01	54.8
EA	0.49	0.51	0.00	2.51	1.07	48.9
E	0.33	0.67	0.00	2.67	1.01	31.3
Eg	0.42	0.58	0.00	2.58	1.02	61.9
Bg	0.56	0.44	0.00	2.44	1.03	8.47

[a] *R*-factor = $\Sigma_i(\text{data}_i - \text{fit}_i)^2/\Sigma_i\text{data}_i$.

Figure 3.2 illustrates Mn valence fractions and AOS grouped according to main soil horizons. As expected by the shift of absorption edges towards lower energy (Fig. 3.1), soil O horizons comprised significantly higher Mn^{2+} contents as compared to A and B horizons (one-way ANOVA on ranks), whereas differences in Mn^{2+} contents between A and B horizons were insignificant. We also detected no significant differences in Mn^{3+} fractions between O, A, and B horizons. In contrast, Mn^{4+} was significantly depleted in O as compared to both A and B horizons, but Mn^{4+} shares in A and B horizons did not differ significantly. As a result, Mn AOS was significantly lower in O than in A and B horizons, and did not differ between A and B horizons. Note that transition horizons (CB, EA, EB) as well as E and C horizons were excluded from statistical analysis; the latter two because of their limited number.

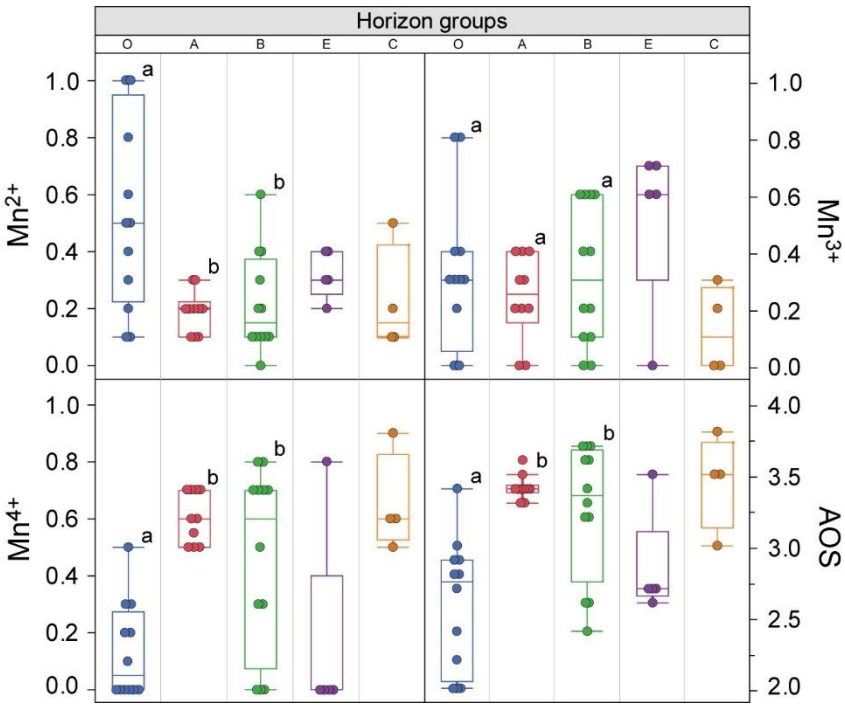

Figure 3.2. Boxplots illustrating XANES-derived Mn^{2+}, Mn^{3+}, and Mn^{4+} fractions and Mn AOS for soil horizon groups without transition horizons. The boxes contain 50% of the data (interquartile range, IQR). The middle line represents the median (50th percentile). Whiskers include data within 1.5 × IQR. Lowercase letters indicate significant (p <0.05) differences in species composition (one-way ANOVA on ranks). E and C horizons were excluded from statistical analysis.

In the next step, we evaluated correlations between XANES-derived fractional Mn valences and AOS and physicochemical soil parameters (Table 3.2). Strong positive correlations with r_s ≥0.8 were only observed between Mn^{4+}, Mn AOS, Mn_d, and Mn_o. In contrast, Mn^{3+} was negatively correlated with Mn_d and Mn_o (r_s = -0.77). Likewise, soil pH (H_2O and $CaCl_2$) was positively correlated with Mn^{4+} and Mn AOS, but negatively with Mn^{3+} (r_s ~ ±0.5). In addition, Mn^{4+} was positively (r_s = 0.71) and Mn^{3+} negatively correlated with Mn_{tot} (r_s = -0.65). Both Mn^{4+} and Mn AOS were significantly positively correlated with Fe_d and clay content, albeit less strongly, and Mn^{4+} was also negatively correlated with silt content

(Table 3.2), indicating that high-valence Mn species occur predominantly in the clay fraction and are partially associated with Fe(III) (oxyhydr)oxides. Additionally, Mn^{4+} and Mn AOS showed a significant negative correlation with the C_{org}/N_{tot} ratio (r_s = -0.40 and -0.45, respectively, Table 3.2).

3.3.3. EXAFS ANALYSES

3.3.3.1. LINEAR COMBINATION FITTING

We first fit soil EXAFS spectra with Mn reference spectra, that were positively identified by PCA-TT analysis ('initial LCF'). Results of PCA, including eigenvalues, total and cumulative variances as well as IND values, are summarized in (Table B.5). Based on the Kaiser-Guttman criterion (Guttman, 1954), the number of statistical meaningful PCs (eigenvalues >1) was two and accounted for 92% of the observed variance in the soil EXAFS spectra. However, the minimum of the IND function, which also indicates the number of statistical meaningful PCs, was reached at the fifth PC explaining 97% of the total variance of all soil Mn EXAFS spectra. Therefore, we decided to use five PCs for subsequent TT testing. Fourteen references had excellent SPOIL values, ten were rated good, and six were rated fair. Out of the 14 references with excellent SPOIL values, 11 unique (non-redundant) spectra were selected for initial LCF analysis. We arbitrarily excluded references that did not contribute to the fit by at least a 5% share (O'Day et al., 2004), thereby risking a type-2 error. In addition, a reference spectrum was retained in the fit, if its inclusion improved the *R*-factor by at least 10% (Fig. B.3, Table B.5). Reconciliation of PCA-TT results with spectral features of the soil EXAFS spectra, however, indicated that several Mn species (groups) were missing in the initial LCFs. Spectral fingerprinting showed evidence for the presence of additional Mn species in individual soil horizons, such as the spinel hausmannite (Mn_3O_4) and feitknechtite (β-MnOOH) in the 2Bg1 and 2Bg2 horizon of Cambisol #2, respectively (Fig. 3.3). Some EXAFS features of the Ap horizon of Chernozem #5 suggested silicate-bound Mn as in hendricksite ($K(Zn,Mg,Mn^{2+})_3Si_3AlO_{10}(OH)_2$, trioctahedral mica), although spectral evidence was less conclusive in this case (Fig. 3.3).

Therefore, initial LCFs were refined by considering all non-redundant Mn reference included in the Mn reference database of Zahoransky et al. (2022) (*N* = 25). Each new fit started with the references previously identified by PCA-TT. Additional references were then successively added, starting with those indicated by EXAFS fingerprinting. All references that decreased the *R*-factor by at least 10% and contributed ≥5% to the fit were retained. Finally, all combinations of the so-obtained references were tested and the best fit in terms of *R*-factor and fit sum was selected.

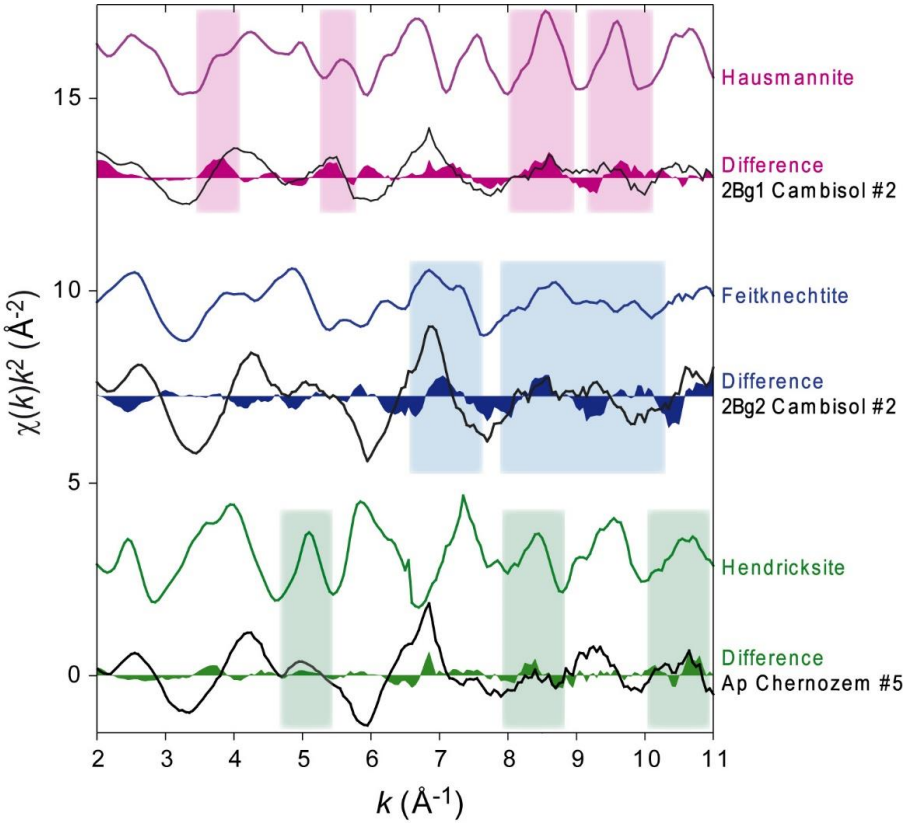

Figure 3.3. Indications for additional Mn species in individual soil horizons from EXAFS fingerprinting: Hausmannite (Mn_3O_4, spinel) and feitknechtite (β-MnOOH, Mn(III) oxyhydroxide) in the 2Bg1 and 2Bg2 horizon of Cambisol #2, respectively, and hendricksite ($K(Zn,Mg,Mn^{2+})_3Si_3AlO_{10}(OH)_2$, trioctahedral mica) in the Ap horizon of Chernozem #5. Differences were calculated between experimental spectra and their initial PCA-TT-based LCF (see text for details).

The number of fit references was generally not limited, but fits whose number of references was implausibly high (>7) compared to the number of PCA components were not considered. The fit quality (*R*-factors) of the refined LCFs was generally better than those of the PCA-TT-based LCFs, albeit not significantly (paired *t*-test). However, fit totals were significantly closer to unity as compared to the initial LCFs (paired *t*-test), and EXAFS LCF-based Mn AOS calculations (see below) for the final fits showed better agreements with XANES-derived Mn AOS than the initial PCA-TT-based LCFs. The final fractions of fit references were conservatively combined into Mn species groups based on EXAFS evaluations of Mn reference compounds (Zahoransky et al., 2022) (see *Supplementary material*). These included (1) manganates, (2) organically complexed Mn, (3) Mn(III) oxyhydroxides, (4) silicate-bound Mn, (5) Mn oxides without tunnel- or layer structure, and (6) physisorbed Mn.

Soil-Mn EXAFS spectra along with their final LCFs are illustrated in Figure 3.4 and fit results are summarized in Table 3.4. Generally, LCFs reproduced soil EXAFS spectra well (Fig. 3.4). However, low-signal-to noise ratios and misfits, potentially caused by the lack of appropriate references, resulted in partially mediocre *R*-factors (Table 3.4). Therefore, fit totals of each Mn species group are more reliable than fit fractions of individual reference species.

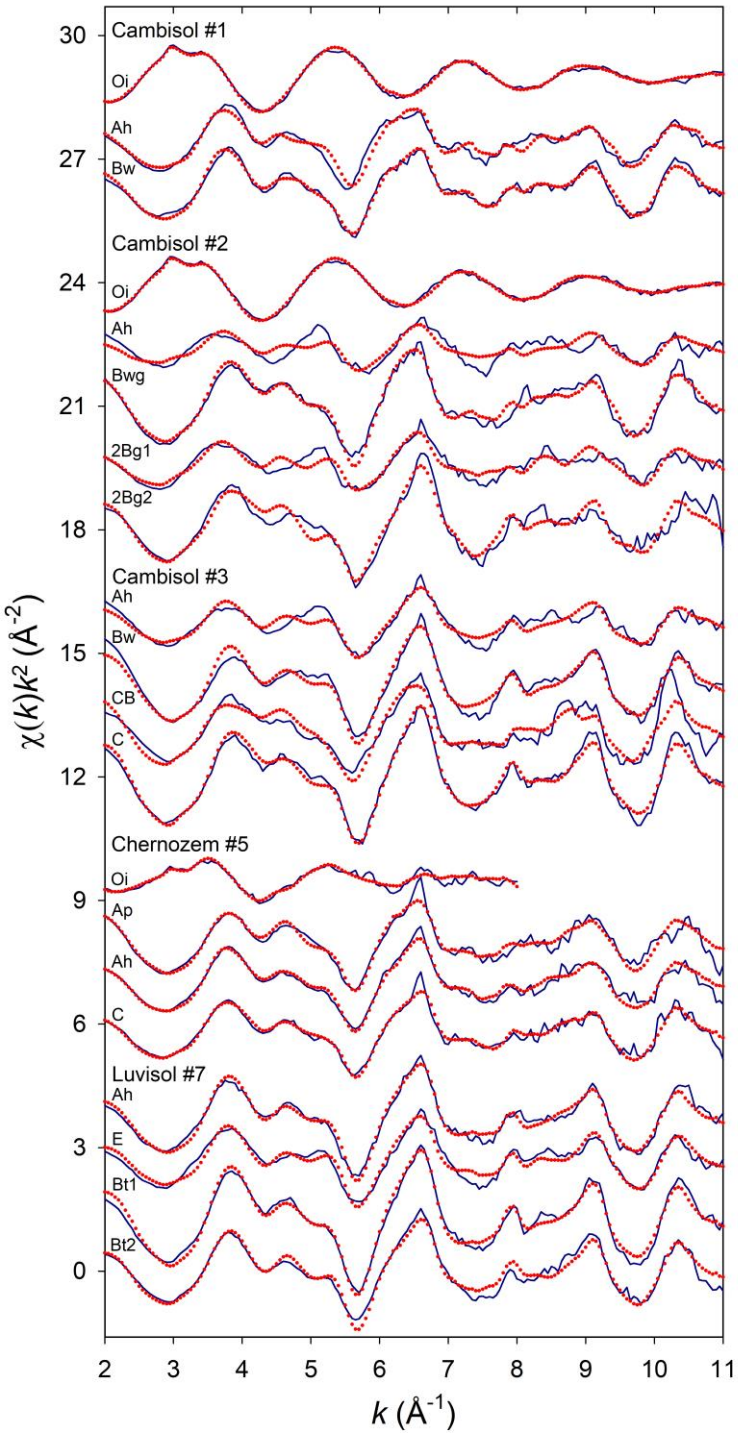

Figure 3.4. Stacked k^2-weighted Mn K-edge EXAFS spectra and LCFs of soil samples. LCF results are summarized in Table 3.4.

Table 3.4. Speciation of Mn in bulk soil samples obtained from LCF analysis of k^2-weighted Mn K-edge EXAFS spectra[a]

	Manganates							Organically complexed Mn				Oxyhydro-xides			Silicates				Oxides			Physi-sorbed	Fit sum	*R*-factor[c]	Mn AOS_{EXAFS}[d]	Mn AOS_{XANES}
	AcB	δ-Mn	NaB	Hol	Rmn	Tdr	Total	Ac	Ox	Peat	Total	Fkn	Gro	Total	Bnt	Hds	Msu	Total	Bxb	Hsm	Total	Illite				
	3.86[b]	3.90	3.84	3.75	3.82	3.77		2.00	2.05	2.00		3.02	3.17		2.99	2.21	2.49		3.08	2.72		2.35				
Dystric Skeletic Cambisol (Hyperhumic, Loamic) #1																										
Oi	-	-	-	-	-	-	**0.00**	-	0.07	0.84	**0.91**	-	-	**0.00**	-	-	-	**0.00**	-	-	**0.00**	**0.09**	0.96	0.02	2.04	2.00
Ah	-	-	-	0.25	0.26	-	**0.51**	-	-	-	**0.00**	-	0.20	**0.20**	-	-	0.17	**0.17**	-	0.12	**0.12**	**0.00**	1.05	0.11	3.31	3.45
Bw	0.21	-	-	0.15	0.21	-	**0.57**	-	-	-	**0.00**	-	0.07	**0.07**	-	-	0.17	**0.17**	0.09	0.08	**0.18**	**0.00**	1.16	0.03	3.38	3.34
Eutric Stagnic Cambisol (Loamic) #2																										
Oi	-	-	-	-	-	-	**0.00**	-	0.08	0.77	**0.85**	-	-	**0.00**	-	-	-	**0.00**	-	-	**0.00**	**0.15**	0.96	0.01	2.06	2.00
Ah	-	0.44	-	-	-	-	**0.44**	-	-	0.39	**0.39**	-	-	**0.00**	-	-	-	**0.00**	0.11	0.06	**0.17**	**0.00**	0.85	0.35	2.99	3.36
Bwg	-	0.32	-	0.06	0.40	-	**0.78**	-	-	-	**0.00**	-	-	**0.00**	-	-	-	**0.00**	-	0.16	**0.16**	**0.07**	1.10	0.05	3.57	3.68
2Bg1	-	0.37	-	-	-	-	**0.37**	-	-	0.33	**0.33**	0.19	-	**0.19**	-	-	-	**0.00**	-	0.11	**0.11**	**0.00**	1.10	0.21	2.98	3.42
2Bg2	0.57	-	-	-	0.06	-	**0.63**	-	-	-	**0.00**	0.37	-	**0.37**	-	-	-	**0.00**	-	-	**0.00**	**0.00**	1.03	0.13	3.55	3.59
Calcaric Skeletic Cambisol (Clayic, Humic) #3																										
Ah	0.19	-	-	-	-	0.31	**0.50**	-	-	0.33	**0.33**	0.17	-	**0.17**	-	-	-	**0.00**	-	-	**0.00**	**0.00**	0.99	0.15	3.08	3.43
Bw	0.44	-	-	-	-	0.41	**0.85**	0.15	-	-	**0.15**	-	-	**0.00**	-	-	-	**0.00**	-	-	**0.00**	**0.00**	1.04	0.05	3.54	3.67
CB	-	-	0.27	-	0.43	-	**0.70**	-	-	-	**0.00**	-	-	**0.00**	0.30	-	-	**0.30**	-	-	**0.00**	**0.00**	1.04	0.17	3.57	3.68
C	0.40	0.42	-	-	-	-	**0.81**	-	-	-	**0.00**	-	-	**0.00**	0.19	-	-	**0.19**	-	-	**0.00**	**0.00**	1.16	0.03	3.71	3.78
Haplic Chernozem (Loamic, Pachic) #5																										
Oi[e]	0.06	-	-	-	-	-	**0.06**	-	-	0.58	**0.58**	-	0.23	**0.23**	-	-	0.13	**0.13**	-	-	**0.00**	**0.00**	0.85	0.11	2.44	2.40
Ap	-	0.27	-	0.42	-	0.17	**0.86**	-	-	-	**0.00**	-	-	**0.00**	-	0.14	-	**0.14**	-	-	**0.00**	**0.00**	1.04	0.10	3.58	3.40
Ah	0.27	-	-	0.35	-	-	**0.63**	-	-	-	**0.00**	0.15	-	**0.15**	-	-	0.08	**0.08**	-	-	**0.00**	**0.14**	1.19	0.06	3.37	3.56
C	0.20	-	-	-	0.41	-	**0.61**	-	-	0.21	**0.21**	-	-	**0.00**	0.19	-	-	**0.19**	-	-	**0.00**	**0.00**	1.13	0.07	3.30	3.47
Haplic Luvisol (Cutanic, Loamic, Oligeoeutric) #7																										
Ah	0.39	-	-	-	0.43	-	**0.82**	0.18	-	-	**0.18**	-	-	**0.00**	-	-	-	**0.00**	-	-	**0.00**	**0.00**	1.09	0.04	3.51	3.51
E	0.50	-	-	-	0.12	-	**0.62**	-	-	0.26	**0.26**	-	-	**0.00**	-	-	-	**0.00**	-	0.12	**0.12**	**0.00**	1.08	0.08	3.23	3.53
Bt1	0.62	-	-	-	0.32	-	**0.94**	-	-	-	**0.00**	-	-	**0.00**	-	-	0.06	**0.06**	-	-	**0.00**	**0.00**	1.12	0.03	3.77	3.73
Bt2	0.51	-	-	-	0.30	-	**0.82**	-	0.07	-	**0.07**	-	-	**0.00**	-	0.12	-	**0.12**	-	-	**0.00**	**0.00**	1.05	0.06	3.54	3.60

[a]Fractions were recalculated to a component sum of 100%. Their relative uncertainty is 10% at best. Abbreviations of fit references: AcB: Acid birnessite (hex., syn), δ-Mn: δ-MnO_2 (syn), NaB: Na-birnessite (tricl.), Hol: Hollandite *s.s.*, Rmn: Romanèchite, Tdr: Todorokite, Ac: Mn(II) acetate tetrahydrate (syn), Ox: Mn(II) oxalate dihydrate (syn), Peat: Mn(II) adsorbed to peat (pH7), Fkn: Feitknechtite, Gro: Groutite, Bnt: Braunite, Hds: Hendricksite, Msu: Masutomilite, Bxb: Bixbyite, Hsm: Hausmannite, Illite: Mn(II) adsorbed to illite (pH7).

[b]Mn AOS determined by the 'Combo' XANES-LCF method (Zahoransky et al., 2022).

[c]R-factor = $\Sigma_i(data_i - fit_i)^2/\Sigma_i data_i$.

[d]Calculated from fit fractions and Mn AOS of each fit reference.

[e]Spectrum analyzed over k = 2.0-8.0 $Å^{-1}$.

According to the LCF results, organically complexed Mn predominated with 58-91% of Mn_{tot} ($\bar{x}$ = 78%) in all Oi horizons investigated (Cambisols #1, #2; Chernozem #5). In addition, noticeable proportions (9 and 15%) of physisorbed Mn species were found in both Cambisol Oi horizons (Table 3.4). XANES analysis of the Cambisol litter horizons showed exclusively Mn^{2+} (Table 3.3), consistent with the absence of $Mn^{3+/4+}$ in mineral structures. Besides organically complexed Mn (58%), the Oi horizon of Chernozem #5 contained substantial amounts of Mn^{3+} in the form of Mn(III) oxyhydroxides (23%), silicate-bound Mn (13%), and a minor fraction of manganate-Mn (6%) (Table 4). These results correspond well with the XANES analysis, which showed 61% Mn^{2+} and 39% Mn^{3+} (Table 3.3).

Mineral soil horizons were by far dominated by manganates, which accounted for 37-94% of Mn_{tot} ($\bar{x}$ = 67%, Table 3.4). Concentrations (mg/kg) of manganate-Mn, calculated from fitted manganate fractions and Mn_{tot} values (N = 17), were positively correlated with Mn_{tot} (r_s = 0.89, p <0.001), Mn_d (r_s = 0.90, p <0.001), and Mn_o (r_s = 0.89, p <0.001) (Table B.6). Significant slopes of linear regressions (p <0.0001) between manganate-Mn and Mn_{tot} (0.72±0.09), Mn_d (0.93±0.12), or Mn_o (0.99±0.13) (Fig. B.4) reaffirm that manganates are the dominant Mn species in these soils and are almost quantitatively dissolved by dithionite and oxalate extractants. Remarkably, we found no significant correlations between manganate-Mn and Fe_d, Fe_o, and clay content (Table B.6).

Manganese(III) oxyhydroxides, contributing ≤37% to Mn_{tot} in mineral horizons ($\bar{x}$ = 7%, Table 3.4), were present in four out of the five soils. Their occurrence was tied to individual A and B horizons (N = 6) with no clear profile trends observable (Table 3.4). Likewise, organically complexed Mn was identified in several mineral horizons with contributions ≤39% ($\bar{x}$ = 11%, Table 3.4). The highest concentrations of organically complexed Mn were found in the Ah and 2Bg1 horizons of Cambisol #2, and Ah horizon of Cambisol #3. Remarkably, the C horizon of Chernozem #5 comprised 21% organically complexed Mn, which is plausible given the C_{org} content of this horizon and the sorption capacity of humic materials at pH 7.5 of approximately 17.8 mg/g Mn^{2+} (Zhao et al., 2020). Solid-solution formation of $Ca_xMn_{1-x}CO_3$ may also explain this result. In this case, the local Mn coordination would be similar to that of organic Mn complexes (R_{Mn-C}~3.2 Å) and thus contribute to the fraction of organically complexed Mn. Regardless of this issue, we observed no significant correlation between organically complexed Mn and C_{org} in mineral horizons.

Silicate-bound Mn contributed ≤30% to Mn_{tot} ($\bar{x}$ = 8%, Table 3.4) in mineral horizons. No significant correlation was observed between silicate-bound Mn and (Mn_{tot} – Mn_d) concentration, an indicator of silicate-bound Mn (Table B.6).

Manganese present in oxide structures other than phyllo- and tectomanganates was of minor importance in all mineral horizons (≤18%, $\bar{x}$ = 5%, Table 3.4). It was detected in A and B horizons of Cambisols #1 and #2, and in the E horizon of Luvisol #7, where it comprised 11-18% of Mn_{tot} (Table 3.4). Physisorbed Mn in mineral horizons, which we interpret as Mn^{2+} associated with negatively

charged soil surfaces (see *Supplementary material*), was only present in the Bwg horizon of Cambisol #2 (7%) and the Ah horizon of Chernozem #5 (14%) (Table 3.4).

The validity of EXAFS-LCF results was examined by linear combination reconstructions of soil XANES spectra (6,530-6,600 eV) based on the fractions of EXAFS references used in each fit (Fig. 3.5). In the majority of cases, the reconstructions agreed well with the soil XANES spectra (*R*-factors: <60×10^{-4}). Larger misfits (*R*-factors: >70×10^{-4}) were observed, for example, for the Ah and 2Bg horizons of Cambisol #2, likely due to the oxidation state of fit references not adequately reflecting the Mn oxidation state of the respective soil Mn species.

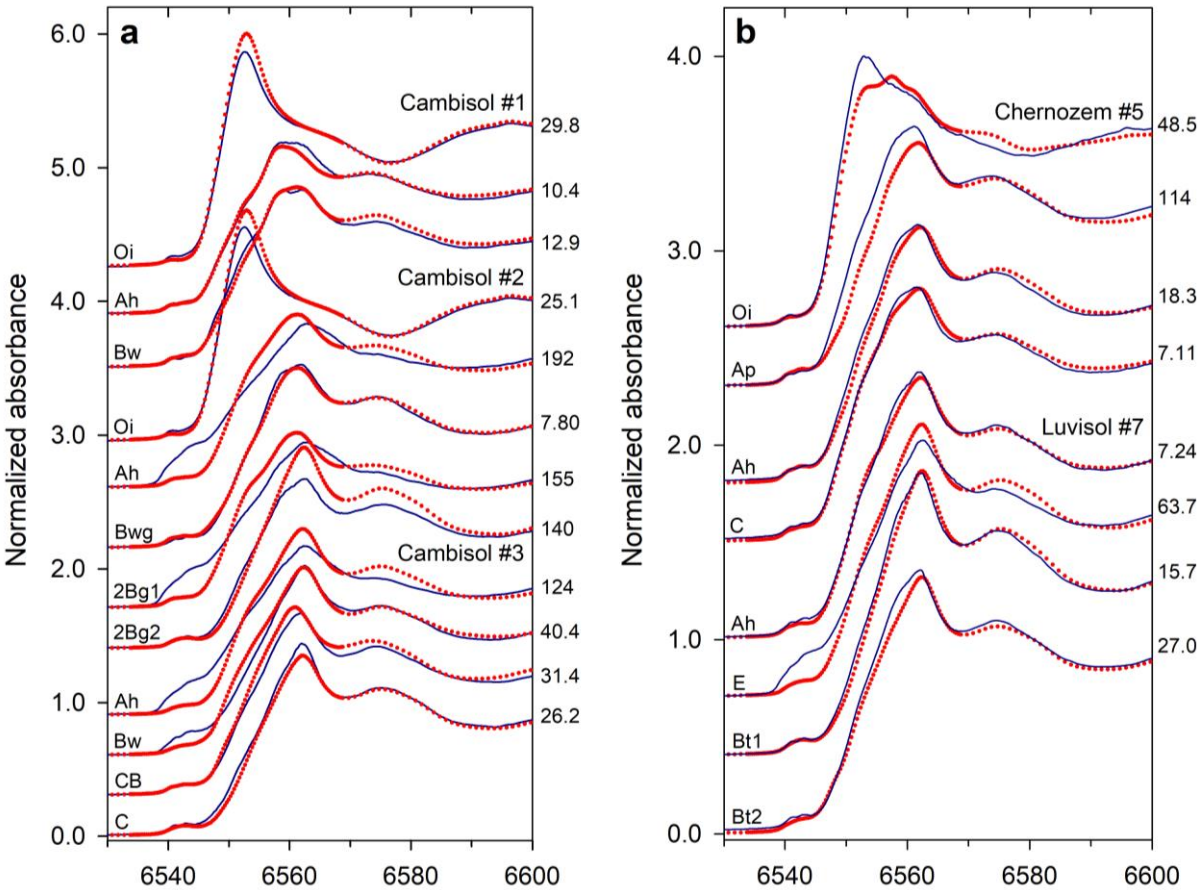

Figure 3.5. Stacked linear combination reconstructions of XANES spectra (6,530-6,600 eV) of (a) Cambisols #1, #2, and #3 and (b) Chernozem #5 and Luvisol #7 calculated from EXAFS-LCF results. Numbers on the right indicate the *R*-factor (×10^{4}) of each reconstruction.

We also compared EXAFS-derived Mn AOS (AOS_{EXAFS}) with those obtained from soil XANES analysis (AOS_{XANES}). Manganese AOS_{EXAFS} values were calculated from the LCF fraction of each reference compound and its XANES-derived Mn AOS, as determined by Zahoransky et al. (2022) (Table 3.4). Manganese AOS_{EXAFS} values deviated ≤0.2 v.u. from the soil-Mn AOS_{XANES} values in 80% of cases (Table 3.4). For Oi horizons (*N* = 3), differences were <0.1 v.u. (<3%, $\bar{x}$ = 2%), for A horizons (*N* = 6) <0.4 v.u.

(≤11%, $\bar{x}$ = 6%), and deviations ≤0.4 v.u. (<13%, $\bar{x}$ = 4%) were also recorded for B, E, and C horizons (N = 11) (Table 3.4). Overall, we found a good correspondence between Mn AOS_{EXAFS} and soil-Mn AOS_{XANES} values. Larger discrepancies most likely originate from Mn oxidation-state differences between the fit references and their respective soil analogues.

3.3.3.2. SHELL FITTING

The local Mn coordination environment in 19 soil samples of Cambisols, Chernozem #5, and Luvisol #7 was additionally analyzed by EXAFS shell fitting. Figure 3.6 exemplarily shows k^3-weighted Mn K-edge EXAFS spectra and Fourier transforms of soil horizons of Cambisol #2 and Chernozem #5 along with their model fits. The figure illustrates that soil Mn coordination can change substantially in soils developed from strata of different parent material (Cambisol), whereas Mn coordination in soils formed on homogeneous parent materials such as loess (Chernozem) may change only slightly. Spectra and model fits of the remaining soil samples are shown in Figure B.5, and EXAFS shell-fit parameters of all soil samples are compiled in Table 3.5.

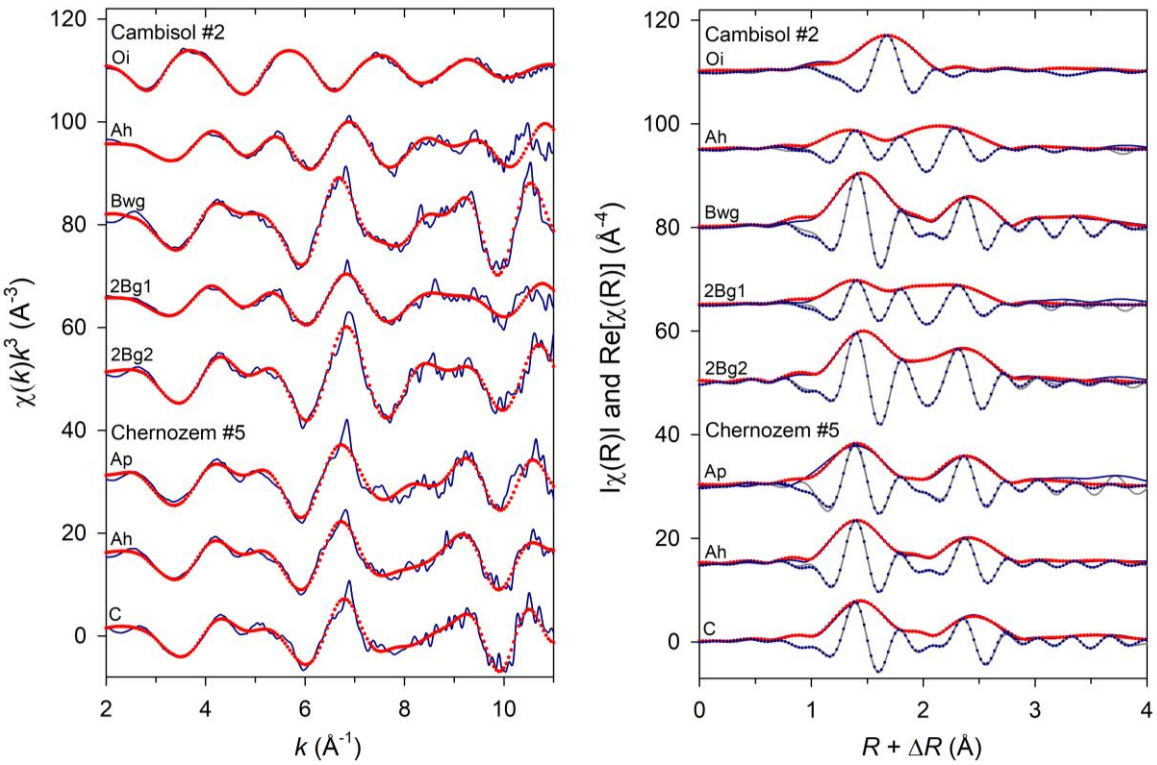

Figure 3.6. Stacked k^3-weighted Mn K-edge EXAFS spectra (left) as well as corresponding Fourier-transform magnitudes and real parts (right) of selected soil samples. Solid lines represent experimental data and dotted lines model fits. All EXAFS parameters are summarized in Table 3.5 and interatomic distances are visualized in Figure 3.7.

Table 3.5. EXAFS parameters determined by shell fitting of k^3-weighted Mn K-edge EXAFS spectra of soil samples[a]

Sample	*R*-factor[b]	χ_v^{2b}	N_{idp}[c] *k*-range fit	N_{var}[c] *R*-range fit	ΔE_0 (eV)[d]	*CN* (-)[e] σ^2 (Å²)[f]	*R* (Å)[g]	*CN* (-) σ^2 (Å²)	*R* (Å)	*CN* (-) σ^2 (Å²)	*R* (Å)	*CN* (-) σ^2 (Å²)	*R* (Å)
Dystric Skeletic Cambisol (Hyperhumic, Loamic) #1													
Oi	0.009	21	16.7 2.2-9.8	5 1.0-4.5	3.4(6)	O: 7.5(5) 0.0081(3)	2.18(0)	C: 1.8(9) 0.0081	3.16(4)	MS[h]: 8.0 0.0122	4.41(2)		
Ah	0.010	11	15.2 1.5-10.8	7 1.0-3.6	-0.2(7)	O: 3.1(3) 0.0025(4)	1.91(4)	Mn: 4.1(11) 0.0108(7)	2.91(1)	Mn: 3.1(12) 0.0049(6)	3.45(1)		
Bw	0.009	21	14.48 1.6-10.8	6 1.0-3.5	-0.1(7)	O: 2.9(3) 0.0011(4)	1.89(0)	Mn: 3.0(2) 0.0052(4)	2.88(1)	Mn: 3.6(4) 0.0052	3.43(1)		
Eutric Stagnic Cambisol (Loamic) #2													
Oi	0.006	19	16.4 2.2-9.7	5 1.0-4.5	3.9(5)	O: 7.1(4) 0.0077(3)	2.18(0)	C: 1.9(8) 0.0077	3.18(3)	MS[h]: 8.0 0.0115	4.37(2)		
Ah	0.001	2.6	10.6 2.0-9.7	6 1.0-3.2	-1.1(5)	O1: 2.5(1) 0.0037(3) O2: 1.7(2) 0.0037	1.90(0) 2.20(1)	Mn: 4.9(3) 0.0108(7) Mn: 3.0(2) 0.0049(6)	2.81(0) 3.01(1)				
Bwg	0.006	12	15.3 2.1-10.2	10 1.0-4.0	0.5(11)	O1: 4.8(5) 0.0026(4) O2: 1.3(4) 0.0026	1.91(1) 2.25(2)	Mn1: 2.6(16) 0.0021(7) Mn2: 2.7 0.0106(15)	2.87(1) 3.05(4)	Mn: 4.2(16) 0.0106	3.51(3)	Mn: 4.50(13) 0.0106	3.79(1)
2Bg1	0.004	5.4	10.3 1.9-10.2	7 1.0-3.0	-2.6(10)	O1: 3.1(3) 0.0043(5) O2: 1.8(3) 0.0043	1.90(1) 2.22(1)	Mn: 5.2(9) 0.0097(5) Mn: 3.0(4) 0.0097	2.81(1) 3.01(2)				
2Bg2	0.002	8.5	10.3 2.2-10.3	7 1.0-3.0	-2.6(10)	O1: 4.2(6) 0.0022(3) O2: 1.7(5) 0.0022	1.90(1) 2.22(1)	Mn: 6.0(18) 0.0072(5) Mn: 2.5(6) 0.0072	2.81(1) 3.01(2)				
Calcaric Skeletic Cambisol (Clayic, Humic) #3													
Ah	0.004	9.7	12.6 2.2-10.2	8 1.0-3.5	-2.6(9)	O1: 3.1(20) 0.0036(3) O2: 1.7(3) 0.0036	1.90(0) 2.24(1)	Mn1: 5.6(6) 0.0094(4) Mn2: 2.2(7) 0.0094	2.83(1) 3.06(1)	Mn: 1.0 0.0094	3.41(3)		
Bw	0.004	20	10.7 2.2-10.3	7 1.0-3.1	1.0(10)	O1: 4.8(4) 0.0037(6) O2: 2.0(4) 0.0037	1.91(1) 2.25(1)	Mn1: 4.5(6) 0.0051(6) Mn2: 1.6(5) 0.0051	2.87(1) 3.08(2)				
CB	0.024	34	11.2 2.1-10.6	6 1.0-3.1	3.2(21)	O1: 4.2(8) 0.0011(9) O2: 1.4(6) 0.0011	1.92(1) 2.21(3)	Mn: 2.5 0.0026(10)	2.90(1)				

Table 3.5 *(continued)*

Sample	*R*-factor[b]	χ_v^{2b}	N_{idp}[c] *k*-range fit	N_{var}[c] *R*-range fit	ΔE_0 (eV)[d]	*CN* (-)[e] σ^2 (Å²)[f]	*R* (Å)[g]	*CN* (-) σ^2 (Å²)	*R* (Å)	*CN* (-) σ^2 (Å²)	*R* (Å)	*CN* (-) σ^2 (Å²)	*R* (Å)
Eutric Calcaric Skeletic Cambisol (Clayic, Humic) #3 (continued)													
C	0.011	34	11.0 2.0-10.3	6 1.0-3.1	3.1(21)	O1: 5.0(8) 0.0018(5) O2: 1.0(6) 0.0018	1.89(1) 2.27(4)	Mn: 3.2(9) 0.0014(5)	2.85(1)				
Haplic Chernozem (Loamic, Pachic) #5													
Ap	0.014	12	14.3 2.1-10.3	8 1.0-3.8	-2.2(13)	O1: 4.5(11) 0.0049(6) O2: 0.5 0.0049	1.87(1) 2.25(7)	Mn: 3.9(7) 0.0073(7)	2.86(1)	Mn: 3.3(9) 0.0073	3.51(1)	Mn: 3.3(11) 0.0073	3.75(2)
Ah	0.004	4.6	14.3 2.0-10.2	8 1.0-3.8	-1.0(6)	O: 3.2(2) 0.0012(2)	1.88(0)	Mn: 4.3(5) 0.0091(4)	2.87(0)	Mn: 3.3(4) 0.0091	3.51(1)	Mn: 3.1(4) 0.0091	3.73(2)
C	0.005	3.5	14.3 2.0-10.2	8 1.0-3.8	3.9(8)	O1: 3.7(4) 0.0034(3) O2: 0.8(3) 0.0034	1.90(1) 2.25(3)	Mn: 2.9(4) 0.0057(5)	2.88(1)	Mn: 2.7(3) 0.0057	3.52(1)	Mn: 3.0(4) 0.0057	3.74(1)
Haplic Luvisol (Cutanic, Loamic, Oligeoeutric) #7													
Ah	0.003	5.2	11.8 2.6-10.1	7 1.0-3.5	-0.0(7)	O1: 3.6(3) 0.0014(4) O2: 1.2(4) 0.0014	1.90(0) 2.21(1)	Mn: 3.2(3) 0.0033(3)	2.85(0)	Mn: 1.5(3) 0.0033	3.42(1)		
E	0.005	19	11.8 2.6-10.1	7 1.0-3.5	-1.0(10)	O1: 3.2(2) 0.0021(4) O2: 1.9(4) 0.0021	1.90(1) 2.20(1)	Mn: 3.6(5) 0.0058(4)	2.82(1)	Mn: 1.5(4) 0.0058	3.43(2)		
Bt1	0.003	20	11.3 3.0-10.2	7 1.0-3.5	3.5(10)	O1: 5.5(6) 0.0024(3) O2: 1.2(4) 0.0024	1.90(0) 2.25(2)	Mn: 3.8(5) 0.0027(3)	2.86(1)	Mn: 1.3(3) 0.0027	3.45(1)		
Bt2	0.016	45	13.1 2.0-10.3	7 1.0-3.5	3.4(15)	O1: 4.2(6) 0.0011(7) O2: 1.0(5) 0.0011	1.90(1) 2.18(1)	Mn: 4.2(10) 0.0066(8)	2.86(1)	Mn: 1.3(7) 0.0066	3.48(3)		

[a]The passive amplitude reduction factor, S_0^2, was set to 0.8 in all fits. Parameter uncertainties are given in parenthesis for the last significant figure. Parameters without error assignment were fit and fixed in the final fit.

[b]*R*-factor = $\Sigma_i(\text{data}_i - \text{fit}_i)^2/\Sigma_i\text{data}_i$ and reduced $\chi^2 = (N_{idp}/N_{pts})\Sigma_i((\text{data}_i - \text{fit}_i)/\varepsilon_i)^2(N_{idp} - N_{var}) - 1$, where N_{idp} is the number of independent points in the model fit, N_{pts} the total number of data points, N_{var} the number of fit variables in the final fit, and ε_i the uncertainty of the ith data point.

[c]Number of independent data points and number of fit variables in final fit. [d]Energy-shift parameter.

[e]Coordination number (path degeneracy).

[f]Debye-Waller parameter. If no uncertainties are indicated, parameters were constrained. [g]Mean half path length.

[h]Mn-C-O obtuse triangle multiple-scattering (MS) path; σ^2 defined as $1.5\sigma^2$(Mn-O) (Zahoransky et al., 2022).

All Mn K-edge EXAFS spectra could be adequately fit with Mn-O, Mn-Mn, and Mn-C single scattering paths (Figs. 3.6 and B.5, Table 3.5). We found that the spectra of all mineral horizons were dominated by O and Mn scattering, as the inclusion of low-Z elements with low scattering amplitudes (e.g., C, Al, Si) into the fit models proved unsuccessful because their signals were superimposed by those of Mn located at similar distances. Since EXAFS amplitudes and thus coordination numbers (*CN*s) are influenced by crystallinity and relative proportion of Mn compounds as well as possible overabsorption by ferromanganese nodules (Stagnosol), we focused on interatomic distances to further elucidate Mn speciation in the soil samples.

Figure 3.7 summarizes interatomic Mn-O, Mn-C, and Mn-Mn distances detected in each soil profile along with interatomic distances of selected Mn reference compounds for comparison.

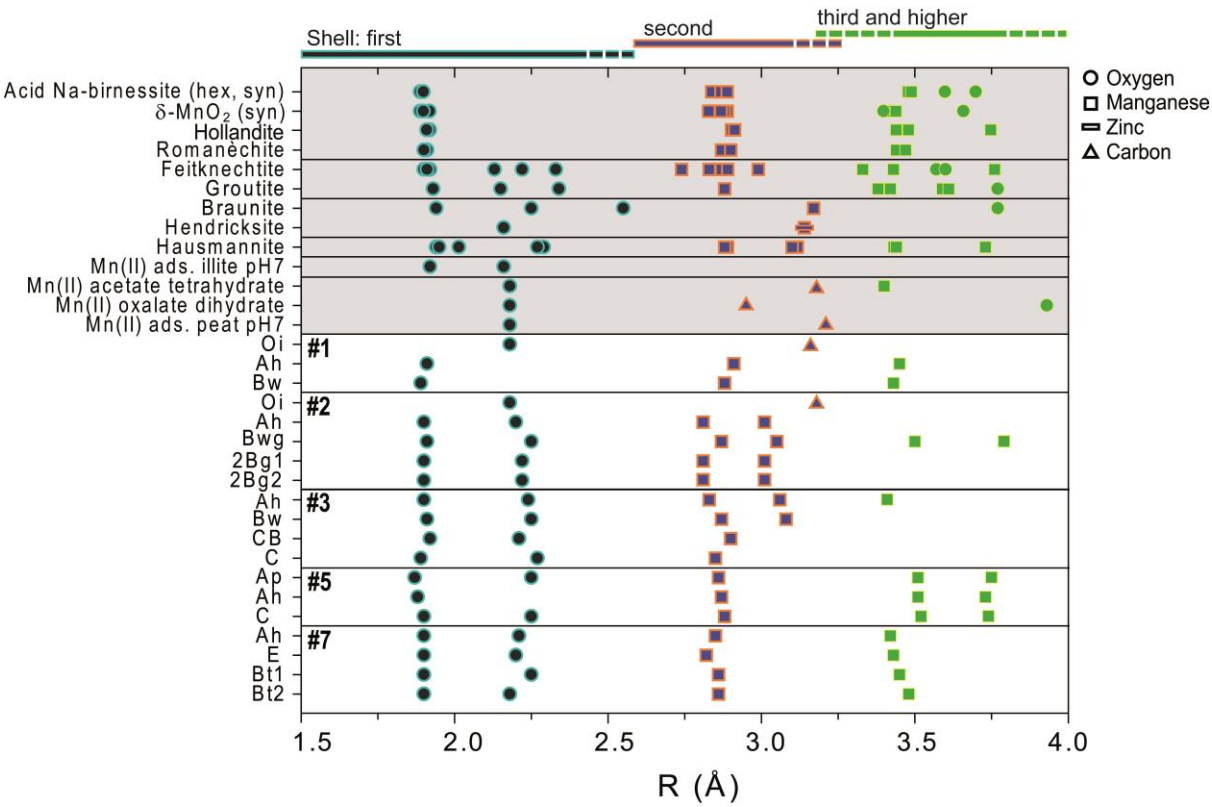

Figure 3.7. Interatomic distances between Mn and neighboring atoms in soil horizons of Cambisols #1, #2, and #3, Chernozem #5, and Luvisol #7 obtained from shell fitting of Mn K-edge EXAFS spectra. Distances found in selected Mn reference compounds are shown for comparison (Zahoransky et al. (2022) and references therein). The reference compounds are ordered as follows (top-down): Manganates, Mn(III) oxyhydroxides, silicates, spinel, physisorbed Mn, and organically comlexed Mn.

Most soil samples (*N* = 14) showed two O subshells at an average distance of 1.90±0.01 and 2.23±0.03 Å (±*σ*), and up to three Mn shells. Soil Oi horizons (Cambisols #1 and #2) were characterized by a single O shell at ~2.18 Å, a lack of Mn shells, and the presence of C atoms at ~3.17 Å – a similar Mn-C distance as those found in Mn(II) acetate tetrahydrate and Mn(II) adsorbed to peat (Fig. 3.7, Table 3.5;

Zahoransky et al., 2022). These findings are in agreement with the EXAFS-LCF results (Table 3.4), and suggest the binding of Mn to 1-2 carboxyl groups in these litter horizons. In contrast, all mineral soil samples contained Mn atoms at ~2.9 Å, diagnostic for edge-sharing MnO_6 octahedra. Interatomic distances of Mn atoms at *R* >3.0 Å varied considerably among A, B, and C horizons of different soils, but were consistent within individual soil profiles (Chernozem #5, Luvisol #7; Fig. 3.7).

In the Ah and Bw horizons of Cambisol #1, the single O shell and the presence of edge-sharing and double corner-sharing Mn at ~2.9 and ~3.4 Å, respectively, revealed the presence of manganate minerals, which accounted for 51-57% of Mn_{tot} according to EXAFS-LCF analysis (Table 3.4).

Mineral horizons of Cambisol #2 showed two O subshells at ~1.9 and ~2.2 Å (Fig. 3.7, Table 3.5). Unlike most other soil samples, samples of Cambisol #2 possessed two Mn subshells of edge-sharing MnO_6 octahedra at ~2.8 and ~3.0 Å. The occurrence of two short Mn-Mn distances points to the presence of hausmannite and/or Mn(III) oxyhydroxides (Zahoransky et al., 2022). This finding is supported by LCF results (Table 3.4) and two additional Mn shells at 3.51(3) and 3.79(1) Å in the Bwg horizon (Fig. 3.7, Table 3.5), which fit the crystal structure of hausmannite (Jarosch, 1987; Zahoransky et al., 2022).

Spectra of mineral horizons of Cambisol #3 were all fit with two O subshells at ~1.9 and ~2.2 Å, and a Mn shell at ~2.9 Å, indicating the presence of manganate minerals in addition to other Mn species. The Ah and Bw horizons also exhibited Mn shells at ~3.1 Å (Ah/Bw) and 3.41(3) Å (Ah) (Fig. 3.7, Table 3.5). These distances comply with those in hausmannite (3.10(0) and 3.44(1) Å) and in Mn(III) oxyhydroxides such as feitknechtite or groutite (~3.0 and ~3.4 Å) (Zahoransky et al., 2022). While hausmannite was not positively identified, the presence of Mn(III) oxyhydroxides in the Ah horizon is supported by EXAFS LCF (17% of Mn_{tot}, Table 3.4). Atom types and distances found in the CB and C horizons underline the dominance of manganate minerals. The second O shell at ~2.2 Å in these horizons may arise from Mn in braunite-like silicate structures, which according to LCF analysis accounted for 30% (CB) and 19% (C) of Mn_{tot} (Table 3.4).

In Chernozem #5, we observed a single O shell at ~1.9 Å in the Ah horizon (Fig. 3.7, Table 3.5), clearly signifying the presence of manganate minerals (Zahoransky et al., 2022). This is corroborated by Mn shells at ~2.9 and ~3.5 Å (Fig. 3.7, Table 3.5). Both Mn-Mn distances are consistent with manganates such as birnessite or todorokite (3×3 tectomanganate) (Zahoransky et al., 2022). A third Mn shell at ~3.7 Å, observed in all Chernozem mineral horizons, suggests the presence of hollandite (2×2 tectomanganate) (McKeown and Post, 2001; Zahoransky et al., 2022). This interpretation is supported by EXAFS-LCF results for both A horizons (Table 3.4). For the Ap and Ck horizons of Chernozem #5, minor contributions of a second O shell at ~2.2 Å indicate the presence of additional Mn species, likely silicate-bound Mn, as suggested by EXAFS-LCF analysis (Table 3.4).

Luvisol #7 spectra were fit with two O subshells at ~1.9 and 2.2 Å, and two Mn shells at ~2.9 and ~3.4 Å (Fig. 3.7, Table 3.5). The split O shell again suggests the presence of at least one Mn species in addition to manganates (Zahoransky et al., 2022). According to our EXAFS-LCF results, the second O shell may arise from either organically complexed Mn (Ah, E, and Bt2 horizons), silicate-bound Mn (Bt1 and Bt2 horizons), or Mn present in non-manganate oxide structures (E horizon) (Table 3.4).

In summary, EXAFS shell fits support the predominance of organically complexed Mn(II/III) species in litter (Oi) horizons and of manganates and Mn(III) oxyhydroxides in mineral soil horizons. Additionally, EXAFS shell fits provided evidence for spinel phases (hausmannite) and potentially silicate-bound Mn (braunite, hendricksite, masutomilite). However, Al or Si neighbors of Mn in aluminosilicates as well as contributions of Mn-C scattering in mineral horizons remained 'invisible' in the fits because their EXAFS signals were superimposed by Mn-Mn scattering, implying limitations of EXAFS shell-fit analysis of samples dominated by Mn (oxyhydr)oxides.

3.4. Discussion

3.4.1. Soil parameter correlations with Mn

Soil extractions by dithionite-citrate and acid ammonium oxalate are typically used to discriminate poorly and well crystalline Fe (oxyhydr)oxides (Fe_o/Fe_d ratio) (Blume and Schwertmann, 1969; Durn et al., 2001; Courchesne and Turmel, 2008). Dithionite-extractable Mn is thought to comprise exchangeable and organically complexed Mn as well as Mn present in Fe and Mn (oxyhydr)oxide compounds, whereas no Mn is extracted from crystalline aluminosilicates (Guest et al., 2002; Courchesne and Turmel, 2008). In this study, we found no relationship between (Mn_{tot} – Mn_d) and silicate-bound Mn as determined by spectroscopy. This may imply that dithionite-citrate also extracts Mn from silicate minerals and/or that EXAFS LCF is unable to reliably quantify low-abundance species such as silicate-bound Mn.

Chemical forms of oxalate-extractable Mn are not well resolved and differences to dithionite-extractable Mn are not easy to interpret (Courchesne and Turmel, 2008). Oxalate is assumed to extract exchangeable, organically complexed, and poorly crystallized inorganic forms of Mn (McKeague and Day, 1966; Xue et al., 2006; Rennert et al., 2021). However, dithionite-citrate and oxalate extraction efficiencies strongly depend on solid-solution ratio, ligand concentration, pH, and extraction time (Rennert et al., 2021). The almost identical extraction efficiency of dithionite and oxalate observed in this study implies that both methods target similar Mn pools, which is in line with earlier studies (Blume and Schwertmann, 1969; Mirabella and Carnicelli, 1992; Haidouti and Massas, 1998). Thus, unlike for Fe, Mn_o and Mn_d do not allow the differentiation between poorly and well crystalline Mn (oxyhydr)oxides, as assumed by Haidouti and Massas (1998). This conclusion is also supported by

higher Mn_o than Mn_d contents in several soil horizons (Table 3.1). Since our data show only weak correlations between Mn_o and Fe_o as well as Mn_d and Fe_d, both methods appear to target Mn pools other than Mn in Fe(III) (oxyhydr)oxides. This is confirmed by strong correlations of spectroscopically derived contents of manganate-Mn and Mn extracted by dithionite and oxalate (Fig. B.4). Therefore, low dithionite- and oxalate-extractable Mn concentrations in Luvisol #6, Podzol #8, and Stagnosol #9 (Table 3.1) point to a depletion in manganate minerals in horizons characterized by eluviation processes and stagnating surface water, which is also supported by the low Mn^{4+} contents in these horizons (Table 3.3).

The positive correlation of Mn_{tot}, Mn_d, and Mn_o with clay content as well as their positive correlation with DC- and AAO-extractable Fe (Table 3.2), indicates that Mn occurs mainly in the clay fraction and that Mn- and Fe(III) (oxyhydr)oxides partly coexist and/or Mn substitutes for Fe in Fe(III) (oxyhydr)oxides (e.g., Scheinost et al., 2001). However, the relatively weak and negative correlation between Mn^{3+} and Fe_d suggests that isomorphic substitution is not important in the studied soils. Similar correlations between Mn_{tot} and clay content have been reported by Shuman (1979) for soils from the southern United States ($r_s = 0.89$, $p < 0.001$, $N = 10$). These results are contrasted by those of Yaalon et al. (1972), showing a negative correlation (Pearson $r_p = -0.62$, $p < 0.001$, $N = 35$) for Mediterranean soils developed on basalt, dolomite, and limestone. Vodyanitskii (2009) found no correlation between total Mn and clay fraction in agrosoddy-podzolic soils (Mozhaisk district, Moscow oblast). Nonsignificant correlations between Mn and clay content were also observed for B horizons of Terra Rossa soils developed on limestone and dolomite in Istria ($N = 40$) (Durn et al., 2001), Ap horizons of Serbian Vertisols ($N = 10$) (Milivojević et al., 2011), and for Calcisols, Gypsisols, Solonchaks, and Solonetzs from Spain ($N = 12$) (Navas and Lindhorfer, 2003). All available data suggest that the Mn distribution within particle size fractions is variable and depends on parent material, climate, and soil development.

3.4.2. Manganese oxidation states

The general dominance of Mn^{2+} species in fresh, undecomposed plant residues (Oi horizons) complies with other studies (Herndon et al., 2014; Keiluweit et al., 2015). It was previously shown that fresh plant litter, roots, and stems can contain organically complexed Mn^{3+} (Herndon et al., 2014) or Mn^{3+} in inorganic form such as manganite, hausmannite, and Mn_2O_3 (potentially bixbyite) (Blamey et al., 2018). Our data also revealed substantial amounts of Mn^{3+} (29-40%) and Mn^{4+} (23-32%) in Oi horizons and a generally high redox variability of Mn in organic surface layers (Table 3.3). High-valence Mn species in organic surface layers may support the idea that these species are formed via biological oxidation of soluble Mn^{2+} to Mn^{3+} and subsequent precipitation of Mn (oxyhydr)oxides (Keiluweit et al., 2015). The progressive formation of Mn (oxyhydr)oxides upon litter decomposition is substantiated by the low

shares of Mn^{4+} in the Oi horizon compared to the Oe horizon of Luvisol #6. In contrast, the observation of declining Mn^{4+} contents in O horizons of Stagnosol #9 with depth (Table 3.3) indicates that manganate-Mn present in organic surface layers is increasingly utilized as terminal electron acceptor during microbial oxidation of organic matter under increasingly anoxic conditions. Abiotic oxidation of organic matter, especially of phenolic compounds (Chorover and Amistadi, 2001), may additionally contribute to the increasing presence of more reduced Mn in organic surface layers with depth. The continuously decreasing Mn^{2+} shares from the Oi to the Oa horizon of Podzol #8 in combination with negligible Mn^{4+} contents support an active redox cycling between Mn^{2+} and Mn^{3+} in this soil (Keiluweit et al., 2015). The negative correlation between soil Mn^{4+} content (Mn AOS) and C_{org}/N_{tot} ratio (Table 3.3), an indicator of organic matter decomposition, suggests that organically complexed Mn^{2+} released upon organic matter decomposition is oxidized and precipitates as manganates.

As opposed to organic soil horizons, mineral soil horizons were enriched in Mn^{3+} and Mn^{4+}. The positive correlation of Mn^{4+} (Mn AOS) and negative correlation of Mn^{3+} with soil clay content (Table 3.2) imply that clay fractions of the studied soils are enriched in manganates. Given the net negative surface charge of phyllosilicates and manganates in the pH range of the studied soils, which renders direct association of these phases unfavorable, we assume this correlation to result either from interactions of manganates with positively charged clay-sized Fe(III) (oxyhydr)oxides or to simply reflect the fact that soil manganates are predominately clay-sized. Both assumptions are supported by significant positive correlations between Mn^{4+} (Mn AOS), Fe_d, and clay content (Table 3.2).

The positive correlation of Mn^{4+} (Mn AOS) and negative correlation of Mn^{3+} with soil pH (Table 3.2) suggest that more alkaline soil conditions stabilize Mn in its tetravalent oxidation state. This may be ascribed to faster microbial Mn oxidation under less acidic conditions (Hastings and Emerson, 1986; Zhang et al., 2002) and/or generally lower Mn^{2+} solution concentrations at higher pH, which would limit comproportionation-disproportionation reactions of manganates (Tu et al., 1994; Mandernack et al., 1995; Bargar et al., 2005; Zhu et al., 2010).

3.4.3. EXAFS-BASED MN SPECIATION

3.4.3.1. DATA INTERPRETATION

EXAFS LCF and shell fitting may lead to seemingly conflicting results for some samples. For example, Cambisol #1 Ah and Bw horizons did not exhibit two Mn-O bond distances at ~1.9 and ~2.2 Å, despite that LCF implied up to 20% Mn(III) oxyhydroxides (groutite) and up to 12% hausmannite. Nominally, O1 and O2 shells of groutite have *CN*s of ~4.2 and ~0.9, respectively (Zahoransky et al., 2022). A fraction of 20% groutite, as obtained by LCF, in a sample containing no other Mn species with split O shells would correspond to a $CN_{Mn\text{-}O2}$ of <0.2, which is impossible to determine reliably from shell fits. The

same argument holds for the Mn-O2 shell of hausmannite. On the other hand, it is difficult to discriminate individual manganates by EXAFS LCF, notably phyllomanganates and tectomanganates with large tunnel sizes (Zahoransky et al., 2022). However, since tectomanganates contain both edge- and corner-sharing MnO_6 octahedra, EXAFS shell fitting can aid the identification and quantification of tectomanganates in mixtures with phyllomanganates. These examples illustrate that certain Mn species cannot be identified by EXAFS shell fitting if they are present below a critical concentration threshold, and that EXAFS LCF and shell fitting can yield complementary species information. Generally, care must be taken not to overinterpret EXAFS-LCF fractions of individual Mn reference compounds with similar EXAFS spectra. In this case, fractions of reference compounds need to be combined into chemically or structurally meaningful species groups.

3.4.3.2. EXAFS SPECIATION OF SOIL SAMPLES

The EXAFS-LCF analyses of 20 samples from five soils provided evidence for manganates, organically complexed Mn, Mn(III) oxyhydroxides, silicate-bound Mn, Mn oxides without layer or tunnel structure, and physisorbed Mn (Table 3.4). Several Mn species with distinct EXAFS features (Zahoransky et al., 2022) were not observed in any studied soil sample. These include tectomanganates with small tunnel sizes like pyrolusite (1×1) or ramsdellite (1×2), manganite (γ-MnOOH), rhodochrosite ($MnCO_3$), and polynuclear organic Mn(III) complexes. Apparently, such phases either do not occur in soil or only in undetectable concentrations.

Litter horizons consisting of largely undecomposed beech (*Fagus sylvatica*) and birch (*Betula pendula*) leaves comprised predominantly organically complexed Mn (58-91%, $\bar{x}$ = 78%) and physisorbed Mn (≤15%), but we also identified manganates (6%), Mn(III) oxyhydroxides (23%), and silicate-bound Mn (13%) in individual litter horizons (Table 3.4). The latter may be attributed to Mn^{2+} association with phytoliths, which represent preferential structures for encapsulation of heavy metals like Mn (Delplace et al., 2020), alleviating metal stress in plants (Buján, 2013). However, hausmannite, Mn_2O_3 (probably bixbyite), and manganite, whose presence in leaves of cultivated plants has been linked to Mn toxicity (Blamey et al., 2018), were not observed in any Oi horizon. Bioturbation as a source of Mn (oxyhydr)oxides in Oi horizons can be excluded because great care was taken during sampling to avoid contamination by mineral soil material.

In mineral soil horizons, manganates were by far the most abundant Mn species group (37-94%, $\bar{x}$ = 67%), as suspected by Manceau et al. (2002). They were followed by organically complexed Mn (≤39%, $\bar{x}$ = 11%) and silicate-bound Mn (≤30%, $\bar{x}$ = 8%), about equal quantities of Mn(III) oxyhydroxides and Mn oxides, such as bixbyite and hausmannite (≤37%, $\bar{x}$ ~6%), and physisorbed Mn (≤14%, $\bar{x}$ <1%); the latter being consistent with negligible concentrations of exchangeable Mn in all

soils (Table 3.1). Our results suggest that a considerable portion of manganates in the studied soils are tectomanganates (Table 3.4), even though phyllo- and tectomanganates are hard to distinguish spectroscopically (Zahoransky et al., 2022). The occurrence of tectomanganates may be related to Mn^{2+} oxidation by microorganisms (Remucal and Ginder-Vogel, 2014) such as fungi (Saratovsky et al., 2009) and bacteria (Villalobos et al., 2003), or to abiotic transformation of hexagonal phyllomanganates (Yang et al., 2018; Wu et al., 2021). Our results also indicate that soil phyllomanganates generally exhibit hexagonal MnO_6 layer symmetry (Table 4). Only in one case (CB horizon of Cambisol #3, pH 8.0; Table 4), the spectrum of triclinic birnessite significantly improved the fit, suggesting that triclinic birnessites can form in oxic and alkaline soils, probably via interactions of aqueous Mn^{2+} with hexagonal birnessites (Bargar et al., 2005). Since we found no correlation between manganate-Mn and Fe_d (Fe_o), we conclude that most soil manganates are not associated with Fe(III) (oxyhydr)oxides, which contrasts findings of their co-occurrence in ferromanganese nodules or concretions of redox-affected soils (Vodyanitskii and Sivtsov, 2004; Vodyanitskii, 2006; Blöthe et al., 2015; Ettler et al., 2017). Similarly, we found no correlation between manganate-Mn and clay content, although there was a significant positive correlation between Mn^{4+} (Mn AOS) and clay content. This may indicate that manganates in clay fractions are enriched in Mn^{4+}.

Manganese(III) oxyhydroxides are typically considered rare in soils since they disproportionate to MnO_2 and Mn^{2+} at pH <7 (Vodyanitskii, 2009; Blume et al., 2016). In this study, EXAFS LCF, fingerprinting, and shell fitting confirmed the presence of feitknechtite and/or groutite in few acidic to near neutral soil horizons (e.g., 2Bg horizons of Cambisol #2, pH ~5; Table 3.4). The occurrence of Mn(III) oxyhydroxides in acidic soils is noteworthy, as XRD and XAS data showed no transformation of vernadite (δ-MnO_2) into feitknechtite during 73 days of continuous interaction with dissolved Mn^{2+} at pH 5 (Elzinga, 2016); similar observations have been made by Lefkowitz et al. (2013). However, Tu et al. (1994) reported the precipitation of groutite from aqueous Mn^{2+} on surfaces of hexagonal birnessite at pH 6, attributing its formation to direct solid-state conversion as opposed to dissolution-reprecipitation reactions. Other laboratory studies showed abiotic formation of feitknechtite, manganite, and/or groutite either by reaction of Mn^{2+} with phyllomanganates at pH >7 (Bargar et al., 2005), albite, hematite, and goethite at pH 7.8-8.7 (Junta and Hochella, 1994), and ferrihydrite at pH 6.5-8.5 (Wang et al., 2015), or by Mn^{2+} oxidation by atmospheric O_2 at pH 7.5-9.5 (Hem and Lind, 1983). Even though microbial formation of Mn(III) oxyhydroxides in acidic soils is conceivable, previous research only reported their biologically mediated formation at pH >6.5 (Greene and Madgwick, 1991; Mandernack et al., 1995), which could also be the result of secondary abiotic reactions (Bargar et al. 2005). The absence of manganite in all soil samples implies that the formation pathway of soil birnessites does not proceed via a manganite precursor, as suggested by McKenzie (1972).

Silicate-bound Mn was found in most mineral soil horizons, except for Cambisol #2, but in low proportions with an average of 8% of Mn_{tot} (Table 3.4). In rocks, Mn is present in phyllosilicate clays (Guest et al., 2002) and ferromagnesian silicates such as olivine (100-6,500 mg/kg), pyroxene (600-8,000 mg/kg), amphibole (400-7,000 mg/kg), and biotite (100-10,000 mg/kg) (Gilkes and McKenzie, 1988). Except for the phyllosilicate clays, all other primary Mn-bearing minerals are highly susceptible to weathering, which explains the minor contribution of Mn still bound in silicate structures and the prevalence of secondary minerals in the studied soils. This was most striking in Cambisol #1, which was formed on basalt that probably contained nearly all Mn in highly weatherable primary phases. EXAFS-LCF, fingerprint, and shell-fit analyses also provided evidence of the spinel hausmannite. This mineral was first described by Chukhrov and Gorshkov (1981) as isometric grains in a Chernozem subsoil (pH 8.3; Priazov district, former USSR) and in a subsoil of a 'meadow soil' (pH 8.1; Prisalair district, former USSR). Similar to Mn (III) oxyhydroxides, the occurrence of hausmannite in acidic soils was unexpected, as previous laboratory studies showed its formation only at pH >7 by Mn^{2+}-induced reduction of birnessite with feitknechtite as an reaction intermediate (Lefkowitz et al., 2013) or as a product of microbial Mn^{2+} oxidation (Hastings and Emerson, 1986; Mann et al., 1988). The existence of hausmannite under acidic conditions suggests that its presumed dissolution at pH <7 (Luo et al., 2018) is hindered under natural soil conditions by chemical, physical and/or kinetic factors, similar to other Mn minerals in the environment (Webb et al., 2005).

3.5. Summary and Conclusion

We assessed bulk Mn speciation in 46 soil samples from nine typical Central European soils and evaluated its relationship to major soil properties. By employing Mn K-edge EXAFS spectroscopy, we provide the first quantitative insights into the Mn species inventory of bulk soils. EXAFS analyses of 20 organic and mineral soil samples revealed the presence of six major Mn species groups: (1) manganates, (2) organically complexed Mn, (3) Mn(III) oxyhydroxides, (4) silicate-bound Mn, (5) Mn oxides without tunnel- or layer structure, and (6) physisorbed Mn.

Litter (Oi) horizons showed predominantly Mn^{2+} in organic complexes or in exchangeable form, but also contained non-organic Mn species, such as manganates, Mn(III) oxyhydroxides, and silicate-bound Mn. The high redox variability of Mn in organic surface horizons is likely related to variable concentrations of inorganic Mn species.

Manganates were dominant in all mineral soils with a mean abundance of 67% of Mn_{tot}, and likely consisted of mixtures of hexagonal phyllo- and tectomanganates. Our results demonstrate that these minerals are almost quantitatively dissolved during dithionite and oxalate extractions. In addition, our results suggest that Mn^{4+}-rich manganates preferentially form under less acidic soil

conditions, partly by oxidation of organically complexed Mn(II), and that they are enriched in the soil clay fraction.

Compared to manganates, other Mn species in mineral soils were far less abundant. Surprisingly, topsoil A horizons contained little organically complexed Mn. Small amounts of silicate-bound Mn in mineral soils developed during the Holocene on Pleistocene sediments (loess) and pre-Quaternary rocks (basalt, phyllite, limestone) corroborate the release of Mn from primary mineral already at early stages of weathering and soil formation. Similarly, the negligible concentrations of physisorbed Mn in mineral soil suggest that this Mn pool is rapidly converted into Mn (oxyhydr)oxides under oxic soil conditions. The unexpected detection of Mn(III) oxyhydroxides such as feitknechtite or groutite as well as of the spinel hausmannite in acidic soils warrants further research.

3.6. ACKNOWLEDGEMENTS

We are indebted to Leopold Sauheitl, Ulrike Pieper, Rebekka Stünkel, and Anne Herwig who contributed to the determination of basic soil parameters. Use of the Stanford Synchrotron Radiation Lightsource, SLAC National Accelerator Laboratory, was supported by the U.S. Department of Energy, Office of Science, Office of Basic Energy Sciences under Contract No. DE-AC02-76SF00515s. Use of the Advanced Photon Source, an Office of Science User Facility operated for the U.S. Department of Energy (DOE) Office of Science by Argonne National Laboratory, was supported by the U.S. DOE under Contract No. DE-AC02-06CH11357. We are also thankful to PETRA III at DESY for providing us with beamtime. Assistance at synchrotron facilities by Ritimukta Sarangi (SSRL), Qing Ma (APS), and Wolfgang Caliebe, Akhil Tayal, and Vadim Murzin (all DESY) is gratefully acknowledged. This work was financially supported by the DFG (project no. 326242261).

3.7. REFERENCES

Ahmad, A., van der Wal, A., Bhattacharya, P. and van Genuchten, C.M. (2019) Characteristics of Fe and Mn bearing precipitates generated by Fe(II) and Mn(II) co-oxidation with O_2, MnO_4 and HOCl in the presence of groundwater ions. *Water Res.* **161**, 505-516.

Anand, R. and Gilkes, R. (1984) Mineralogical and chemical properties of weathered magnetite grains from lateritic saprolite. *J. Soil Sci.* **35**, 559-567.

Ankudinov, A.L., Ravel, B., Rehr, J.J. and Conradson, S.D. (1998) Real-space multiple-scattering calculation and interpretation of X-ray-absorption near-edge structure. *Phys. Rev. B* **58**, 7565.

Bargar, J.R., Tebo, B.M., Bergmann, U., Webb, S.M., Glatzel, P., Chiu, V.Q. and Villalobos, M. (2005) Biotic and abiotic products of Mn(II) oxidation by spores of the marine *Bacillus sp*. strain SG-1. *Am. Mineral.* **90**, 143-154.

Becknell, N., Lopes, P.P., Hatsukade, T., Zhou, X., Liu, Y., Fisher, B., Chung, D.Y., Kanatzidis, M.G., Markovic, N.M. and Tepavcevic, S. (2021) Employing the dynamics of the electrochemical interface at aqueous zinc-ion battery cathode. *Adv. Funct. Mater.*, 2102135.

Blamey, F.P.C., McKenna, B.A., Li, C., Cheng, M., Tang, C., Jiang, H., Howard, D.L., Paterson, D.J., Kappen, P. and Wang, P. (2018) Manganese distribution and speciation help to explain the effects of silicate and phosphate on manganese toxicity in four crop species. *New Phytol.* **217**, 1146-1160.

Blöthe, M., Wegorzewski, A., Müller, C., Simon, F., Kuhn, T. and Schippers, A. (2015) Manganese-cycling microbial communities inside deep-sea manganese nodules. *Environ. Sci. Technol.* **49**, 7692-7700.

Blume, H., Brümmer, G., Fleige, H., Horn, R., Kandeler, E., Kögel-Knabner, I., Kretzschmar, R., Stahr, K. and Wilke, B. (2016) *Scheffer/Schachtschabel Soil Science*. Springer: Berlin Heidelberg, Germany.

Blume, H. and Schwertmann, U. (1969) Genetic evaluation of profile distribution of aluminum, iron, and manganese oxides. *Soil. Sci. Soc. Am. J.* **33**, 438-444.

Broadley, M., Brown, P., Cakmak, I., Rengel, Z. and Zhao, F. (2012) Function of Nutrients: Micronutrients. In: *Marschner's Mineral Nutrition of Higher Plants* (ed. P. Marschner), 3rd ed. Academic Press, pp. 191-248.

Buján, E. (2013) Elemental composition of phytoliths in modern plants (Ericaceae). *Quat. Int.* **287**, 114-120.

Calvin, S. (2013) *XAFS for Everyone*, 1st ed. CRC press, Boca Raton.

Carroll, S., O'Day, P.A., Esser, B. and Randall, S. (2002) Speciation and fate of trace metals in estuarine sediments under reduced and oxidized conditions, Seaplane Lagoon, Alameda Naval Air Station (USA). *Geochem. Trans.* **3**, 81-101.

Chorover, J. and Amistadi, M.K. (2001) Reaction of forest floor organic matter at goethite, birnessite and smectite surfaces. *Geochim. Cosmochim. Acta* **65**, 95-109.

Chukhrov, F.V. and Gorshkov, A.I. (1981) Iron and manganese oxide minerals in soils. *Trans. Royal Soc. Edinb. Earth Sci.* **72**, 195-200.

Cornu, S., Deschatrettes, V., Salvador-Blanes, S., Clozel, B., Hardy, M., Branchut, S. and Le Forestier, L. (2005) Trace element accumulation in Mn-Fe-oxide nodules of a planosolic horizon. *Geoderma* **125**, 11-24.

Courchesne, F. and Turmel, M. (2008) Extractable Al, Fe, Mn, and Si. In: *Soil Sampling and Methods of Analysis* eds. M.R. Carter, E.G. Gregorich). Canadian Society of Soil Science and CRC Press, Boca Raton, Florida, USA, pp. 307-315.

De Bakker, A.P., Tokashiki, Y. and Arachchi, L.P.V. (2003) Mineralogy of Okinawan terrestrial Fe/Mn nodules and their surrounding soils. *Clay Sci.* **12**, 121-130.

Delplace, G., Schreck, E., Pokrovsky, O.S., Zouiten, C., Blondet, I., Darrozes, J. and Viers, J. (2020) Accumulation of heavy metals in phytoliths from reeds growing on mining environments in Southern Europe. *Sci. Total. Environ.* **712**, 135595.

Durn, G., Slovenec, D. and Čović, M. (2001) Distribution of iron and manganese in Terra Rossa from Istria and its genetic implications. *Geol. Croat.* **54**, 27-36.

Ehlert, K., Mikutta, C. and Kretzschmar, R. (2016) Effects of manganese oxide on arsenic reduction and leaching from contaminated floodplain soil. *Environ. Sci. Technol.* **50**, 9251-9261.

Elzinga, E.J. (2016) ^{54}Mn radiotracers demonstrate continuous dissolution and reprecipitation of vernadite (δ-MnO_2) during interaction with aqueous Mn(II). *Environ. Sci. Technol.* **50**, 8670-8677.

Ettler, V., Chren, M., Mihaljevič, M., Drahota, P., Kříbek, B., Veselovský, F., Sracek, O., Vaněk, A., Penížek, V. and Komárek, M. (2017) Characterization of Fe-Mn concentric nodules from Luvisol irrigated by mine water in a semi-arid agricultural area. *Geoderma* **299**, 32-42.

FAO (2006) *Guidelines for Soil Description*, Rome.

Flynn, E.D. and Catalano, J.G. (2019) Reductive transformations of layered manganese oxides by small organic acids and the fate of trace metals. *Geochim. Cosmochim. Acta* **250**, 149-172.

Friedl, G., Wehrli, B. and Manceau, A. (1997) Solid phases in the cycling of manganese in eutrophic lakes: New insights from EXAFS spectroscopy. *Geochim. Cosmochim. Acta* **61**, 275-290.

Frommer, J., Voegelin, A., Dittmar, J., Marcus, M.A. and Kretzschmar, R. (2011) Biogeochemical processes and arsenic enrichment around rice roots in paddy soil: Results from micro-focused X-ray spectroscopy. *Eur. J. Soil. Sci.* **62**, 305-317.

Gee, G.W. and Bauder, J. (1986) Particle-size analysis In: *Methods of Soil Analysis, Part 1: Physical and Mineralogical Methods* (ed. A. Klute), 2nd ed. Soil Science Society of America and American Society of Agronomy, Madison, Wisconsin, USA, pp. 383-411.

Gilkes, R. and McKenzie, R. (1988) Geochemistry and mineralogy of manganese in soils. In: *Manganese in Soils and Plants*. Springer, pp. 23-35.

Gillman, G. (1979) A proposed method for the measurement of exchange properties of highly weathered soils. *Soil Res.* **17**, 129-139.

Glatzel, P., Bergmann, U., Yano, J., Visser, H., Robblee, J.H., Gu, W., de Groot, F.M., Christou, G., Pecoraro, V.L. and Cramer, S.P. (2004) The electronic structure of Mn in oxides, coordination complexes, and the oxygen-evolving complex of photosystem II studied by resonant inelastic X-ray scattering. *J. Am. Chem. Soc.* **126**, 9946-9959.

Golden, D., Dixon, J. and Kanehiro, Y. (1993) The manganese oxide mineral, lithiophorite, in an oxisol from Hawaii. *Soil Res.* **31**, 51-66.

Greene, A.C. and Madgwick, J.C. (1991) Microbial formation of manganese oxides. *Appl. Environ. Microbiol.* **57**, 1114-1120.

Guest, C.A., Schulze, D.G., Thompson, I.A. and Huber, D.M. (2002) Correlating manganese X-ray absorption near-edge structure spectra with extractable soil manganese. *Soil. Sci. Soc. Am. J.* **66**, 1172-1181.

Guttman, L. (1954) Some necessary conditions for common-factor analysis. *Psychometrika* **19**, 149-161.

Habibah, J., Khairiah, J., Ismail, B. and Kadderi, M. (2014) Manganese speciation in selected agricultural soils of peninsular Malaysia. *Am. J. Environ. Sci.* **10**, 148-156.

Haidouti, C. and Massas, I. (1998) Distribution of iron and manganese oxides in Haploxeralfs and Rhodoxeralfs and their relation to the degree of soil development and soil colour. *Z. Pflanzenernähr. Bodenkd.* **161**, 141-145.

Hartge, K. and Horn, R. (1992) *Die physikalische Untersuchung von Böden*. Ferdinand Enke Verlag, Stuttgart.

Hass, A. and Fine, P. (2010) Sequential selective extraction procedures for the study of heavy metals in soils, sediments, and waste materials - a critical review. *Crit. Rev. Environ. Sci. Technol.* **40**, 365-399.

Hastings, D. and Emerson, S. (1986) Oxidation of manganese by spores of a marine bacillus: Kinetic and thermodynamic considerations. *Geochim. Cosmochim. Acta* **50**, 1819-1824.

Hem, J.D. and Lind, C.J. (1983) Nonequilibrium models for predicting forms of precipitated manganese oxides. *Geochim. Cosmochim. Acta* **47**, 2037-2046.

Hendershot, W., Lalande, H. and Duquette, M. (2008a) Ion exchange and exchangeable cations. In: *Soil Sampling and Methods of Analysis* eds. M.R. Carter, E.G. Gregorich). Canadian Society of Soil Science and CRC Press, Boca Raton, Florida, USA, pp. 197-204.

Hendershot, W., Lalande, H. and Duquette, M. (2008b) Soil reaction and exchangeable acidity. In: *Soil Sampling and Methods of Analysis* eds. M.R. Carter, E.G. Gregorich). Canadian Society of Soil Science and CRC Press, Boca Raton, Florida, USA, pp. 173-178.

Hernandez-Soriano, M.C., Degryse, F., Lombi, E. and Smolders, E. (2012) Manganese toxicity in barley is controlled by solution manganese and soil manganese speciation. *Soil. Sci. Soc. Am. J.* **76**, 399-407.

Herndon, E.M., Martínez, C.E. and Brantley, S.L. (2014) Spectroscopic (XANES/XRF) characterization of contaminant manganese cycling in a temperate watershed. *Biogeochemistry* **121**, 505-517.

Hjorth, T. (2004) Effects of freeze-drying on partitioning patterns of major elements and trace metals in lake sediments. *Anal. Chim. Acta* **526**, 95-102.

Hofrichter, M. (2002) Review: Lignin conversion by manganese peroxidase (MnP). *Enzyme Microb. Technol.* **30**, 454-466.

IUSS Working Group WRB (2014) *International Soil Classification System for Naming Soils and Creating Legends for Soil Maps*. FAO, Rome.

Jarosch, D. (1987) Crystal structure refinement and reflectance measurements of hausmannite, Mn_3O_4. *Mineral. Petrol.* **37**, 15-23.

Jensen, K.A., Bao, W., Kawai, S., Srebotnik, E. and Hammel, K.E. (1996) Manganese-dependent cleavage of nonphenolic lignin structures by *Ceriporiopsis subvermispora* in the absence of lignin peroxidase. *Appl. Environ. Microbiol.* **62**, 3679-3686.

Ji, J. and Chen, J. (2000) An EPR study on the chemical form of Mn^{2+} in the Chinese loess samples. *Spectroscopy Letters* **33**, 201-209.

Junta, J.L. and Hochella, M.F., Jr. (1994) Manganese(II) oxidation at mineral surfaces: A microscopic and spectroscopic study. *Geochim. Cosmochim. Acta* **58**, 4985-4999.

Kalembkiewicz, J., Sitarz-Palczak, E. and Zapała, L. (2008) A study of the chemical forms or species of manganese found in coal fly ash and soil. *Microchem. J.* **90**, 37-43.

Keiluweit, M., Nico, P., Harmon, M.E., Mao, J., Pett-Ridge, J. and Kleber, M. (2015) Long-term litter decomposition controlled by manganese redox cycling. *Proc. Natl. Acad. Sci.* **112**, E5253-E5260.

Langner, P., Mikutta, C. and Kretzschmar, R. (2012) Arsenic sequestration by organic sulphur in peat. *Nature Geosci.* **5**, 66-73.

Lefkowitz, J.P., Rouff, A.A. and Elzinga, E.J. (2013) Influence of pH on the reductive transformation of birnessite by aqueous Mn(II). *Environ. Sci. Technol.* **47**, 10364-10371.

Liu, F., Colombo, C., Adamo, P., He, J.Z. and Violante, A. (2002) Trace elements in manganese-iron nodules from a Chinese Alfisol. *Soil. Sci. Soc. Am. J.* **66**, 661-670.

Luo, Y., Tan, W., Suib, S.L., Qiu, G. and Liu, F. (2018) Dissolution and phase transformation processes of hausmannite in acidic aqueous systems under anoxic conditions. *Chem. Geol.* **487**, 54-62.

Malinowski, E.R. (1977) Determination of the number of factors and the experimental error in a data matrix. *Anal. Chem.* **49**, 612-617.

Malinowski, E.R. (1978) Theory of error for target factor analysis with applications to mass spectrometry and nuclear magnetic resonance spectrometry. *Anal. Chim. Acta* **103**, 339-354.

Manceau, A., Marcus, M.A. and Grangeon, S. (2012) Determination of Mn valence states in mixed-valent manganates by XANES spectroscopy. *Am. Mineral.* **97**, 816-827.

Manceau, A., Marcus, M.A. and Tamura, N. (2002) Quantitative speciation of heavy metals in soils and sediments by synchrotron X-ray techniques. *Rev. Mineral. Geochem.* **49**, 341-428.

Manceau, A. and Nagy, K.L. (2012) Quantitative analysis of sulfur functional groups in natural organic matter by XANES spectroscopy. *Geochim. Cosmochim. Acta* **99**, 206-223.

Manceau, A., Tamura, N., Celestre, R.S., MacDowell, A.A., Geoffroy, N., Sposito, G. and Padmore, H.A. (2003) Molecular-scale speciation of Zn and Ni in soil ferromanganese nodules from loess soils of the Mississippi Basin. *Environ. Sci. Technol.* **37**, 75-80.

Manceau, A., Tommaseo, C., Rihs, S., Geoffroy, N., Chateigner, D., Schlegel, M., Tisserand, D., Marcus, M.A., Tamura, N. and Chen, Z.-S. (2005) Natural speciation of Mn, Ni, and Zn at the micrometer scale in a clayey paddy soil using X-ray fluorescence, absorption, and diffraction. *Geochim. Cosmochim. Acta* **69**, 4007-4034.

Mandernack, K.W., Post, J. and Tebo, B.M. (1995) Manganese mineral formation by bacterial spores of the marine *Bacillus*, strain SG-1: Evidence for the direct oxidation of Mn(II) to Mn(IV). *Geochim. Cosmochim. Acta* **59**, 4393-4408.

Mann, S., Sparks, N., Scott, G. and De Vrind-De Jong, E. (1988) Oxidation of manganese and formation of Mn_3O_4 (hausmannite) by spore coats of a marine *Bacillus* sp. *Appl. Environ. Microbiol.* **54**, 2140-2143.

Martin, S.T. (2005) Precipitation and dissolution of iron and manganese oxides. In: *Environmental Catalysis* (ed. V.H. Grassian). CRC Press, Boca Raton, Florida, pp. 61-82.

Mayanna, S., Peacock, C.L., Schäffner, F., Grawunder, A., Merten, D., Kothe, E. and Büchel, G. (2015) Biogenic precipitation of manganese oxides and enrichment of heavy metals at acidic soil pH. *Chem. Geol.* **402**, 6-17.

McKeague, J.A. and Day, J.H. (1966) Dithionite-and oxalate-extractable Fe and Al as aids in differentiating various classes of soils. *Can. J. Soil. Sci.* **46**, 13-22.

McKenzie, R. (1972) The sorption of some heavy metals by the lower oxides of manganese. *Geoderma* **8**, 29-35.

McKeown, D.A. and Post, J.E. (2001) Characterization of manganese oxide mineralogy in rock varnish and dendrites using X-ray absorption spectroscopy. *Am. Mineral.* **86**, 701-713.

Mikutta, C. and Rothwell, J.J. (2016) Peat bogs as hotspots for organoarsenical formation and persistence. *Environ. Sci. Technol.* **50**, 4314-4323.

Milivojević, J.Ž., Đalović, I.G., Jelić, M.Ž., Trifunović, S.R., Bogdanović, D.M., Milošev, D.S., Nedeljković, B.D. and Bjelić, D.Đ. (2011) Distribution and forms of manganese in vertisols of Serbia. *J. Serb. Chem. Soc.* **76**, 1177-1190.

Mirabella, A. and Carnicelli, S. (1992) Iron oxide mineralogy in red and brown soils developed on calcareous rocks in central Italy. *Geoderma* **55**, 95-109.

Navas, A. and Lindhorfer, H. (2003) Geochemical speciation of heavy metals in semiarid soils of the central Ebro Valley (Spain). *Environ. Int.* **29**, 61-68.

Negra, C., Ross, D.S. and Lanzirotti, A. (2005) Oxidizing behavior of soil manganese: Interactions among abundance, oxidation state, and pH. *Soil. Sci. Soc. Am. J.* **69**, 87-95.

Neubauer, E., Schenkeveld, W.D., Plathe, K.L., Rentenberger, C., Von Der Kammer, F., Kraemer, S.M. and Hofmann, T. (2013) The influence of pH on iron speciation in podzol extracts: Iron complexes with natural organic matter, and iron mineral nanoparticles. *Sci. Total. Environ.* **461**, 108-116.

O'Day, P.A., Carroll, S.A., Randall, S., Martinelli, R.E., Anderson, S.L., Jelinski, J. and Knezovich, J.P. (2000) Metal speciation and bioavailability in contaminated estuary sediments, Alameda Naval Air Station, California. *Environ. Sci. Technol.* **34**, 3665-3673.

O'Day, P.A., Rivera, N., Jr., Root, R. and Carroll, S.A. (2004) X-ray absorption spectroscopic study of Fe reference compounds for the analysis of natural sediments. *Am. Mineral.* **89**, 572-585.

Porter, G., Bajita-Locke, J., Hue, N. and Strand, D. (2004) Manganese solubility and phytotoxicity affected by soil moisture, oxygen levels, and green manure additions. *Commun. Soil. Sci. Plant. Anal.* **35**, 99-116.

Prietzel, J., Thieme, J., Eusterhues, K. and Eichert, D. (2007) Iron speciation in soils and soil aggregates by synchrotron-based X-ray microspectroscopy (XANES, μ-XANES). *Eur. J. Soil. Sci.* **58**, 1027-1041.

Ravel, B. and Newville, M. (2005) *ATHENA, ARTEMIS, HEPHAESTUS*: Data analysis for X-ray absorption spectroscopy using *IFEFFIT*. *J. Synchrotron Rad.* **12**, 537-541.

Reddy, K.R. and DeLaune, R.D. (2008) *Biogeochemistry of Wetlands: Science and Applications*. CRC Press, Boca Raton.

Redžić, S., Sijarić, G., Muhić-Šarac, T., Pehić, E. and Hrnjica, D. (2014) Distribution and bioavailability of manganese in soil in the vicinity of the 'Bužim' abandoned mine. *Geol. Croat.* **67**, 45-58.

Remucal, C.K. and Ginder-Vogel, M. (2014) A critical review of the reactivity of manganese oxides with organic contaminants. *Environ. Sci.: Process. Impacts* **16**, 1247-1266.

Rennert, T., Dietel, J., Heilek, S., Dohrmann, R. and Mansfeldt, T. (2021) Assessing poorly crystalline and mineral-organic species by extracting Al, Fe, Mn, and Si using (citrate-) ascorbate and oxalate. *Geoderma* **397**, 115095.

Rossberg, A., Reich, T. and Bernhard, G. (2003) Complexation of uranium(VI) with protocatechuic acid – application of iterative transformation factor analysis to EXAFS spectroscopy. *Anal. Bioanal. Chem.* **376**, 631-638.

Saratovsky, I., Gurr, S.J. and Hayward, M.A. (2009) The structure of manganese oxide formed by the fungus *Acremonium* sp. strain KR21-2. *Geochim. Cosmochim. Acta* **73**, 3291-3300.

Scheckel, K.G. and Ryan, J.A. (2004) Spectroscopic speciation and quantification of lead in phosphate-amended soils. *J. Environ. Qual.* **33**, 1288-1295.

Scheinost, A.C., Kretzschmar, R., Pfister, S. and Roberts, D.R. (2002) Combining selective sequential extractions, X-ray absorption spectroscopy, and principal component analysis for quantitative zinc speciation in soil. *Environ. Sci. Technol.* **36**, 5021-5028.

Scheinost, A.C., Stanjek, H., Schulze, D.G., Gasser, U. and Sparks, D.L. (2001) Structural environment and oxidation state of Mn in goethite-groutite solid-solutions. *Am. Mineral.* **86**, 139-146.

Shindo, H., Oshita, T., Matsudomi, N., Usui, K. and Boon Goh, T. (1996) Catalytic role of Mn(IV) oxide in the formation of humic-enzyme complexes in the soil ecosystem. *Soil Sci. Plant Nutr.* **42**, 141-146.

Shuman, L. (1979) Zinc, manganese, and copper in soil fractions. *Soil Science* **127**, 10-17.

Sjöstedt, C., Persson, I., Hesterberg, D., Kleja, D.B., Borg, H. and Gustafsson, J.P. (2013) Iron speciation in soft-water lakes and soils as determined by EXAFS spectroscopy and geochemical modelling. *Geochim. Cosmochim. Acta* **105**, 172-186.

Szymański, W., Skiba, M. and Błachowski, A. (2014) Mineralogy of Fe-Mn nodules in Albeluvisols in the Carpathian Foothills, Poland. *Geoderma* **217**, 102-110.

Tam, S.C., Sposito, G. and Senesi, N. (1991) Spectroscopic and chemical evidence of variability across a pine litter layer. *Soil. Sci. Soc. Am. J.* **55**, 1320-1325.

Taylor, R., McKenzie, R. and Norrish, K. (1964) The mineralogy and chemistry of manganese in some Australian soils. *Soil Res.* **2**, 235-248.

Tebo, B.M., Bargar, J.R., Clement, B.G., Dick, G.J., Murray, K.J., Parker, D., Verity, R. and Webb, S.M. (2004) Biogenic manganese oxides: Properties and mechanisms of formation. *Annu. Rev. Earth Planet. Sci.* **32**, 287-328.

Tokashiki, Y., Dixon, J. and Golden, D. (1986) Manganese oxide analysis in soils by combined X-ray diffraction and selective dissolution methods. *Soil. Sci. Soc. Am. J.* **50**, 1079-1084.

Tu, S., Racz, G.J. and Goh, T.B. (1994) Transformations of synthetic birnessite as affected by pH and manganese concentration. *Clays Clay Miner.* **42**, 321-330.

Ure, A. and Berrow, M. (1982) The elemental constituents of soil. *Environ. Chem.* **2**, 94-204.

Uzochukwu, G. and Dixon, J. (1986) Managanese oxide minerals in nodules of two soils of Texas and Alabama. *Soil. Sci. Soc. Am. J.* **50**, 1358-1363.

Villalobos, M., Toner, B., Bargar, J. and Sposito, G. (2003) Characterization of the manganese oxide produced by *Pseudomonas putida* strain MnB1. *Geochim. Cosmochim. Acta* **67**, 2649-2662.

Vodyanitskii, Y.N. (2006) The composition of Fe-Mn nodules as determined by synchrotron X-ray analysis (Review of publications). *Eurasian Soil Sci.* **39**, 147-156.

Vodyanitskii, Y.N. (2009) Mineralogy and geochemistry of manganese: A review of publications. *Eurasian Soil Sci.* **42**, 1170-1178.

Vodyanitskii, Y.N., Gorshkov, A. and Sivtsov, A. (2002) Peculiarities of manganese oxides in soils of the Russian Plain. *Eurasian Soil Sci. C/C of Pochvovedenie* **35**, 1037-1045.

Vodyanitskii, Y.N. and Sivtsov, A. (2004) Formation of ferrihydrite, ferroxyhyte, and vernadite in soil. *Eurasian Soil Sci. C/C of Pochvovedenie* **37**, 863-875.

Wang, X., Lan, S., Zhu, M., Ginder-Vogel, M., Yin, H., Liu, F., Tan, W. and Feng, X. (2015) The presence of ferrihydrite promotes abiotic formation of manganese (oxyhydr) oxides. *Soil. Sci. Soc. Am. J.* **79**, 1297-1305.

Webb, S.M. (2005) SIXpack: A graphical user interface for XAS analysis using IFEFFIT. *Phys. Scr.* **T115**, 1011-1014.

Webb, S.M., Tebo, B.M. and Bargar, J.R. (2005) Structural characterization of biogenic Mn oxides produced in seawater by the marine *Bacillus sp.* strain SG-1. *Am. Mineral.* **90**, 1342-1357.

Wu, Z., Lanson, B., Feng, X., Yin, H., Tan, W., He, F. and Liu, F. (2021) Transformation of the phyllomanganate vernadite to tectomanganates with small tunnel sizes: Favorable geochemical conditions and fate of associated Co. *Geochim. Cosmochim. Acta* **295**, 224-236.

Xue, N., Seip, H.M., Guo, J., Liao, B. and Zeng, Q. (2006) Distribution of Al-, Fe-and Mn-pools and their correlation in soils from two acid deposition small catchments in Hunan, China. *Chemosphere* **65**, 2468-2476.

Yang, P., Lee, S., Post, J.E., Xu, H., Wang, Q., Xu, W. and Zhu, M. (2018) Trivalent manganese on vacancies triggers rapid transformation of layered to tunneled manganese oxides (TMOs): Implications for occurrence of TMOs in low-temperature environment. *Geochim. Cosmochim. Acta* **240**, 173-190.

Yaalon, D., Jungreis, C. and Koyumdjisky, H. (1972) Distribution and reorganization of manganese in three catenas of Mediterranean soils. *Geoderma* **7**, 71-78.

Yano, J. and Yachandra, V.K. (2008) Where water is oxidized to dioxygen: Structure of the photosynthetic Mn_4Ca cluster from X-ray spectroscopy. *Inorg. Chem.* **47**, 1711-1726.

Zahoransky, T., Wegorzewski, A.V., Huong, W. and Mikutta, C. (2022) X-ray absorption spectroscopy study of Mn reference compounds for Mn speciation in terrestrial surface environments. *Am. Mineral.* DOI: 10.2138/am-2022-8236.

Zhang, J., Lion, L.W., Nelson, Y.M., Shuler, M.L. and Ghiorse, W.C. (2002) Kinetics of Mn(II) oxidation by *Leptothrix discophora* SS1. *Geochim. Cosmochim. Acta* **66**, 773-781.

Zhang, M. and Karathanasis, A. (1997) Characterization of iron-manganese concretions in Kentucky Alfisols with perched water tables. *Clays Clay Miner.* **45**, 428-439.

Zhao, W., Ren, B., Hursthouse, A. & Feng, J. (2022) The adsorption of Mn(II) by insolubilized humic acid. *Wat. Sci. Technol.* 82, 747-758.

Zhu, M., Ginder-Vogel, M., Parikh, S.J., Feng, X.-H. and Sparks, D.L. (2010) Cation effects on the layer structure of biogenic Mn-oxides. *Environ. Sci. Technol.* **44**, 4465-4471.

Zhu, Y., Liang, X., Zhao, H., Yin, H., Liu, M., Liu, F. and Feng, X. (2017) Rapid determination of the Mn average oxidation state of Mn oxides with a novel two-step colorimetric method. *Anal. Methods.* **9**, 103-109.

B. Supporting information to chapter 3

B.1. Sampling site description

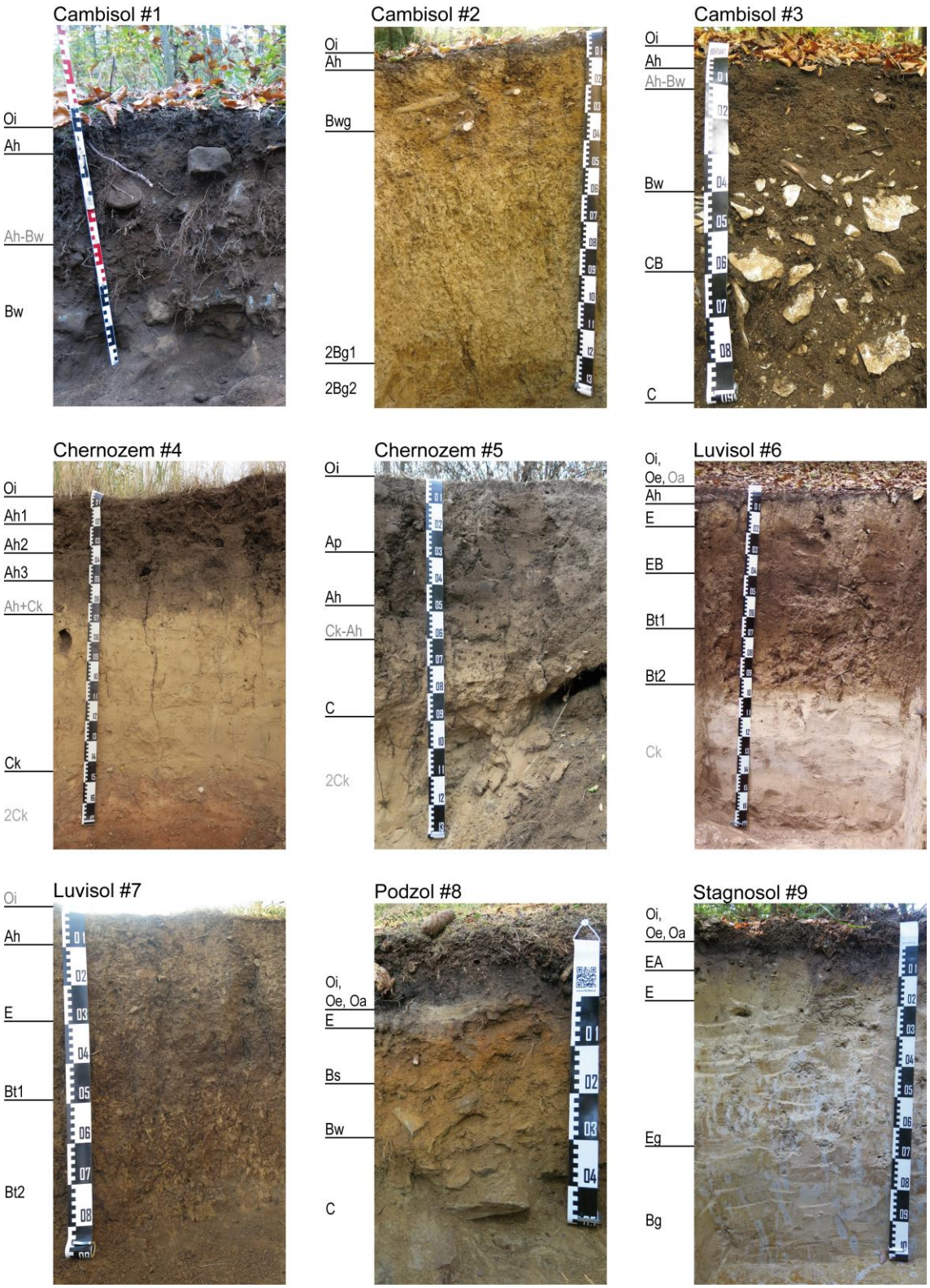

Figure B.1. Photographs of soil profiles. Soil horizon names in gray denote horizons that were not sampled.

Table B.1. Coordinates, climatic conditions, parent material, and vegetation cover of sampling sites

Latitude (N)	Longitude (E)	Climatic conditions[a]	Parent material	Vegetation
Dystric Skeletic Cambisol (Hyperhumic, Loamic) #1				
50°21`07.06''	9°55'44.39''	947 mm, 7.9 °C	Basalt	Deciduous forest (*Fagus sylvatica*, *Acer pseudoplatanu*)
Eutric Stagnic Cambisol (Loamic) #2				
49°53'20.6"	11°01'08.6"	812 mm, 9.1 °C	Mixed loamy solifluction layer over claystone	Deciduous forest (*Fagus sylvatica*, *Carpinus betulus*, *Quercus petraea*)
Calcaric Skeletic Cambisol (Clayic, Humic) #3				
49°53'15.4"	11°02'05.9"	812 mm, 9.1 °C	Limestone	Deciduous forest (*Fagus sylvatica*)
Haplic Chernozem (Pachic, Silitc) #4				
51°26'19.0"	11°45'22.9"	515 mm, 9.4 °C	Loess over glacial till	Grassland (former arable land)
Haplic Chernozem (Loamic, Pachic) #5				
51°30'11.2"	12°01'39.1"	515 mm, 9.4 °C	Loess-rich sandy alluvium over fluvial deposit	Scrubby former arable land (*Prunus spinosa, Rosa canina*)
Haplic Luvisol (Cutanic, Hypereutric, Siltic) #6				
51°23'08.6"	11°03'18.7"	579 mm, 8.1 °C	Loess	Deciduous forest (*Fagus sylvatica*, *Betula pendula*)
Haplic Luvisol (Cutanic, Loamic, Oligeoeutric) #7				
49°58'24.1"	11°37'21.7"	757 mm, 8.5 °C	Loess-rich alluvium mixed with granite-derived river gravel	Grassland (former arable land), *Populus tremula*
Skeletic Albic Podzol (Loamic) #8				
49°59'28.62''	11°48'06.25''	1210 mm, 6.4 °C	Phyllite	Coniferous forest (*Picea abies*)
Dystric Albic Folic Stagnosol (Nechic, Siltic) #9				
51°16`50.05"	12°58`54.10"	578 mm, 9.4 °C	Reworked loess	Mixed forest (*Fagus sylvatica*, *Vaccinium myrtillus*, sporadic *Quercus rubra* and *Pinus sylvestris*)

[a]Mean annual precipitation and mean annual temperature. Data are averages for the 1981-2010 climate reference period (DWD Climate Data Center (CDC), 2022).

B.2. ADDITIONAL SOIL PROPERTIES

Table B.2. Additional properties of soil samples

Sample	Munsell color (field-moist)	Soil texture	pH($CaCl_2$)	EC[a] (µS/cm)	C_{inorg} (%)
Dystric Skeletic Cambisol (Hyperhumic, Loamic) #1					
Ah	10YR3/3	silty clay loam	3.6	70.6	-
Bw	10YR4/4	silt loam	4.3	26.0	-
Eutric Stagnic Cambisol (Loamic) #2					
Ah	10YR3/3	loam	3.9	68.7	-
Bwg	10YR4/4	loam	3.6	47.1	-
2Bg1	7.5YR5/6, 2.5Y7/2	clay	3.9	52.8	-
2Bg2	7.5YR3/4, 5Y6/2	clay loam	4.2	73.3	-
Calcaric Skeletic Cambisol (Clayic, Humic) #3					
Ah	7.5YR3/4	silty clay	4.4	53.9	-
Bw	7.5YR4/4	silty clay loam	6.7	89.9	-
CB	10YR4/4	silty clay	7.3	180	0.66
C	10YR4/6	clay	7.4	160	3.30
Haplic Chernozem (Pachic, Silitc) #4					
Ah1	10YR3/2	silt loam	6.9	152	-
Ah2	10YR3/2	silt loam	7.3	174	0.02
Ah3	10YR3/4	silt loam	7.4	205	0.05
Ck	10YR5/6	silt	7.9	857	1.39
Haplic Chernozem (Loamic, Pachic) #5					
Ap	10YR3/2	silt loam	5.8	57.7	-
Ah	10YR4/3	silt loam	6.4	43.7	-
C	10YR6/6	silt loam	7.4	94.9	0.01
Haplic Luvisol (Cutanic, Hypereutric, Siltic) #6					
Ah	7.5YR2/2	silt loam	5.2	75.5	-
E	7.5YR5/4	silt loam	4.2	48.7	-
EB	7.5YR4/4	silt loam	4.9	42.6	-
Bt1	7.5YR4/6	silt loam	4.4	80.1	-
Bt2	7.5YR6/4	silt loam	4.9	150	-
Haplic Luvisol (Cutanic, Loamic, Oligeoeutric) #7					
Ah	10YR3/2	silt loam	5.0	80.6	-
E	10YR4/2	silt loam	5.6	58.4	-
Bt1	10YR3/3	loam	5.8	41.6	-
Bt2	10YR4/3	silty clay loam	6.2	43.2	-
Skeletic Albic Podzol (Loamic) #8					
E	10YR5/3	silt loam	3.0	64.3	-
Bs	7.5YR4/6	loam	3.7	38.4	-
Bw	10YR5/6	silt loam	4.4	24.1	-
C	2.5Y3/4	sandy loam	4.4	18.7	-
Dystric Albic Folic Stagnosol (Nechic, Siltic) #9					
EA	10YR4/3	silt loam	3.5	69.7	-
E	10YR6/4	silt loam	3.9	45.7	-
Eg	10YR7/2, 7.5YR6/4	silt loam	3.8	48.2	-
Bg	7.5YR5/6, 5YR7/1	silt loam	3.7	34.5	-

[a]Electrical conductivity.

B.3. SELECTIVE MN EXTRACTION

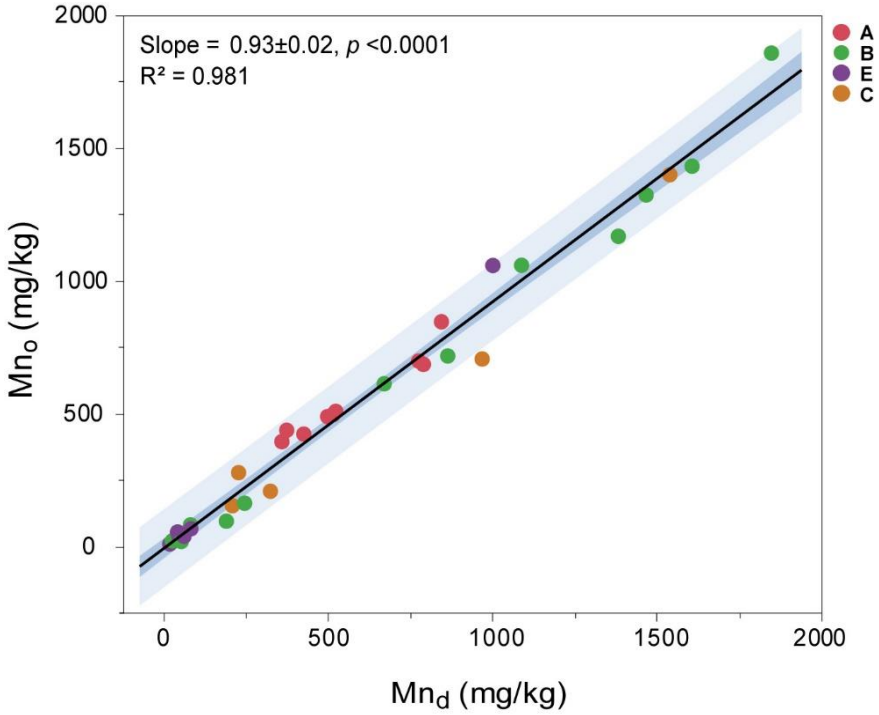

Figure B.2. Linear regression between Mn_d and Mn_o of mineral soil horizons (*N* = 37). Confidence and prediction bands (95%) are indicated by dark and light blue color, respectively. Transition horizons (CB, EA, EB) were included in their respective master horizon group.

B.4. MANGANESE K-EDGE X-RAY ABSORPTION SPECTROSCOPY

Table B.3. Primary XANES absorption and first-derivative peaks of soil samples

	Absorption			First derivative					
	1	2	3	1	2	3	4	5	6
Dystric Skeletic Cambisol (Hyperhumic, Loamic) #1									
Oi	6552.6			6539.6			6549.2		
Ah		6560.2	6573.8	6539.8	6542.4	6547.0	6551.0	6556.2	6571.4
Bw		6560.4	6574.4	6540.2	6542.6	6547.1	6551.2	6556.4	6571.4
Eutric Stagnic Cambisol (Loamic) #2									
Oi	6552.5			6539.5		6548.6			
Ah		6562.9		6539.1	6542.3	6549.3		6556.6	6571.9
Bwg		6562.1	6574.9	6540.6	6542.5	6550.8		6556.3	6573.4
2Bg1		6562.7		6538.8	6542.2	6550.7		6556.5	6574.2
2Bg2		6562.6	6575.8	6540.6	6542.5	6551.2		6557.2	6572.7
Eutric Calcaric Skeletic Cambisol (Clayic, Humic) #3									
Ah		6562.4		6539.1	6542.3	6551.5		6557.2	6572.9
Bw		6562.6		6540.7	6542.5			6557.1	6573.1
CB		6561.9	6574.5	6540.1	6542.1	6550.9		6556.0	6571.9
C		6562.1	6575.3	6540.3	6542.4	6550.8		6556.5	6572.5
Haplic Chernozem (Pachic, Silitc) #4									
Oi	6553.5	6561.2		6539.4	6542.4	6548.1	6549.9	6558.5	
Ah1		6561.5	6574.8	6540.3	6542.4	6547.8	6550.2	6556.6	6571.4
Ah2		6561.8	6574.4	6540.6	6542.8	6547.9	6551.3	6556.6	6571.7
Ah3		6562.0	6574.9	6540.3	6542.7	6547.8	6551.4	6556.5	6571.8
Ck	6552.5	6561.5		6540.0	6542.7	6548.1	6551.1	6556.7	6560.1
Haplic Chernozem (Loamic, Pachic) #5									
Oi	6552.9			6539.8		6548.7			
Ap		6561.1	6574.3	6539.8	6541.9		6550.2	6556.0	6570.2
Ah		6561.7	6574.1	6540.5	6542.6	6548.2	6551.2	6556.1	6571.9
C		6561.6	6574.7	6540.0	6542.4	6547.7	6550.8	6556.1	6571.3
Haplic Luvisol (Cutanic, Hypereutric, Siltic) #6									
Oi		6561.9	6574.3	6540.1	6543.0		6549.2	6557.9	6571.0
Oe		6561.8	6574.5	6540.5	6542.5		6549.5	6557.3	6572.0
Ah		6561.8	6575.3	6540.5	6542.6		6551.0	6556.6	6572.0
E	6553.1	6557.4	6570.1	6540.3		6547.8	6551.3	6555.8	6568.9
EB	6552.8	6557.4	6569.9	6540.2		6547.8	6551.1	6555.8	6568.9
Bt1		6557.9	6570.9	6539.9		6548.1	6551.0	6556.2	6569.3
Bt2	6553.1	6557.1	6570.8	6539.8		6547.4	6551.3	6555.4	6568.7
Haplic Luvisol (Cutanic, Loamic, Oligeoeutric) #7									
Ah		6562.1	6574.9	6540.5	6442.1	6550.5		6556.3	6572.2
E		6562.5	6574.4	6538.9	6542.3	6550.4		6556.6	6573.6
Bt1		6562.1	6574.9	6540.3	6542.4	6550.9		6557.8	6571.4
Bt2		6562.2	6574.7	6540.3	6542.4	6550.5		6556.2	6572.4
Skeletic Albic Podzol (Loamic) #8									
Oi	6553.1			6539.9		6548.3	6549.4		
Oe	6553.1			6539.9		6547.8	6549.5	6555.2	6569.7
Oa		6557.6	6571.1	6540.2		6547.1	6550.4		6568.8
E		6557.1				6549.5			
Bs		6559.2	6574.1	6540.2		6548.5	6551.3	6555.5	6571.2
Bw		6558.8	6573.5	6540.2		6547.7	6551.3	6556.1	6571.4
C		6560.0	6574.1	6540.0		6548.1	6551.1	6555.9	6571.5
Dystric Albic Folic Stagnosol (Nechic, Siltic) #9									
Oi		6561.7	6573.9	6540.2	6542.4	6548.9		6557.3	6571.8
Oe	6553.7	6561.8		6540.0		6548.6		6559.1	
Oa	6552.5	6557.0	6569.6	6539.6		6546.5	6550.4	6555.8	6568.4
EA	6554.8			6539.1		6547.5	6550.3		6568.8
E		6557.1	6571.3	6539.9		6548.1			6569.7
Eg		6557.2	6570.7	6539.4		6548.4		6555.0	6568.5
Bg	6553.3			6539.2		6547.9	6550.6	6558.1	6566.8

Table B.4. Output parameters for the first ten PCs obtained from PCA analysis of k^2-weighted soil EXAFS spectra (k = 2.0-11.0 Å^{-1}, E_0 = 6,563 eV)

Component	Eigenvalue	Total variance	Cumulative eigenvalue	Cumulative variance	IND (×10^3)[a]
1	15.46	0.81	15.46	0.81	0.1017
2	1.98	0.10	17.45	0.92	0.0778
3	0.56	0.03	18.00	0.95	0.0725
4	0.31	0.02	18.31	0.96	0.0709
5	0.20	0.01	18.51	0.97	0.0709
6	0.15	0.01	18.66	0.98	0.0710
7	0.09	0.00	18.75	0.99	0.0747
8	0.05	0.00	18.80	0.99	0.0830
9	0.05	0.00	18.85	0.99	0.0914
10	0.04	0.00	18.89	0.99	0.1010

[a]IND function calculated with the program package "ITFA" (Rossberg et al., 2003).

B4.1. EXAFS-LINEAR COMBINATION FIT INTERPRETATION SCHEME

(1) k^2-weighted EXAFS spectra of phyllomanganates, such as δ-MnO_2 and birnessite (triclinic and hexagonal), and those of tectomanganates, such as hollandite *s.s.* (2 × 2 tunnels), romanèchite (2 × 3 tunnels), and todorokite (3 × 3 tunnels) are highly correlated. Their subtle spectral differences are probably not sufficient to uniquely identify and quantify these mineral phases in mixtures (Zahoransky et al., 2022). However, the need to fit tectomanganate reference spectra in addition to those of phyllomanganates may be taken as an indication of the presence of tectomanganates in soils, regardless of their exact nature.

(2) Organically complexed Mn was estimated from summed fit fractions of k^2-weighted EXAFS spectra of Mn(II) acetate tetrahydrate, Mn(II) oxalate dihydrate, and Mn^{2+} adsorbed to a natural peat sample at pH 7 (Zahoransky et al., 2022).

(3) The content of Mn(III) oxyhydroxides was assessed by EXAFS reference spectra of the polymorphs feitknechtite (β-MnOOH) and groutite (α-MnOOH). These minerals possess similar k^2-weighted EXAFS spectra, but these differ significantly between 8 and 10 Å^{-1}, which allows for their unambiguous identification (Zahoransky et al., 2022).

(4) Silicate-bound Mn was estimated from summed fit fractions of k^2-weighted EXAFS spectra of masutomilite and hendricksite, both trioctahedral phyllosilicates containing Mn^{2+} in their octahedral layers, and braunite, a nesosilicate containing Mn^{2+} and Mn^{3+}. These reference compounds show distinct features in their k^2-weighted EXAFS spectra (Zahoransky et al., 2022), but owing to the diversity of Mn coordination environments in silicates, this does not allow for the identification of specific Mn-bearing silicates.

(5) Manganese in oxides without layer- or tunnel structure was estimated from summed fit fractions of the Mn^{2+}- and Mn^{3+}-containing spinel hausmannite and the Mn^{3+} containing oxide bixbyite. Both minerals exhibit unique spectral characteristics that facilitate their identification in mixtures (Zahoransky et al., 2022).

(6) The reference 'Mn(II) ads. illite (pH7)' refers to Mn^{2+} adsorbed to a natural 85:15-90:10 illite-smectite phase with R3 ordering at pH 7 (<2-µm fraction; Dohrmann 2009). This reference compound is representative of $Mn^{2+/3+}$ species without detectable atomic contributions beyond the first O shell in their Fourier-transformed EXAFS spectra (Zahoransky et al., 2022). Such species include outersphere complexes of $Mn^{2+/3+}$ at mineral or organic surfaces ('physisorbed' Mn).

B4.2. INITIAL PCA-TT-BASED EXAFS LINEAR COMBINATION FITS

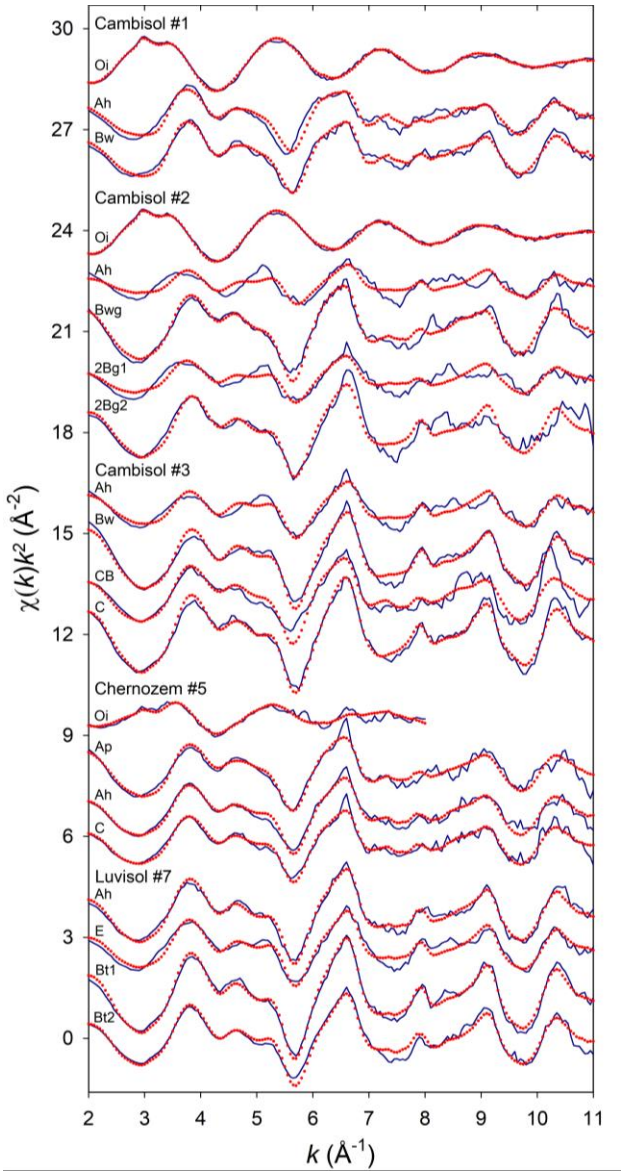

Figure B.3. Stacked k^2-weighted Mn K-edge EXAFS spectra and initial PCA-TT-based LCFs of soil samples. LCF results are summarized in Table B.5.

Table B.5. Speciation of Mn in bulk soil samples obtained from initial PCA-TT-based LCFs of k^2-weighted Mn K-edge EXAFS spectra[a]

	Manganates						Organically complexed Mn				Silicates	Physisorbed	Fit sum	*R*-factor[b]
	AcB	δ-Mn	Hol	Rmn	Tdr	Total	Ac	Ox	Peat	Total	Msu	Illite		
Dystric Skeletic Cambisol (Hyperhumic, Loamic) #1														
Oi	-	-	-	-	-	**0.00**	-	0.07	0.84	**0.91**	-	**0.09**	0.96	0.02
Ah	-	-	0.21	0.60	-	**0.81**	-	-	-	**0.00**	**0.19**	-	0.85	0.13
Bw	0.18	-	0.14	0.48	-	**0.80**	-	-	-	**0.00**	**0.20**	-	0.96	0.06
Eutric Stagnic Cambisol (Loamic) #2														
Oi	-	-	-	-	-	**0.00**	-	0.08	0.77	**0.85**	-	**0.15**	0.96	0.01
Ah	0.36	0.07	-	-	0.14	**0.57**	-	-	0.43	**0.43**	-	-	0.70	0.38
Bwg	-	0.28	0.23	0.39	-	**0.90**	-	-	-	**0.00**	-	**0.10**	1.06	0.07
2Bg1	-	0.40	-	0.18	-	**0.57**	-	-	0.23	**0.23**	-	**0.19**	0.87	0.28
2Bg2	0.66	-	-	0.25	-	**0.91**	0.09	-	-	**0.09**	-	-	0.89	0.16
Eutric Calcaric Skeletic Cambisol (Clayic, Humic) #3														
Ah	0.34	-	-	-	0.32	**0.66**	-	-	0.34	**0.34**	-	-	0.83	0.17
Bw	0.38	-	-	-	0.44	**0.82**	-	-	0.18	**0.18**	-	-	1.07	0.05
CB	0.27	-	0.52	0.05	-	**0.85**	-	-	-	**0.00**	-	**0.15**	1.07	0.19
C	0.27	0.52	-	0.09	-	**0.87**	0.13	-	-	**0.13**	-	-	1.19	0.03
Haplic Chernozem (Loamic, Pachic) #5														
Oi[c]	-	0.19	-	-	-	**0.19**	-	-	0.18	**0.18**	**0.09**	**0.55**	0.80	0.16
Ap	-	0.30	0.40	-	0.18	**0.88**	-	-	-	**0.00**	**0.12**	-	0.91	0.11
Ah	0.24	0.08	0.40	-	-	**0.73**	-	-	-	**0.00**	-	**0.27**	1.11	0.07
C	0.25	-	0.31	0.13	-	**0.70**	-	-	-	**0.00**	-	**0.30**	1.08	0.08
Haplic Luvisol (Cutanic, Loamic, Oligeoeutric) #7														
Ah	0.38	-	-	0.39	-	**0.77**	-	-	0.10	**0.10**	-	**0.13**	1.18	0.04
E	0.46	-	-	0.22	-	**0.68**	-	-	0.19	**0.19**	-	**0.13**	1.04	0.09
Bt1	0.54	-	0.11	0.17	-	**0.81**	-	-	-	**0.00**	-	**0.19**	1.35	0.02
Bt2	0.49	-	0.22	-	-	**0.71**	-	-	-	**0.00**	-	**0.29**	1.23	0.06

[a]Fractions were recalculated to a component sum of 100%. Their relative uncertainty is 10% at best. Abbreviations of fit references: AcB: Acid birnessite (hex., syn), δ-Mn: δ-MnO_2 (syn), Hol: Hollandite *s.s.*, Rmn: Romanèchite, Tdr: Todorokite, Ac: Mn(II) acetate tetrahydrate (syn), Ox: Mn(II) oxalate dihydrate (syn), Peat: Mn(II) ads. peat (pH7), Msu: Masutomilite, Illite: Mn(II) ads. illite (pH7).

[b]*R*-factor = $\Sigma_i(\text{data}_i - \text{fit}_i)^2/\Sigma_i\text{data}_i$.

[c]Spectrum analyzed over k = 2.0-8.0 $Å^{-1}$.

Table B.6. Spearman rank order correlations (r_s) of Mn species pools in mineral soil horizons (N = 17) with selected soil properties. Significant correlations at p <0.05 and <0.01 are marked with * and **, respectively. Correlation coefficients >0.7 are displayed in bold. Concentrations of the six Mn species pools were calculated from final EXAFS- LCF results (Table 3.4) and Mn_{tot} values (Table 3.1)

	Manganate-Mn (mg/kg)	**Organic Mn (mg/kg)**	**Oxyhydroxide-Mn (mg/kg)**	**Silicate-Mn (mg/kg)**	**Oxide-Mn (mg/kg)**	**Physisorbed Mn (mg/kg)**
Mn_{tot} (mg/kg)	**0.89****	0.07	0.10	0.11	0.08	-0.41
Mn_d (mg/kg)	**0.90****	0.07	0.03	0.09	-0.08	-0.37
Mn_o (mg/kg)	**0.89****	0.09	0.04	0.03	-0.11	-0.34
$Mn_{tot} - Mn_d$ (mg/kg)	0.29	0.24	0.44	-0.05	0.48	-0.40
Clay (%)	0.38	0.02	0.17	0.04	-0.21	-0.23
Fe_d (g/kg)	0.36	0.13	0.23	-0.33	0.12	0.01
Fe_o (g/kg)	0.34	-0.04	0.56*	-0.19	0.66*	-0.11
C_{org} (%)	0.01	0.04	0.00	0.13	0.33	-0.19

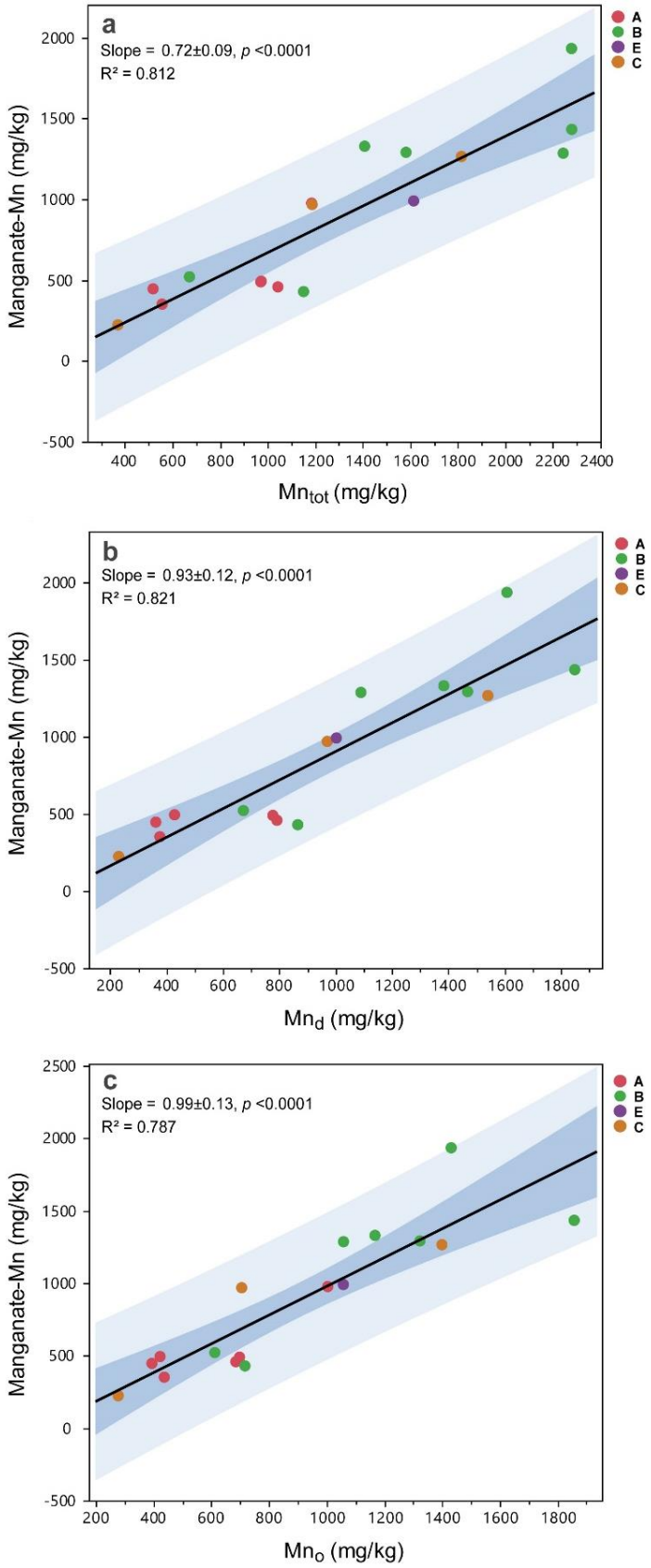

Figure B.4. Linear regressions between (a) Mn_{tot}, (b) Mn_d, and (c) Mn_o and manganate-Mn in mineral soil master horizons (*N* = 17). Concentrations of manganate-Mn were calculated from fitted manganate fractions (Table 3.4) and Mn_{tot} values (Table 3.1). Confidence and prediction bands (95%) are indicated by dark and light blue color, respectively.

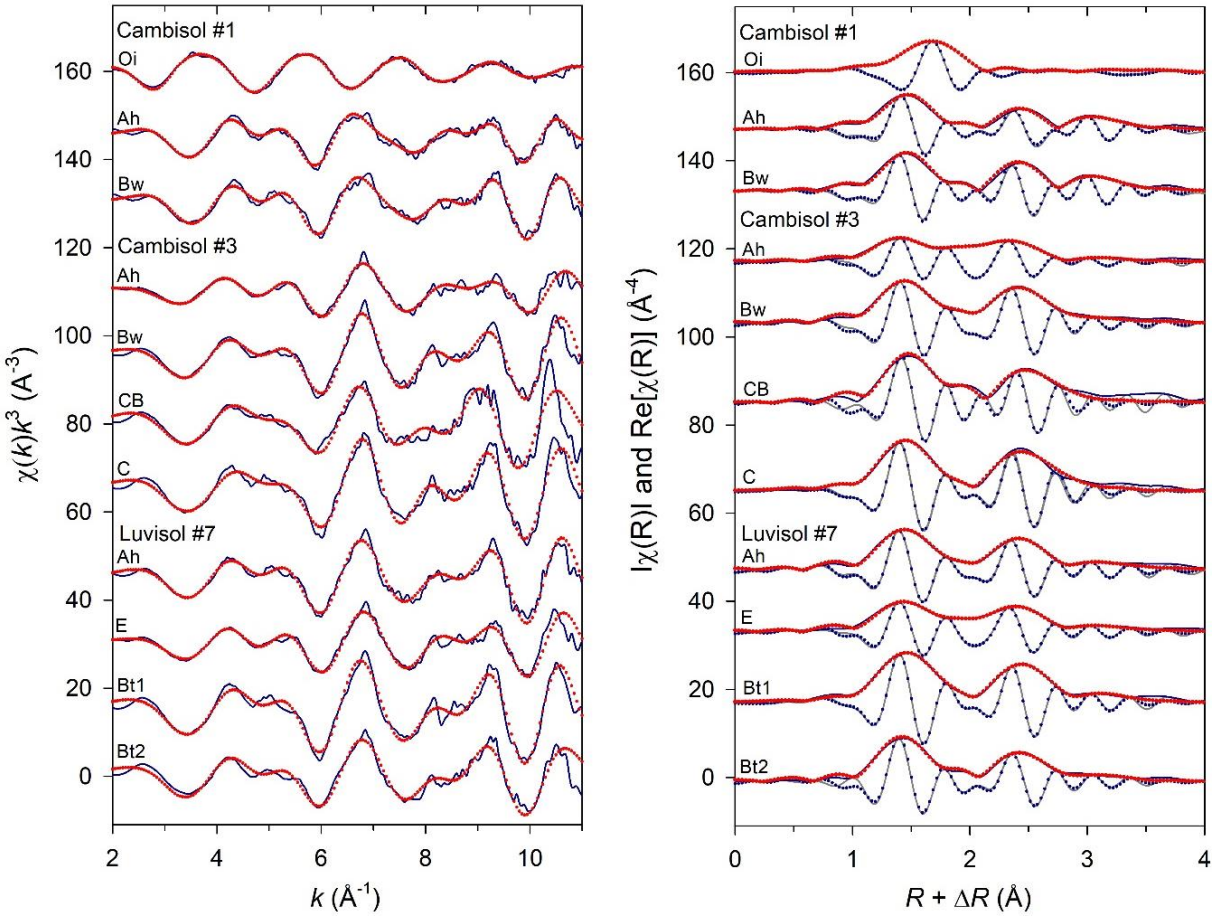

Figure B.5. Stacked k^3-weighted Mn K-edge EXAFS spectra (left) as well as corresponding Fourier-transform magnitudes and real parts (right) of Cambisols #1 and #3 and Luvisol #7. Solid lines represent experimental data and dotted lines model fits. EXAFS parameters are summarized in Table 3.5 and interatomic distances are visualized in Figure 3.7.

B.5. References

Dohrmann, R., Rüping, K.B., Kleber, M., Ufer, K. and Jahn, R. (2009) Variation of preferred orientation in oriented clay mounts as a result of sample preparation and composition. *Clays Clay Miner.* **57**, 686-694.

DWD Climate Data Center (CDC): *Vieljährige Stationsmittelwerte für die Klimareferenzperiode 1981-2010, für aktuellen Standort und Bezugsstandort,* 2022.

Zahoransky, T., Wegorzewski, A.V., Huong, W. and Mikutta, C. (2022) X-ray absorption spectroscopy study of Mn reference compounds for Mn speciation in terrestrial surface environments. *Am. Mineral.* DOI: 10.2138/am-2022-8236.

4. Conclusions, Implications, and Perspectives

This thesis focused on clarifying how well and to what extent individual Mn species or groups can be differentiated by XAS, and ultimately concentrated on the identification and quantification of the Mn species inventory in major Central European soil types. The strength of this study lies in the fact that it is not tied to local, spatially resolved Mn species information, but instead examines the bulk inventory of Mn species in soils. The overall objective was to enhance the understanding of the quantitative Mn species distribution in soils differing in their pedogenic background in order to promote knowledge of the Mn cycle in terrestrial surface environments. Analytical emphasis was set on Mn K-edge XAS-based techniques, and I connected the so-obtained Mn speciation knowledge with an array of complementary physical (grain-size distribution), geochemical (basic soil properties determination, EPMA, ICP-OES, redox titration, XRF), and structural (XRD) analysis, as well as statistical methods (descriptive statistics, ANOVA, cluster analysis, PCA). With that, I comprehensively characterized (in)organic Mn reference compounds and soil samples, validated XAS results, and examined dependencies between Mn speciation and physicochemical soil properties.

This thesis shows that linear combination fit (LCF) analysis of normalized XANES spectra can confidently quantify the Mn AOS within ~0.1 v.u. in the range +2 to +4. This was ascertained by validating XANES-derived Mn AOS results with those obtained by redox titration of a suite of 32 mixed- and monovalent Mn reference compounds including Mn (oxyhydr)oxides, carbonate, phosphate, and silicate minerals, as well as organic and adsorbed Mn species. The obtained information on the accuracy of XANES-LCF based Mn AOS determination is most useful for future analysis of natural, inhomogeneous matrices such as soils, where other redox-active elements such as Fe are typically abundant and wet-chemical methods that include redox titration thus fail in the determination of the Mn AOS.

Further investigation of these Mn reference compounds allowed the definition of spectral fingerprints in the normalized XANES spectrum and its first derivative, as well as in the EXAFS domain. This spectral-fingerprint characterization contributes to recognize single Mn species or species groups – even more so since some of these species (i.e., compounds with physisorbed Mn^{2+}, organic $Mn^{2+/3+}$ compounds, Mn containing silicates and phosphates) have never been studied by XAS or EXAFS in particular before.

As pointed out in the foregoing chapters, spectral uniqueness is a topic of fundamental importance in reference-dependent XAS techniques like LCF. EXAFS spectra were shown to be clearly more ‘characteristic’ and thus suitable for the identification and quantification of Mn species than XANES spectra or their first derivatives. The high spectral correlation of the latter two demonstrates that they are less suited for an accurate LCF-based Mn species analysis of environmental samples.

Although exceptions of Mn minerals with clearly identifiable XANES exist (e.g., pyrolusite, ramsdellite, and perhaps lithiophorite), the XANES spectrum can additionally be influenced by factors other than the Mn oxidation state, such as the chemical composition and crystallinity of Mn compounds, which limits their robustness and thus suitability for LCF analysis. While most of the studied Mn minerals exhibited unique EXAFS signatures, manganate minerals were shown to be almost indistinguishable by their EXAFS signal, except for pyrolusite, which shows two distinct troughs at 7.8 and 8.1 $Å^{-1}$. Nevertheless, a gradually emerging left-side shoulder of the 6.7-$Å^{-1}$ oscillation with decreasing tunnel size may aid in the distinction of phyllo- and tectomanganates.

The application of PCA and cluster analysis of k^2-weighted EXAFS spectra of Mn reference compounds revealed that among all 32 Mn reference compounds, at least five Mn species supergroups exhibit spectral uniqueness, supporting their identification and quantification in multicomponent matrices such as soils by EXAFS-LCF. These supergroups are: (1) Mn(III/IV) phyllo- and tectomanganates with large tunnel sizes (2×2 and larger; hollandite, romanèchite, todorokite), (2) Mn(III/IV) tectomanganates with small tunnel sizes (2×2 and smaller; cryptomelane, pyrolusite, ramsdellite), (3) Mn(III)-dominated species (nesosilicates, oxyhydroxides, organic compounds, spinels), (4) Mn(II) species (carbonate, phosphate, and phyllosilicate minerals, adsorbed and organic species), and (5) manganosite.

Following these results, I used the potential of Mn K-edge XAS to assess bulk Mn speciation in 47 soil horizons from nine typical Central European soils (Cambisols, Chernozems, Luvisols, Podzol, and Stagnosol). As outlined in chapter 2, it can be deduced from existing literature that manganate minerals are ubiquitous in mineral soils. However, due to the paucity of quantitative analytical evidence, it has remained largely unclear until know, whether this ubiquity also meant 'predominance'. The results of this PhD project provide the first quantitative results on Mn species distribution in major soil types of Central Europe. For a complete XAS-based Mn speciation analysis, I included the determination of Mn valences and the resulting Mn AOS following the 'Combo' method of Manceau et al. (2012), and assessed 20 soil horizons by EXAFS LCF analyses based on PCA-TT results and EXAFS shell-fit analyses for the validation of LCF results. The obtained XAS results were subsequently related to physicochemical soil properties.

Organic soil horizons showed a clear dominance of Mn^{2+} species. In Oi horizons, these were mainly present as organic complexes and physisorbed Mn, but also manganates, Mn(III) oxyhydroxides, and silicate-bound Mn were detected therein. Mineral soil horizons showed abundant presence of Mn^{4+}. LCF analysis revealed that manganates (likely mixtures of phyllomanganates with hexagonal layer symmetry and tectomanganates) were dominating in mineral soil horizons, and correlation analysis showed that they dissolve completely during dithionite-citrate and acid ammonium oxalate extractions. Manganese^{4+} was strongly positively correlated with pH and clay,

while Mn^{3+} showed inverse correlations, respectively. It is therefore suggested that Mn^{4+}-rich manganates – and not manganates in general – form preferentially under less acidic soil conditions and are enriched in the soil clay fraction. Evidence of both feitknechtite and groutite was given by EXAFS LCF, while manganite, another Mn(III) oxyhydroxide polymorph, was completely absent. Since the formation of Mn(III) oxyhydroxides has previously been reported only under neutral to alkaline pH conditions in the laboratory (Junta and Hochella, 1994; Tu et al., 1994; Bargar et al., 2005; Elzinga, 2016), their natural formation pathways in soils could be an interesting aspect for future research. In addition, the proposed formation of soil birnessites via a manganite precursor (McKenzie, 1972) should be validated, considering the total absence of manganite in all soils analyzed by EXAFS LCF in this work. The low occurrence of silicate-bound Mn in the relatively young soils, which likely formed after the last ice age (<10,000 years), confirms the release of Mn from primary minerals already at early stages of soil formation. Low concentrations of physisorbed Mn demonstrate that exchangeable Mn is rapidly converted in oxic soils, likely into manganates. Interestingly, organically complexed Mn was also not very abundant in mineral soil horizons, not even in organic-rich Ah horizons, where it might have been most expected and where contribution of Mn to ECEC was higher than in directly underlying horizons. This indicates that the organically-complexed Mn pool is readily accessible for rapid subsequent (microbial) conversion.

The observed clear prevalence of manganates in all mineral soils of this study has profound implications on soil functionality and biogeochemical element cycling, owing to the important role these minerals play in metal sequestration, plant nutrition, and redox-related processes (*cf*. Fig. 1.1).

In summary, the project provides fundamental insights into the speciation of soil Mn and important geochemical controls of the Mn cycle in the critical zone. The results of this thesis highlight the potential of Mn K-edge EXAFS spectroscopy to assess bulk Mn speciation in soils and sediments, which we performed for the first time in five different soil types. The compilation of the Mn reference spectrum library lays the foundation for further process-oriented and hypothesis-driven environmental Mn research and provides the first comprehensive framework for the analysis and interpretation of Mn-XAS spectra of natural samples. In doing so, I hope that knowledge and the evaluation of the role of Mn in environmental processes can be greatly advanced in the near future.

One of the remaining questions is the representativity of the results of this work for soils outside Central Europe. Among the oxic soils studied, Cambisols, Luvisols and Podzols are widespread on Earth, covering 1.5×10^9, 230×10^6, and 490×10^6 ha, respectively, worldwide (Zech et al., 2014), which corresponds to ~10, ~4 and ~3% of the total landmass extending above sea level. I expect climatic conditions (temperature, humidity, rainfall), the degree of soil development, and age of the soil to have a profound impact on their Mn species inventory. For example, Nahton et al. (1982) showed that lateritic weathering products of the silicate mineral tephroite ($Mn^{2+}{}_2SiO_4$) under humid, tropical

conditions leads to the formation of intermediate, Mn^{2+}-containing smectites and I thus suspect that the Mn species inventory of such soils may be significantly altered compared to the soils of this study. Podzols, which are generally typical soils of the boreal coniferous forest zone in temperate climates, may also occur in humid tropics, where chemical weathering is pronounced and Al and Fe oxides accumulate. Assuming that supply of Mn in tropical soils is sufficient, the extent of Mn species formation, their association with other minerals, and quantification of Mn species developing under such conditions would be of scientific interest. In Luvisols, the influence of higher temperatures can lead to the development of chromic horizons (Zech et al., 2014), including the possibility of Mn-rich hematite (α-$(Mn,Fe)_2O_3$) formation (Anthony et al., 2003). Mn species distribution and transformation processes in Luvisols with waterlogged and anoxic horizons could reveal a very different Mn species inventory compared to the two Luvisols studied in this work, with a dominance of lower valent Mn species. For example, it is possible that physisorbed Mn^{2+} species could play a more dominant role in reduced soils and Mn^{2+} containing carbonates such as rhodochrosite may occur in soils at anoxic or suboxic conditions and pH >8 (Otero et al., 2006; Barreto et al., 2016). Since this Mn pool is, however, at the same time more accessible for microbial conversion and/or plant uptake, the final Mn species quantification in these soils remains an exciting question. Chernozems, another oxic soil type of this thesis, are globally less abundant, covering ~1.5% of the total landmass extending above sea level, but they are of vast importance since they are among the most fertile arable soils. The clear absence of organically complexed Mn in the Ap and Ah horizons could indicate that these Mn pools are effectively utilized by crops as a readily accessible source of Mn. Future speciation studies in conjunction with sustainable soil optimization could be valuable for those countries practicing arable agriculture on Chernozems. The overall dominance of manganates in all soils investigated in this work raises the question, whether the formation of manganates in such soil types is a worldwide phenomenon. Since pH, Eh, and climatic factors largely control Mn speciation, I suspect that very different Mn species inventories can be found in soils outside of Central Europe, especially when characterized by anoxic conditions.

The need for future research is also warranted by other findings of this work: Generally, the ability of LCF analysis to discriminate between phyllo- and tectomanganates could be further verified by complementary µ-XAS analysis, which allow spatial resolution of metal species (Manceau et al., 2002). Triclinic birnessite was nearly totally absent in the soils studied. Its potential formation in high pH oxic soils by interaction of aqueous Mn^{2+} with hexagonal birnessites (Bargar et al., 2005) is another topic to investigate further.

The results of this study show a strong correlation between Mn_{tot} and the clay particle fraction (<2 µm) and the question remains, in what chemical form Mn is present therein. The results of chapter 2 suggest Mn^{4+}-rich manganates, and verification by, for example, µ-XAS analysis – could increase the

validity of this finding. Further illumination of the association of Mn with other minerals therein (e.g., clay minerals, Fe(III) (oxyhydr)oxides) and quantitative exploration of Mn species in other particle size fractions (e.g., silt fraction) could assist in further deciphering the fate of metals in soils, since particle size and type may influence adsorption, distribution, and environmental behavior of other metals in soils (Huang et al., 2020).

It would be additionally of utmost importance to increase the number of soil types studied for their Mn speciation, since the results of this study are related to oxic soils in Central Europe. As suggested earlier, it would therefore be of great relevance to explore the Mn species inventory of anoxic or suboxic (e.g., Cryosols, Gleysols, Stagnosols), as well as of additional oxic soil types (e.g., Histosols, Lixisols, Nitisols, Retisols, Ultisols, Vertisols) in future scientific investigations. Similarly, to ensure the suitability of the Mn reference library for (anoxic) soils and sediments as well, the existing Mn reference library needs to be expanded. Manganates, Mn(III) oxyhydroxides, and oxide minerals without layer or tunnel structure are, on my opinion, currently well represented and can effectively map their Mn pools in different soil types. However, particularly the reference-pool of Mn silicates could be further extended, e.g., by primary Mn containing silicates such as tephroite, pyroxene, and amphibole and clay minerals such as Mn containing smectites and biotites (Gilkes and McKenzie, 1988).

As outlined in the introduction (chapter 1), the accuracy and effectiveness of existing SE protocols is difficult to verify. The future application of the EXAFS LCF procedure used in this work and of different XANES and EXAFS techniques in general (XANES and EXAFS fingerprinting, EXAFS shell-fitting) should aim to validate widely used SE methods for the species analysis of Mn in soils and sediments, similar to the study on Zn and Pb speciation by Peltier et al. (2005). Validation of SE results on Mn speciation after each extraction step with EXAFS analysis could help to improve existing protocols for cost- and time-efficient SE methods, providing a solid basis of confidence that has been lacking so far.

4.1. REFERENCES

Anthony, J.W., Bideaux, R.A., Bladh, K.W. and Nichols, M.C. (2003) *Handbook of Mineralogy*. Mineralogical Society of America, Chantilly, VA 20151-1110, USA.

Bargar, J.R., Tebo, B.M., Bergmann, U., Webb, S.M., Glatzel, P., Chiu, V.Q. and Villalobos, M. (2005) Biotic and abiotic products of Mn(II) oxidation by spores of the marine *Bacillus sp*. strain SG-1. *Am. Mineral.* **90**, 143-154.

Barreto, M.B., Mónaco, S.L., Díaz, R., Barreto-Pittol, E., López, L. and Peralba, M.d.C.R. (2016) Soil organic carbon of mangrove forests (*Rhizophora* and *Avicennia*) of the Venezuelan Caribbean coast. *Org. Geochem.* **100**, 51-61.

Elzinga, E.J. (2016) ^{54}Mn radiotracers demonstrate continuous dissolution and reprecipitation of vernadite (δ-MnO_2) during interaction with aqueous Mn(II). *Environ. Sci. Technol.* **50**, 8670-8677.

Huang, B., Yuan, Z., Li, D., Zheng, M., Nie, X. and Liao, Y. (2020) Effects of soil particle size on the adsorption, distribution, and migration behaviors of heavy metal(loid)s in soil: A review. *Environ. Sci.: Process. Impacts* **22**, 1596-1615.

Junta, J.L. and Hochella, M.F., Jr. (1994) Manganese(II) oxidation at mineral surfaces: A microscopic and spectroscopic study. *Geochim. Cosmochim. Acta* **58**, 4985-4999.

Manceau, A., Marcus, M.A. and Grangeon, S. (2012) Determination of Mn valence states in mixed-valent manganates by XANES spectroscopy. *Am. Mineral.* **97**, 816-827.

Manceau, A., Marcus, M.A. and Tamura, N. (2002) Quantitative speciation of heavy metals in soils and sediments by synchrotron X-ray techniques. *Rev. Mineral. Geochem.* **49**, 341-428.

McKenzie, R. (1972) The sorption of some heavy metals by the lower oxides of manganese. *Geoderma* **8**, 29-35.

Nahton, D., Colin, F. and Y., T. (1982) Formation and distribution of Mg, Fe, Mn-smectites in the first stages of the lateritic weathering of forsterite and tephroite. *Clay Miner.* **17**, 339-348.

Otero, X., Ferreira, T., Vidal-Torrado, P. and Macías, F. (2006) Spatial variation in pore water geochemistry in a mangrove system (Pai Matos island, Cananeia-Brazil). *Appl. Geochem.* **21**, 2171-2186.

Peltier, E., Dahl, A.L. and Gaillard, J.-F. (2005) Metal speciation in anoxic sediments: When sulfides can be construed as oxides. *Environ. Sci. Technol.* **39**, 311-316.

Tu, S., Racz, G.J. and Goh, T.B. (1994) Transformations of synthetic birnessite as affected by pH and manganese concentration. *Clays Clay Miner.* **42**, 321-330.

Zech, W., Schad, P. and Hintermaier-Erhard, G. (2014) *Böden der Welt: Ein Bildatlas*. Springer-Verlag.

CURRICULUM VITAE

Personal details

Name	Zahoransky, Teresa Elisabeth
Date of birth	03.01.1989
Place of birth	Lörrach
Citizenship	German

Education

07/2018 – today	PhD student Gottfried Wilhelm Leibniz Universität Hannover Thesis: 'Manganese speciation in Soil Studied by Mn K-edge X-ray absorption spectroscopy', supervised by Prof. Dr. Christian Mikutta
04/2013 – 05/2018	Master's studies in Mineralogy and Petrology Eberhard Karls Universität Tübingen Thesis: 'Chemical control of colour, luminescence and tenebrescence of natural sodalites', supervised by PD Dr. Michael Marks and Prof. Dr. Henrik Friis, in cooperation with the Natural History Museum Oslo, Norway
10/2009 – 09/2012	Bachelor's studies in Geosciences Eberhard Karls Universität Tübingen
10/2008 – 09/2009	'Studium Generale' at the Leibniz Kolleg Tübingen
2008	A-levels Gymnasium Schönau

Work experience

Since July 2018	PhD-Student of Soil Mineralogy, Institute of Mineralogy, Gottfried Wilhelm Leibniz Universität Hannover
2016 – 2018	Mine Geologist at the potash mine 'K+S', Werk Werra
2015/2016	Internship at 'K+S' potash mining company
November 2015	Internship at 'Terratec' geophysical services

2013-2015	Student research assistant at the mineralogical collections, Eberhard Karls Universität Tübingen
Spring 2013	Internship at the Natural History Museum Berlin
Winter 2012	Internship at the Natural History Museum Oslo, Norway
2011	Two months internship at the GFZ Potsdam, section 3.3 'Chemistry and Physics of geomaterials', Germany
2010 – 2012	Student research assistant (Petrology and Mineralogy), Eberhard Karls Universität Tübingen
Summer 2010	Student research assistant (Geomicrobiology), Eberhard Karls Universität Tübingen

Award

September 2021	1st price for the best oral presentation of young scientists, GeoKarlsruhe (DGGV)

LIST OF PUBLICATIONS

Journal Articles

Zahoransky, T., Kaiser, K., and Mikutta, C. (2022) High manganese redox variability and manganate predominance in temperate soil profiles as determined by X-ray absorption spectroscopy. *Geochimica et Cosmochimica Acta*, DOI: 10.1016/j.gca.2022.10.016.

Zahoransky, T., Wegorzewski, A.V., Huong, W. and Mikutta, C. (2022) X-ray absorption spectroscopy study of Mn reference compounds for Mn speciation in terrestrial surface environments. *American Mineralogist*, DOI: 10.2138/am-2022-8236.

Zahoransky, T., Friis, H., and Marks, M. A. (2016) Luminescence and tenebrescence of natural sodalites: a chemical and structural study. *Physics and Chemistry of Minerals*, *43*(7), 459-480.

Conference Talks

GeoKarlsruhe 2021 (DGGV):

Zahoransky, T., Wegorzewski, A.V., Huong, W. and Mikutta, C. X-ray absorption spectroscopy study of Mn reference compounds for the identification and quantification of Mn species in soils.

Annual DBG Meeting 2022:

Zahoransky, T., Kaiser, K., Mikutta, C. Manganspeziierung in Böden mittels Röntgen-absorptionsspektroskopie.

Poster

Hugo-Obermaier-Tagung Heidenheim 2015:

Loy, A. F. M., Mena, J. A., Ochs, U., Rebentisch, A., Schürch, B., Taipale, N., ... & **Zahoransky, T**. (2015) Chaîne opératoire of Molly, an Indian elephant from the Wilhelmina in Stuttgart-Bad Canstatt: Results of a workshop in Blaubeuren on the processing of Proboscidian ribs as raw material for tools.